DEVELOPMENT OF AN ACTIVE PULSED RADAR RECEIVER FOR A MONO-STATIC BOREHOLE-RADAR TOOL

Brian Keith Woods

(Thesis presented in partial fulfilment of the degree of Master of Engineering at the University of Stellenbosch)

March 2003

Study leaders
Prof. K.D. Palmer and Prof J.H. Cloete

UNIV.STELLENBOSCH
300 783 1073

Declaration

I, the undersigned, hereby declare that the work contained in this thesis is my own original work (unless otherwise indicated) and that I have not previously in its entirety or in part submitted it at any university for a degree.

Brian Woods

Date

Abstract

Borehole radar applications are far reaching in various fields, none more so than in the mining industry, where accurate, high resolution mapping of hidden geological structures and events is invaluable for mine development and planning. Borehole radar technology and methods have been under development for a number of years, and experimental surveys have delivered exciting and useful results. The tools used in existing borehole radar systems are generally bi-static, pulsed radar systems.

A brief study of an existing, operational borehole radar system is performed. Two sub-systems are identified for consideration in this report, namely the receiver and the radiating structure. The aim is to develop these sub-systems of the borehole radar system so that they can be employed in a mono-static borehole radar tool.

Computational methods are introduced and verified for analysis of radiating structures. Time domain methods and definitions are suggested to enable direct comparison. Existing radiating structures are critically analysed and a new symmetrical antenna form is suggested for mono-static application. Frequency and time domain characterization of the suggested antenna topology, with various resistive loading profiles in a simplified environment is performed. A parametric lumped element representation of the typical antenna impedance is extracted. The operational borehole radar environment is defined, and the effects of different environmental factors on the antenna structure are considered. A final antenna structure is suggested for mono-static application. A prototype antenna and probe structure is designed for field-testing purposes.

The operational requirements of a borehole radar receiver are considered, and receivers used in existing bi-static systems are characterized by measurement. The limiting factors of existing receivers for mono-static application are identified. A new receiver chain is suggested, and the identified limitations are addressed by the implementation of variable gain in the amplifier chain. The realized receiver circuit is characterized by measurement and comparatively verified during experimental field-testing. The operation of an integrated mono-static system is presented and verified by bench measurement. Data gathered during field-testing of the different mono-static sub-systems is also presented.

The antenna investigation presented suggests that the use of different structures in different operational environments may be necessary to facilitate acceptable and stable isolation. The variable gain receiver is able to operate in the mono-static configuration. Noise figure and sweep transient effects must still receive attention, however.

Opsomming

Boorgatradar het toepassings in verskeie velde; veral in die mynwese, waar akkurate, hoë resolusie uitbeeldings van versteekte geologiese strukture van onskatbare waarde is vir mynontwikkeling en -beplanning. Boorgatradar tegnologie en metodes word al vir etlike jare ontwikkel, en eksperimentele veldtoetse het reeds belowende en nuttige resultate opgelewer. Die instrumentasie wat in bestaande boorgatradarstelsels gebruik word kan oor die algemeen as bi-statiese, pulsradarstelsels beskryf word.

'n Studie van 'n bestaande, operasionele boorgatradarstesel word vlugtig beskryf en twee substelsels van die radar word geïdentifiseer vir verdere ondersoek: die ontvanger-elektronika en die stralingstruktuur van die stelsel. Die doel is om hierdie stelsels te ontwikkel tot 'n punt waar hulle as deel van 'n monostatiese boorgatradar instrument geïntegreer kan word.

Numeriese modeleringsmetodes word voorgestel en geverifiëer vir die analise van straling-strukture. Tydgebied-metodes en definisies word spesifiek voorgestel om direkte vergelyking te kan bewerkstellig. Bestaande stralingstrukture word krities evalueer en 'n simmetriese antenna word voorgestel vir die monostatiese toepassing. Frekwensie- en tydgebied karakterisering van die voorgestelde antennetopologie, met verskillende weerstandsprofiele in 'n vereenvoudigde omgewing, word uitgevoer. 'n Parametriese, diskrete komponent voorstelling van die tipiese antenna impedansie word onttrek. Die operasionele boorgatradar omgewing word gedefiniëer, en die effek van verskeie omgewingsfaktore op die funksionering van die antenna word kortliks ondersoek. 'n Finale antennastruktuur vir monostatiese toepassing word voorgelê, en 'n prototipe antenna en probestruktuur word ontwerp vir veldtoets-doeleindes.

Die operasionele vereistes van 'n boorgat-radarontvanger word oorweeg en 'n bestaande bi-statiese ontvangerstelsel word gekarakteriseer deur meting. Die beperkings wat die aanwending van so 'n ontvanger in 'n monostatiese toepassing verhoed, word geïdentifiseer. 'n Nuwe ontvanger word voorgestel, en die monostatiese beperkinge word deur middel van die implementering van verstelbare aanwins in die ontvangerketting aangespreek. Die onvangerbaan word deur meting gekarakteriseer en geverifiëer gedurende eksperimentele veldtoetse. Die operasie van 'n volledig geïntegreerde, monostatiese radar word voorgelê deur middel van laborarorium metings en data versamel tydens veldtoetse.

Die antenna-ondersoek wat voorgelê word in hierdie verslag stel voor dat die gebruik van verskeie antennes in verskillende omgewings dalk nodig sal wees om aanvaarbare isolasie in die monostatiese stelsel te bewerkstellig. Die verstelbare aanwins ontvangerkonsep lewer 'n ontvanger op wat in staat is om onder monostatiese omstandighede te funksioneer. Ruissyfer en ongewensde oorgangsverkynsels tydens aanwinsverstelling moet aandag kry.

Acknowledgements

First and foremost I would like to thank God for affording me both the opportunity and the ability complete this thesis.

To Prof J.H Cloete and Prof K.D Palmer: Thank you for your guidance, wisdom and enthusiasm during the past two years. You have both truly been an inspiration.

To Prof I Mason: Thank you for taking such a keen interest in everything that we do. I have learnt a lot from you, and look forward to learning even more.

To Paul Van der Merwe: It has been great working with you the last two years. See you again next year. (GEOMOLE SA bo!)

To Paul Herselman, Beukes Kotze, Wernich De Villiers and the *Molshoop:* Thanks for being a great bunch. Working with you all was an immense pleasure (and a bit of fun every now and then).

Wessel Croukamp: Thank you for all your patience, hard work and willingness to help. It is much appreciated.

To Ant: You are the best.

To my father and brothers: Thanks for your support and love. You all mean a lot to me.

Lastly, I would like to extend my gratitude to DEFENCETEK for their financial support during the course of my study.

Table of contents

List of figures

List of tables

Chapter 1 Background

1.1. Introduction

In this thesis, a number of issues are considered, with the final goal of delivering a well-characterized receiver and antenna structure suited to application in a mono-static borehole radar system. These objectives are stated in detail in section 1.5, after relevant background information has been presented in sections 1.2 to 1.4. During the development process, prototyping of designs is discussed and results of field tests are used to motivate improvements and design changes.

The study development documented in this report can be depicted as in the flow chart of Figure 1.

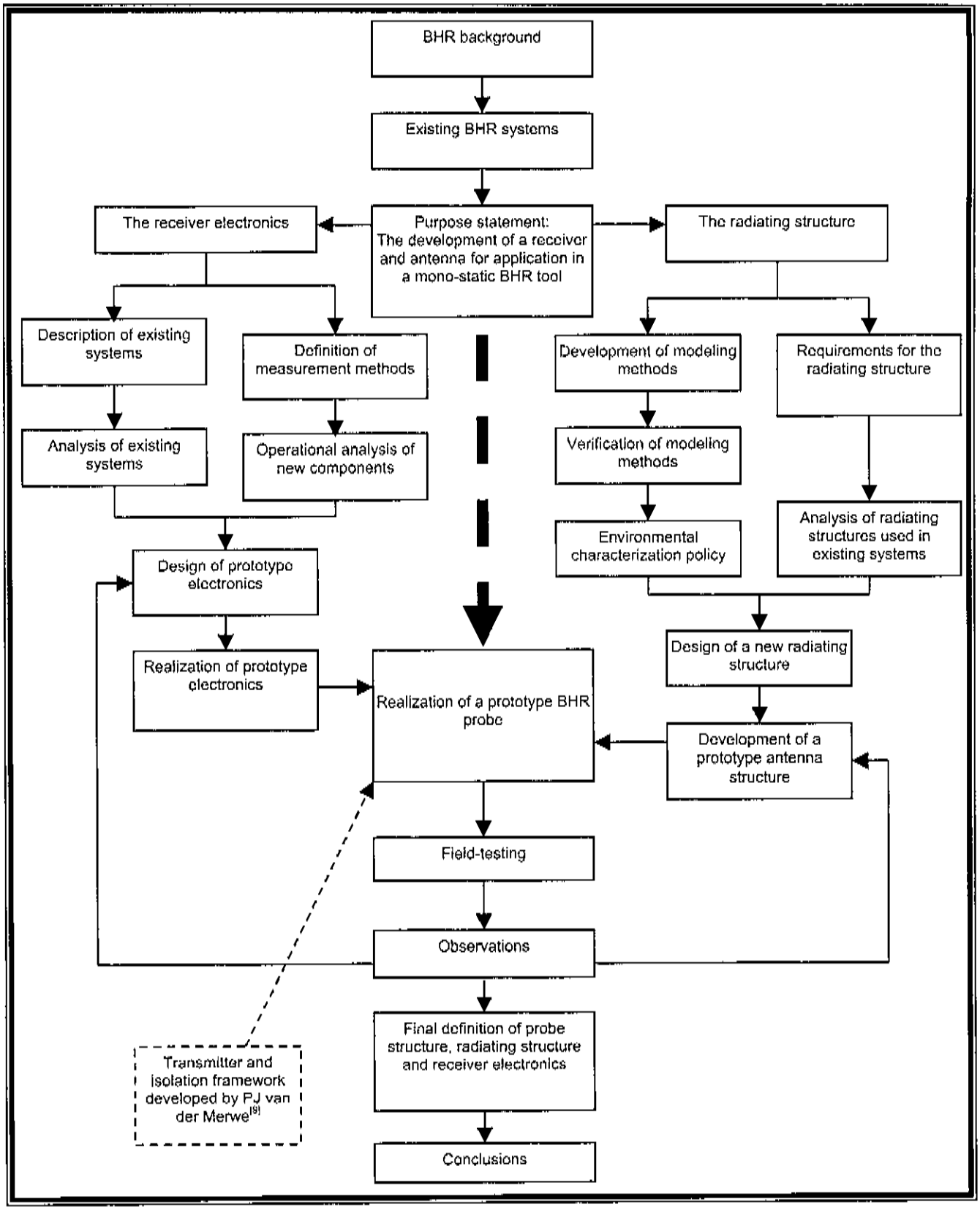

Figure 1 A flow chart detailing the study approach documented in this report

1.2. Introduction to GPR

In this section, we will present a short description of the ideas and concepts that form a basis for ground penetrating radar (GPR).

Ground or surface penetration radar (GPR) refers to the use of high and medium power radio and microwave frequency signals (approximately 1-2000 MHz) to generate an image of any underground object or anomaly without physical removal of the ground surrounding the object. This form of radar generally has applications in the delineation and characterization of structures under the earth's surface (geological or otherwise), but similar ideas and systems can be used for non-destructive study of the internal structure of non-geological objects. In this report, the geological applications of GPR will be under consideration, particularly with respect to subsurface surveys ahead of mining.

The basic principle of operation of subsurface radar is the same as any conventional radar. A number of intrinsic differences however exist, mainly due to the different electromagnetic properties of the media surrounding the radar targets of interest.

Traditional subsurface radar measurements are made by transmitting radar signals from the surface into the propagation media, and again receiving the reflected data at the surface for processing and analysis. The three main deployment methods for conventional GPR surveys are shown in Figure 2 [2].

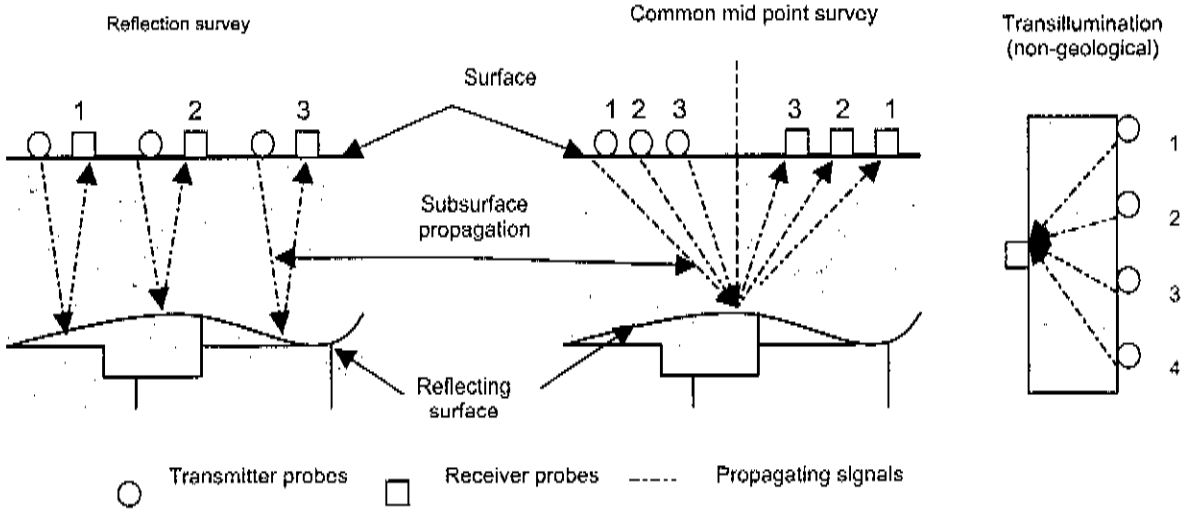

Figure 2 The progression of three generic GPR deployment topologies

Borehole radar (BHR) uses the same principles as GPR, but both the transmission and receiving of the radar signals occur below the surface resulting in structural information referenced to an internal point instead of to a point on the surface. The advantages of BHR are obvious in the case of geological imaging, where objects of interest are too far from the surface to be studied with sufficient resolution by

traditional GPR without the transmission of impractical amounts of power. In such a case, the region of interest can be approached by sinking a small diameter borehole and geological data then gathered using BHR.

Knowledge of the geological structure ahead of mining has two main advantages. The first advantage is that knowledge of the positions of potentially dangerous areas means that better preparation can be made to prevent accidents. The second advantage is that the most economical method of reaching a targeted ore body can be determined before mining, minimizing cost and effort.

1.2.1. Some basic GPR theory

Basic GPR theory is very strongly linked to the characteristics of propagation of electromagnetic energy and the effects of material properties on this propagation. In the far-field, EM signals consist of coupled time varying electric and magnetic fields perpendicular to each other and to the direction of propagation. The electric and magnetic properties of the propagation medium have a large effect on the spreading of energy and any well-defined sudden variation in the material properties will result in reflection, refraction or diffraction of a percentage of the incident energy. The analysis of these reflections forms the basis of GPR image extraction.

The accurate analysis and characterization of the propagation properties of various composite materials is a complex problem, dependant on a number of variables including the percentage content of the various constituent elements, the water content and ion densities of the rock material etc. A short summary of the symbolic calculation of relevant propagation characteristics will be given in this section. A closer look at the mechanics of propagation and a short discussion of its influence on the GPR problem can be found in Appendix A.1. Further information is available in the literature[2], [3],[12],[21],[16].

The two main propagation characteristics based on the material properties that can be identified in connection with GPR theory are the attenuation and propagation velocity of travelling EM energy as defined by equation (1.1).

$$W(x,t) = e^{i(kx-\omega t)}$$

$$where$$

$$k = \frac{\omega}{v} - i\alpha$$

$$and$$

W = The time and frequency dependant amplitude of a traveling EM wave (1.1)

x = The distance traveled by the EM wave

t = Time

ω = Frequency in radians per second

v = The propagation velocity

α = Attenuation (neper/m)

k = The propagation constant

In most cases of interest to GPR applications these properties for a particular propagation material can be approximated by equations (1.2) to (1.4), where the various material properties are: ϵ=relative permitivity, tanδ=dielectric loss tangent and σ=conductivity in mS/m.

$$\tan\delta \approx \frac{17.8\sigma}{\varepsilon f_{MHz}} \tag{1.2}$$

$$v = \frac{3\times10^{8}}{\sqrt{\varepsilon}} m/s \tag{1.3}$$

$$\alpha = 1.64\frac{\sigma}{\sqrt{\varepsilon}} dB/m \tag{1.4}$$

At a border defining a change in the attenuation and propagation velocity properties of the propagation medium, reflection of incident energy occurs which can be described in terms of a reflection coefficient defining the percentage energy reflection. This relationship is based on the relative dielectric properties of the two materials. If an incident EM plane-wave of energy E travelling in a medium of dielectric constant ϵ_1 reaches a border with a material of dielectric constant ϵ_2, then a fraction $|\Gamma|^2$ of the energy will be reflected at the border, and fraction, $|\tau|^2$, of the energy will be transmitted, and propagate into material two. τ and Γ are defined by equation (1.5). (Note that these definitions assume lossless materials.)

$$\begin{aligned} \Gamma &= \frac{\sqrt{\varepsilon_1}-\sqrt{\varepsilon_2}}{\sqrt{\varepsilon_1}+\sqrt{\varepsilon_2}} \\ \tau &= 1-\Gamma \\ E_{reflected} &= |\Gamma|^2 E \\ E_{transmitted} &= |\tau|^2 E \end{aligned} \tag{1.5}$$

The acquisition and processing of the data resulting from sensing of these reflections forms the basis on which the whole GPR imaging theory is built. From calculations based on the time that a transmitted EM wave takes to travel to and return from a target, the distance to the target can be determined. The geometric as well as material properties of the target can then also be extracted based on the form, magnitude and time/space variation of the reflected signal.

The second consideration affecting the magnitude of signals in a GPR, and indeed any radar system, is the drop in magnitude of a transmitted signal, due to the spreading of energy. This effect is described by the radar or Friis equation [10]. According to the radar equation, the drop-off in signal magnitude is proportional to $1/R^4$ where R is the propagation distance to and from a point target. Following the same

derivation of the Friis equation for normal incidence on a planar target the drop off in signal magnitude, because of spreading of energy, is with an R^2 factor.

1.2.2. Specialization to Borehole radar applications

The application of general GPR to a typical borehole radar environment imposes a number of new challenges that must be considered in the design process. Most of these problems arise due to the spatial limitations of the borehole, which affect the possible physical dimensions of the system, the methods of deployment, etc. and the great variation in the electromagnetic properties of the environments in which the system must operate.

In order to facilitate the introduction of a few of these challenges, and the way in which they have been approached in existing systems, a summary of a report documenting the realization of an ST-type borehole radar system[1] will be given in this section. This report details the state of the BHR technology at the commencement of this thesis.

We will begin by considering the general structure of the full system, and then summarize the detail of the main components of the ST-type system - the transmitter, the receiver and the spacer.

1.3. Description of the 'ST' borehole radar system

The 'ST'-type borehole radar system derives its name from the use of 'ST'-type optical connections in the internal probe structure, as opposed to LEMO connections used in earlier borehole radar systems.

1.3.1. Overview of the ST-type system

The ST borehole radar system consists of five separate sub-systems as shown in Figure 3.

The transmitter probe is a free-running pulse radiator, radiating broadband pulses into the surrounding rock at regular time intervals. The transmitter probe is connected to the receiver probe by a short optical section, or spacer.

The optical channel on the spacer conveys a trigger pulse from the transmitter, used to facilitate coherent data processing. The main purpose of the spacer section is to physically separate the receiver and transmitter probes, providing spatial isolation for the sensitive receiver electronics during the transmit period.

The receiver probe contains a low noise amplifier chain and an optical modulator that transmits any received reflections to the surface located data acquisition system for digitisation, storage and processing. The optical cable that carries the received data has a second channel that conveys the trigger signal from the transmitter probe to the DAQ.

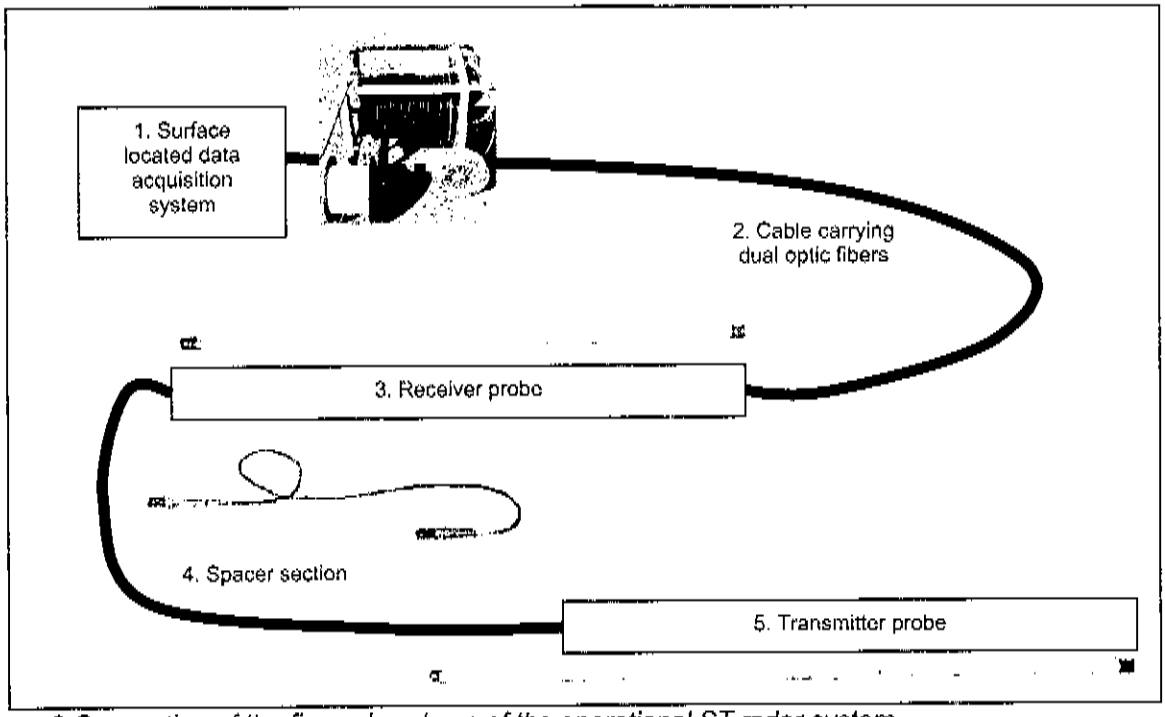

Figure 3 Connection of the five subsystems of the operational ST radar system

The application of a BHR system to map structures and events of importance in the mining industry results in two general configurations shown in Figure 4 that are used to gather information.

The first configuration consists of a single borehole into which both a transmitter and receiver probe are inserted, separated by a spacer. All geological reflections as the radar moves along the shot line, can then be recorded. The transmitter and receiver are assumed to be co-located during data post-processing.

The second configuration employs a number of boreholes. A transmitter (or a transmitter/receiver combination) probe is sent along the one borehole, while receiver-probes are deployed in the other holes. By coordinating the positions of the various probes with respect to each other, data about both the time propagation properties between the transmitter and various receiver probes and any resultant geographical reflections can be gathered.

The second deployment configuration will in general generate more information about the environment and will cover a larger area with a single measurement. Practical considerations, like the positioning and availability of boreholes, the need for multiple probes and the needed capacity for simultaneous acquisition of a number of data streams may however limit the application of this survey technique.

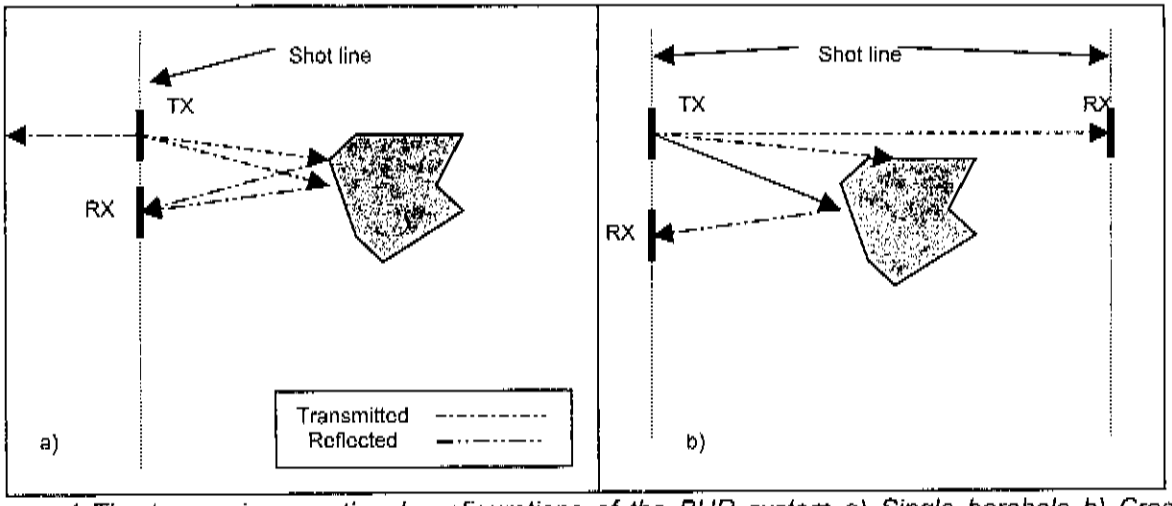

Figure 4 The two main operational configurations of the BHR system a) Single borehole b) Cross-borehole

1.3.2. The ST transmitter

1.3.2.1. Functional overview

The ST transmitter probe layout is sketched on a system level in Figure 6.

A simple resistively loaded Wu-King type antenna is used in both the transmitter and receiver probes[22]. This antenna is not symmetrical, with a single resistively loaded arm, driven against a copper pipe housing the transmitter electronics and the battery pack. This housing forms the ground of the probe electronics.

1.3.2.2. The functional blocks of the transmitter electronics

The operation of the ST-transmitter is based on the switching of a high-voltage line to ground in a short period, using a MOSFET[3]. Broadband radiation is achieved on the resultant sharp falling edge.

A. The power supply and voltage regulation

The power supply for the TX-module is a 24V battery pack comprising a battery of 20x1.2V, 1400mAh NiCd cells, recharged at a standard 140mA for 14 hours.

Standard voltage regulators are used to generate regulated 5V and 12V supplies required for the various components of the circuitry from the battery pack voltage. The LM7812CT is used for the 12V regulation and the MC78L05CD for the 5V regulation.

The maximum theoretical operating time of the TX-probe is approximately 16 hours.

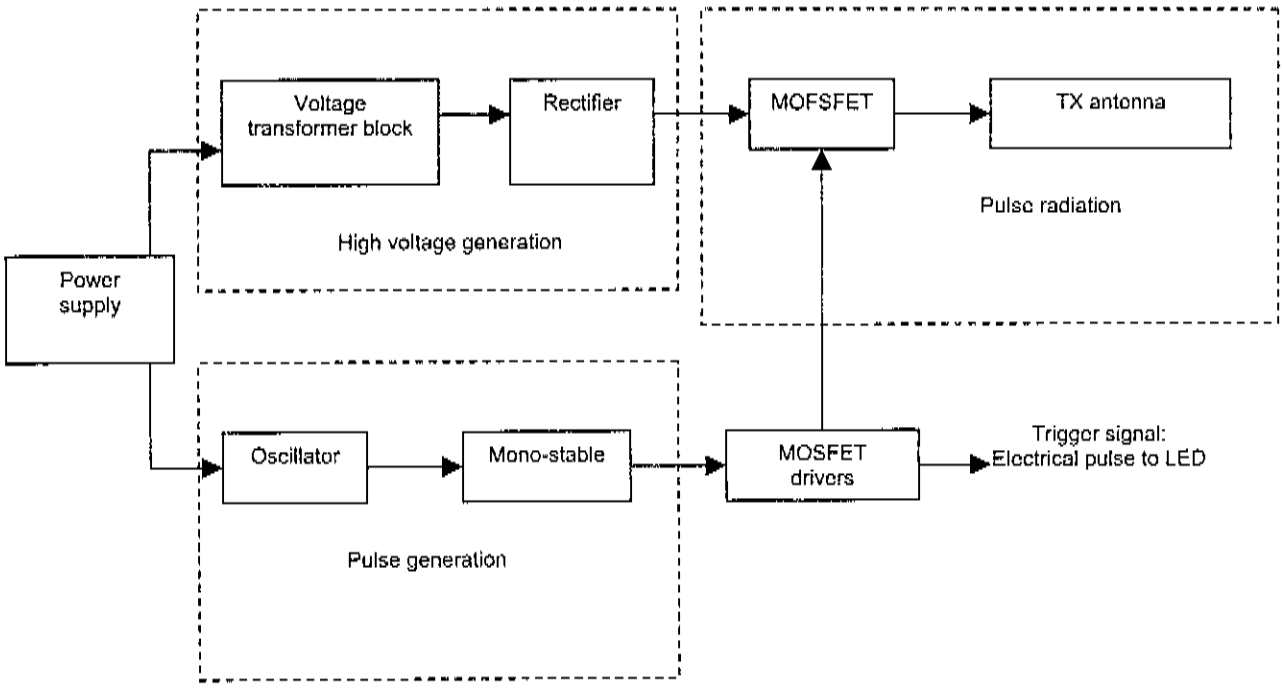

Figure 5 A functional block diagram of the transmitter circuitry.

B. The Pulse Generation Block

The pulse generation block is used to generate the pulses that switch the MOSFET drivers. An oscillator sets the PRF, and a one-shot mono-stable alters the pulse width, and the pulse form. A '555-timer' (LM7555) is used to generate a square wave at the desired PRF. A mono-stable (74HCT221D) is driven from the 555-output signal, to generate the pulses that drive the MOSFET drivers, which in turn pulse the antenna-driving MOSFET and generate the optical trigger signal.

Measurements made on the current TX design show a PRF frequency of 1.225kHz with a duty cycle of 62,7%.

The mono-stable output of the TX circuitry was measured as a 300nS pulse. The fall and rise time for all the measured pulses was measured in the order of 4nS.

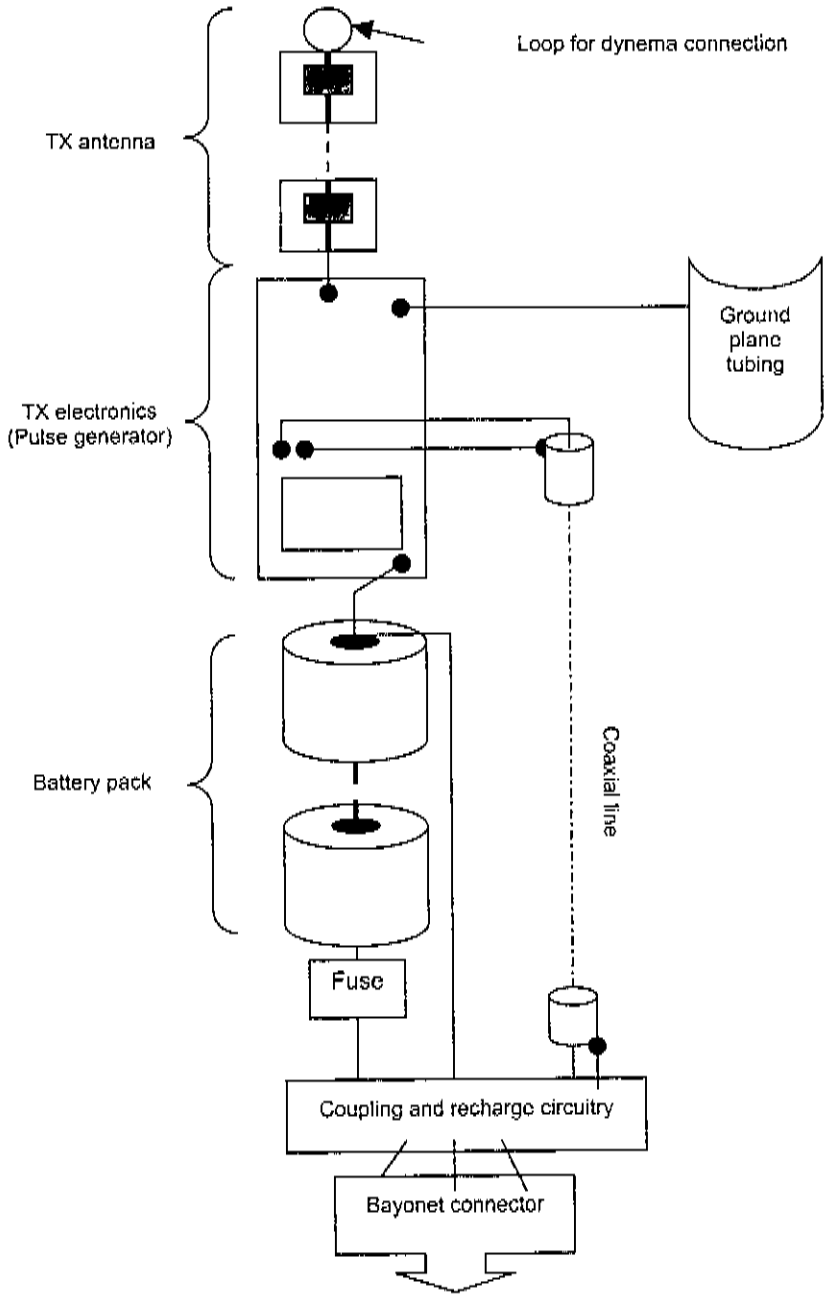

Figure 6 Functional representation of the transmitter probe structure

C. The pulse radiation block

This block consists of a MOSFET (STU6NA90), driven by the MOSFET driver circuitry used to switch the antenna. The application schematic of the MOSFET switching structure is shown Figure 7.

The MOSFET connects the antenna feed to ground potential through a small impedance when it is switched on. The feed is held at the voltage of the high voltage generation block during the MOSFET

off period. The sharp falling edge during switching generates a broad-spectrum pulse that travels along the antenna, and radiates into the surrounding media.

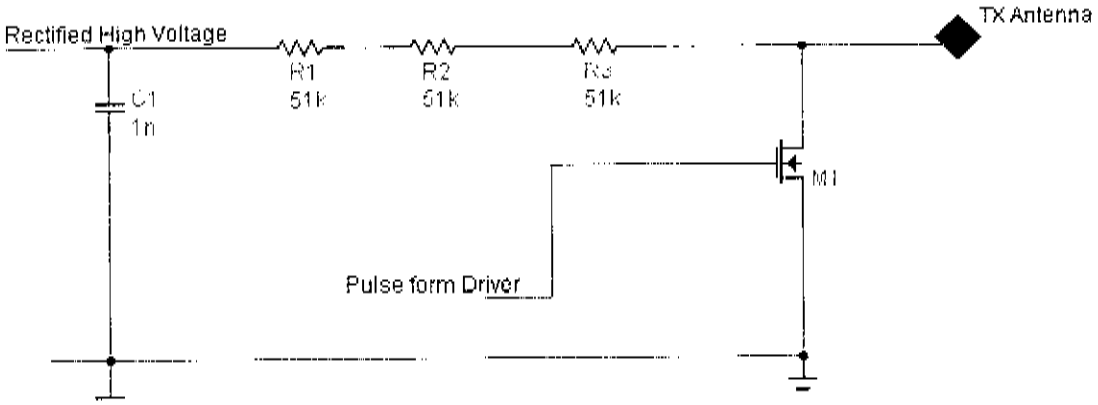

Figure 7 The MOSFET connection to the antenna structure.

The form of the pulse, generated by the MOSFET circuitry, at the unloaded antenna feed (i.e. no antenna connected) is shown in Figure 8. The sharp falling edge of the pulse is clear from Figure 8, but the rise time of the pulse is much longer (measured as 19,3 µS rise time and a further 44 µS settling time). Radiation over a broad spectrum will result from the falling edge. The rising edge will not cause much radiation in the band of interest.

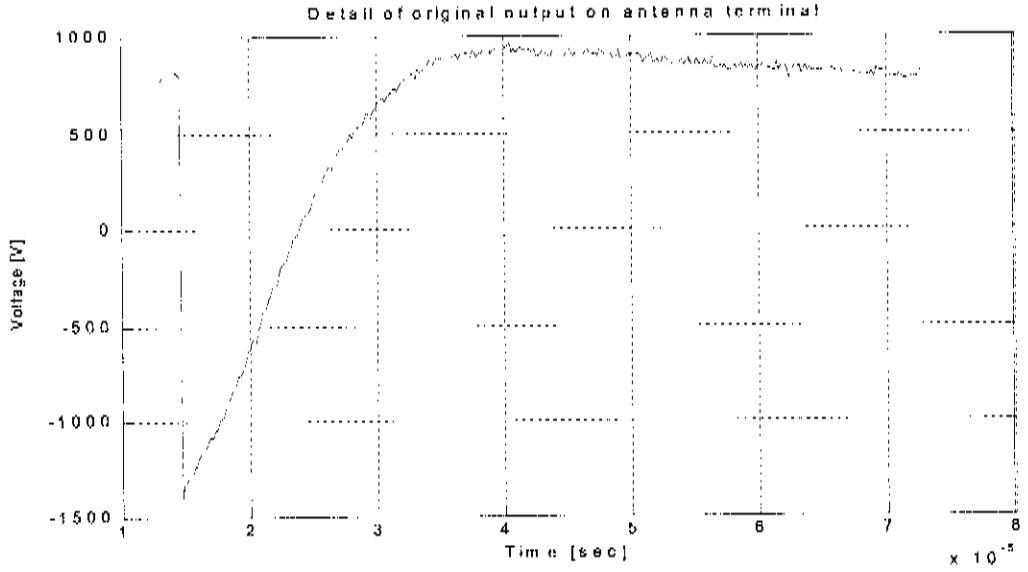

Figure 8 The measured transmission pulse in the current system

The measured value of the high-voltage line is 785V. It is clear that a fast transition from this high voltage to ground is realized by the circuitry. This transition can be used to drive a radiating structure over a broad frequency band. Fourier analysis of the measured pulse form indicates that it has

considerable spectral components up to around 100MHz, although their magnitude does drop off with an increase in frequency. This pulse is thus acceptable for the broadband requirement of the BHR application.

D. The MOSFET driver circuitry

Two MOSFET driver chips (TC4422CPA) are used in parallel to drive the antenna-switching MOSFET, and one to drive the LED driver for the trigger signal.

An extremely fast fall time of approximately 8nS is achieved with the MOSFET switching scheme used in this probe. The driver pulse form and timing seems to be independent of the loading within conceivable boundaries.

E. The high voltage level generation block

This block converts the battery voltage (~24V) up to a high voltage, which is then rectified and filtered to give the high DC voltage that is used to charge the antenna.

A Datatronic (PT27707) voltage transformer is used. The circuitry of the PT27707 is standard, and comprises a few discrete components to form the oscillator circuit for the up-converter. The schematic of the high voltage generation block is shown in Figure 9.

The voltage after rectification is measured as approximately 820V in the current circuit, with ~100V variation around this mean value. A capacitor is used to smooth this variation. The ripple on the rectifier output was measured and is shown in Figure 10.

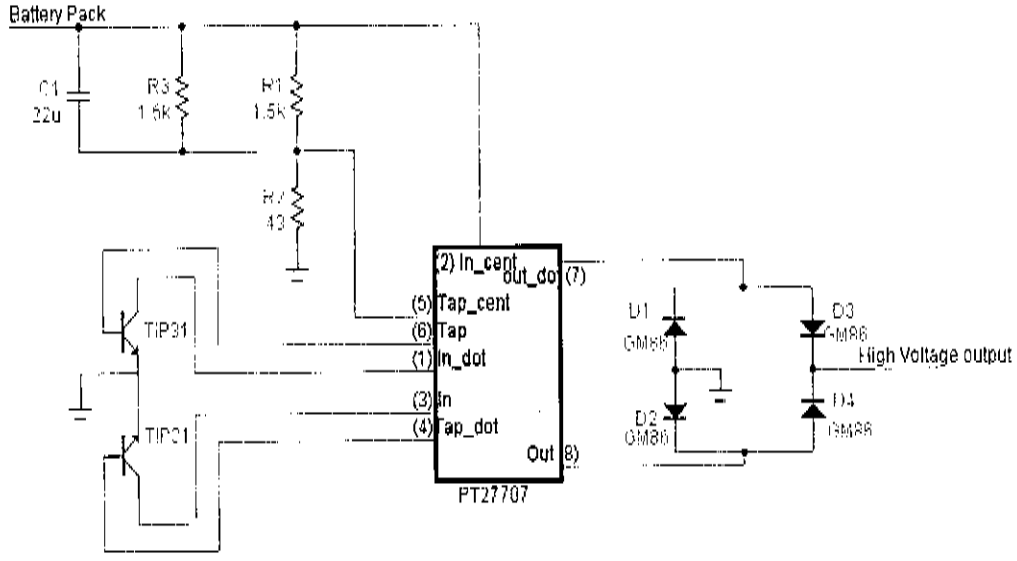

Figure 9 The schematic showing the application of the PT27707 in the high voltage block of the ST system TX-probe.

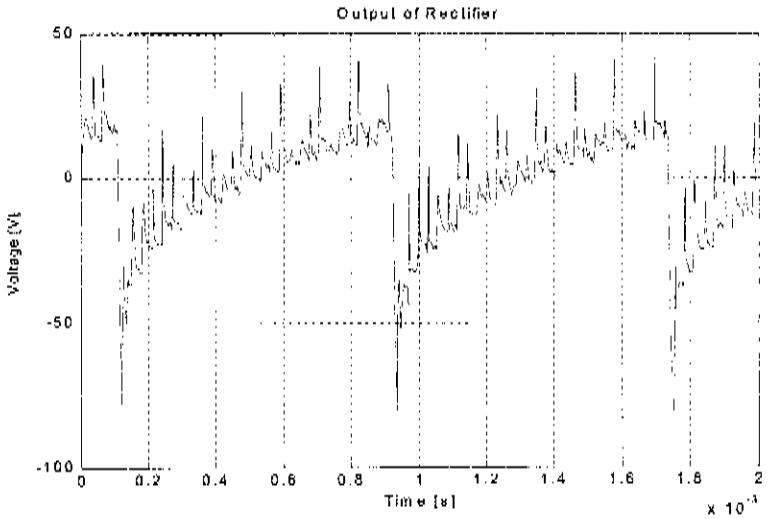

Figure 10 The measured rectified output of the high voltage generation circuit (the measurement is an AC-coupled one, and the shown output ripple is thus superimposed on 820V DC)

F. The trigger signal

The data acquisition system needs a reference to determine the beginning of each acquisition cycle, so that accurate calculation of the propagation times of received data can be made during data processing. The pulse from the mono-stable is thus transmitted to the DAQ as an optical signal on a separate channel to serve as the trigger reference. To eliminate the need for a make-break connection in the optical fibre, the signal is carried across the connector (between transmitter and spacer) electrically and fed into an LED optical converter located inside the spacer connector. This signal is sent via a coaxial cable past the batteries to the connector, as is will not interfere with, or be affected by the radiation of the antenna while inside the copper pipe.

The trigger pulse that is used to drive the spacer located LED is measured as shown in Figure 11, with a higher resolution form of the actual pulse shown in Figure 12.

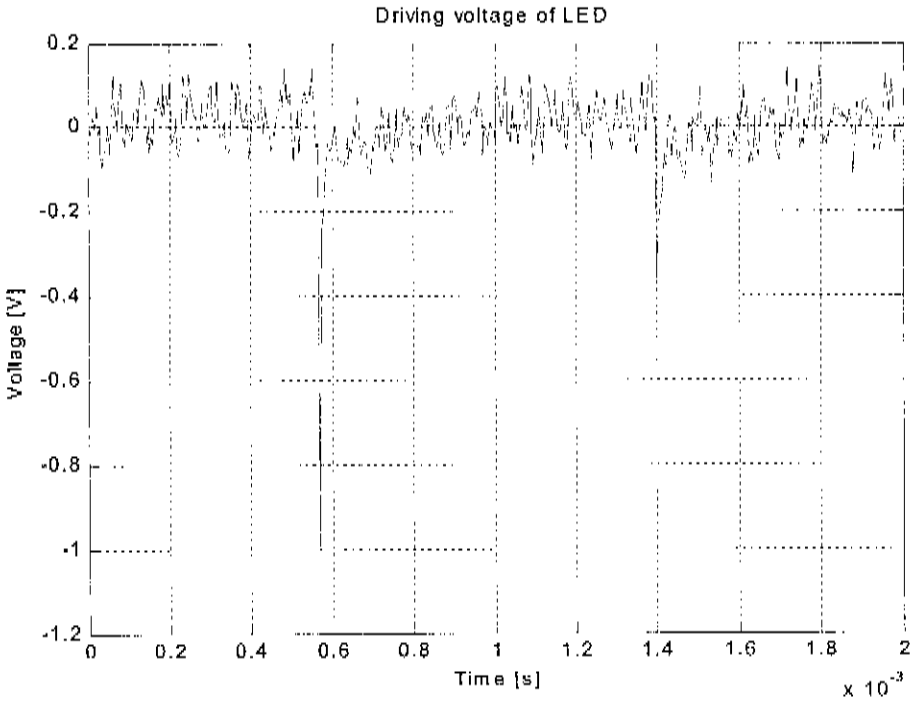

Figure 11 The measured DAQ trigger pulse

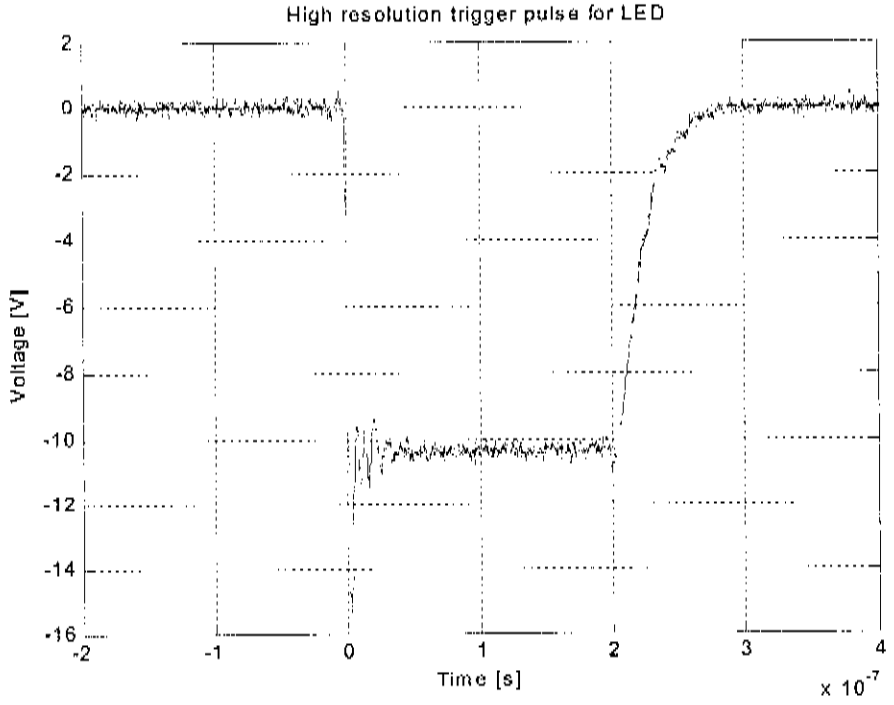

Figure 12 The high-resolution shape of the trigger pulse

1.3.3. The spacer

In the 'ST'-type system, the 'ST' optical connections are employed, as opposed to LEMO connections used in other systems. The advantages of this advance are twofold. Firstly, dependence on expensive LEMO components with long lead times is solved, and exclusively electrical spacer-probe connections are realized, making optics-free probe construction possible.

1.3.3.1. Functional Overview

The spacer is used in a single borehole survey, where the transmitter and receiver probes are deployed in the same borehole at the same time. The non-conducting spacer serves two purposes in such a case. The main purpose is to limit the direct coupling between the receiver and the transmitter when it fires. The second purpose of the spacer is to conduct the trigger signal generated by the transmitter, to the receiver probe. In order to maintain the spatial isolation between the TX and RX probe, an optical channel is used in the spacer. A functional block diagram of the spacer structure is shown in Figure 13.

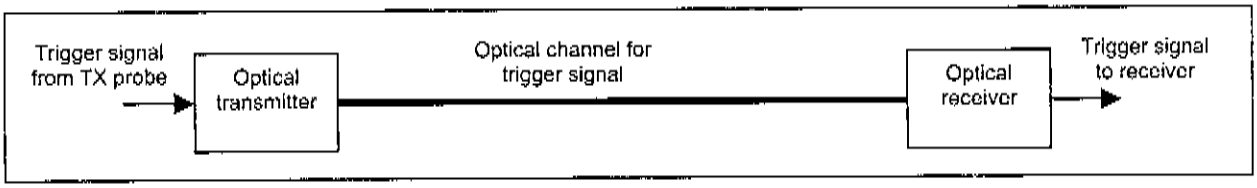

Figure 13 The functional structure of the spacer

1.3.3.2. The functional blocks of the spacer electronics

The spacer electronics are simple, and are powered from the connections to the transmit and receive probes. The TX side is simply an optical LED pulsed by the trigger signal, while the RX-side electronics are used to convert the optical trigger signal back into an electrical form.

A. Optical transmitter

The spacer electronics on the TX-side consist of a simple LED in series with a current limiting resistor. The circuit is shown in Figure 14.

The connection between the spacer and the TX-probe is a single coaxial MCX-connector, which conducts the trigger signal to the spacer.

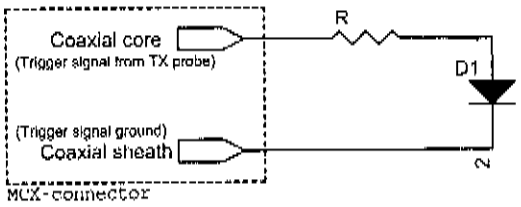

Figure 14 The TX-side electronics of the spacer.

B. Optical demodulator

At the RX-side of the spacer, the optical trigger signal has to be demodulated to an electrical one that can be passed through the connection to the RX-probe, where it will again be optically modulated and transmitted to the surface-located data acquisition system on one of the two fibre-optic connections to the surface. The circuit used for the demodulation is shown in Figure 15.

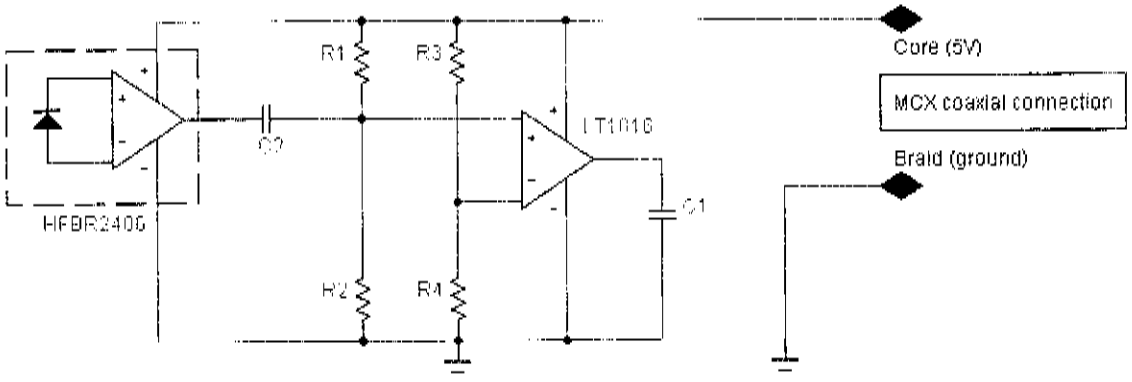

Figure 15 A schematic of the RX-side spacer electronics.

The operation of the circuit is clear if we note that, in the case of a pulse input into the optical receiver component (the HFBR2406), the positive input of the LT1016 op-amp will be pulsed below the reference level set by the resistors R3 and R4. Because there is no feedback in the op-amp circuit, the op-amp will try and drive its output to the opposite rail. Now, by letting the capacitive load on the op-amp (C1) be large, we can induce a spike on the 5V supply line as the op-amp tries to charge the capacitor. As we have noted earlier, the form of the trigger pulse is not of importance, and the pulse formed on the 5V coaxial power line can thus be used as a trigger reference in the receiver.

1.3.4. The receiver

1.3.4.1. Functional Overview

A systems level layout of the receiver probe is shown in Figure 16. It includes both the mechanical and electronic subsystems. An enlargement of the electronics is shown as well. A detailed discussion of the individual functional blocks follows.

A reflected signal is received by die receiver's antenna, which is then amplified by the electronics and converted to an optic signal. Power is supplied to the electronics via a battery pack and additional circuitry is included to charge the batteries and switch the system on.

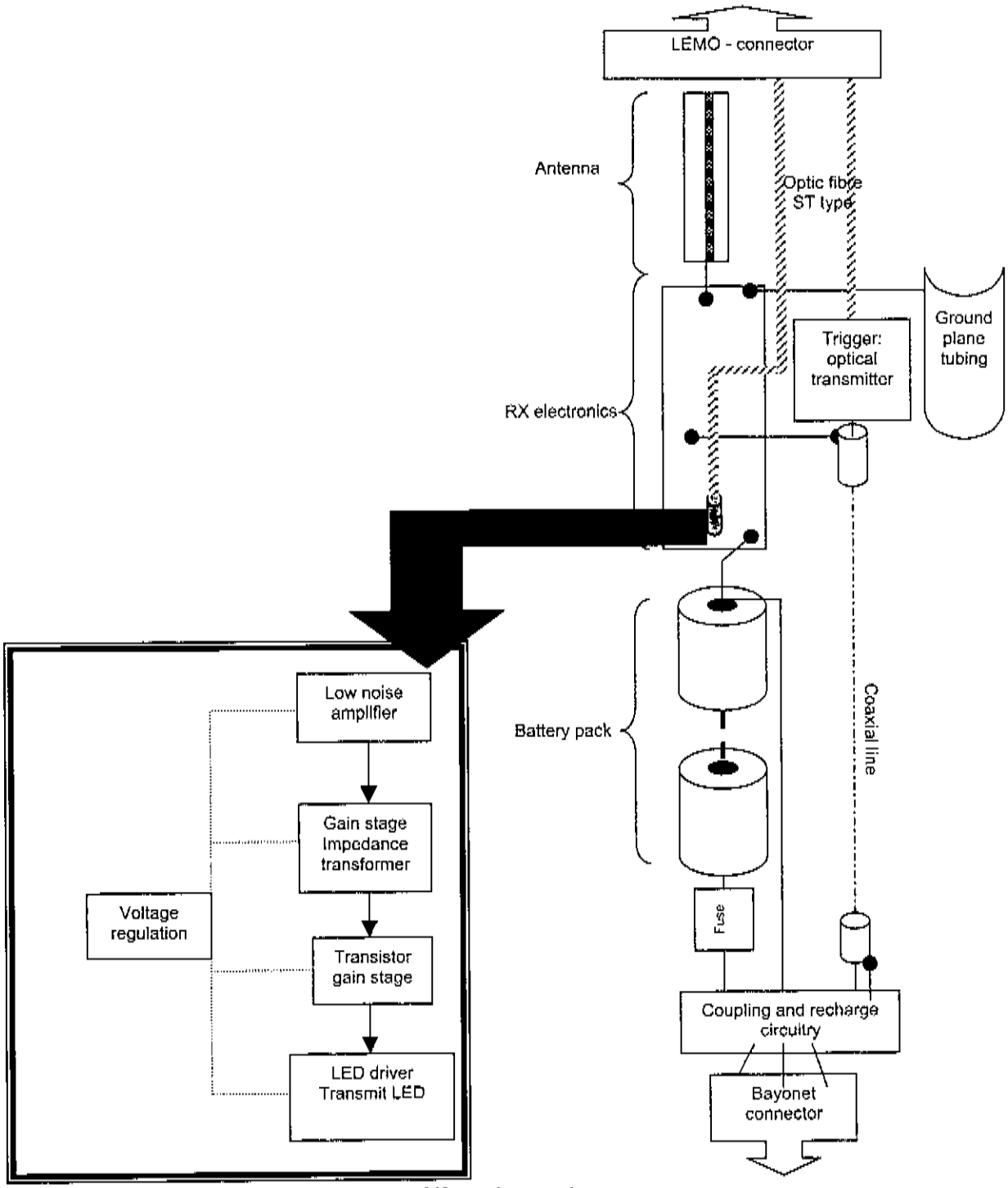

Figure 16 Functional block diagram of the ST receiver probe

1.3.4.2. The functional blocks of the receiver electronics

A. Battery pack and voltage regulation

The battery pack supplies approximately 18V, which is regulated down to 12V and 8V levels with the following components: 8L08A (8V) and LM340S (12V).

The battery pack of the receiver probe consists of a battery of 15 x 1.2V, 1400mAh NiCd cells that supply 18V when fully charged. The 8V-regulator output supplies power to the 2nd amplifier stage, while the 12V-regulator supplies power to the low noise amplifier, the transistor stage and the LED-circuitry. The operational lifetime of the probe is calculated at 15.2 hours from a fully charged battery pack.

B. Low Noise Amplifier stage

A Low Noise Amplifier (LNA) is the first amplification stage in the receiver. It amplifies the signal received on the antenna and feeds it to the second gain stage. The component used is an Amplifonix TN7101. The circuit is shown in Figure 17.

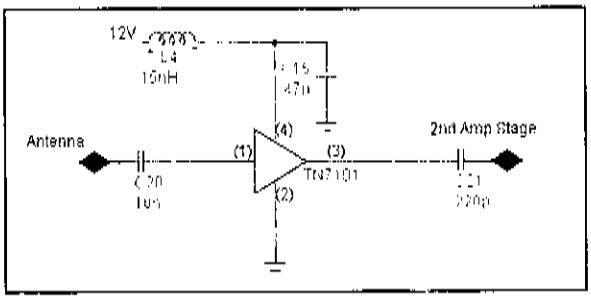

Figure 17 Circuit diagram of LNA-stage

This stage is critical to the operation of the receiver, and it must have both low-noise and relatively high gain characteristics. The LN7101 has a minimum specified gain of 26 dB over a frequency band from 10 MHz to 150 MHz, with a worst-case noise figure of 2.5 dB. The input impedance of the amplifier varies around 50 ohm.

C. 2nd Amplifier stage

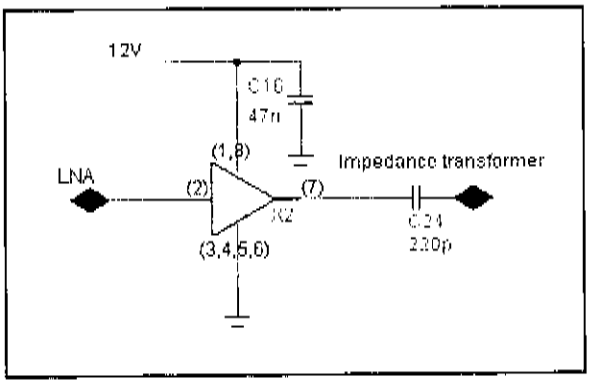

Figure 18 Circuit diagram of 2nd gain stage of the ST receiver

Additional gain is achieved by the 2nd gain stage, which comprises of a Philips NE5204 (alternatively NE5204A) amplifier. The circuit diagram is shown in Figure 18.

This component can be modelled as a simple gain block of 20dB with a –3dB bandwidth of 350 MHz. The noise figure (6dB) is much higher than that of the previous stage though. The component will saturate at an output of 7dBm (5mW)– which translates to 0.5V into a 50Ω load.

D. Impedance transformer

An impedance transformer is used to match the 50Ω output of the last amplifier stage to the 450Ω input of the transistor stage that follows it. A Mini-Circuits TMO-9-1 transformer is used.

The component is specified to have an impedance ratio of 9:1 in the frequency band from 150 kHz to 200MHz. The input is driven by the 2nd amplifier stage; the input is 50Ω and output 450Ω. Since the transistor stage is in effect, a transducer gain (voltage to current) the output voltage is more important than the output power. The power into and out of the transformer stays the same while the characteristic impedance increases 9 times, resulting in a voltage gain of three (9.54dB).

E. Transistor amplifier

A transistor amplifier stage is used to create a voltage controlled current source to drive the LED-module.

It consists of:

- Common emitter configuration (using a Silicon electronics BFR92P NPN transistor.)
- Current gain (using a Zetec ZTX325 NPN transistor.)

The common emitter circuit is carefully designed as an RF amplifier and should have a bandwidth that reaches from at least 10 MHz to 100MHz. The bandwidth of this stage is investigated through simulation. The simulated frequency response of the transfer function is shown in Figure 19.

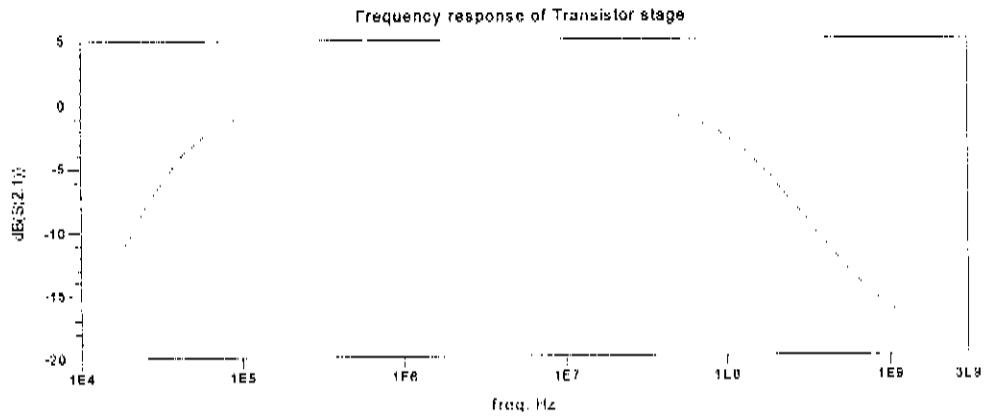

Figure 19 Frequency response (transfer function) of transistor stage (normalized amplitude)

F. Trigger signal electronics

The trigger signal from the spacer enters the RX-probe in an electrical form. The coaxial-type connection carrying the trigger signal enters a simple electrical-to-optical conversion circuit where it is converted into an optical signal that can be transmitted to the DAQ on one of the channels of the fibre-optic cable. A schematic of the circuit is shown in Figure 20. A High speed Linear Technology LT1016 comparator is used.

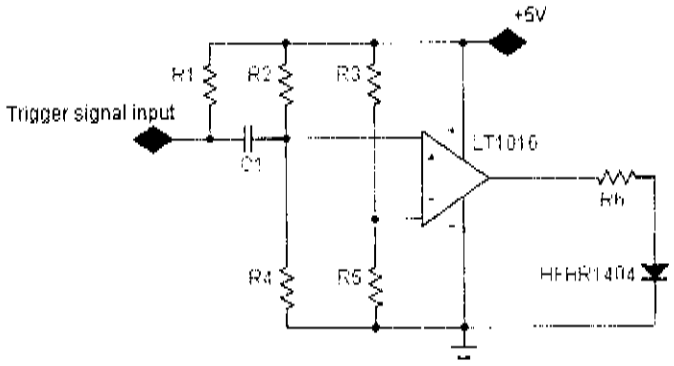

Figure 20 Circuit diagram of trigger electronics in the ST receiver probe

The signal received from the coaxial core is in fact the supply voltage of the spacer's comparator, which indicates a trigger signal by a slight voltage dip.

1.3.5. The Data acquisition system (DAQ)

The data acquisition system used the ST-system employs a PC-104 application specific embedded system, with ADC expansion boards to acquire, stack and store the received data and trigger signals. A functional block diagram of the system is shown in Figure 21. The system building blocks and their functions are as follows.

The optical cable: This is a 2-fiber cable, supplied by OCC (optic cable corporation). It has a 100/140μm core, specified as having 4dB loss per kilometre. The phase response of the cable is linear over the frequency range of interest.

The optical demodulator and signal conditioning circuitry: An Agilent HFBR2406 optical demodulator is used on each of the two channels to convert the optical trigger and RX signal back to an electrical form. The electrical signals are amplified after demodulation to remove the effect of any losses in the cable, and to boost the signal level. The SCU used in the current DAQ has an effective gain of 34dB.

The PC104 processor platform: A PC104 dedicated processor is used to control the digitisation of the demodulated signals. The PC104 system is housed inside the drum of the winch used to wind the optical cable as it is pulled into and out of the borehole.

The high speed ADC: A high speed PC104 compliant analog to digital converter card from Chase ADC (8-bit; 4nS sampling interval) is used to digitise the received signals, under the control of the PC104 central processor.

The handheld data storage device: A Psion 'workabout' handheld computer is used to store the data acquired during the deployment of the BHR system. The Psion allows the operator to adjust a number of acquisition variables during a measurement, including the file in which the data must be stored, the number of sequential traces that are stacked before the resultant summed trace is stored and the digitisation interval (i.e. the relative maximum digitisation voltage swing of the ADC process).

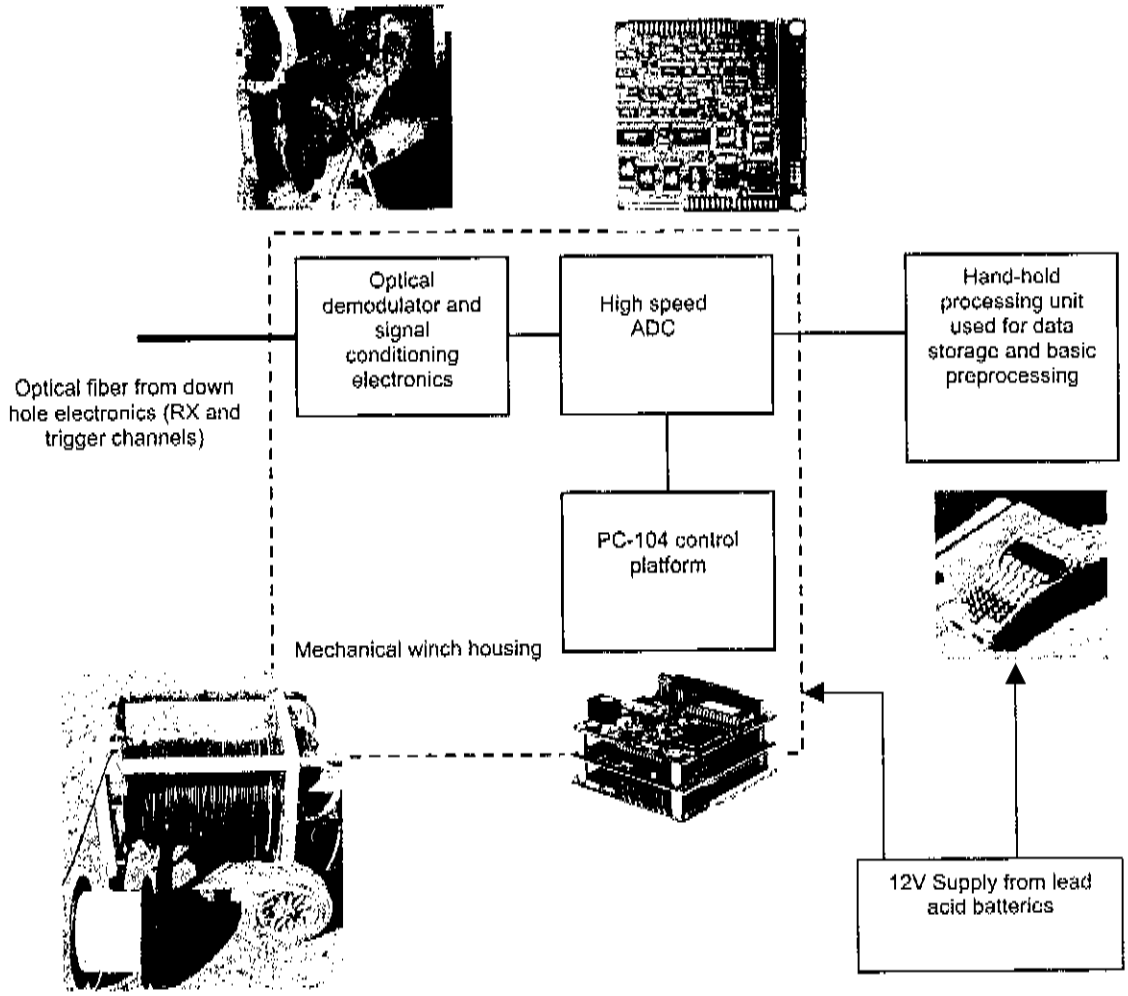

Figure 21 A function block diagram of the 'ST' system DAQ unit

1.4. Limitations identified in the current 'ST' technology

1.4.1. The receiver electronics

The receiver used in the ST probe is effective, and performs well. Only a few problems, mostly to do with the physical layout and design complexity of the electronics can be identified by cursory consideration. These factors are:

- The receiver consists of three gain stages, delivering a total theoretical gain of 72dB (assuming perfect matching and power transfer). The third stage employs a discrete transistor amplifier design, which is relatively complex, and uses a large number of components. The performance of this stage suggests that its operation does not justify this complexity. At higher frequencies, the simulated response of this stage begins to cut off, affecting the bandwidth of the system.

- The antenna used in the RX probe has an approximate real input impedance of 180Ω and a capacitive imaginary impedance of around 30pF over the frequency band of interest. The antenna is fed directly into the LNA front-end component, which has a rated input impedance of 50Ω. This mismatch will result in a loss of received power. Theoretical return losses are calculated as 4.956dB (return losses defined as in [10] p67).

- A Mini-circuits impedance matching transformer is used to match the 50Ω output of the second gain stage to the discrete transistor amplifier stage. The impedance ratio of the transformer is 9:1, and the output is shunted to ground with a 450Ω resistor, as the input impedance of the transistor stage is high. This shunt resistor will cause a power loss in the RF path of the receiver.

- The receiver is a very high gain chain, and it is very sensitive to saturation from large input signals. The saturation and recovery characteristics of the system operation must be carefully considered, and may make it unacceptable for mono-static application.

- A detailed analysis, including measurement of the ST-system receiver electronics is presented in 3.3.1.

1.4.2. The transmitter electronics

The transmitter electronics are relatively simple, and a number of limiting factors can be identified.

- The transmitter does not allow for an external trigger signal, and can thus not be used with a self-triggering DAQ of any type. The self-triggering transmitter introduces jitter effects and sampling uncertainty during the acquisition process.

- A Datatronic DC-DC converter is used to generate the high voltage level used to pulse the antenna. This component is very large, and requires a number of additional components. Smaller, self-contained converters are available which will be more appropriate for this application.

- The radiation of the pulse generated by the transmitter occurs only on a single falling edge, with very little radiation on the recovery edge. Low frequency energy, outside of the band of interest, is thus dissipated inside the electronics and not radiated. A different pulse form may be more efficient in the frequency band of interest. Another practical implication is that the maximum PRF that can be achieved is limited to the time needed for the long recovery after the transmit pulse.

- From a mono-static radar point of view, the slow recovery time, and the shunting of the antenna during the recovery period (i.e. the receive period) are not acceptable as all received reflections will be shunted at the receiver input during the receive period.

- The transmitter will not be considered further in this report, but the results of an investigation by Van der Merwe [9] will be referred to and is summarized in Chapter 4.

1.4.3. The probe structure

Three observations in connection with the general probe structure are:

- The antenna used in both the RX and TX probes is an unsymmetrical structure, which implies unbalanced operation, and an unsymmetrical radiation pattern[22].

- The antenna structures are not very efficient due to the resistive loading used, and due to feed mismatches. The inefficiency is largely related to the resistive loading used to realize non-dispersive behaviour. This trade-off between dispersive operation and efficiency cannot be circumvented, but must be optimised.

- The operation time of the probes with the current battery packs is far longer than necessary for a standard deployment. If this capacity were decreased, the size of the battery pack could be reduced, allowing for a smaller structure, and more freedom in the probe layout and antenna design.

- A study of the probe structure, with particular attention paid to the antenna structure will be presented in this report.

1.4.4. The overall system operation and deployment capabilities

There are a number of issues related to system deployment that must be noted. Simplification and improvement of the deployment process would result in more efficient data gathering and a reduction in the risk of system failure.

- The system operation relies heavily on the use of optical connections, both inside and outside of the probe structures. This dependence is necessary for electrical isolation, but makes the manufacture and deployment of the radar system cumbersome.

- The use of an optical spacer to provide isolation between the transmitter and receiver complicates both the system operation and deployment. The assumption of co-location of the receiver and transmitter probe during data processing is not completely accurate, due to the use of a spacer section, which is non-ideal, although the effect is generally small and can be accounted for during processing.

- The DAQ used in the ST system is cumbersome from both a deployment and operational point of view. Simplification of the acquisition process would have a large effect on the improvement of the effective deployment of the system.

- The digitisation noise and bandwidth performance of the DAQ is relatively poor, reducing the dynamic range and bandwidth capabilities of the data acquisition.

1.5. Issues to be considered in this report

In this report, we will be considering three main aspects of the BHR system, with the main aim of developing these aspects to such a point that the resultant sub-systems can be employed as part of a single, self-contained probe for deployment in a mono-static radar system.

1.5.1. The radiating structure

The first aspect is that of the radiation structure. Both the critical analysis of existing BHR antenna structures, and the design of a new structure will be considered. The goal is to develop a broadside directed, wideband antenna, with a good pulse response, and optimal radiation efficiency, while adhering to the structural requirements imposed by the operational BHR environment, and the operational requirements imposed by the mono-static probe concept.

1.5.2. The receive electronics

The second aspect is the receiver electronics. Both the characterization of existing electronics and the design of a receiver for application in a mono-static system will be considered. The goal is the development of a low-noise active receiving structure that can share an antenna with the transmitter,

and is not sensitive to saturation by the nearby transmitter in the mono-static configuration. The receiver must be compatible with the circulator isolation topology in such a way that reflection signals received on the antenna will be accurately amplified to an acceptable level for acquisition and storage.

1.5.3. Structural considerations

The last aspect that will be considered in this report is the structural design of a probe housing, and issues of importance in the system layout in order to accommodate the mono-static BHR system. The goal is to realize a simple, functional radar probe structure that adheres to the spatial prerequisites of the mine environment, and is easy to build and deploy. This structure will be used in field-testing of the sub-systems developed during the period of this report.

1.5.4. Other

There are three other main aspects that can be identified in the realization of a complete autonomous, operational mono-static BHR system, these are:

- The transmitter topology
- The receiver-transmitter isolation policy
- The simplification and automation of the DAQ structure

These three aspects are considered separately by Van der Merwe (the transmitter and isolation problems for a mono-static BHR structure [9]) and by Jonathan Hargreaves (a DAQ system for autonomous probe operation) and will be referred to in this regard. These sub-systems will be integrated with those presented in this report during field-testing and laboratory measurement.

Chapter 2 Antenna considerations

In this chapter, we will consider the radiation structure of the BHR system. We will first introduce and verify the computational tools and methods. Next, we will consider the characterization and modelling of the operational BHR environment from an electromagnetic point of view. We will shortly outline the main requirements and constraints on the antenna structure for BHR application. We will begin the development of a radiating structure by considering the intuitive and simulated operation of radiation structures employed in existing BHR systems. These structures are in general asymmetrical. In the final section of this chapter, a symmetrical radiating structure for the mono-static probe will be motivated, developed and analysed. The actual operation of a prototype antenna will be considered based on results of measurements and field tests in Chapter 6.

2.1. Tool development

In this section we will introduce and verify the computational and mathematical tools that will be used in the characterization and development of the radiating structures referred to in this report. We will also describe and verify the methods in which the computational tools will be employed.

2.1.1. Characterization and measurement of a simple wire dipole structure for computational verification

In this section, we will present the results of measurements performed on a 135mm arm-length simple wire dipole structure. The results will be referred to later for comparative verification of the computational tools and methods.

In (2.1) the theoretical computation of a few of the characteristics of interest of the measured dipole structure is given. Due to the finite thickness of the wire, we take the length to diameter ratio of the dipole wire into account, and adjust the computation accordingly (see Figure 22 and [11] p172).

$$l = 269mm; d = 1.2mm$$

$$\frac{l}{d} = 213.33$$

$$\therefore l \approx 0.4772\lambda \Rightarrow \lambda = 563.70mm$$

$$f_{resonant} = \frac{c_o}{\lambda} = 531.83MHz \qquad (2.1)$$

$$\text{Input resistance} = \begin{cases} 20\pi^2\left(\frac{l}{\lambda}\right)^2 ; 0 < l < \frac{\lambda}{4} \\ 24.7\left(\pi\frac{l}{\lambda}\right)^{2.4} ; \frac{\lambda}{4} < l < \frac{\lambda}{2} \\ 11.14\left(\pi\frac{l}{\lambda}\right)^{4.17} ; \frac{\lambda}{2} < l < \frac{100\lambda}{157} \end{cases}$$

3dB Bandwidth = 8% to 12%

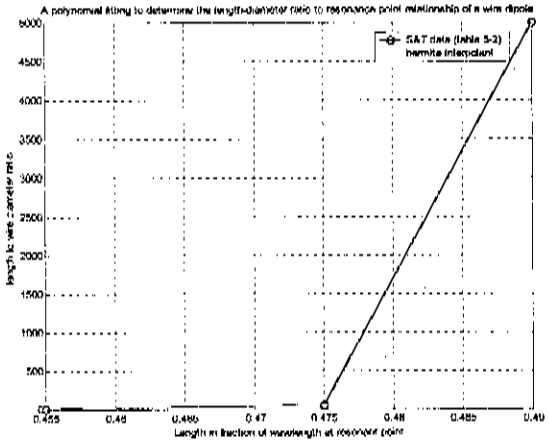

Figure 22 The relationship between the length to diameter ratio and the resonant frequency of a wire dipole of a given length

The form of the antenna structure is shown in Figure 23. Measurement was performed using a balanced measurement method described in Appendix B.1. The raw and processed measurement results are shown in Figure 24.

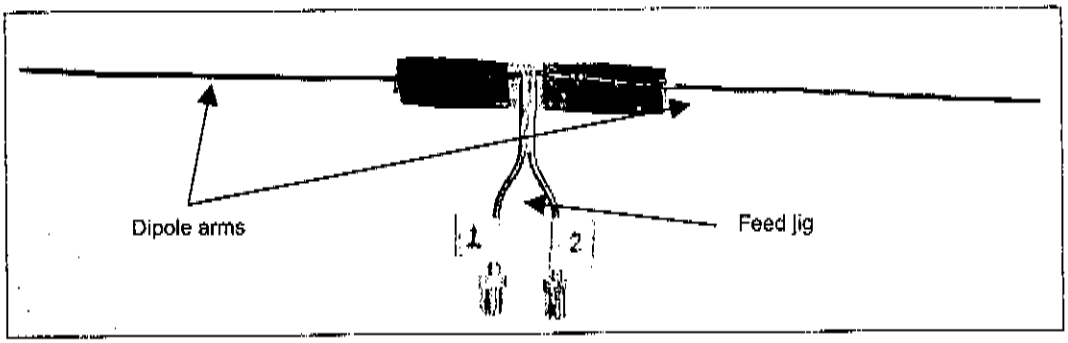

Figure 23 The wire dipole structure used for computational verification, showing the balancing jig feed

The data in Figure 24 was processed in MATLAB using procedures written by Van Rooyen [5] and modified by the author.

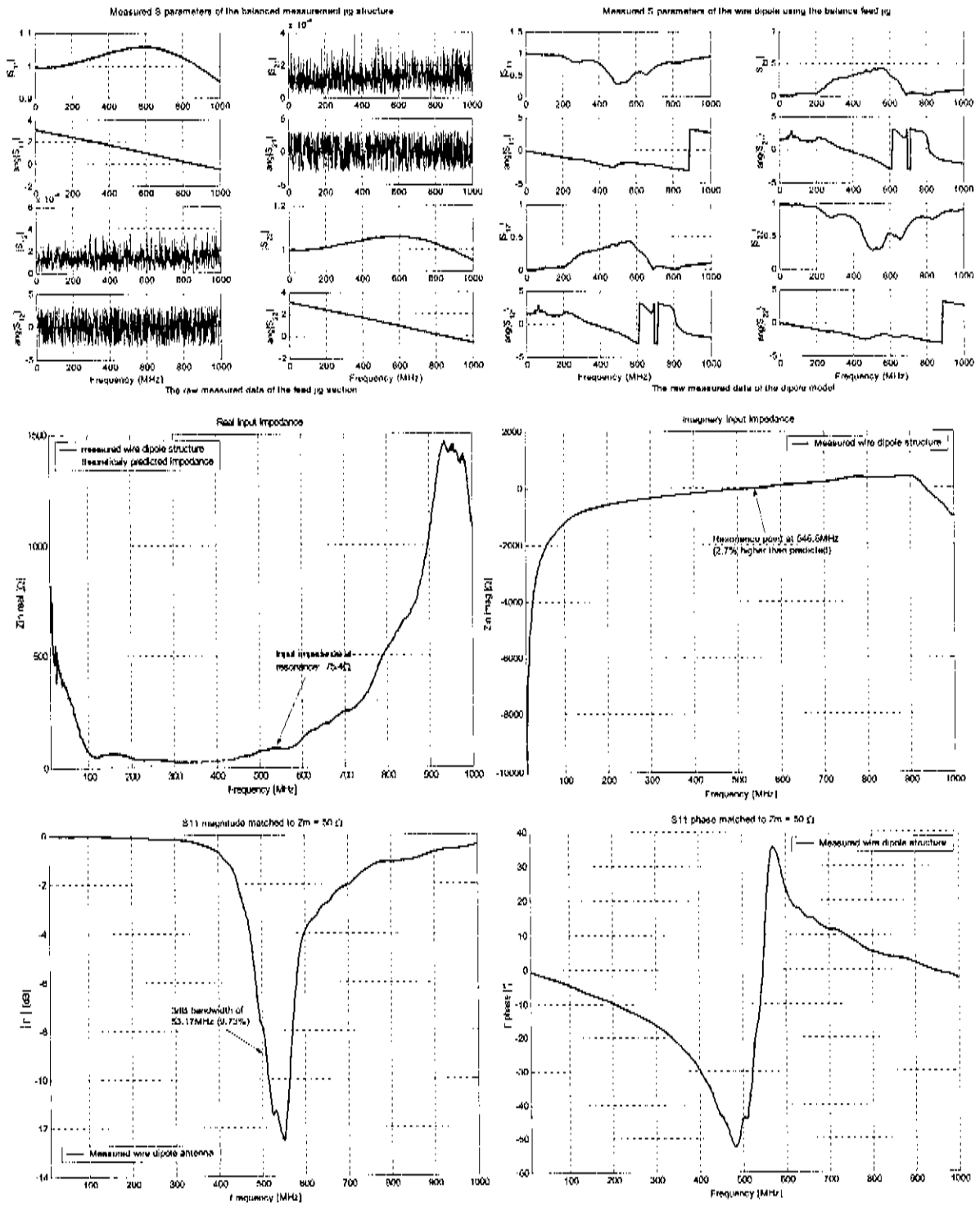

Figure 24 The measured impedance and reflection coefficient of a 1.2mm diameter, 269mm length wire dipole antenna (Raw data shown in top two figures)

The processed measurement results show a very good correlation (less than 5% difference) to the theoretically predicted characteristics of the dipole structure. This suggests that the wide-band balanced antenna measurement method is accurate. Further verification of this measurement method may be found in the literature [5].

2.1.2. Verification of FEKO simulations using a simple wire dipole structure

We will consider the development of a computational model of both a simple wire dipole structure, and a more complex resistively loaded dipole structure. The results of characterization of these structures will be compared with practical measurement results in order to verify the computational tools and models used.

Frequency domain computational analysis of antenna structures was performed, using a method of moments (MoM) based electromagnetic simulation package, FEKO. In this computational method, the surface of the structure under consideration is divided into a set of basis elements. The electric surface currents on the elements representing conductive surfaces and the magnetic and electric surface currents induced on the surface elements of dielectric structures are computed. This is done by solving a system of linear equations describing the relationships between the basis functions of the basis elements, based on the structural geometry. From the computed surface currents, other information like antenna S-parameters, near and far fields etc. can be derived for a given excitation. Further information about the operation and functioning of FEKO may be found in Appendix B.2.

In order to verify the operation of FEKO, the simple dipole structure measured in the previous section was computationally characterized. A FEKO model of a thick (1,5mm diameter) centre fed wire dipole with a total length of 269mm was generated. The detail of the structure is shown in Figure 25.

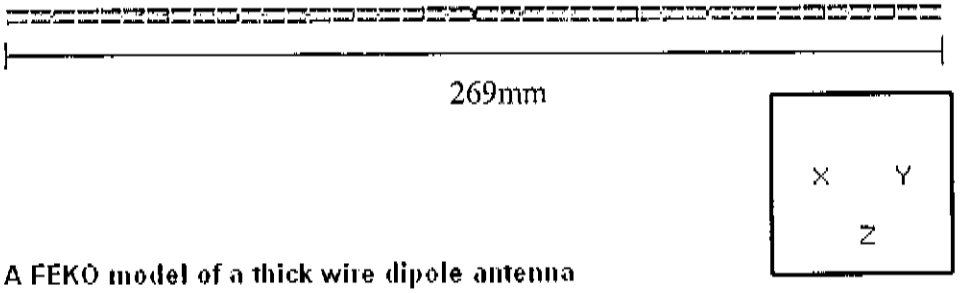

Figure 25 The FEKO model of a 269mm long centre-fed wire-dipole antenna structure

The antenna structure is excited at the centre using a voltage gap excitation on the feed segment, and simulated in free space over the frequency range 10MHz to 1GHz. The FEKO simulation results are shown in Figure 26, along with the measurements described in the previous section. Theoretical

computation of the characteristics of interest is shown in (2.2) [13],[11], taking the length to diameter ratio of the model into account (see Figure 22 and [11] p172).

$$
\begin{aligned}
l &= 269mm \\
d &= 1.5mm \\
\frac{l}{d} &= 179.33 \\
\therefore \lambda &\approx \frac{l}{0.477} = 563.94mm \\
f_{resonant} &= 531.60MHz \\
\text{Input resistance} &= \begin{cases} 20\pi^2\left(\frac{l}{\lambda}\right)^2 ; 0 < l < \frac{\lambda}{4} \\ 24.7\left(\pi\frac{l}{\lambda}\right)^{2.4} ; \frac{\lambda}{4} < l < \frac{\lambda}{2} \\ 11.14\left(\pi\frac{l}{\lambda}\right)^{4.17} ; \frac{\lambda}{2} < l < \frac{100\lambda}{157} \end{cases} \qquad (2.2) \\
\text{3dB Bandwidth} &= 8\% \text{ to } 12\%
\end{aligned}
$$

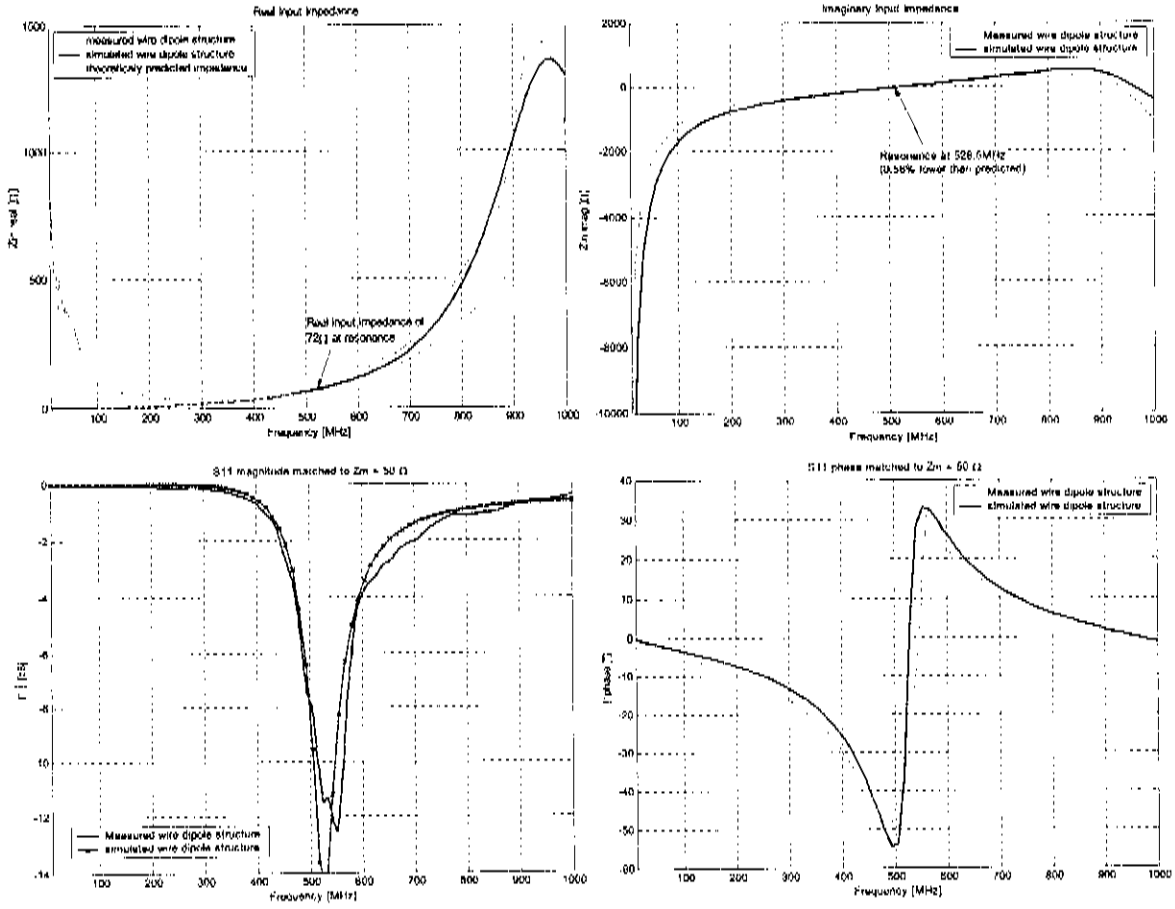

Figure 26 The simulated characteristics of a 1.5mm diameter, 269mm-length wire-dipole structure simulated in free space in FEKO, along with the measurements of Figure 24

It is clear that the computational and measured characteristics of the dipole structure are very similar. As shown in the computations of (2.1) and (2.2), the small difference in resonant frequency (2.8% difference) can be ascribed partly to the different wire diameters of the two structures, and partly to measurement inaccuracy.

In order to confirm the accuracy of FEKO modelling of more complex antenna structures, an identical comparative measurement to the one performed using the simple wire dipole structure was performed using a symmetrical wire dipole structure with discrete lumped resistive elements placed along the length of the arms. The physical structure and FEKO model is shown in Figure 27, and the comparative measured and simulated results in Figure 28. The expected theoretical properties of this structure are difficult to predict by simple computation.

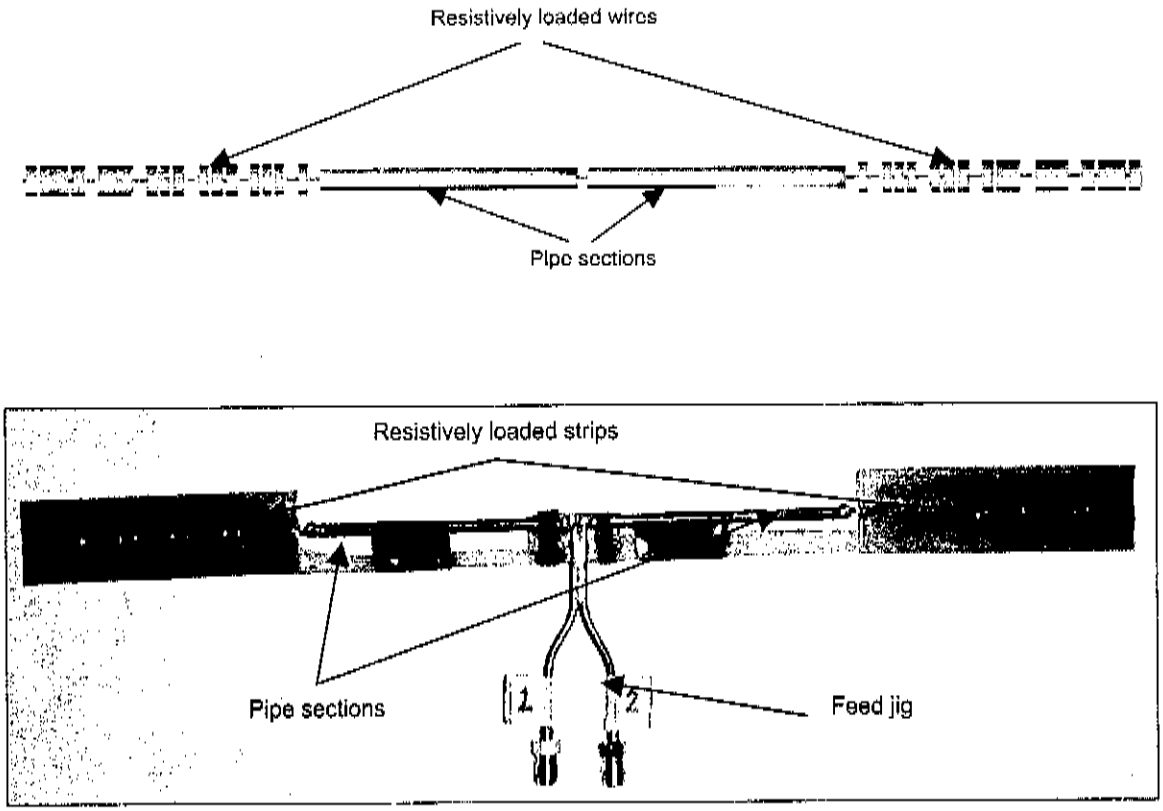

Figure 27 The physical structure and FEKO model of the measured and simulated loaded dipole antenna

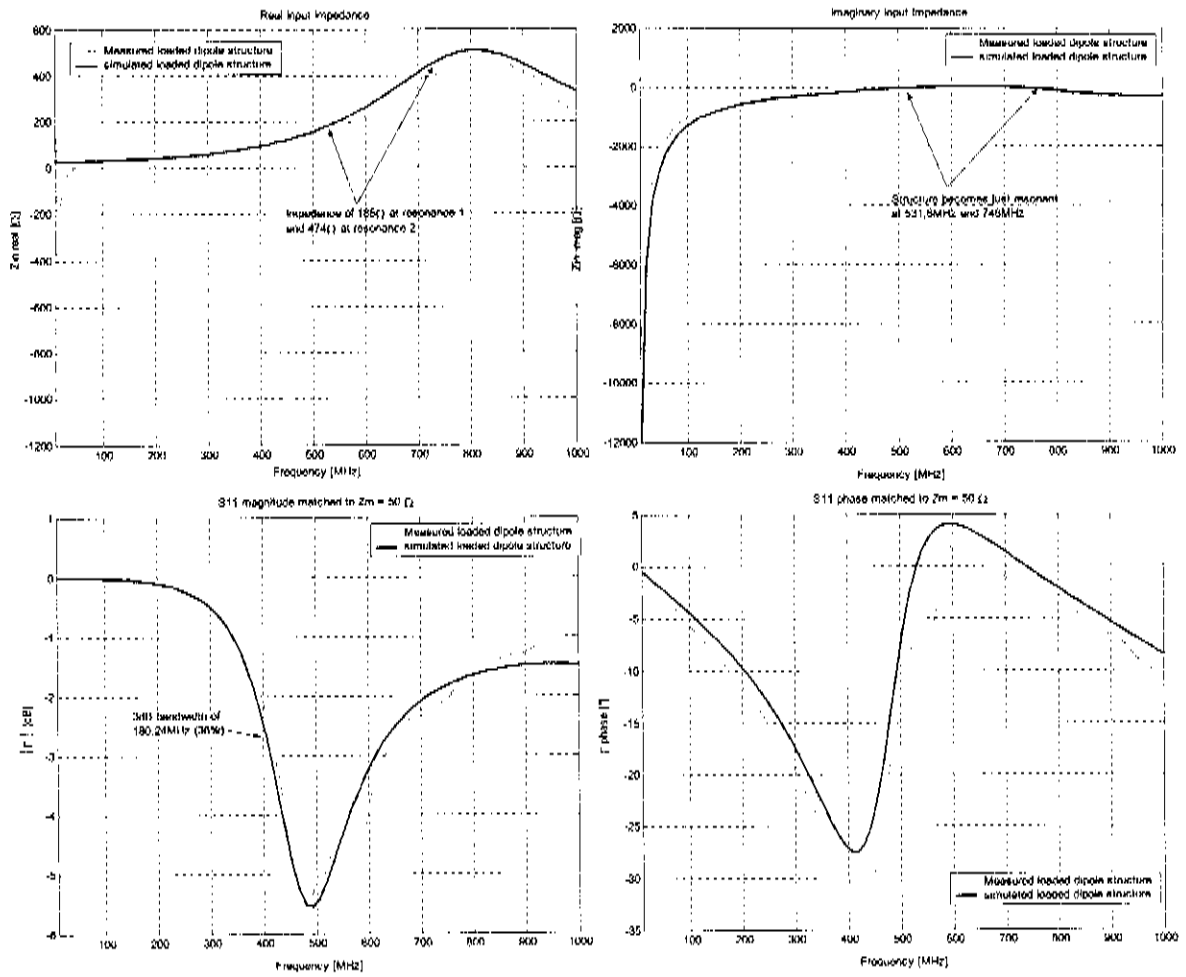

Figure 28 The processed measured and simulated data for a loaded dipole structure as shown in Figure 27

Again it is clear that the FEKO simulated data and the measured data agree very well. This suggests that the FEKO models of the structures are good, and that results achieved by FEKO modelling are accurate enough to base observations about the operation of a given antenna structure on.

2.1.3. Development of FEKO/ADS modelling methods

We will consider methods to concurrently characterize the time-domain operation of a BHR radiating structure, and the effects on the electronics used to drive the antenna. This is achieved by transforming frequency domain MoM computational results into the time domain, and combining them with time-domain circuit modelling methods. The methods that are developed will be theoretically verified.

Time and frequency domain computational circuit analysis was done using the advanced computational circuit simulation package, ADS (Advanced Design System). By integrating FEKO simulation results into ADS, time-domain characterization of an antenna structure and computational characterization of the interaction between the antenna and electronics is made possible. For verification purposes, we will

again consider a simple dipole structure, and compare the results to those of qualitative practical predictions.

2.1.3.1. The input impedance and feed currents

FEKO is used to simulate the input reflection coefficient (S_{11}; magnitude and phase) of an antenna structure. In the simplified case of a small, un-damped, or relatively lossless structure, these results are sufficient to compute the approximate radiated field for a given excitation, as effectively all the energy on the antenna must be dissipated over the radiation resistance of the antenna. The short (relative to excitation wavelength) antenna will also operate as a quasi-static structure, with little or no distributed effects.

The simulated S_{11}, representing the input impedance of the small lossless radiating structure is imported into ADS, to realize a one-port load component representation of the antenna. If this component is connected to an excitation source, and the time-domain current that flows at the antenna feed point is computed, the form of the far E-field pulse that will be radiated by the antenna load can be approximately derived. This is done by noting that, in the far field of an ideal radiating element, the radiated E-field is for all intensive purpose proportional to the derivative of the current on the element, or equivalently, to the second derivative of the charge on the structure. We only compute the current at one point on the antenna in ADS, and thus, this is only true if the antenna is small relative to the shortest wavelength of the highest frequency component of the excitation ([15] p.545 (14)). As the relative size of the structure increases, the radiated field will deviate more and more from this ideal assumption. In order to apply this idea to large antenna structures, knowledge of the time current at all points on the antenna is necessary, and we must compute the radiated fields by superposition (see [15] p 555).

As the relative length of the structure increases, distributed effects will cause a change in the relation between the excitation and the radiated field, due to the considerable propagation time from the feed point to radiating points on the structure (this effect will be discussed in more detail in section 2.3.2).

The relational magnitude of the radiated fields at a point must be approximately determined by independently considering the effects of spreading and propagation losses in the propagation material.

2.1.3.2. Direct computation of radiated E-fields for general structures

In the general case of large, damped or lossy antenna structures, the relationship between the radiated field and the current at the feed of the antenna is less trivial. Phase effects and current distribution, and dissipation ratio between the intrinsic loading or loss resistance and the radiation resistance must be considered in the derivation of such a relationship. For small structures, a lumped element model of the antenna may be used to determine the current division between the dissipation-loss and radiation resistances, although for a general antenna with a distributed resistive loading, such a lumped resistive

model can be complex. Characterization of the distributed radiation phase effects is possible by assuming a current distribution along the antenna structure, relative to the feed current, and applying superposition, but generally only steady-state radiation can be approximated. It is very difficult to characterize the transient effects in this way. A more advanced simulation method is thus necessary to determine the radiated field of a general structure for a given transient and/or steady state excitation.

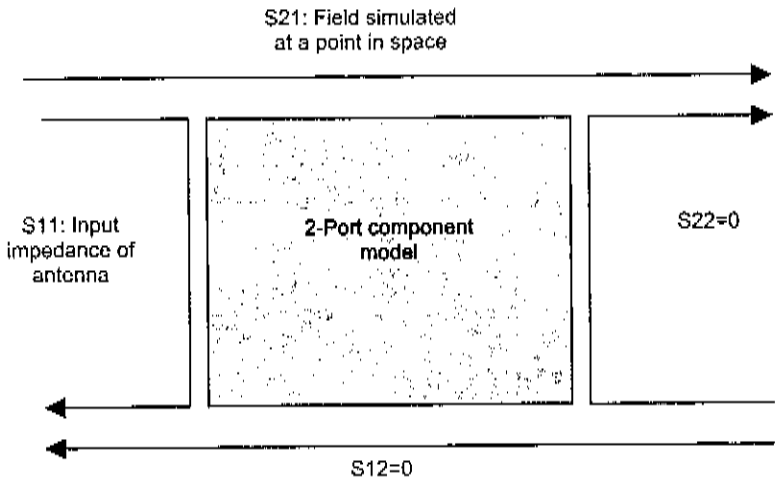

Figure 29 A schematic representation of the 2-port model used to characterize the radiated pulse of a general antenna structure

The radiated field at a given point (magnitude and phase, for a unity voltage excitation magnitude) can be computed in the frequency domain in FEKO, in addition to the input reflection coefficient of the structure. This information can be extracted from FEKO, and used to generate an ADS 2-port model, with S_{11} as the computed feed reflection coefficient of the antenna structure, and S_{21} as the unity excitation-E-field relationship computed in FEKO. The field at the point simulated in FEKO can then be computed directly in the time domain for any applied time domain excitation (both transient and steady state response). This method of computation can be used to include the additional effects of the properties of the propagation media and the antenna environment on the antenna pulse radiation properties. A simple schematic representation of ADS 2-port antenna component is shown in Figure 29. The computational process used to extract and use this model of a given antenna structure is summarized in the flow-chart of Figure 30.

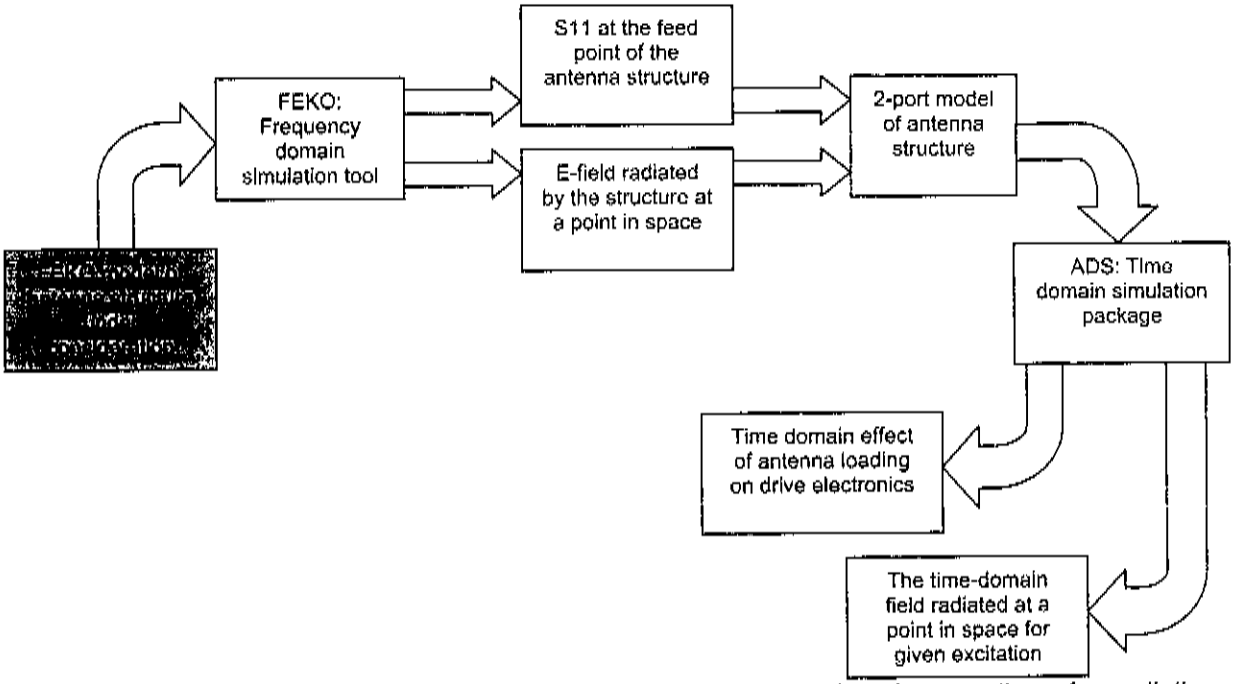

Figure 30 A flow chart of the process used to determine the time domain operation of a radiating structure

A more detailed description of the ADS time-domain antenna modelling procedures can be found in Appendix B.2.

In order to show the operation of both the unloaded and general modelling methods, we will consider the simulation of a 2m long wire-dipole antenna structure imbedded in rock (ϵ_r=9).

The erratic impedance characteristics of a wire-dipole antenna structure are clear from the measurements of section 2.1, and we thus expect that although the structure will be an efficient radiator (all energy must be dissipated over the radiation resistance), the excitation pulse form will be strongly deformed during radiation due to a distributed transient response. FEKO simulation results were used to generate 1- and 2-port ADS representations of the dipole structure (as discussed in section 2.1.3.1 and 2.1.3.2 respectively). We consider both the ADS simulated current drawn by the antenna load (using the simple 1-port model) and the magnitude of the time-domain E-field expected 5m from the antenna on bore sight (using the 2-port component). The two ADS models, and the computed time domain fields and currents are shown in Figure 31 for the shown applied continuous wave and pulsed excitation.

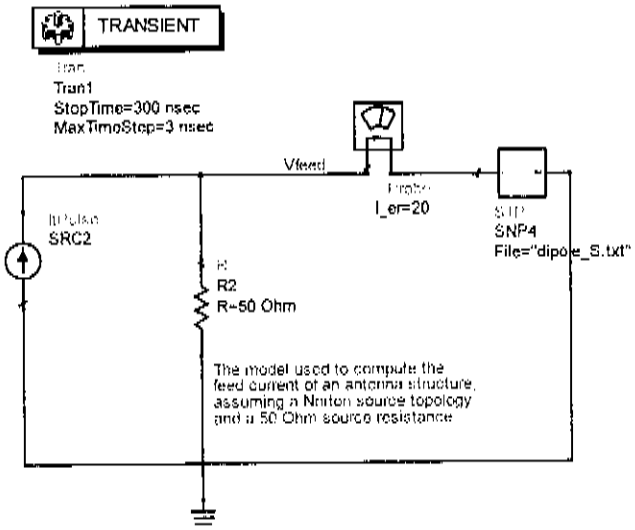
TRANSIENT
Tran1
StopTime=300 nsec
MaxTimeStep=3 nsec
Vfeed
I_er=20
SNP4
File="dipole_S.txt"
SRC2
R2
R=50 Ohm
The model used to compute the feed current of an antenna structure, assuming a Norton source topology and a 50 Ohm source resistance

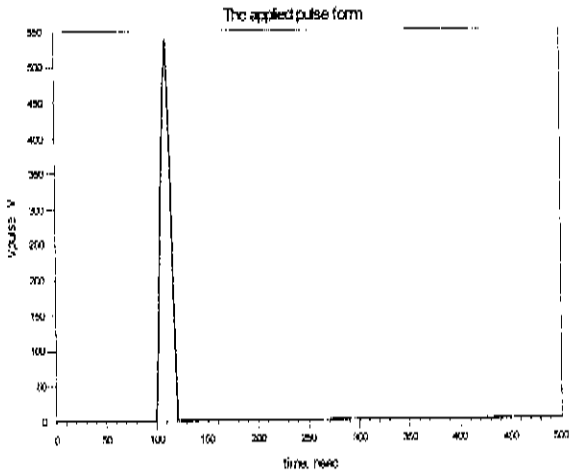
The applied pulse form
time, nsec

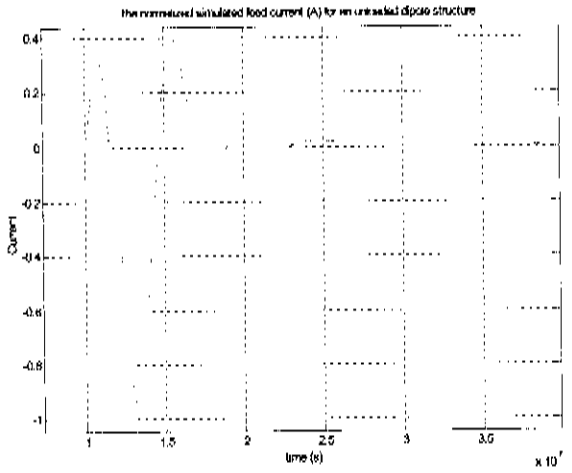
Current
time (s)

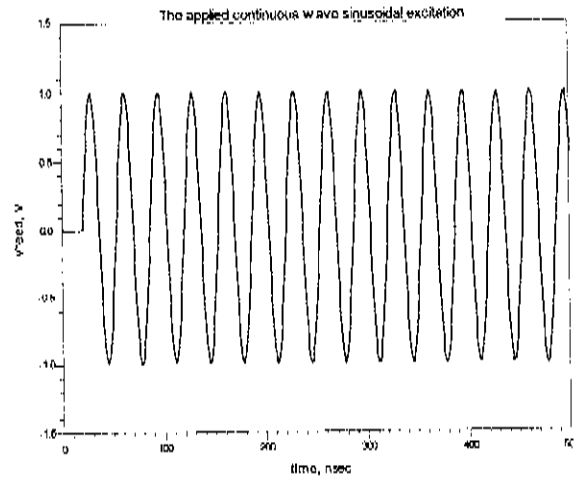
The applied continuous wave sinusoidal excitation
vfeed, v
time, nsec

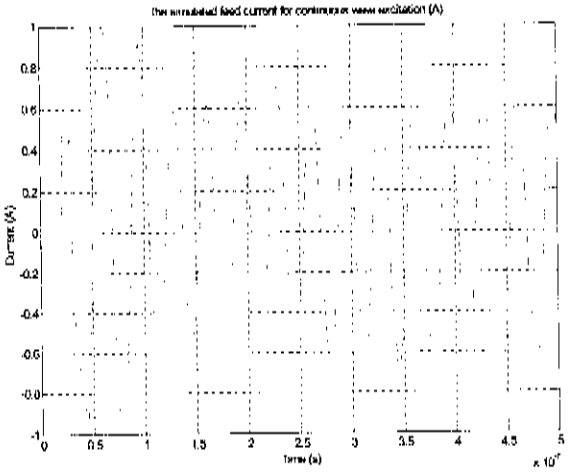
Current (A)
Time (s)

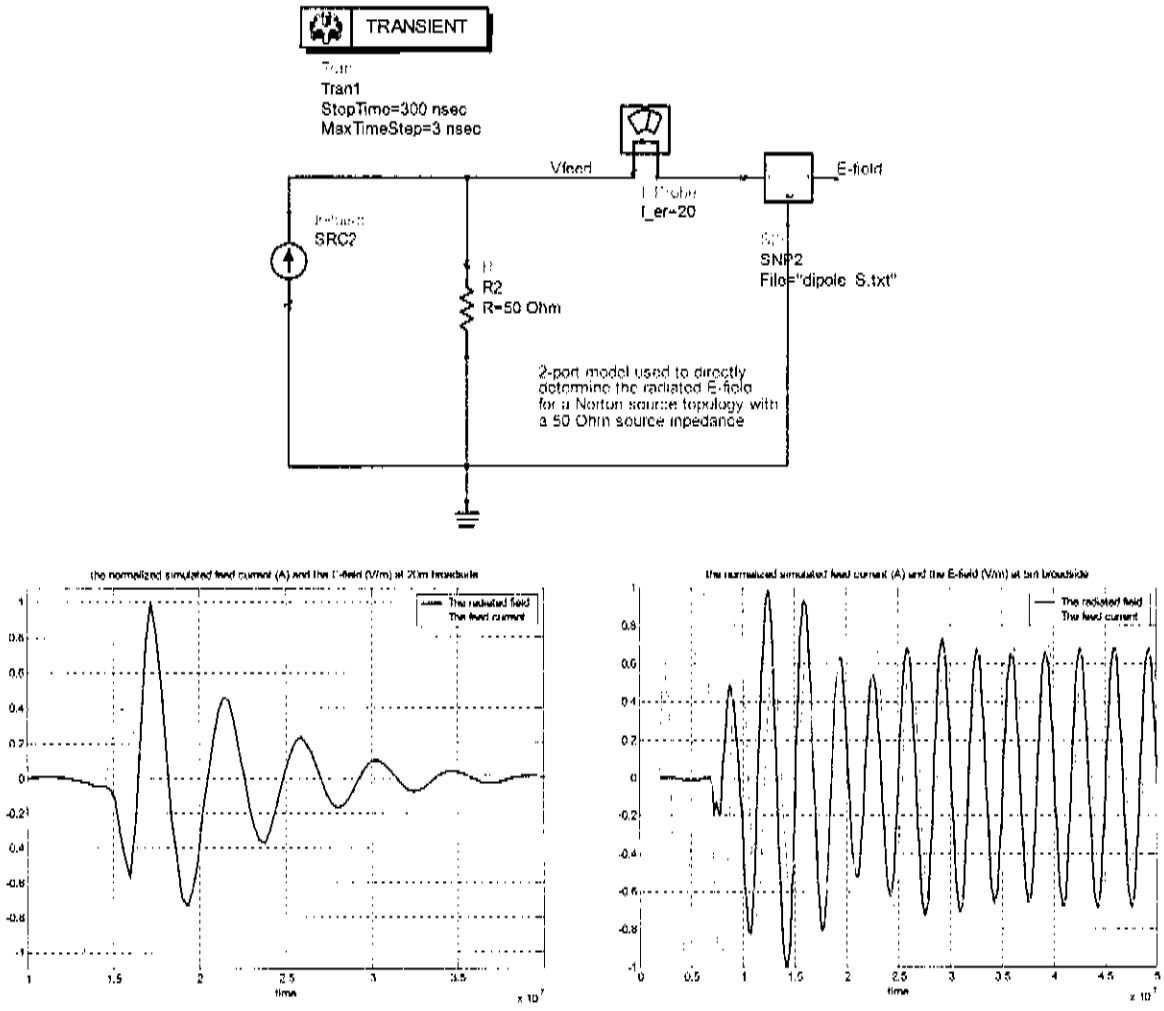

Figure 31 The ADS S-parameter models used to simulate an un-damped dipole antenna; time-domain simulation results for feed currents and radiated E-fields with pulsed and continuous wave excitation

According to radiation theory for short structures, the ideal E-field radiated in the far field will be proportional to the second derivative of the charge on the antenna structure, or alternatively, to the derivative of the current that flows on the structure, as shown in (2.3) [15].

$$E_{far-field} \propto I'\left(t-\frac{r}{c}\right)_{antenna} = q''\left(t-\frac{r}{c}\right)_{antenna} \quad (2.3)$$

We now take the derivative of the current at the antenna feed point for both sinusoidal and pulsed excitation, by direct numerical differentiation (defined in (2.4) [18]) and by fitting a polynomial to the computed current waveform. (Various polynomial order fittings are shown in Figure 32.) The derivative computed using a 20th order fitting is shown in Figure 33, along with the simulated radiated E-field.

$$\left(\frac{dx(w_n)}{dw} = \frac{x(w_n + dw) - x(w)}{dw}\right)_{n=1toN} \tag{2.4}$$

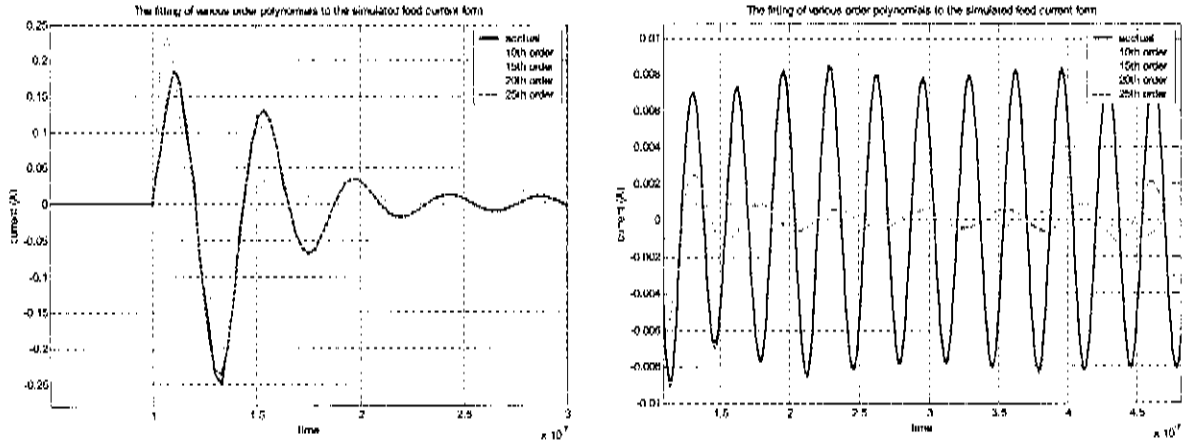

Figure 32 The accuracy of polynomial fittings of various orders to the simulated feed current forms for pulsed and continuous wave excitation; the 20th and 25th order fittings are good

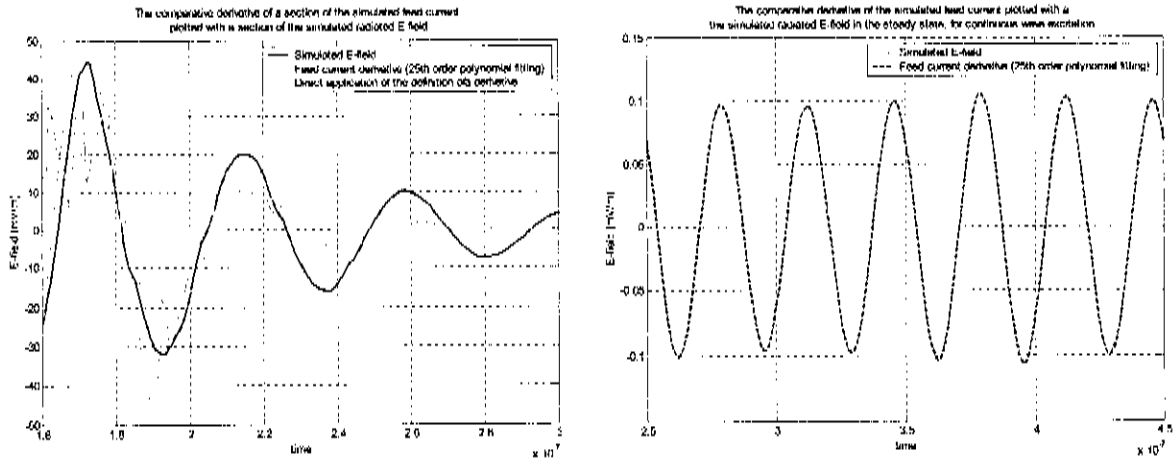

Figure 33 The derivative of the dipole antenna current and the computed E-field for pulsed and continuous wave excitation (steady state), both normalized to take spreading losses (1/r) into account.

For pulsed excitation, the computed E-field and the derivative of the antenna current have a similar form for the first 50nS, but the effect of the delayed pulse radiation at the dipole ends, due to the dipole length is evident (this effect for long axial structures is discussed in section 2.3.2). If we consider the steady state radiation for a sinusoidal excitation, we see that the derivative of the feed current and the radiated field do indeed have the same form. Observation suggests that by generating an ADS model of an antenna from FEKO simulations, a good time domain representation of the radiated field at a given point can indeed be determined for a given excitation, including both transient and steady state effects.

An antenna structure with a distributed resistive loading was modelled using the same methods discussed thus far in this section. The radiated field for a given excitation pulse is shown in Figure 34. The effect of the loading on the time-domain pulse form is clear in the damped ringing of the transmitted pulse, and the damped feed current. Notice that the relative spreading of the pulse transmitted by the loaded structure is a lot less, even though the radiation is less efficient, with a peak E-field magnitude of 30% that of the unloaded dipole antenna.

In order to quantify the effect of the propagation distance on the radiated field as it propagates through the rock, a number of ADS simulations were performed using a model of a 275mm dipole antenna in air, incorporating the E-fields computed at a few distances from the antenna. These results were used to generate Figure 35. The 1/*r* decay in the field strength with distance, as predicted by spreading loss theory, is clear on the normalized spatial section, A-A, also shown in Figure 35.

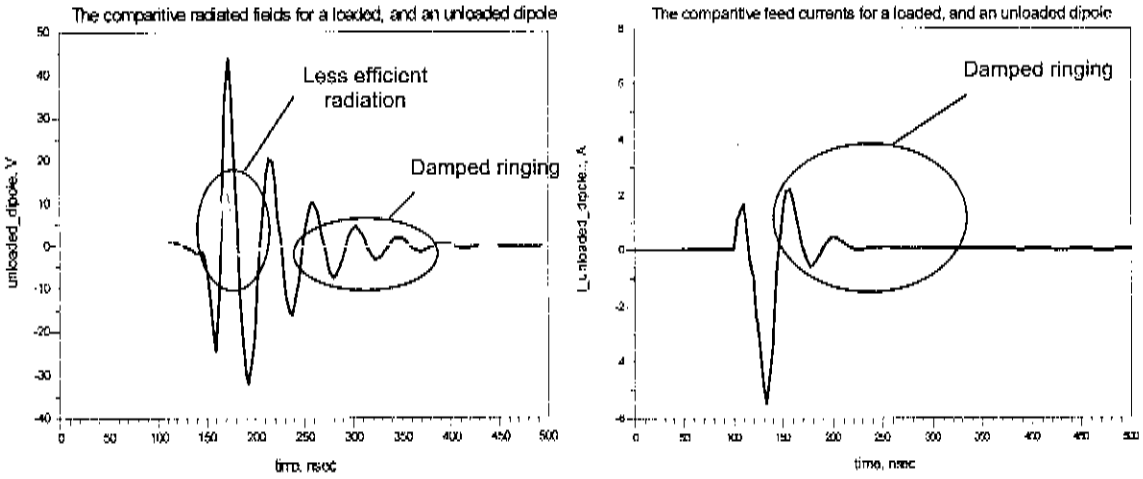

Figure 34 The ADS computed time domain E-field and feed current of a loaded dipole antenna structure (1/2 Wu-King profile [4]) plotted with the computed results of an unloaded dipole of the same dimensions

The methods described in this section can be extended in a number of ways to provide powerful evaluation tools for modelling of the operation of the whole mono-static system. The concurrent computational modelling of a full mono-static system in ADS to theoretically determine the radiation fields, the interaction of the electronics with the antenna, the realized isolation etc. is shortly discussed in Appendix B.2.

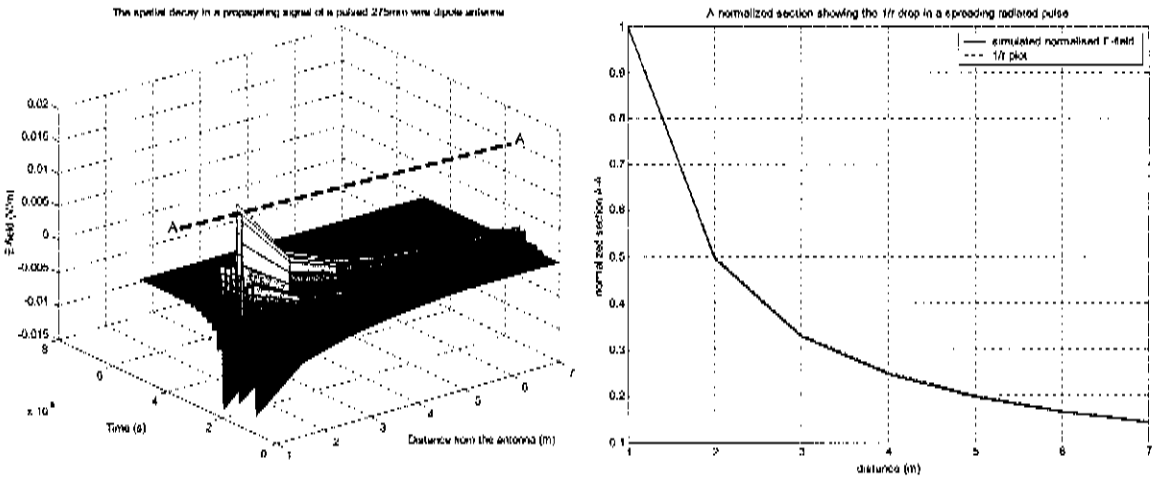

Figure 35 The 1/r drop in field strength with distance for a time-domain simulated travelling wave from a pulsed wire dipole antenna in a non-lossy propagation medium

2.2. Modelling of the BHR operational environment

In this section, we will consider the BHR operational environment, and methods of modelling its effect on the operation of the antenna. We will define the parameters and structure of the operational environment of a BHR probe. These parameters will then be used to define a computational model and strategy to quantify the effects of the environment on the operation of the radiating structure employed in a BHR system.

In order to characterize any BHR antenna structure confidently, we must consider its operation in a computational environment that approximates the operational environment as closely as possible.

The operational environment of the BHR radiating structure is generally cylindrically symmetrical, with a number of coaxially located layers with different dielectric and conductive properties, as shown in Figure 36. (Note that we have here assumed that the BHR probe is centrally located in the borehole, in order to simplify the model. Non-central location will be considered separately.)

In order to model the antenna environment, we must begin by determining the properties of interest of the materials in each of the regions shown in Figure 36. The properties of the PVC piping are standard, but the properties of the material in the borehole, and the rock structure can vary considerably. The relationships between the basic dielectric material properties of interest are summarized in (2.5) (see [13] section2.8; [12] p.11; [10]). An approximation of the expected variation of each of these basic properties is shown in Table 1. (Note that the assumed values for ϵ_r and σ are themselves frequency dependant, but an approximate constant value is allocated that is close to the actual value at all frequencies of interest.)

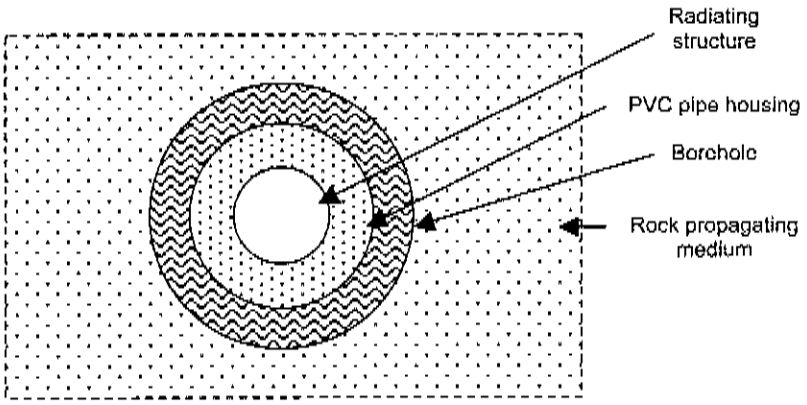

Figure 36 A cross section showing the coaxial symmetry of the BHR operating environment

$$\varepsilon = \varepsilon_r \varepsilon_o$$

$$\text{where: } \varepsilon_o = 8.854 \times 10^{-12}$$

$$\varepsilon_r = \varepsilon_r' - j\varepsilon_r'' = \varepsilon_r' - j\frac{\sigma}{\omega \varepsilon_o} \qquad (2.5)$$

$$\tan\delta = \frac{\varepsilon_r''}{\varepsilon_r'} = \frac{1}{Q}$$

Material	Relative permitivity (ε_r)	Conductivity (σ)	Loss tangent (tanδ)
Pipe housing			
PVC	3.7	8.33×10^{-15} S/m	539.588×10^{-15}
Material in borehole			
Air	1.0006	0	0
Distilled water	81	2×10^{-4} S/m	591.790×10^{-6}
Sea water	81	4 S/m	11.84
Rock material			
Dry soil	5	10^{-5} S/m	4.79×10^{-3}
Wet soil	20	10^{-3} S/m	11.98×10^{-3}
Various clays	5-40	2×10^{-3} to 0.3 S/m	60×10^{-3} to 1.79
Bleskop rock (norite)	8.125	1.695×10^{-3} S/m	50×10^{-3}
Various rock types	4-12	10^{-5} to 10^{-2} S/m	600×10^{-6} to 200×10^{-3}

Relationships computed at 75MHz

Table 1 The approximate properties of the propagation materials in the BHR environment

Using this information, we can consider any BHR radiating structure by studying its operation in a realistic environment with variation of the material properties in the model of Figure 36 over the ranges summarized in Table 1.

Modelling of non-coaxial probe location is possible, but it introduces a number of difficulties. Practically applicable modelling conclusions will be achieved by alternative methods. In order to take the effects of non-coaxial location of the probe in the borehole into consideration during modelling, we will define two

extreme cases. The first case is where coaxial probe location is assumed, and the probe outer diameter is narrower than the borehole. The second case again assumes a coaxial system, but the probe is in direct contact with the rock (i.e. probe outer diameter=borehole diameter). Both of these extremes, shown diagrammatically in Figure 37, are practically improbable cases, but all practical cases will lie somewhere between these two extremes. Thus, by characterizing the extremes, for various material properties, we can determine the maximum operational variation in the characteristics of the antenna structure in its operational environment. The effect on the symmetry of the antenna radiation pattern due to non-coaxial location is not considered by this strategy, and must be considered separately.

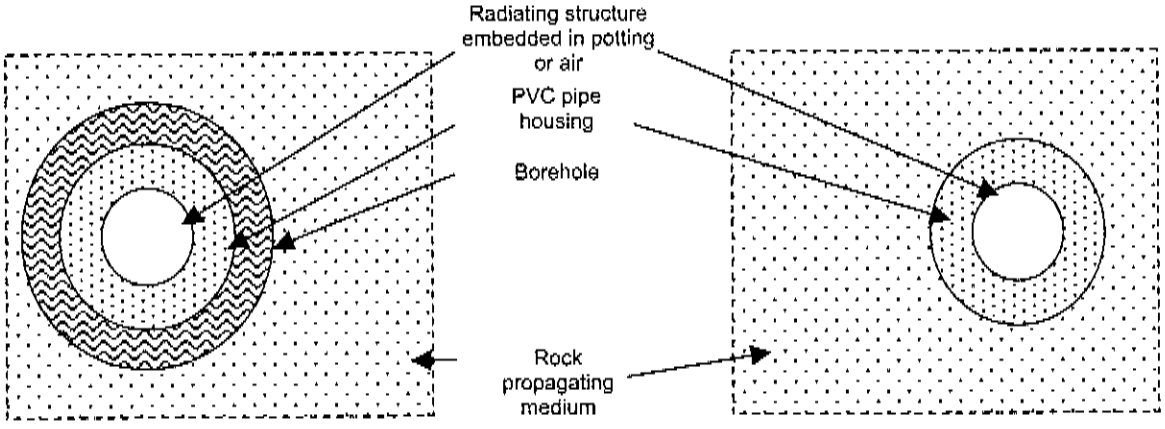

Figure 37 Cross sections showing the two extreme cases used to characterize the variation in the BHR antenna operational characteristics

A more detailed description of the FEKO realization of these two environmental models can be found in Appendix B.3.

2.3. Antenna requirements

In this section we will identify, define and quantify the requirements placed on a radiation structure suitable for application in a BHR system.

We must begin by considering the physical and operational constraints and requirements placed on the antenna. Once we have done this, existing antennas can be introduced, analysed and critically compared to determine how well they adhere to these requirements. Using the existing antennas as a starting point, a new structure can then be suggested, optimised and characterized.

2.3.1. Structural constraints

A critical consideration in the design of BHR radiating structures is the physical constraints imposed on the structure. The standard borehole in which the radar is to be deployed has a diameter of only 48mm.

In general, the borehole is not straight, but may gently curve in a given direction. The BHR probe must be easily inserted and moved around in such a borehole. This limits the radiating structure to an axially long structure with a radius of less than 20mm, in order to provide good clearance for any small obstructions or debris in the borehole, and to allow for gradual changes of direction in the borehole trajectory. The length of the BHR probe structure must not be excessive, so that moving it around in the spatially confined mine environment is not too difficult.

The antenna structure must make provision for the housing of the electronics and battery pack of the probe in such a way that the antenna operation is not affected by, and does not affect the electronics in any way.

2.3.2. Impedance and operational requirements

The purpose of the radiating structure of a BHR system is simply that it must effectively couple energy applied at its feed point, in the form of a voltage pulse, into the rock, in the form of an electromagnetic travelling wave. For the mono-static case the antenna must also be able to perform the inverse of this, and effectively convert incident electromagnetic energy to a voltage signal over a given load impedance of the receiver amplifier. The radiating structure must thus be compatible with both transmit and receive electronics.

The second major requirement of the antenna structure is that the antenna must be able to reliably and efficiently couple a pulse form with spectral content in a given range from the antenna feed to a propagating EM wave, or from an incident EM wave to the antenna feed, with minimal effect on the pulse form (spectral-phase effects).

2.3.2.1. Bandwidth

For the BHR applications under consideration in this report, the frequency band of interest over which we want to effectively transmit energy into the propagating medium in the form of an accurately reproduced pulse, is between 10MHz and 100MHz (10:1 bandwidth ratio). The ideal transmitter voltage pulse-form that will be assumed (based on observation of the transmitter topology, see Chapter 4) is shown in Figure 38, along with its spectral characteristic. The pulse has 10ns rise and fall times, and takes the form of a $\left(\sin\frac{2\pi t}{\tau}+0.5\right)$ function over the period $0<t<\tau$, and zero elsewhere. It is clear that the pulse has considerable spectral content over the whole frequency band of interest. (For computational purposes, this practical pulse can be approximated by a simple triangular pulse form also shown in Figure 38.)

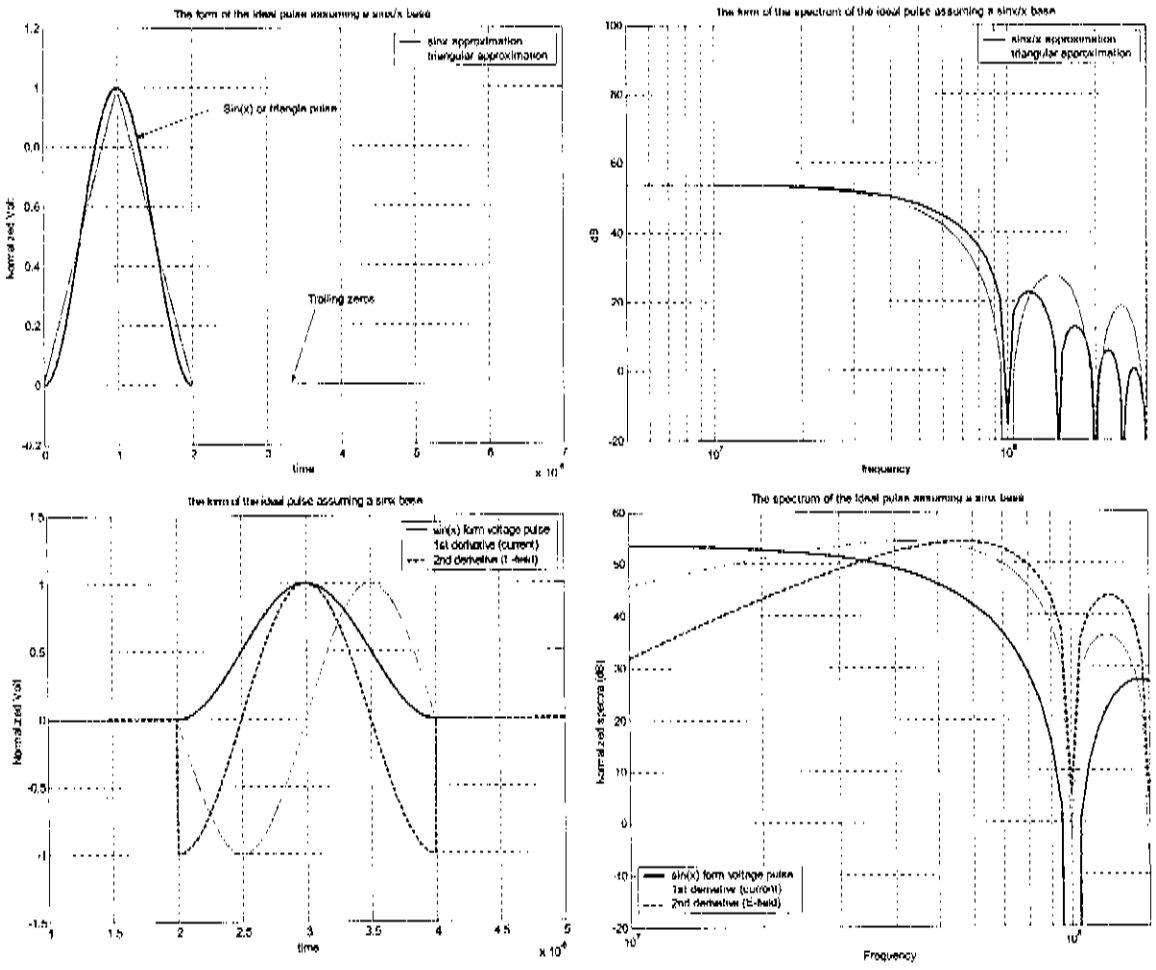

Figure 38 The form and spectral content of the ideal pulse form assumed for the BHR system, and a triangular approximation useful for computational application; the 1st and second derivative of the ideal pulse form

We require a radiation structure that can accept and radiate a broadband pulse of this form with minimal time-deformation of the pulse-form and thus also its spectral content. The general BHR antenna structure is capacitive over the operation band and thus, ideally, the current on the structure will have the approximate form of the derivative of the feed voltage $\left(I = C\frac{dV}{dt} \right)$. The radiated field will then again have the characteristic form of the derivative of the antenna current, or the second derivative of the feed voltage pulse form. Under such theoretically ideal conditions (i.e. assuming a short, quasistatic, capacitive ideal dipole type antenna structure), the form of the antenna current and the radiated field will be as shown in Figure 38. In a practical antenna the physical radiation process must be considered to get an idea of the actual radiated pulse form, and how it deviates from the ideal case. Consideration of the antenna as a travelling wave structure, with distributed radiation effects, as a

pulse travels along its length from the excitation point to the ends of the structure will be presented in the next section.

2.3.2.2. The pulse radiation process of axially long structures

In order to quantify the physical pulse-radiation process of typical BHR radiation structures, we must consider the pulse-radiation of an axially long, dipole type structure.

Referring to Figure 39, the source driving the antenna excites a pulse at the feed point, and short dipole element type radiation will occur due to charge acceleration at the feed point ([15] pp.543-548). The excited pulse will then move along the antenna towards the extreme edges. This pulse will propagate with very little radiation along the low impedance path of the antenna arms, and the only radiation will occur if the propagating charge is accelerated due to the non-infinite conductivity of the antenna material, or due to lossy, resistive structures on the antenna. When the propagating pulse reaches the extreme edges of the antenna structure, radiation will again occur, in the form of a point source located at the edges of the antenna, as the pulse is reflected at the open circuit end of the antenna, and the fields around the antenna adjust to adhere to the boundary conditions. The reflected current pulse will propagate back along the antenna structure toward the feed point with little radiation, and be reflected at the feed mismatch. The process will repeat itself until the energy in the pulse has been exhausted by the radiation process and in any material losses on the antenna structure.

A FEKO simulation of the currents on a few segments of a simple dipole model, embedded in an ε_r=5, σ=1x10^{-3} dielectric, are shown in Figure 40. In these results, the 'bouncing' of current between the feed point and the edge of the antenna arm can clearly be seen. These results also demonstrate and verify a number of other points relating to the radiation process described in the previous paragraph. Firstly, the current magnitude changes relatively little as it travels along the length of the antenna structure, but the return current (and thus also energy) that returns after reflection at the edge of the antenna is a lot smaller. This suggests that a large percentage of the energy in the travelling pulse is radiated at the end of the antenna, even though there is still a considerable reflection. If we consider the rate of propagation of the pulse along the dipole structure, as shown by the dashed grey lines in Figure 40, we expect that the pulse will propagate at a velocity given by $c = \frac{c_0}{\sqrt{\varepsilon_r}} = \frac{3\times10^8}{\sqrt{5}} = 134.07\times10^6 m/s$. ($\epsilon_r$ may generally be a complex property for the propagation material, as shown in (2.5)). For practical materials, the imaginary part of the permitivity is generally very small, but it will have an effect on the propagation of the pulse in the rock material. The consideration of these effects on pulse propagation is rather complex, and we consider only the real part of the permitivity here. The pulse will thus take 7.46ns to propagate along the length of the 1m-antenna arm. The propagation times shown in Figure 40 agree with this prediction.

A more detailed description of the travelling-wave-element radiation model for a long axial structure can be found in the literature ([6] section 3.2).

The distributed pulse radiation process of Figure 39 will result in deviation from the ideal case of Figure 38 for a dipole antenna of any considerable length with respect to the pulse-time and propagation velocity. Resistive loading along the length of the antenna will result in a structure with radiation that can be modelled as a series of point E-field sources along the length of the antenna. The field at any given point in space will then be the sum of all the fields generated by this array of radiating elements (see [15] p555), introducing both additive phase and magnitude effects that will vary with respect to the elevation angle of the particular observation point.

The radiated pulse-form of a general dipole type antenna is thus dependant on a number of factors, including the length of the antenna structure, the quality of the feed point match to the source, the loading or losses along the length of the antenna (position and magnitude), and the observation point. Considering all these factors, we require an antenna with a good feed match, and little or no end reflection of any travelling wave on the structure at the antenna end-points. The antenna should also be as short as possible (this does imply that the antenna will be less efficient in general, but the radiated pulse form will be better, due to the shorter propagation time of a current pulse excited on the structure).

A more detailed consideration of the travelling wave modelling of radiating structures was performed by M van Wyk [6], and further detail can be found in the literature (see [15] p 547).

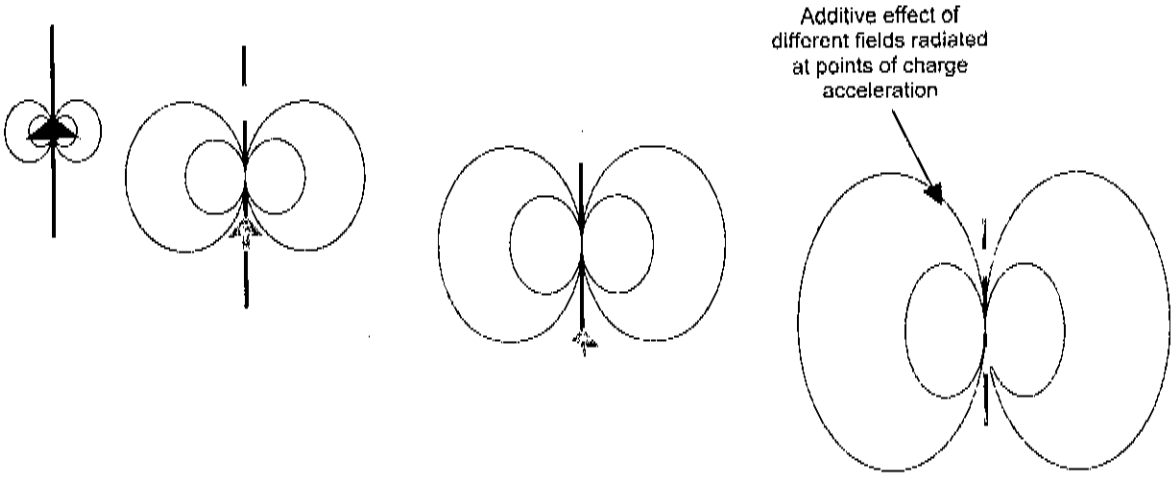

Figure 39 A simple representation of the radiation of a pulse excited long wire-dipole structure indicating the travelling waves on the structure, and the equivalent point radiators at the points of charge acceleration.

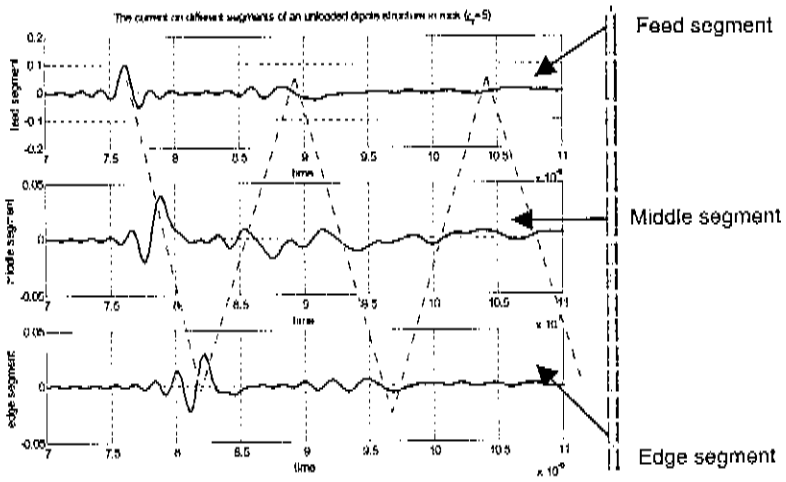

Figure 40 The currents on selected segments of a pulse-excited unloaded wire-dipole structure extracted from FEKO simulation results

There are a number of practical points that must be considered relating to the discussion of the radiation process of an axially long dipole-type structure. Firstly, the distributed radiation effects, due to the propagation delay between the feed point and the radiating edges, will play a role in determining the pulse shape and propagation time to an observation point at a given angle with respect to broadside. If we consider Figure 41, this effect can be shown. In order to compute the difference in propagation time of a radiated pulse between observation point 1, and observation point 2, both on a circle of radius r around the central feed point of the antenna. The path lengths (m, m2, d and d2) can be computed in terms of the dipole arm-length (l), the elevation angle (θ) and the radial distance (r) using simple trigonometry as shown in (2.6), where we have used the cosine rule (see [18]).

If we consider the difference between d and m for a 1m-arm length structure, for various values of r and θ, we get the results shown in Figure 42.

$$\begin{aligned} d &= \sqrt{r^2 - 1} \\ m &= \sqrt{r^2 + l^2 - 2rl\cos(90^\circ - \theta)} \\ d2 &= \sqrt{d^2 + l^2 - 2ld\cos(90^\circ + \theta)} \\ m2 &= m \end{aligned} \tag{2.6}$$

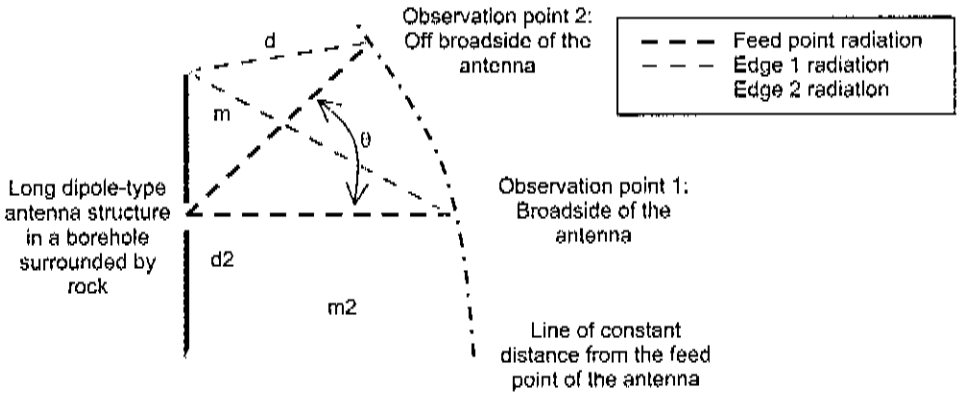

Figure 41 The geometrical layout of two observation points, to determine the effect of elevation angle on the propagation time from feed voltage excitation E-field propagation past the observation point

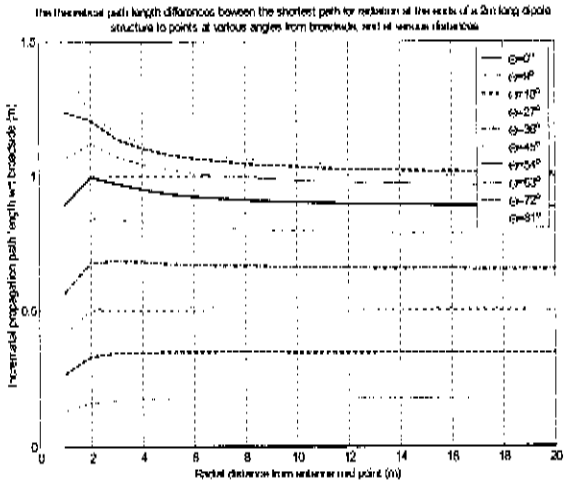

Figure 42 The effect of elevation angle above broadside on the propagation path between the edge of a 1m dipole structure, and a given observation point with respect to a broadside observation point at the same radial distance

It is clear that for any substantial distance from the antenna, the propagation path length difference between broadside and a given angle will be relatively constant. Now, if we consider the propagation delay of a radiated pulse that such a path difference will represent, it is clear that as the permitivity of the propagation medium increases, so the absolute difference in pulse delay with respect to broadside will increase as a function of elevation angle.

The delay between the observed fields radiated at different points on the antenna structure will also be affected by the propagation medium permitivity. One additional factor to keep in mind is that the material that fills a borehole in which the antenna is deployed will directly affect the time that an excited pulse will take to travel from the feed point to the radiating points along the length of the structure. The

propagation will be slower for a medium with higher permitivity. This propagation will directly affect the time properties of the radiated pulse form.

The effects of the elevation angle of the observation point on the radiated pulse form will be considered during the development of the antenna structure in section 2.5, with particular attention paid to the effects of the addition of a borehole model and its damping of this effect.

2.3.2.3. Radiation and pulse efficiency

The standard definition of the efficiency of an antenna structure is given in (2.7). Efficiency is thus the ratio of the total radiated energy in the electromagnetic field, integrated over a closed area around the antenna to the total power accepted by the antenna structure from the drive electronics ([11] p37 to p42). (Note that in this definition we have included the loss effects of the propagation materials in the $e^{2\alpha r}$ term for a given propagation distance, r. This is deviant from the general free-space efficiency definition).

$$Efficiency = \frac{\text{Total power radiated in all directions}}{\text{Total real power on antenna structure}} = \frac{\frac{1}{2}\,\mathrm{Re}\int_0^{\pi}\int_0^{2\pi}\left(E_\theta H_\phi^* \times E_\phi H_\theta^*\right) r^2 e^{2\alpha r}\sin\theta\, d\phi\, d\theta}{\frac{1}{2}\frac{\left|V_{feed}\right|^2}{\left|Z_{antenna}\right|} R_{antenna}} \qquad (2.7)$$

This general definition of efficiency does not take into account the direction of radiation of the energy (antenna directivity) or the relative time at which the energy is radiated (phase delay effects). Both of these, however are critically of interest for BHR analysis.

The directivity of an antenna is generally defined as the ratio of the radiation intensity in a certain direction to the average radiation intensity on a closed sphere, as shown in (2.8).

$$Directivity(\theta,\phi) = \frac{Power_{radiated}(\theta,\phi)}{(\text{Total power radiated})/4\pi} \qquad (2.8)$$

The gain of the radiating structure in a given direction may be found by multiplying the antenna directivity in that direction with the antenna radiation efficiency. In BHR, we are particularly interested in the energy that is radiated in the broadside direction, and would thus like the gain and directivity in the ($\theta=\pi,\phi$) direction to be high at all frequencies.

Because we are interested in the time response of the antenna in the pulsed BHR application, the time spreading of the energy in the radiated pulse form with respect to the excitation pulse must be considered. As discussed, the ideal time-pulse response represented in Figure 38 is not practically realistic. The more general pulsed radiation response of a practical structure will have a form closer to the one shown in Figure 43. In this representation of the expected pulse form, we can clearly see the

'spreading' of the energy in the practical radiated pulse due to the finite propagation time between the points on the antenna structure where charge acceleration, and thus radiation occurs. (i.e. even thought the total power in both pulses may be the same, the energy in the practical pulse is spread out over a longer period of time). In order to quantify the time-characteristic of the energy radiated by an antenna, we can define a number of properties for the antenna. If we consider the time-domain pulse-form, then we can define a number of time-related efficiencies, particularly for pulse radiation applications. These definitions are not general, but will be used in the study documented in this report as a method of comparing the time-radiating operation of the various antennas under consideration.

We begin by defining two time periods, the excitation pulse period (T_e) and the radiation pulse period (T_r) as shown in Figure 43. During the excitation pulse period, a large percentage of the radiated energy is found. We define this as the primary radiated pulse energy. A related definition that will be used is the shifted primary pulse energy. This refers to the energy within the same time-period as the excitation period, computed around the point where the peak field is radiated (thus in the shifted time period T_{es}). This energy is of interest in cases where there is a delay between the excitation and the radiation period, for example in the case of an elevation angle related propagation delay as discussed in Figure 41. Outside of T_e or T_{es}, the remnant of the total energy in the radiated pulse is found. We refer to this as the ringing energy.

A few properties can be based on these definitions. Firstly, the ratio between the primary radiated pulse energy and the ringing energy can be used as a comparative indication of the pulse form quality. We define this as the pulse ratio, or the pulse form factor. Likewise, the ratio between the shifted primary pulse energy and the total radiated energy in the pulse, the shifted pulse ratio can be computed. If we consider the ratio of the power accepted by the antenna to the primary radiated pulse power, or to the shifted primary pulse power, then we can get an concurrent indication of the both the antenna gain and directivity in the direction of the point where the field is measured, and pulse shape quality. We define this as the pulse efficiency. These definitions are shown in (2.9).

$$\varepsilon_{pulse-form} = \frac{\text{Power in the radiated pulse over the excitation pulse period}}{\text{Total power in the radiated pulse}} = \frac{\int_{t_{excitation\ period}} |E|^2 dt}{\int_{t_{radiation-period}} |E|^2 dt} \qquad (2.9)$$

$$\varepsilon_{shifted-pulse-form} = \frac{\text{Power in the radiated pulse over the shifted excitation period}}{\text{Total power in the radiated pulse}}$$

$$\varepsilon_{pulse} = \frac{\text{Power in the radiated pulse over the excitation pulse period}}{\text{Total power in transfered from the source to the antenna}}$$

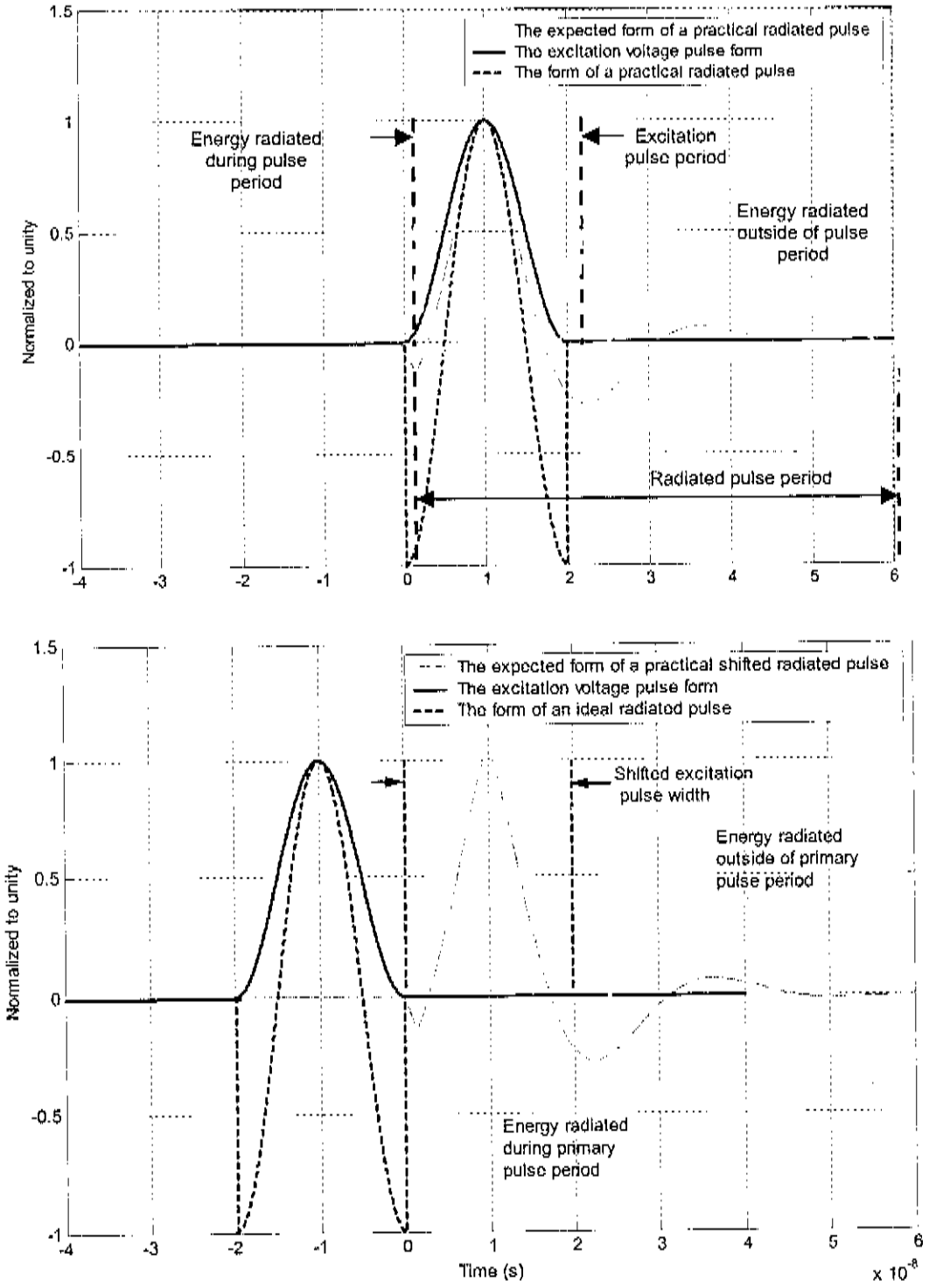

Figure 43 The forms of the expected radiated field pulses in the case of an ideal and a practical antenna structure for the shown excitation voltage pulse

2.3.2.4. Phase response

Another measure of the pulse spreading can be achieved by considering the phase and group delay of the antenna transfer function (radiated field with respect to excitation). A general definition of group and

phase delay is given in (2.10) [10], where $\phi(\omega)$ is the phase characteristic of the transfer function, and ω is the frequency in radians per second.

$$Delay_{phase}(\omega) = \frac{\phi(\omega)}{\omega}$$
$$Delay_{group}(\omega) = \frac{d\phi(\omega)}{d\omega} \quad (2.10)$$

These definitions are generally applicable to narrowband communication systems, where a carrier frequency is modulated with an envelope signal, and the phase- and group- delay then effectively refer to the propagation delay of the envelope and the carrier through the system respectively. For the broadband systems under consideration in this report, little quantitative physical meaning can be attached to the computed group delay of the system. Excessive variation in the delay versus frequency is extremely undesirable as is will cause pulse deformation as different components of the pulse undergo different intrinsic delays.

2.3.2.5. Impedance requirements

The input impedance seen at the feed point of the radiating structure is very important in order to achieve a good energy transfer from the transmitter electronics to the antenna, and from the antenna to the receiver electronics, by minimizing reflection losses. There are two considerations from the perspective of a mono-static system. Firstly, the transmitter topology (discussed in Chapter 4) is a pulsed voltage source, with a low output impedance and the power accepted by the antenna from the transmitter will thus be higher as the real input impedance drops. This is so, because for the case of a voltage source, the real power transfer is given by $P = \frac{\left(\frac{VR_{load}}{R_{load} + R_{source}}\right)^2}{R_{load}}$.

In the case of the receiver (discussed in Chapter 2), the antenna must be matched as close as possible to the input impedance of the RX electronics, in order to achieve maximum power transfer. The impedance of a passive antenna structure is reciprocal, and thus the impedance presented during the receive and transmit periods will be identical. The conflicting load requirements of the transmitter and the receiver must thus be considered, and a compromise found for mono-static application.

The input impedance of an antenna generally consists of both a real and an imaginary component. The real component represents the real ohmic losses on the antenna structure itself, and also the real power losses due to radiation. This component of the antenna impedance is also responsible for thermal noise generation which may affect the receive operation of the system. The imaginary component of the input impedance of an antenna represents the energy stored in the near fields of the structure. An antenna can thus be viewed as a complex load from a circuit theory point of view. For

short dipole-type antenna structures, as will be considered in this report, the imaginary component of the impedance is generally capacitive and large, with a small real component. As the relative length of the dipole structure is reduced, so the efficiency of the structure also falls, and the ohmic losses become of considerable consequence.

In order to achieve broadband antenna operation, the percentage variation of the impedance characteristics over the band of interest must be as little as possible. This impedance is generally affected by variation in the environment of the antenna, and this variation must be carefully considered. For BHR applications, the characteristics of the environment show great variation, and the effects of such variation of the antenna operation must be considered. Of particular importance is the effect of the probe housing, air or water (fresh or otherwise) in the borehole and the properties of rock materials on the antenna operation. Broadband operation is difficult to achieve, particularly given the spatial constraints to which the BHR antenna must adhere with respect to the excitation wavelength. Various methods can however be used to approximate such wideband antenna ([11] Chapter 6).

2.3.3. Determining operational properties of an antenna from measured and simulated data

During the study of the BHR radiating structure, we must be able to determine the operational characteristics of any structure under consideration; both for comparison purposes, and in order to determine how well the structure adheres to the requirements for BHR implementation. In this section we will consider how simulated or measured data can be used to determine and quantify the characteristics of a radiating structure. At the frequencies of interest, and for the complex operational environment of interest, it is generally very difficult to perform accurate and reliable measurements. Antenna characteristics must generally therefore be predicated based on simulation results.

The three main antenna properties that can be easily determined by FEKO simulation are the input impedance, the feed reflection coefficient and the radiation (far and near field) of the antenna in a given plane or at a given point. Based on these results, we can determine the properties of interest as discussed in the previous section.

2.3.3.1. Bandwidth

The bandwidth of an antenna is determined by considering the variation in the feed reflection coefficient over a certain frequency range. Generally the ratio between the upper and lower frequency points where the antenna reflection coefficient is a given number of dB's above the minimum point is defined as the antenna bandwidth. This bandwidth may be the 3dB point or 10dB point etc. Similar bandwidth definitions may be derived from any antenna characteristic, where the bandwidth is chosen as the frequency range in which the relevant characteristic remains within certain boundaries.

2.3.3.2. Quantifying the radiation process

The radiation of an antenna structure can be inferred by considering a number of things. Direct consideration of the radiated fields computed at a point in space in FEKO, or transformed into the time domain for a given excitation using the FEKO/ADS methods described in 2.1.3.2 is the most obvious, and can be used for direct comparison of the radiated fields of different structures. Observation of the actual radiation process however, is more complex. By employing direct time-domain simulation methods like FD-TD methods[6], the time-domain radiation of a structure can be observed. Alternatively, by performing Fourier-type transformations on frequency-domain FEKO data to consider the time behaviour of currents on a given structure, a clear picture of the radiation process for the simple structure can be developed. (This was shortly demonstrated in Figure 69 for a simple dipole antenna)

2.3.3.3. Radiation and pulse efficiency

The efficiency of a radiating structure is generally determined directly by the definition of (2.7). This can be done directly in FEKO, but observations show that when a lossy propagation medium is employed, the FEKO computations are not accurate. FEKO does not take the $e^{2\alpha r}$ term in (2.7) into account for a lossy medium and the efficiency must be computed manually from the definition, using the radiated fields computed over a closed area around the antenna structure[7].

The computation of the time-dependant pulse efficiency characteristics as defined in section 2.3.2.3 is based on time domain pulse responses computed in ADS (see 2.1.3). The energy in a given radiated E-field pulse can be determined by considering the integral of the E-field over the desired period of time, and the impedance of the propagation material ($n^2=\varepsilon/\mu$). Excitation energy can be determined by considering the integrated feed current or feed voltage in conjunction with the effective antenna load impedance, as shown in (2.11).

$$E_{field}(t_2-t_1)=\frac{\int_{t_1}^{t_2}|E(t)|^2\,dt}{\sqrt{\varepsilon/\mu}}$$

$$E_{current}(t_2-t_1)=\frac{1}{2}Z_{load}\int_{t_1}^{t_2}\left|I_{feed}(t)\right|^2\,dt \qquad (2.11)$$

$$E_{voltage}(t_2-t_1)=\frac{1}{2}\frac{1}{Z_{load}}\int_{t_1}^{t_2}\left|V_{feed}(t)\right|^2\,dt$$

2.3.3.4. Phase response

In order to compute the phase delay/group delay of an antenna, the phase of the radiated fields at a certain point, with respect to the excitation phase must be compared, to determine the phase of the antenna transfer function over a given frequency range. The delay can then be directly computed using the definitions of (2.10). It is important to note when considering the relative phase of the E-field at a

point, that a linear phase shift effect will be introduced, due to the propagation distance to the observation point. This linear shift will have no direct effect on the pulse form, and can thus be removed during computation of the delay effects.

2.3.3.5. Antenna load impedance

The feed impedance, directivity, gain and radiation patterns of an antenna structure can be extracted directly in FEKO.

2.4. Introduction to the antennas used in current BHR systems

In this section, we will take a short look at the antenna structures that have been used in a few existing BHR tools. A short analysis and critical evaluation of each of these structures will be made based on the requirements outlined in the previous section. We will begin by considering the theory on which the design of the existing antenna structures is based.

2.4.1. Theory of the symmetrical Wu-King antenna structure

In this section, we will consider the Wu-King resistive loading profile designed to damp resonance on a wire dipole structure. This concept and profile design has been used in the design of existing BHR radiating structures. A summary of the theoretical derivation of the Wu-King profile can be found in Appendix B.4.

In order to improve the broadband characteristics of a simple dipole antenna structure, we can add a distributed resistive loading along the antenna. This is most effective at frequencies where the antenna is long relative to the excitation wavelength, and a travelling wave thus exists on the antenna structure. The purpose of the resistive loading is to absorb the un-radiated energy as the excited wave travels along the antenna, so that reflections of the travelling wave at the antenna termination points (as discussed in 2.3.2) are eliminated, or strongly damped. The Wu-King profile is designed as a set of lumped element resistances that are placed at intervals along the length of the dipole arms. The radiation of such a structure can thus be modelled as a number of point radiation elements at each of the loading positions, the feed point, and the antenna termination points, based of the travelling wave radiation model discussed in 2.3.3.2. An evenly spaced 9-element Wu-King profile for a dipole structure with a 1m-arm length was calculated as shown in Table 2 [4], Appendix B.4. The simulated antenna characteristics of dipole structures, in an ϵ_r=6 medium, with various loading profiles, based on a percentage reduction of the Wu-King loading profile are shown in Figure 44.

9-element loading (1m arm length)									
Position (mm from feed)	55	166	278	389	500	611	722	833	944
Value (Ω)	38	83	95	111	133	167	224	340	733

48-element loading (600mm arm length)																													
Position/s (mm from feed)	6	18.5,31,43.5,56,68.56	81,93.5,106	118.5,131,143.5,156,168.5	181,193.5,206	218.5,231,243.5	256,268.5	281,293.5,306	318.5	331,343.5	356,368.5	381,393.5	406	418.5,431	443.5	456	468.5	481	493.5	506	518.5	531	543.5	556	568.5	581	593.5
Value (Ω)	18	20	22	24	27	30	33	36	39	43	47	51	56	62	68	75	82	91	100	110	130	150	180	220	300	470	910		

Table 2 equally spaced 9-element and a 48-element Wu-King profile computed for a dipole with a 1m-arm length and a 0,6m arm-length respectively

The improved broadband stability of the loaded dipole characteristics is clear if we compare them to the characteristics of the unloaded dipole structure. This is due to the damping of the travelling waves and end reflections on the antenna. The addition of a resistive loading profile to the antenna has a number of other implications, however. The most obvious of these is that the efficiency of the antenna will be negatively affected, as a part of the energy accepted by the structure is dissipated in the resistive profile, instead of being radiated, as it would be in the case of an un-loaded antenna. Radiation is effectively the only mechanism of energy dissipation on the unloaded structures, while resistive losses in the loaded structures are considerable - see the FEKO computed efficiency in Figure 44 as compared to 100% efficiency for an un-loaded dipole structure. For a pulse antenna this drop in efficiency must be played off against the improved broadband characteristics i.e. decreased pulse deformation characteristics and phase delay of the antenna, when choosing a loading profile.

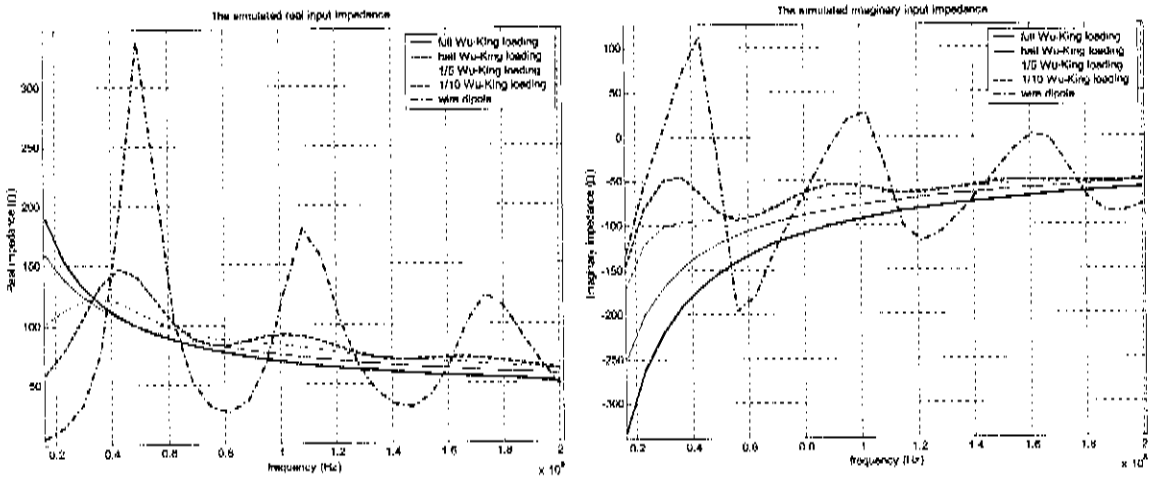

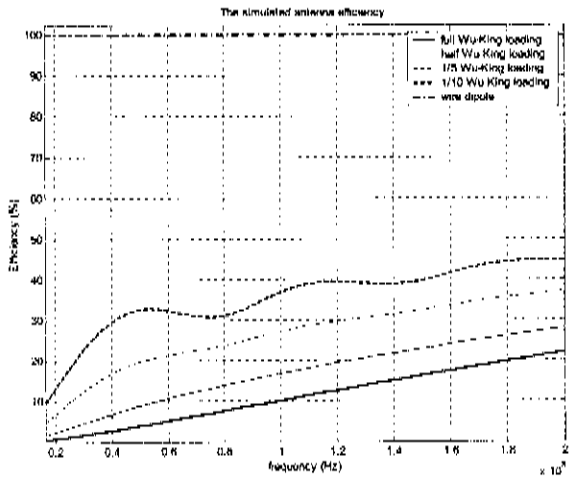

Figure 44 The FEKO simulated input impedance and efficiency of a symmetrical wire dipole (arm-length=1m, wire diameter=28mm) in a loss-less ϵ_r=6 medium, and the effect of loading the dipole with 10%, 20%, 50% and the full 9-element computed Wu-King profile

The Wu-King profile, as computed from the theory of Appendix B.4, will operate perfectly at a single frequency, in a specific medium. Investigations, using FD-TD computational tools, by Marius van Wyk [6] suggest that for broadband pulse radiating applications, the full Wu-King profile's intrinsic inefficiency is a critical factor, and a damping of less than 50% of the full theoretical Wu-King loading is more efficient, without excessive increase in the pulse expansion characteristics, and thus more practically acceptable. This is immediately clear from the results of Figure 44 for the four different percentage loadings of the Wu-King profile, where we require relatively stable characteristics over the frequency range of interest with the highest possible efficiency.

The immediate question that arises from this short consideration of the resistive loading of an antenna is the possibility of using lumped capacitive and inductive elements to achieve the same damping effects with less resistive energy losses.

The first consideration is that we require some form of energy dissipation on the structure, be it by improved radiation efficiency, or by increased ohmic losses. Capacitive and inductive lumped elements do not ideally have a real impedance component, and thus their effect on the antenna operation will have to improve the radiation efficiency. The profile may have to be coupled with a resistive loading for additional ohmic dissipation.

The second consideration is that of the frequency dependant impedance of the lumped element loading will cause a frequency dependant loading on the antenna. For pulse applications, the phase effects of the loading at different frequencies are critical and will affect the radiation pulse form of the antenna. We require that the impedances be large at lower frequencies and small at higher frequencies in order to optimally load the antenna (see [4] pp. 69-75).

During the development of ADS/FEKO computational simulation methods in section 2.1.3, the time domain effects of loading a dipole structure with a Wu-King profile were shortly considered. This will not be revisited here.

2.4.2. Un-symmetrical radiating structures as used in existing BHR systems

In this section, we will describe the physical antenna structures used in a few existing BHR systems.

In existing BHR systems, a modification of the standard Wu-King resistive loading profile (designed to be applied to a symmetrical dipole structure) is applied to a non-symmetrical structure. The general form of the existing structures is shown in Figure 45.

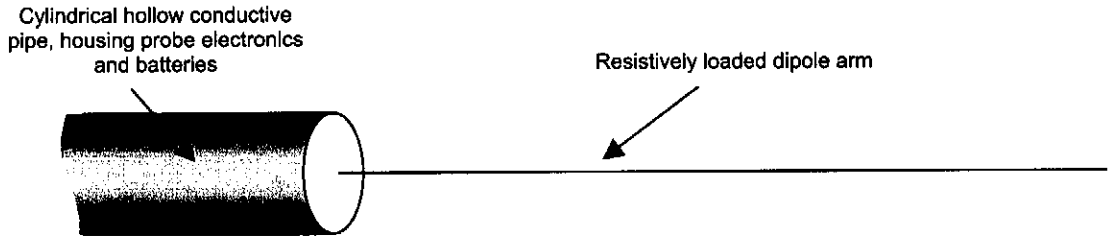

Figure 45 The practical radiating structure employed in existing BHR systems

A single resistively loaded dipole arm is driven against a conductive copper pipe, forming an asymmetrical radiation structure. The copper pipe section houses the battery pack and electronics of the probe (TX or RX electronics). The dimensions of the various radiating structures used in the existing systems are summarized in Table 3.

BHR system	Copper pipe diameter (mm)	Copper pipe length (mm)	Loaded strip length (mm)	Loading profile type
Geomole RX-probe	27.5	650	610	48-element Wu-King
Geomole TX-probe	27.5	1000	610	48-element Wu-King
ST RX-probe	27.5	650	610	48-element Wu-King
ST TX-probe	27.5	1000	610	48-element Wu-King
M. van Wyk RX-probe	27.5	526	1000	9-element 60% Wu-King
P. Herselman TX-probe	27.5	431	1000	9-element 60% Wu-King

9-element and 48-element loading similar to that calculated in Table 2

Table 3 The relative dimensions of interest of the radiating structures used in existing BHR probes

The operation of these probes can be characterized in a number of ways. The tools and methods that were discussed in section 2.1 are used for computational modelling. Some of these modelled results can be verified by practical measurement of the physical radiating structures. This modelling and measurement will be done in the next section in order to characterize the operation of existing antenna structures.

2.4.3. Simulation and operational characterization of existing radiating structures

In this section, we will perform a short computational analysis of the radiating structures used in existing systems (as described in the previous section), using a simple, verified computational model. The properties of the antennas will then be qualitatively considered with respect to the requirements of a good radiating structure for pulsed BHR applications, as discussed in section 2.3.

Measurement of the radiating structure used in the GEOMOLE and 'ST' system receiver probes was performed by Paul Herselman[7]. These measurement results are presented with FEKO predicted computational results in Figure 44. (The verification computations and measurements were performed in air, and are thus only relevant for verification of the computational model.)

The results of FEKO modelling of the antenna characteristics in rock type material (ε_r=7.5 and tanδ=1/20) of the antenna structures of Table 3, using the same model verified in Figure 46, are shown in Figure 47.

The conductive pipe section of the antenna introduces a damped resonance point into the antenna operational characteristics. This damped resonance is dependant on the length of the copper pipe section, and is relatively independent of the loading profile and Wu-King arm-length (see [8]).

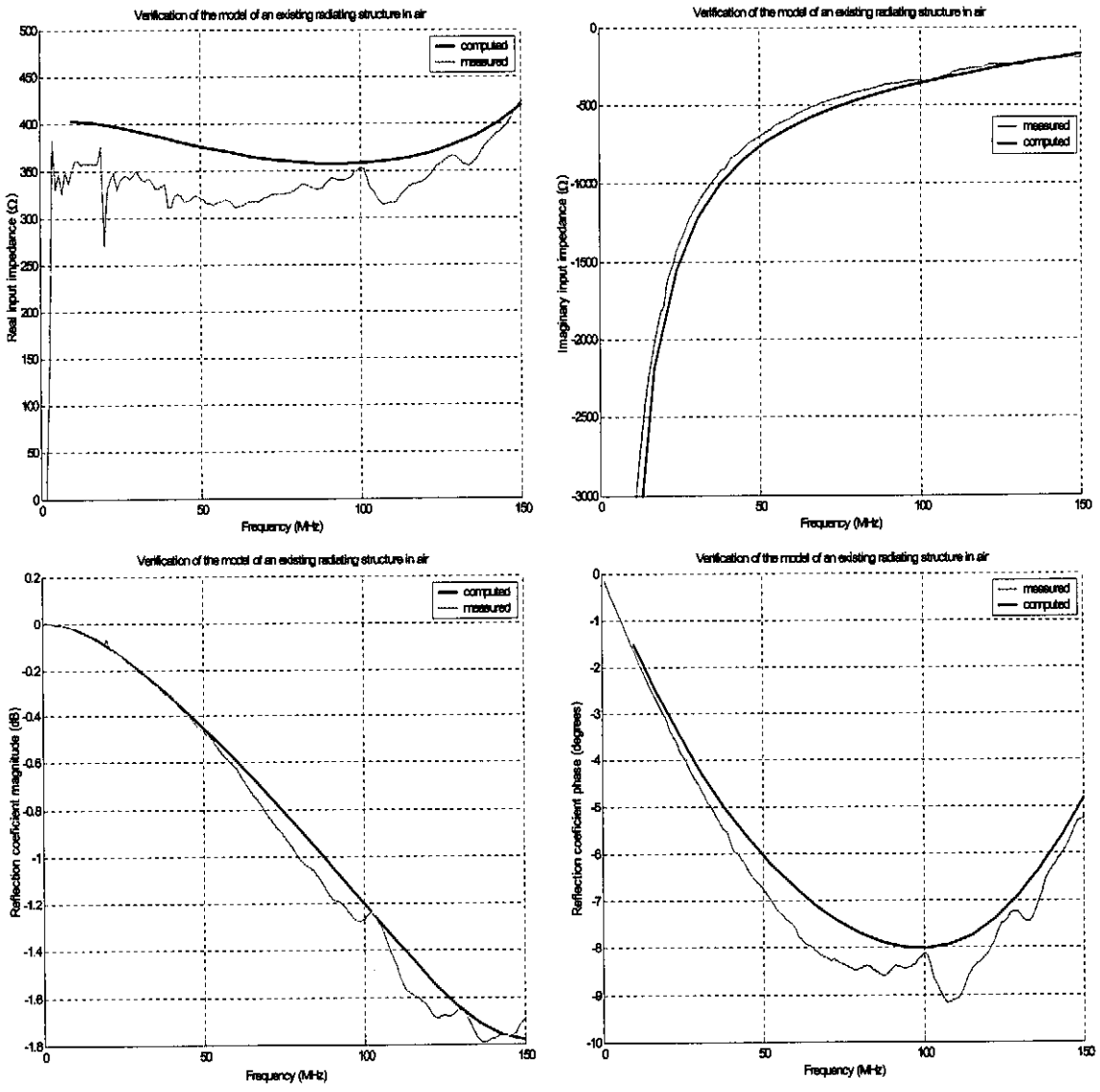

Figure 46 The comparative measured and FEKO modelled characteristics of the radiating structure of the GEOMOLE and ST receiver probes in air for verification purposes

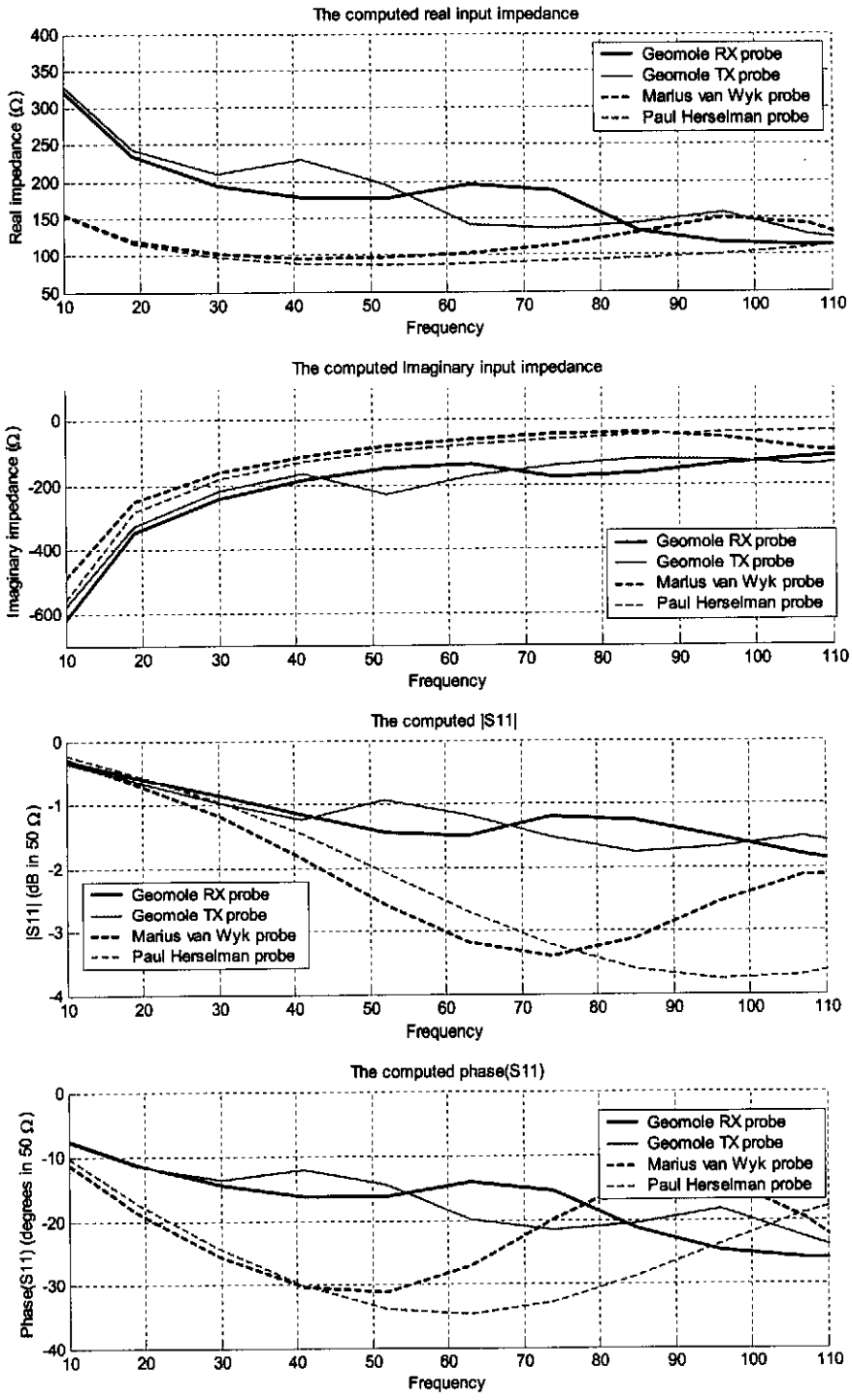

Figure 47 The computed input impedance and reflection coefficient characteristics of the radiating structures used in existing BHR systems

The computational results of Figure 47 do not take into account the effects of the probe housing and any potting material, in order to shorten the simulation time. This assumption has a relatively small effect (see [6] pp. 55-57), on both the form and magnitude of the results. A number of observations and a non-precise operational analysis of the structures are possible based on the results, however. This

type of analysis delivers a good idea of how the radiating structures perform, and provides a good foundation for the development, comparative analysis and improvement of a new radiating structure.

A few observations related to the characteristics of the structures modelled in Figure 47 are:

- The increase in the length of the loaded arms and shortening of the conductive copper pipes in the Marius van Wyk/Paul Herselman structures causes a decrease in the real input impedance and an increase in the capacitive load characteristics of the structure.

- The smaller number of resistive elements used in the loading profiles of the Marius van Wyk and Paul Herselman probes improves the broadband performance and efficiency of the structure. Percentage reduction of the applied Wu-King profile does not effect the broadband operation of the antenna too much (2dB to 3dB more variation in |S11|), but does greatly improve radiation efficiency (this observation is supported by the results presented in [6]).

- Variation in the length of the conductive pipe section causes a frequency shift in the characteristics of the structure, as the damped resonance supported by the unloaded arm is shifted in frequency. The length of this section plays a major role in determining the operating characteristics of the antenna.

- Consideration of the radiation pattern of the antenna structures (see Figure 48) shows that the structural asymmetry causes the radiation pattern to 'squint' slightly towards the resistively loaded section in the lower band of the frequencies of interest, and towards the conductive pipe section as the frequency increases. At the highest frequencies of interest, a secondary lobe begins to form. This observation is worrying, as the ideal antenna for typical BHR application should have a single broad broadside lobe. Further investigation indicates that the addition of a dielectric-filled borehole layer into the computational model results in a drastic reduction of the observed squinting effect, with no considerable side-lobe formation and a maximum squint of around 10° towards the conductive pipe (assuming realistic material properties of the antenna environment). This is much better than the results of Figure 48, but is still very undesirable.

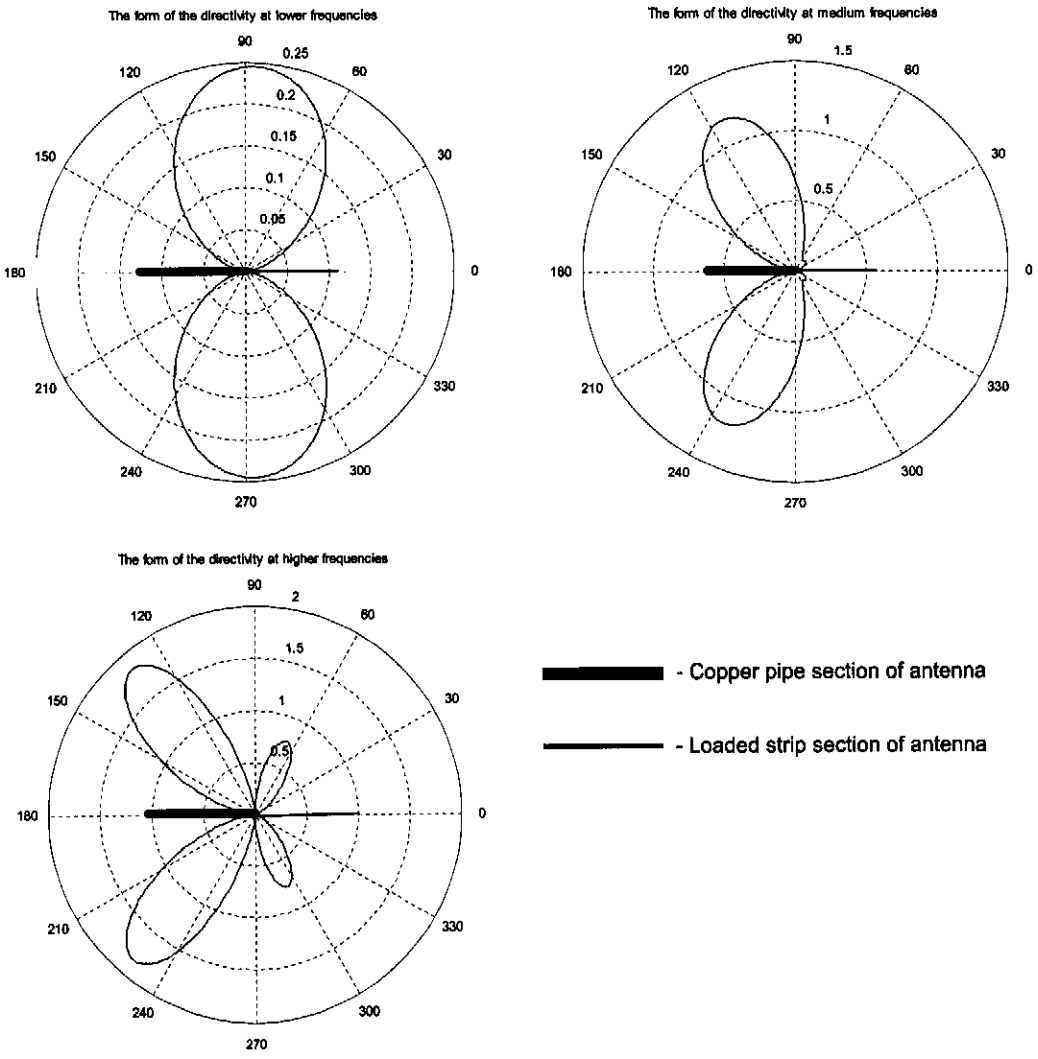

Figure 48 The variation in the radiation pattern of the asymmetrical antenna structures used in existing BHR systems at various relative frequencies

A short (again qualitative rather that quantitative) investigation of the pulse radiating characteristics of the existing antenna structures was performed, and the results of the investigation can be summarized as follows.

For the structures as described in Table 3, FEKO simulation of the radiated fields incorporated into an ADS model using the methods outlined in section 2.1.4 delivered the results shown in Figure 49.

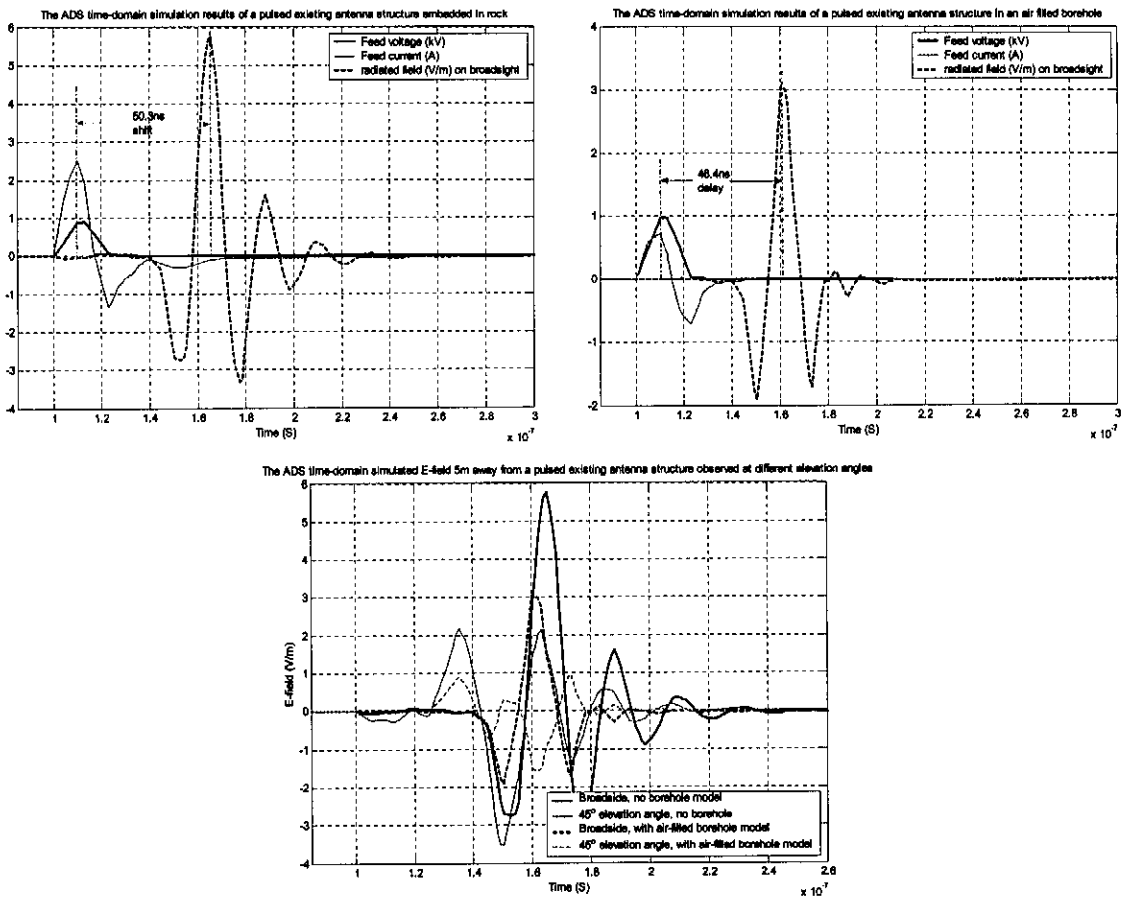

Figure 49 Simulation results of the time-domain operation of an existing antenna in rock ($\varepsilon r=7.5;\tan\delta={}^{1}/_{20}$)

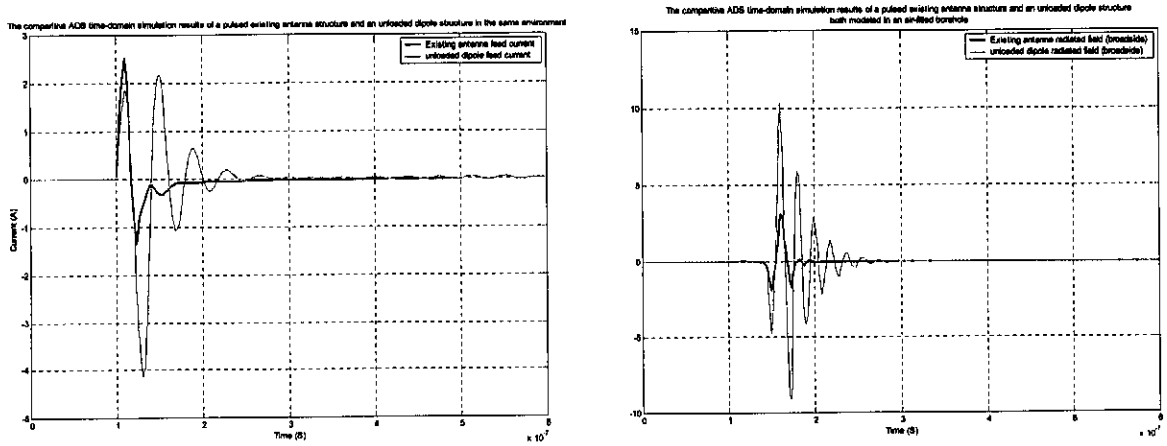

Figure 50 The comparative feed currents and radiated E-fields 5m broadside of an unloaded dipole and a radiating structure used in an existing probe modelled in an air-filled borehole (for the rock: $\varepsilon_r=7.5,\tan\delta=1/20$)

The antenna structure shown in Figure 49 does radiate a pulse with considerably less pulse expansion than an un-damped dipole structure ($\varepsilon_{shifted\text{-}pulse\text{-}form}$=37.35%; t_{shift}=58ns for the unloaded dipole structure and $\varepsilon_{shifted\text{-}pulse\text{-}form}$=71.02%; t_{shift}=55ns for the existing antenna structure,). The peak magnitude of the primary pulse radiated field is relatively small (about 1/3rd of the peak field for the unloaded dipole). $\varepsilon_{shifted\text{-}pulse}$= 0.0992 for the un-damped dipole, and $\varepsilon_{shifted\text{-}pulse}$= 0.018 for the existing structure. For the pulses radiated at a 45° elevation angle, $\varepsilon_{shifted\text{-}pulse\text{-}form}$=36.12%; t_{shift}=57ns for the unloaded dipole structure and $\varepsilon_{shifted\text{-}pulse\text{-}form}$=60.41%; t_{shift}=45ns for the existing antenna structure.

Comparison of the results of Figure 49 and Figure 50 shows that the effect of the addition of an air filled borehole into the environmental model used in the simulation of the existing structure of Figure 50 is twofold. Firstly, the coupling to the rock structure is poorer (approximately 3dB poorer) in the air filled borehole case, as can be seen in the smaller peak and general E-field pulse magnitude.

The second observation is that an intrinsic primary pulse delay is introduced in the antenna radiation. This delay is dependant on the elevation angle and the distance to the observation point. The delay phenomenon can be explained with reference to the radiation procedure discussed in section 2.3.2.2. In the case of an air filled borehole, the propagation time of a travelling wave on the antenna structure from the feed point to the extreme edge of the antenna structure will be at the speed c=3x10^8 (approximately 3.34ns for 1m propagation). When the antenna is imbedded in rock, however, this propagation speed will drop by a factor equal to the square root of the permitivity of the rock material. The propagation time for a 1m distance will thus be approximately 9.14nS. At a radius of 5m, the propagation path length difference (d-m) at θ=45° will be approximately 800mm (see Figure 42). In an ε_r=7.5 material, this will introduce an additional 7.31ns propagation delay between two observation points at 5m radial distance from the antenna feed point. Consideration of the currents on the structure suggests that most radiation will occur at the edges of the antenna. We can therefore expect that radiation from the edge of the structure embedded in rock will reach the 5m radius broadside point 54.8ns after the initial excitation of the antenna, and the 5m radius point at a 45° elevation angle 46.5ns after excitation. For the air filled borehole case, these times will be 3.48ns shorter. These theoretical propagation delays agree very well with those observed in the FEKO/ADS simulation results.

2.5. The design and development of a balanced antenna structure

In this section, we will motivate and outline the development of a balanced antenna structure for use in a mono-static BHR probe. We will begin by considering the most simple antenna structure that will adhere to the spatial requirements of BHR application. Next, we will consider methods of improving the operational characteristics of the structures, taking into account the environmental effects on the antenna operation, by application of numerical modelling methods.

It was decided to employ a balanced structure rather that the unbalanced structure employed in previous BHR systems. This decision can be motivated as follows.

Although the radiating structure used in the current BHR probes is not a symmetrical, balanced structure, it is fed as such. Because the excitation wavelengths of interest are long with respect to the structure, the unsymmetrical structure acts to a large degree as a balanced structure, and is in fact rather poorly defined.

A true symmetrical balanced antenna structure is advantageous from a design point of view to achieve good isolation between the receiver and transmitter of the mono-static system. The reasons for this are discussed in Chapter 4.

The use of a balanced structure is advantageous from a bandwidth and radiation efficiency perspective, as shown by various comparative computational investigations.

A symmetrical structure will intrinsically have a symmetrical radiation pattern in its axial plane at all frequencies for a balanced feed. This is of particular importance if we consider the observations of Figure 48 for the un-symmetrical radiating structure. The direction in which the probe is inserted into the borehole will also have no effect on the system operation.

2.5.1. Basic wire, and cylindrical dipole structures

In this section, we will begin the development of a symmetrical BHR antenna structure by considering the most basic symmetrical structures that adhere to the spatial requirements discussed in section 2.3.1.

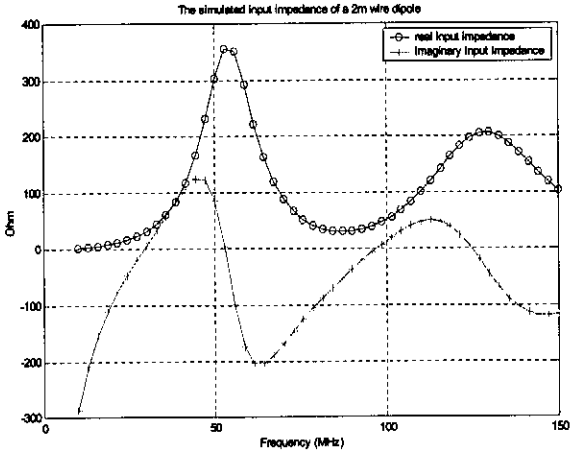

Figure 51 The simulated characteristics of a 2m long, 14mm radius centre fed wire dipole in an ε_r=6 medium

The most simple antenna structure that will conform to the physical constraints of a borehole, as discussed in section 2.3.1, is a symmetrical wire dipole with a radius of less than 20mm. Some results of simulation of a 2m long wire dipole antenna with a 14mm radius, in an ε_r=6 medium (this value is close to many permitivities of geological materials, e.g. coal[19]), using FEKO, are shown in Figure 51.

Although the dipole structure simulated in Figure 51 adheres to the physical constraints placed on the radiating structure of the BHR probe, it is immediately clear that the broadband characteristics of the structure are poor. A simple explanation of the physical reasons for this can be given by considering the radiation process, and noting that at the frequencies under consideration the dipole can be approximately modelled as a transmission line that has been folded open. The current distribution along the antenna can be viewed as a Fourier-type combination of sinusoids at various frequencies that sum to appease the imposed source conditions at the feed point and the zero current requirement at the endpoints of the dipole. The structure will support travelling waves, as would a transmission line. When the structure is excited, a travelling wave originates at the feed point, and propagates along the structure, towards the ends. When the wave reaches the end of the antenna, it is reflected and propagates back toward the feed point. The wave then reflected (for the case of a voltage source feed) 'swaps' arms at the feed point and again propagates out towards the ends of the dipole structure. This process would carry on indefinitely, as there is very little or no loss as the wave propagates along the conducting dipole structure, but each time a wave component is reflected at the feed or the ends of the structure, radiation of a percentage of the energy in the travelling wave occurs, as the fields around the dipole change to adhere to the physically imposed boundary conditions. The amount of energy radiated at a given frequency depends on the wavelength of that component of the excitation with respect to the physical length of the antenna. If the physical dimensions of the structure are such that it can support the excitation as a 'mode', then the radiation will be most effective, this is the cause of the peaks of efficient radiation observed at multiples of a fundamental excitation frequency (such that $l_{dipole} \simeq \frac{\lambda_{excitation}}{2}$). The strong frequency dependant radiation is the cause of the erratic antenna characteristics that make it a poor broadband radiation structure.

Hollow cylindrical dipole-type structures can also adhere to the spatial limitations of the BHR environment. Such structures however provide more freedom for design and adaptation. Comparative consideration of FEKO models of solid wire dipoles and cylindrical dipole structures of the same outer radius deliver very similar results.

The time-domain pulse radiation characterization of an unloaded dipole antenna structure, using the modelling methods of 2.1.3 was shortly considered in the previous section. Figure 50 shows the form of the radiated E-field pulse of a 2m-dipole structure in rock. The shifted pulse form ratio (by the definition of (2.9)) for this specific case was computed as 0.3735. This implies that approximately two thirds of the radiated energy is found outside of the excitation pulse period, and that the pulse spreading effect due to non-linear phase transfer effects is severe.

2.5.2. Addition of a loading profile to improve broadband pulse characteristics

In the literature, a number of methods are discussed to improve the bandwidth of a simple dipole structure. These include the use of a sleeved dipole, folded dipoles, helical structures etc. All of these methods, however, cannot generate an antenna structure with a bandwidth anywhere near the 10:1 requirement of the BHR radar system. Resistive loading of the dipole can be used to achieve much broader bandwidths, at the expense of efficiency as was shown in section 2.4.1.

In this section, we will consider the addition of lumped element loading profiles to the basic structures discussed in the previous section in order to improve their broadband properties, based on the theory discussed in section 2.4.1, and make them more ideal for BHR application. Specific attention will be paid to the prediction of the time domain pulsed operation of the structures under consideration.

2.5.2.1. The starting point

The physical requirements on the antenna structure outlined in section 2.3.1 include a requirement that there must be space in the BHR probe for the probe electronics and battery to be housed, in such a way that they do not affect the antenna operation. The obvious method of doing this is to use a conductive pipe structure as part of the antenna inside of which the electronics can be housed, as is done in the existing BHR probe structures. The hollow cylindrical conductor will operate well as a EM-shielding structure for the probe electronics, as currents on the cylinder will be largely contained within the skin depth of the material at a given frequency. Skin depth at a given frequency for a given non-magnetic conducting material is computed as $\delta = \sqrt{\frac{2}{\omega \mu_o \sigma}}$ (see [12] p 33). At the frequencies of interest, the skin depth for copper is a number of orders smaller than the total thickness of the copper pipe. This implies that two independent current paths are available on the cylindrical conductor. Currents on the antenna structure will therefore flow on the outer path, while currents induced by the operational electronics will flow on the inner path. (This double current-path description of the cylindrical conductors also infers an intrinsic balun as will be discussed in section 5.1.4.)

The chosen symmetrical antenna form, allowing for the housing of the probe electronics and battery pack within a closed conductive cylinder is shown in Figure 52. The placement of the electronics housing at the centre facilitates easy feeding of the radiation structure. We choose to locate the antenna loading away from the feed point to provide for optimal use of the length of the antenna structure.

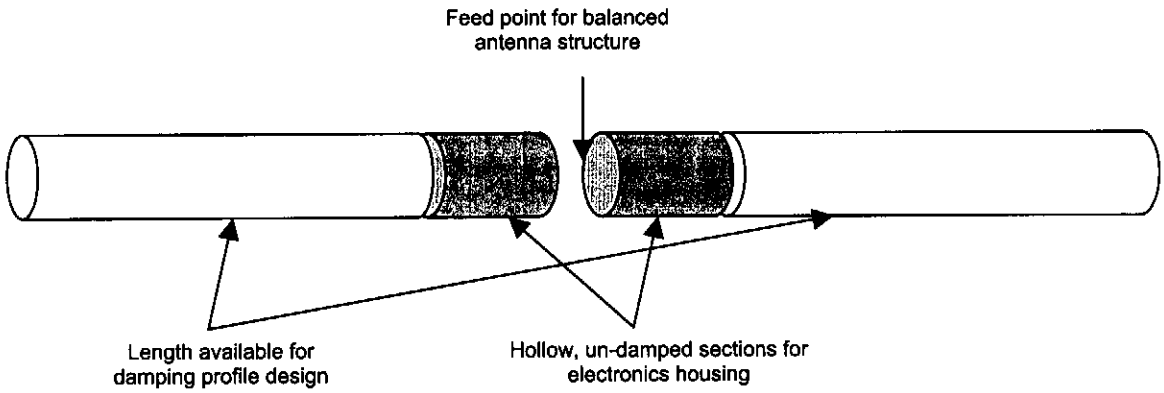

Figure 52 The general form of the balanced antenna structure allowing for the addition of resistive loading and space for electronics housing

The percentage of the probe length necessary for the housing of the electronics depends on the size of both the battery pack and the electronics. It was decided to house the battery pack in the hollow housing of one of the antenna arms, and the electronics in the other. Consideration of both the electronics used in existing systems and the realizable battery pack sizes suggested that a hollow section 400mm in length in either arm should be satisfactory. The total length of the radiation structure, in order to make the resulting BHR probe easily portable in the mine environment was chosen as 2m.

2.5.2.2. Simulation model development

Three computational models of different physical damping structures were developed in FEKO to facilitate simulation of the operation of antenna structures. The first two models are practically viable models, employing conductive cylinder sections and conductive strip sections respectively in the area allocated for profile development in the dipole topology. Both models assume a cylindrical conductor for the un-damped section of the antenna arms. The third model is a simple thick-wire dipole model, with the same outer dimensions as the other two models.

These three models were loaded using a 9-element Wu-King profile designed for a dipole with an arm length of 600mm as shown in Table 2. The comparative simulation results for the three structures embedded in an ε_r=10 propagation medium are shown in Figure 54, along with the respective total simulation times. It is clear that all three models of the radiation structures perform similarly for the shown characteristics of interest, but the simulation times vary, with the wire approximation simulation time being around 100 times less than that of the more exact practical models. Due to this, the wire approximation of the antenna structure was used for initial investigations into the effects of the addition of a loading profile.

The use of the wire dipole approximation was found to be inaccurate for the more complex cases, when the effects of the environment on the operation of the antenna structures have been introduced. For

accurate analysis of these cases, a more complex and physically accurate of the relevant antenna topology will be employed.

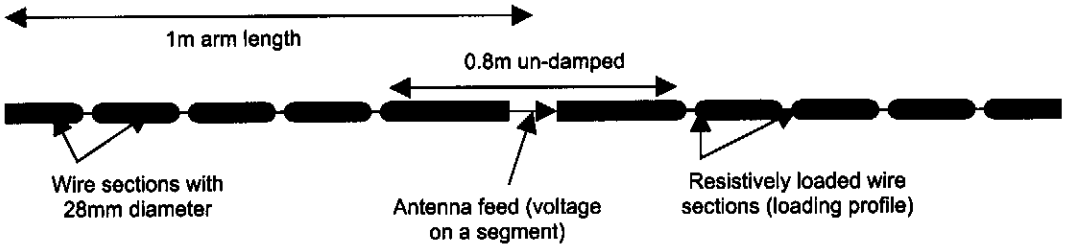

Model 1: Wire model of the antenna structure

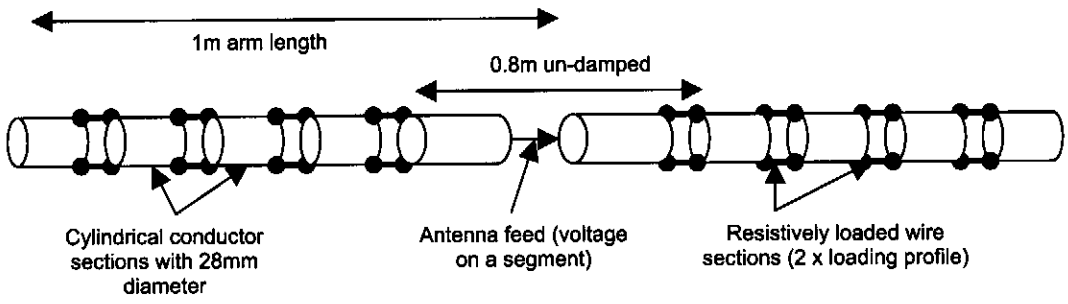

Model 2: full cylinder model of the antenna structure

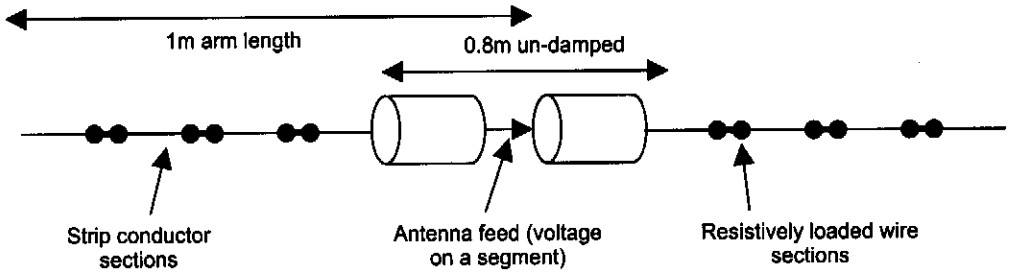

Model 3: Loaded strip model of the antenna structure

Figure 53 Three alternative computational models of the BHR radiating structure

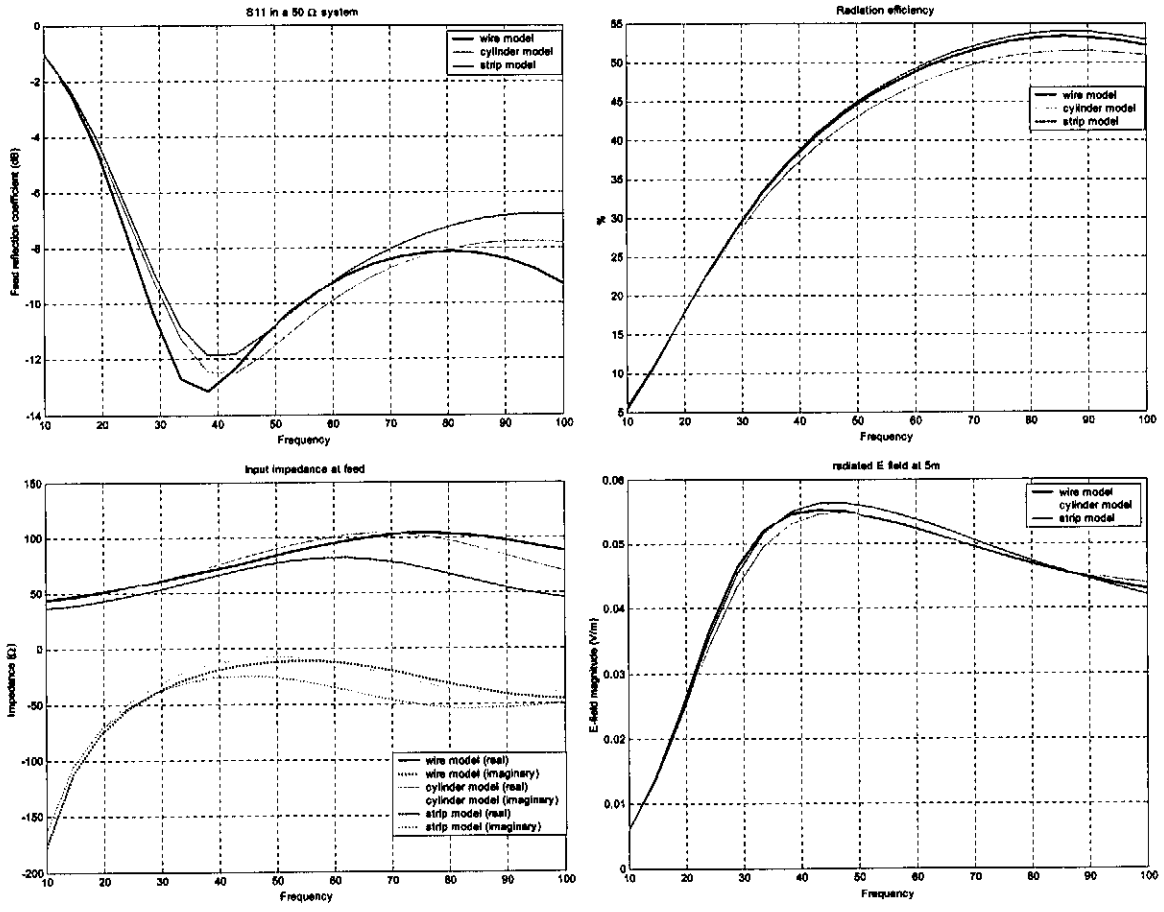

Total simulation times:	Wire model – 2.744 seconds Cylinder model - 270.549 seconds Strip model - 335.172 seconds

Figure 54 Simulation results and times for the Wu-King profile loaded antenna models shown in Figure 53.

Note that the loaded-strip shown in Figure 53 can be replaced with a number of non-centrally located strip sections loaded with the relevant multiple of the profile with minimal effect on the operation of the antenna model. This case, however closely approximates model 2. We will refer to the possibility and advantages of using such a structure later in the report.

2.5.2.3. Computational investigation of the effects of adding lumped resistors to a dipole structure

Using the FEKO models developed in the previous section, a large number of simulations were run, in order to determine by simulation the best resistive loading profile to be used in the antenna structure of Figure 52. A few of the most significant results in the investigation process are presented here, followed by a discussion of the loading profile chosen based on observations made during the profile investigation.

The effects of single resistive elements placed at various points on the dipole structure were considered. The positioning and value of the lumped resistor were found to be critical to the effect that the element has on the antenna characteristics. The process and results of this investigation will not be presented here. We will rather begin by considering a structured loading profile, namely, a modified form of the standard Wu-King loading profile introduced in 2.4.1. Note that the simulation models used in the initial profile investigations is a simple, computationally efficient wire element model, without the consideration of the BHR environmental effects. These initial investigations will deliver qualitative results about the physical operation and radiation of the structures under consideration, on which a more detailed investigation and development will be based in the next sections.

A. Modification of the Wu-King loading policy based on practical observations

The beginning point of the development of a structured loading profile is the Wu-King profile discussed in section 2.4.1. The Wu-King profile is designed to be applied in the form of discrete lumped element loading resistors placed at regular intervals along the whole length of each arm of the dipole structure. This application method must, however, be adapted to allow for an un-damped electronics housing section as depicted in Table 4. As shown in the table, the profile is applied as calculated from the theory, but starting at the elements far enough from the feed point to be located in the damping region, ignoring the elements computed at positions closer to the feed point.

The results of computation of the input impedance of the antenna structure after application of the profile of Table 4 to an antenna structure of the form shown in Figure 52 with 400mm long un-damped central sections and 600mm long loaded sections, using a simple wire dipole model, are shown in Figure 55. The total length of the structure is 2m, and it is imbedded in rock ($\sigma=1x10^{-3}$). Results for two extreme values of permitivity of the propagation medium are presented. For comparison purposes, the input impedance of an un-loaded and a Wu-King loaded dipole, loaded using the standard loading policy, are also shown.

Modified profile from here for a 400mm un-damped cylinder →

Position (mm from feed)	55	166	278		500	611	722	833	944
Value (Ω)	38	83	95		133	167	224	340	733

→ Modified profile from here for a 300mm un-damped cylinder

Table 4 A modification of the Wu-King loading calculated for a 1m dipole arm with 9 resistive elements equally spaced along the arm.

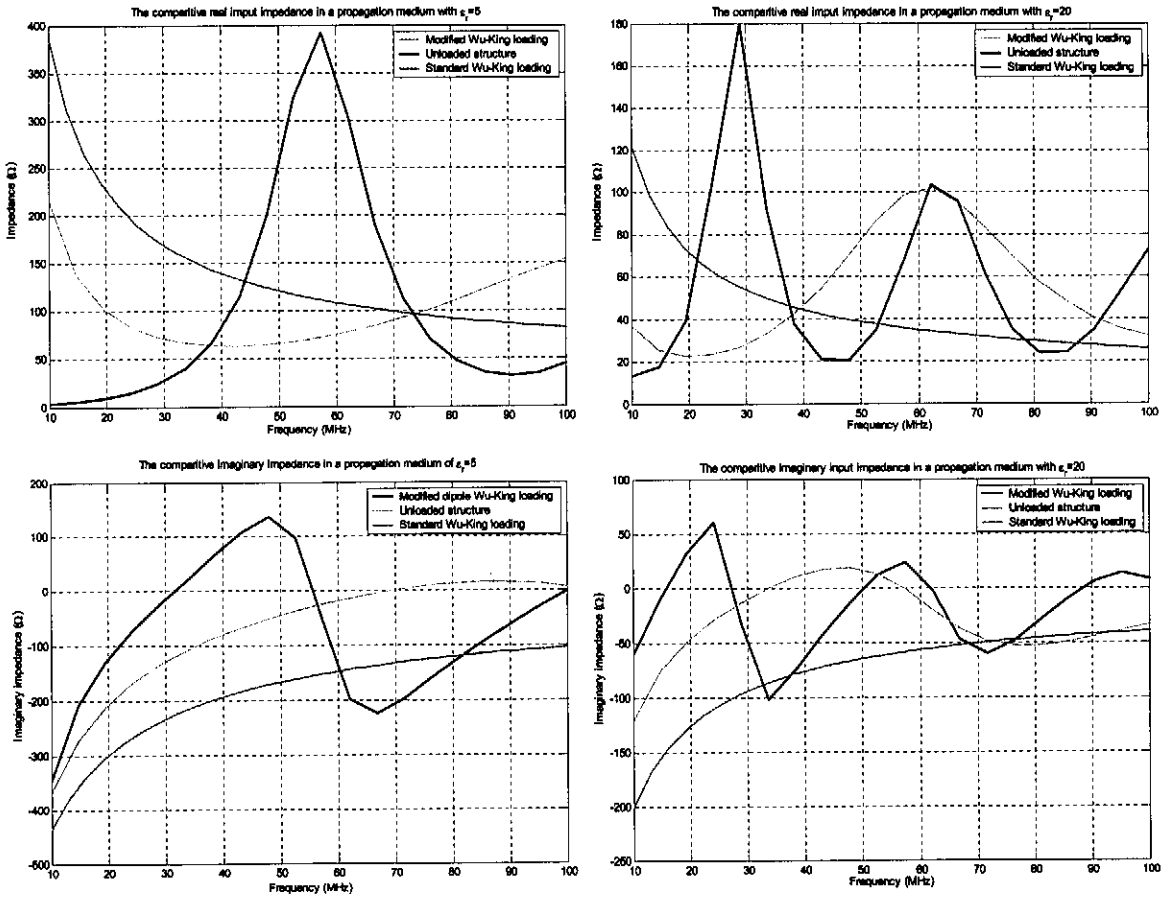

Figure 55 The comparative input impedances of an unloaded, Wu-King, and modified Wu-King loading on a 2m dipole structure embedded in rock material (σ=1x10^{-3})

From these simulation results, we can see that both the standard and modified loading profiles have very favourable affects on the bandwidth properties of the dipole structure. The modified Wu-King profile does not damp the resonance points as well as the standard full Wu-King loaded structure, particularly in the ε_r=20 material. The 800mm un-damped central section of the modified dipole structure would be resonant at 41.89MHz in the ε_r=20 medium and at 83.79MHz in the ε_r=5 material, but the simulation results suggest that the resistively loaded termination arms cause a damping and shifting of this resonance point. It is predicted that if the loading on the termination sections is reduced, this resonance effect will be less pronounced, and shift up in frequency. The damped, shifted resonance of the modified loaded dipole can be seen as a pseudo-resonance due to the inferred mismatch at the interface between the unloaded and loaded sections. The resonant point will be lower for a lighter loading, and the input impedance will become smaller, as the pseudo-resonant length of the structure increases. We will again refer to this idea when we consider the time domain operation of the axially long simple antennas.

In order to improve the operation of the modified Wu-King damping, the resonance points of the structure must be removed. The real input impedance of the modified dipole structure is better than the standard Wu-King impedance, although it still varies considerably over the frequency band of interest. The imaginary input impedance, particularly at the low frequency side of the remains large and capacitive, although the capacitive input load impedance of the modified dipole structure is better than that of the standard Wu-King. The effect of a change in the permitivity of the surrounding medium on an embedded antenna as considered in Figure 55 is two fold. As the permitivity increases, so the properties of the antenna are scaled with frequency. The impedance properties of the antenna are also scaled in magnitude. The simulation results show that both of these scaling effects are with a $\frac{1}{\sqrt{\Delta\varepsilon_r}}$ factor, where $\Delta\varepsilon_r$ is the change in permitivity of the propagation medium.

Consideration of the radiation efficiency of the damped structures indicates, as expected, that the resistive loading causes a drastic drop in efficiency at all frequencies. The percentage variation in radiated field magnitude (dB) over the frequency band of interest however is a lot less than that of the un-damped dipole structure, again showing the improved broadband radiation consistency of the structure. The simulated radiated E-fields and input reflection coefficients are summarized in Figure 66.

B. Simple parametric load impedance model extraction

For both ADS computational use and theoretical design purposes, we would like to develop a lumped element model of the antenna structures. This capability is of particular importance when the isolation topology of the mono-static system (discussed in Chapter 4 of this report) is considered. The isolation strategy is heavily dependant on the ability to provide a lumped-element estimation of the load impedance that will be presented at the antenna port of the mono-static isolator. By extraction of a model, a close initial match between the lumped element load network and a specific antenna operating in a specific environment can be achieved

A simple lumped element model of the standard loaded dipole antenna is shown in Figure 56. The mathematical representation of the impedance is given in (2.12). The form of this model was determined by observation of typical FEKO impedance simulation results. If we consider the form of the input impedance of the standard-application loaded dipole structure presented in Figure 55, we can intuitively derive the form of the model as follows (note that this model is derived by consideration of the impedance properties of the antenna in the frequency range of interest only).

- The imaginary part of the input impedance has the form of series capacitor i.e. large negative impedance at low frequency, decreasing asymptotically towards zero with an increase in frequency. This results in the inclusion of C_s as the beginning point of the model derivation.

- The real impedance is non-zero, as would be the case for a simple series capacitor. This implies the inclusion of R_s in the model.

- The real impedance is not constant over the band, but generally ramps toward a higher value at lower frequencies. This effect is modelled by the addition of the shunt resistor, R_p. C_s induces a frequency dependant current division between R_p and R_s, which results in the realization of a frequency dependant real impedance.

- Practical considerations make it clear that there cannot be continuous DC current on the antenna, and thus the DC path created by the addition of R_p to the model is not acceptable. In order to remove this DC path, we must add C_p to the model.

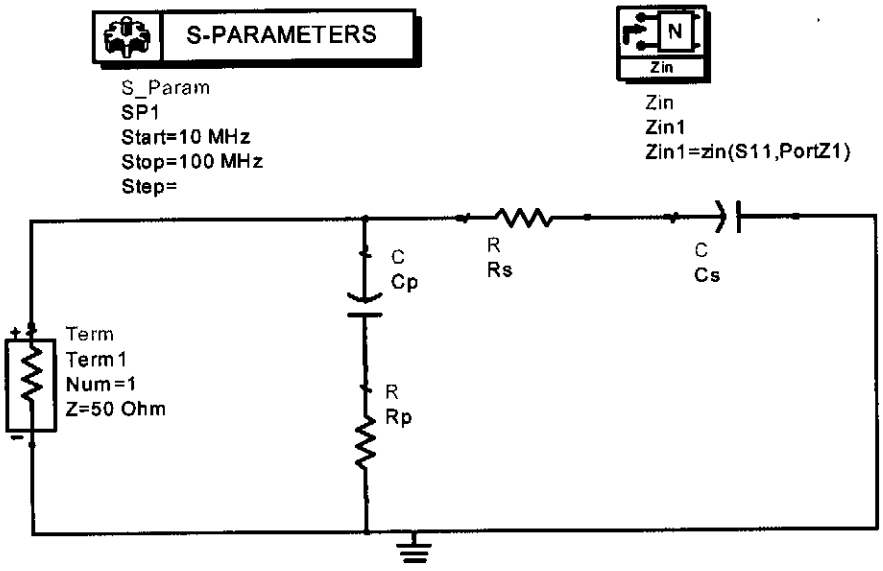

Figure 56 A lumped element model of the standard resistively loaded antenna structure.

$$Z(\omega) = \frac{-(R_s R_p C_s C_p)\omega^2 + j(R_s C_s + R_p C_p)\omega + 1}{-(R_p C_s C_p + R_s C_s C_p)\omega^2 + j(C_s + C_p)\omega} \qquad (2.12)$$

In order to determine what effect the values of the lumped elements has on the impedance of the model, each component was swept over a specific range, while the other values were kept constant. The impedances while sweeping R_s and C_s are shown in Figure 57.

The comparative input impedances of this model for a Wu-King loaded structure in rock with 2 different permitivities are shown in Figure 58. This simple derived model of the impedance of a standard, regularly loaded dipole approximates the simulated impedance of the antenna structure well. The lumped component values of Figure 58 were determined by a least-square-error fit operation. The algorithm for this operation is outlined in Appendix B.5.

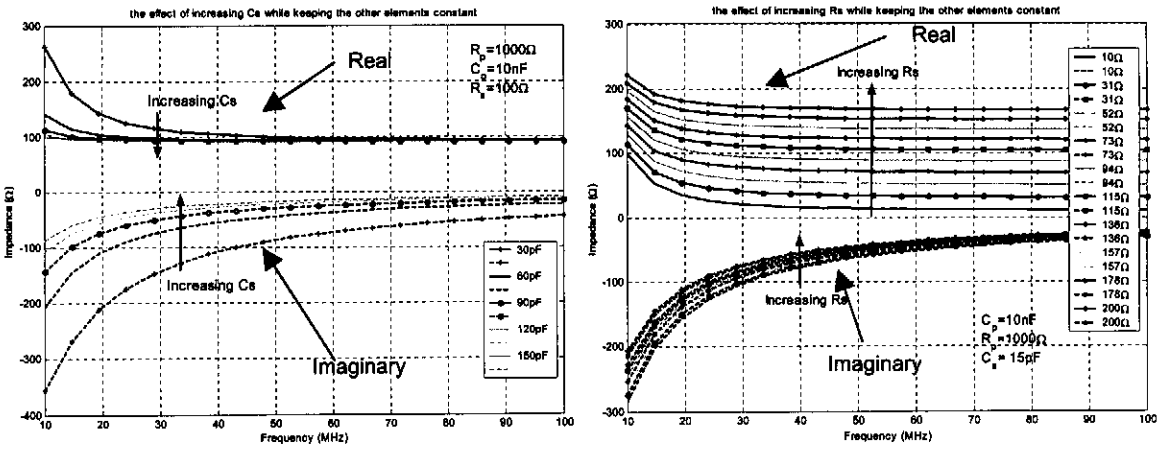

Figure 57 The change in input impedance of the loaded dipole lumped element model for variation in the lumped element values

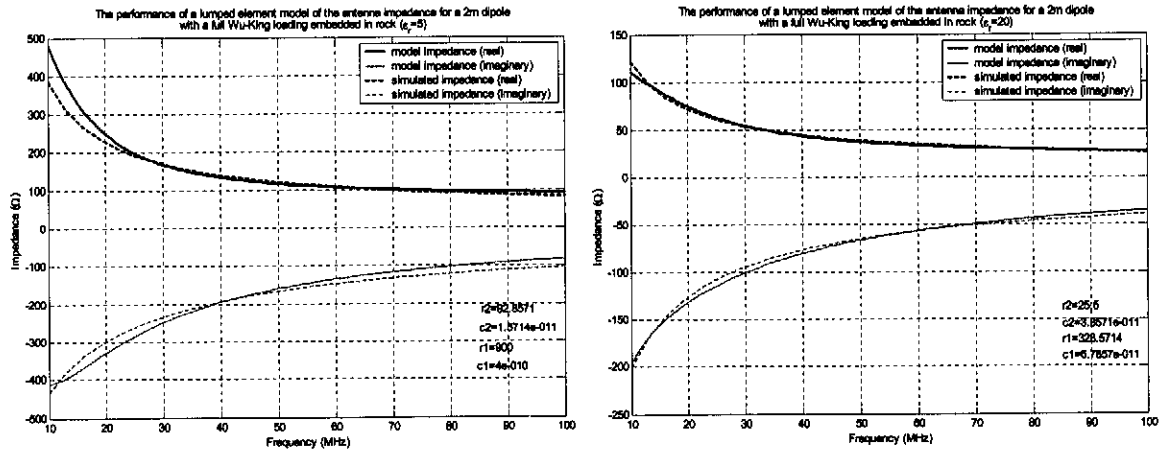

Figure 58 The comparative input impedance of simulated Wu-King loaded dipole structures compared with that of the lumped element antenna model with the shown component values.

Lumped element modelling of the modified-application loaded dipole structure is not so simple, due to the pseudo-resonance observed in the structures input impedance, dependant on both the antenna loading profile, and the surrounding permitivity. The form of the lumped model developed to model the modified loaded dipole structure is shown in Figure 59. The mathematical expression for the impedance of this model is given in (2.13). This model form can be intuitively derived by considering the impedance of the modified loaded structure impedance presented in Figure 55 as follows.

- The components C_p, C_s, R_p and R_s are derived in the same manor as for the standard dipole impedance model of Figure 56.
- The addition of L_s creates a damped series RLC circuit to realize the damped resonance form observed in the frequency range of interest.

- As observed in the impedance of the modified Wu-King loaded structure in the ε_r=20 material, the damped resonance may cause the impedance of the structure to become inductive. In order for the model to cater for this effect, the series inductor, L_1 is added, to effectively shift the imaginary input impedance component of the model up.

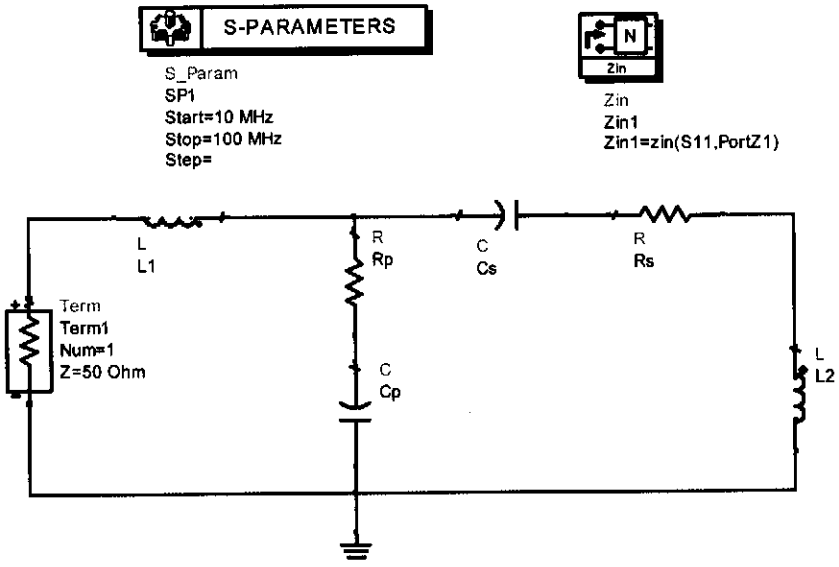

Figure 59 The lumped element model used to approximate the modified loaded dipole structure.

$$Z(\omega) = j\omega L_1 + \left[\frac{-j\left(L_2C_pC_s\right)\omega^3 - \left(R_pR_sC_pC_s + L_2C_s\right)\omega^2 + j\left(R_pC_p + R_sC_s\right)\omega + 1}{-j\left(CpCsL_2\right)\omega^3 - \left(R_pC_pC_s + R_sC_sC_p\right)\omega^2 + j\left(C_s + C_p\right)\omega}\right] \qquad (2.13)$$

The modified loaded dipole model does not perform as well as the model used for the standard loaded dipole structure. This is mainly due to the increased model complexity, and larger number of variables to be optimised. An acceptable approximation of the general trend of the antenna impedance is however achieved.

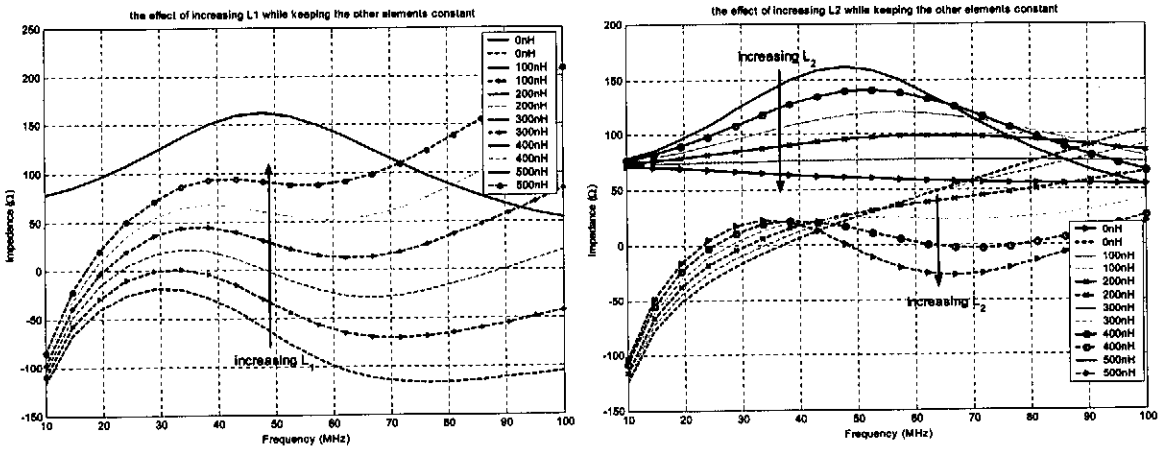

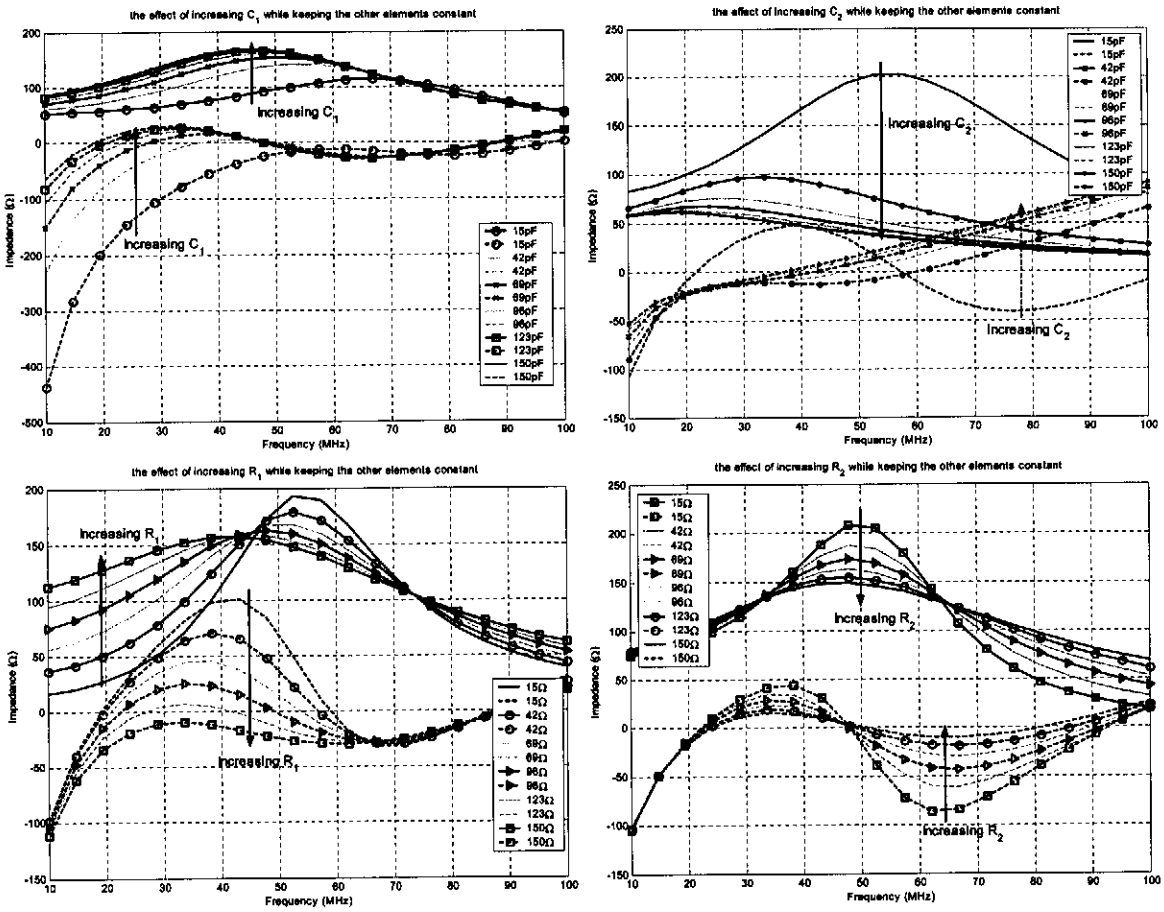

Figure 60 The computed variation in the impedance of the lumped element model used to model the modified dipole structure, with variation in the lumped element values (R_1=100Ω; R_2=100Ω; C_1=20pF; C_2=100pF; L_1=200nH; L_2=500nH where not indicated)

A representation of the effects of the variation of each of the lumped component values is given in Figure 60. A few comparative impedances of the lumped element model and the simulation results are shown in Figure 61. Again the lumped component values were determined by using a least-square-error fitting algorithm with the component values as the six fitting parameters (see Appendix B.5).

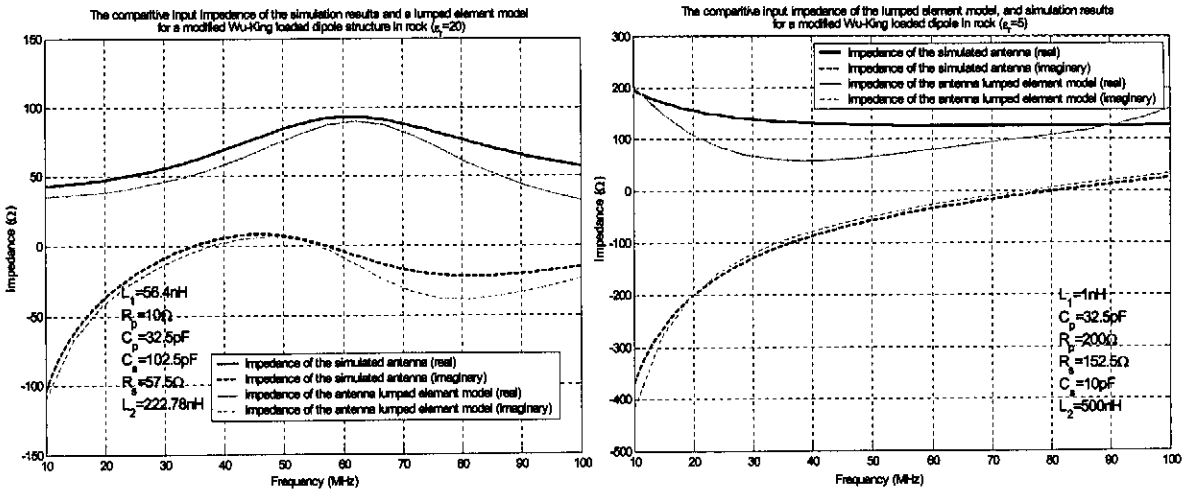

Figure 61 The operation of the lumped element antenna model, compared with simulations of a modified loaded dipole structure imbedded in rock (σ=1x10^{-3})

C. 50% Wu-King loading profile using a wire element model

As noted in section 2.4.1, investigations show that the Wu-King profile is conservative for pulsed antenna applications, and that by reducing the percentage loading, both the efficiency and pulse radiation characteristics can be improved. It is also predicted that the effect of the pseudo-resonance resulting from the interaction of the central unloaded sections and the loaded termination arms, which causes variation in the antenna characteristics, should be reduced by lightening of the loading profile. If we apply 50% of the loading used in Figure 55, we achieve the computed input impedances as shown in Figure 62.

Lumped element model approximation of the impedances of the structures of Figure 62 are shown in Figure 62, with the relevant component values used in the generic models of Figure 56 and Figure 59. The component values were determined using the least-squared-error fitting algorithm discussed in Appendix B.5.

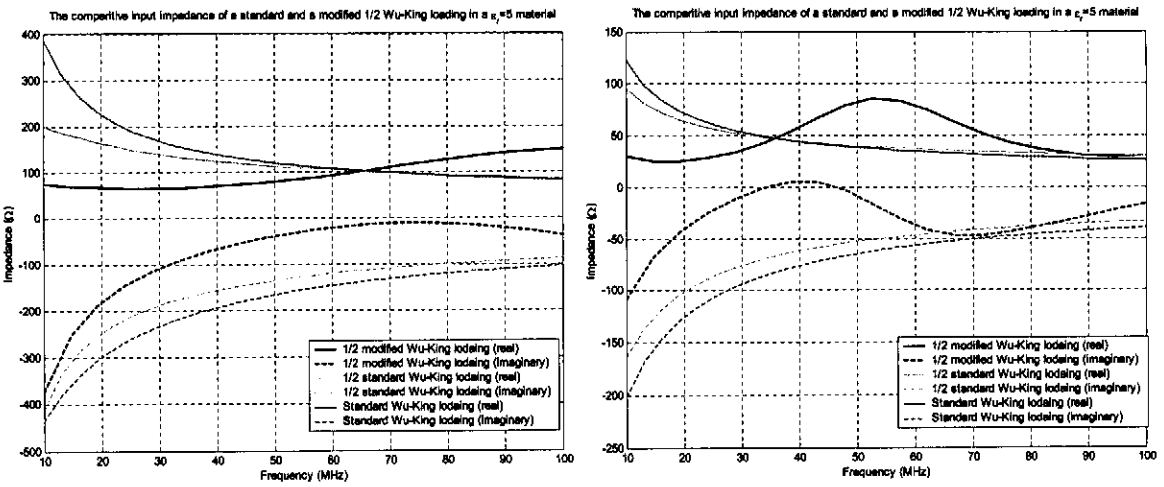

Figure 62 The comparative input impedances of a standard 1/2 Wu-King loading and a modified 1/2 Wu-King loading on a 2m-dipole imbedded in rock (σ=1x10^{-5}) for two different permitivities.

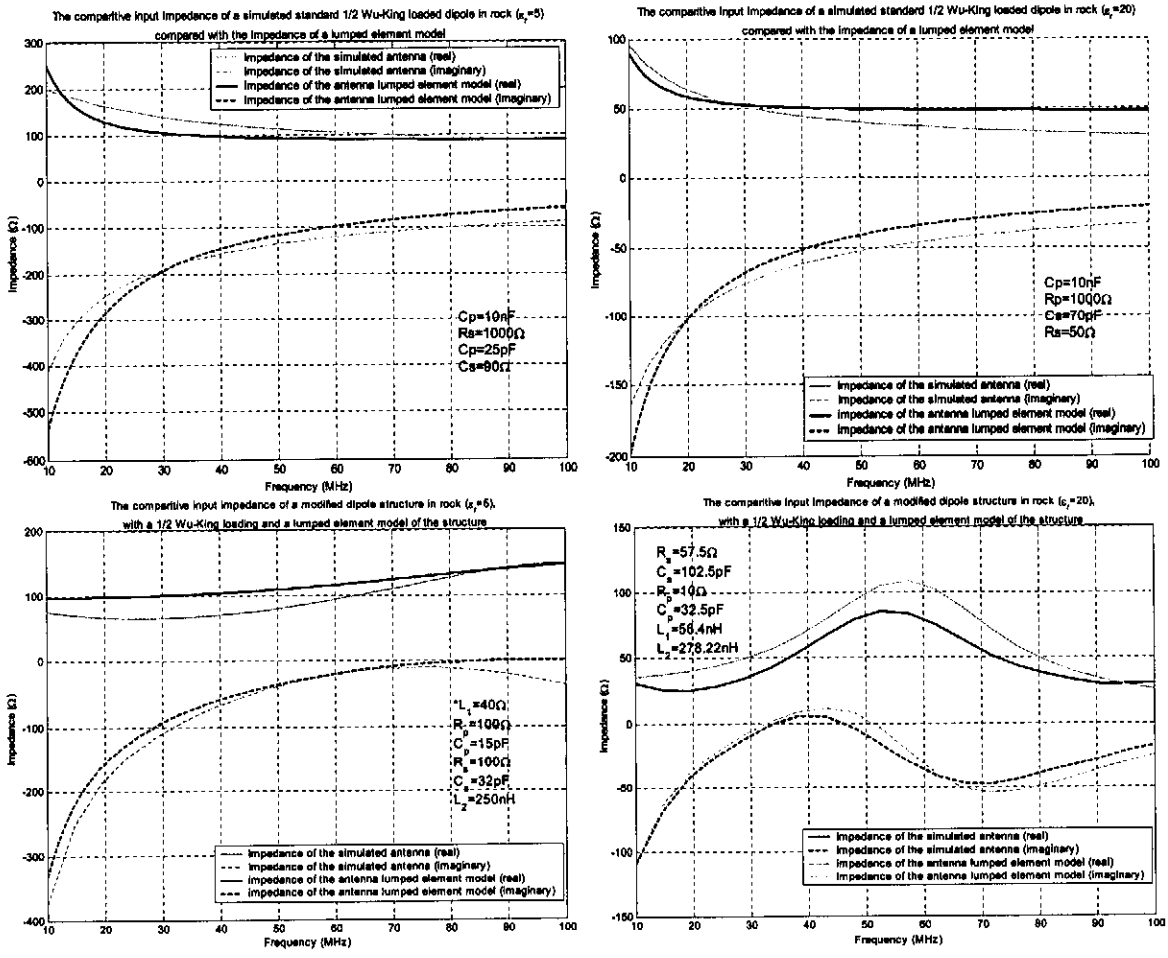

Figure 63 The input impedance and component values of the lumped models of the 1/2 Wu-king loaded antenna structures.

The comparative input reflection coefficient in a 50Ω system and the radiated E-fields at 5m broadside of the modified loaded dipole structures are presented in Figure 66 along with the results for other loadings, for comparison purposes.

The radiation efficiency of the 50% Wu-King loaded structures (modified and standard profile application), computed from the definition of (2.7), is better than that of the Wu-King loaded structure by approximately 7-8% over the whole frequency range of interest, except at the extreme low frequency side (under 20MHz), where the improvement is not very considerable.

As predicted, the reduction of the loading on the loaded sections of the modified dipole structure causes a frequency shift in the pseudo-resonance point of the structure. The resonance moves down in frequency, and the variation in the impedance of the structure over the frequency band of interest is less, implying a longer pseudo-resonant length.

D. 25% Wu-King loading profile using a wire element model

Investigations into further reduction of the loading profile in order to improve the radiation efficiency and stability of the characteristics of the structure were performed, again using a percentage scaled version of the Wu-King profile described in Table 2. By applying 25% of the loading used in Figure 55, we achieve the computed input impedances shown in Figure 64.

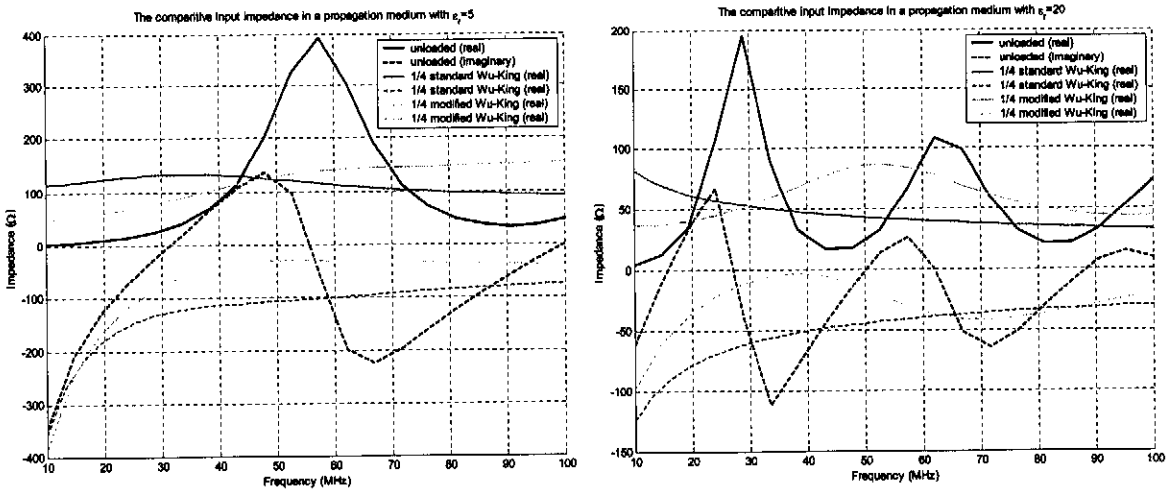

Figure 64 The comparative input impedances of a standard 25% Wu-King loading and a modified 25% Wu-King loading on a 2m-dipole imbedded in rock (σ=1x10^{-5}) for two different permitivities.

Lumped element model approximation of the impedances of the structures of Figure 64 is shown in Figure 65, with the relevant component values used in the generic models of Figure 56 and Figure 59. The component values were determined by using the least-squared-error fitting algorithm of Appendix B.5.

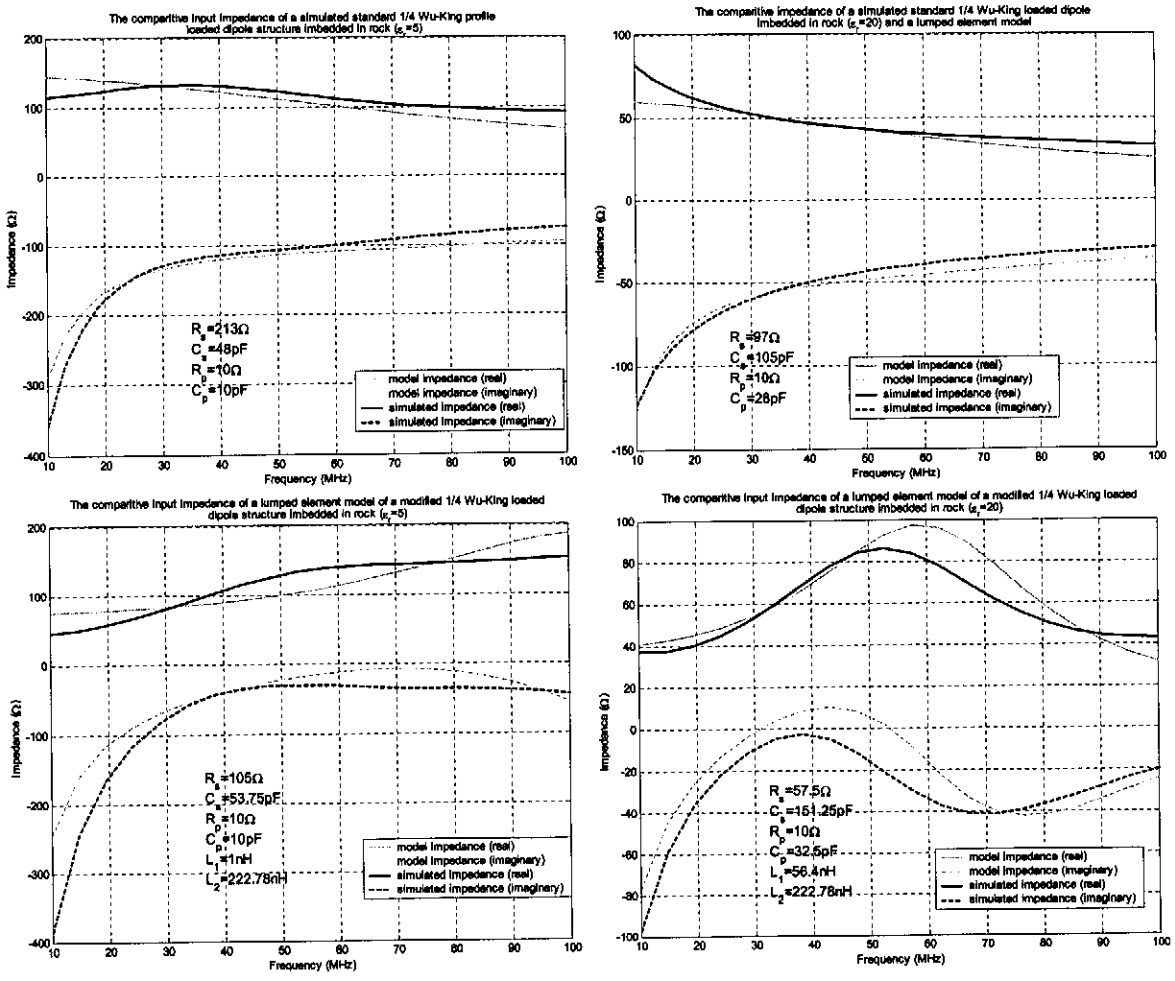

Figure 65 The input impedance and component values of the lumped models of the 25% Wu-king loaded antenna structures.

Again the downward shift in pseudo-resonance and drop in variation of the impedance over the band with the scaling of the loading profile is apparent. The effective radiation efficiency of the 25% Wu-King loaded structure is higher over the band than that of the 50% Wu-King loaded structure (about 5% higher above 50MHz, with a less drastic improvement below 50MHz).

The radiated fields and time-domain analysis is presented in the next section with that of the 100% and 50% Wu-King modified loaded dipole structures for comparison purposes.

E. Comparative summary, and time domain effects of the application of percentage-scaled modified Wu-King loading profiles to wire antennas in rock

Variation in the input impedance, input reflection coefficient and the bore sight radiated E-fields for the three loadings introduced thus far are summarized in Figure 66.

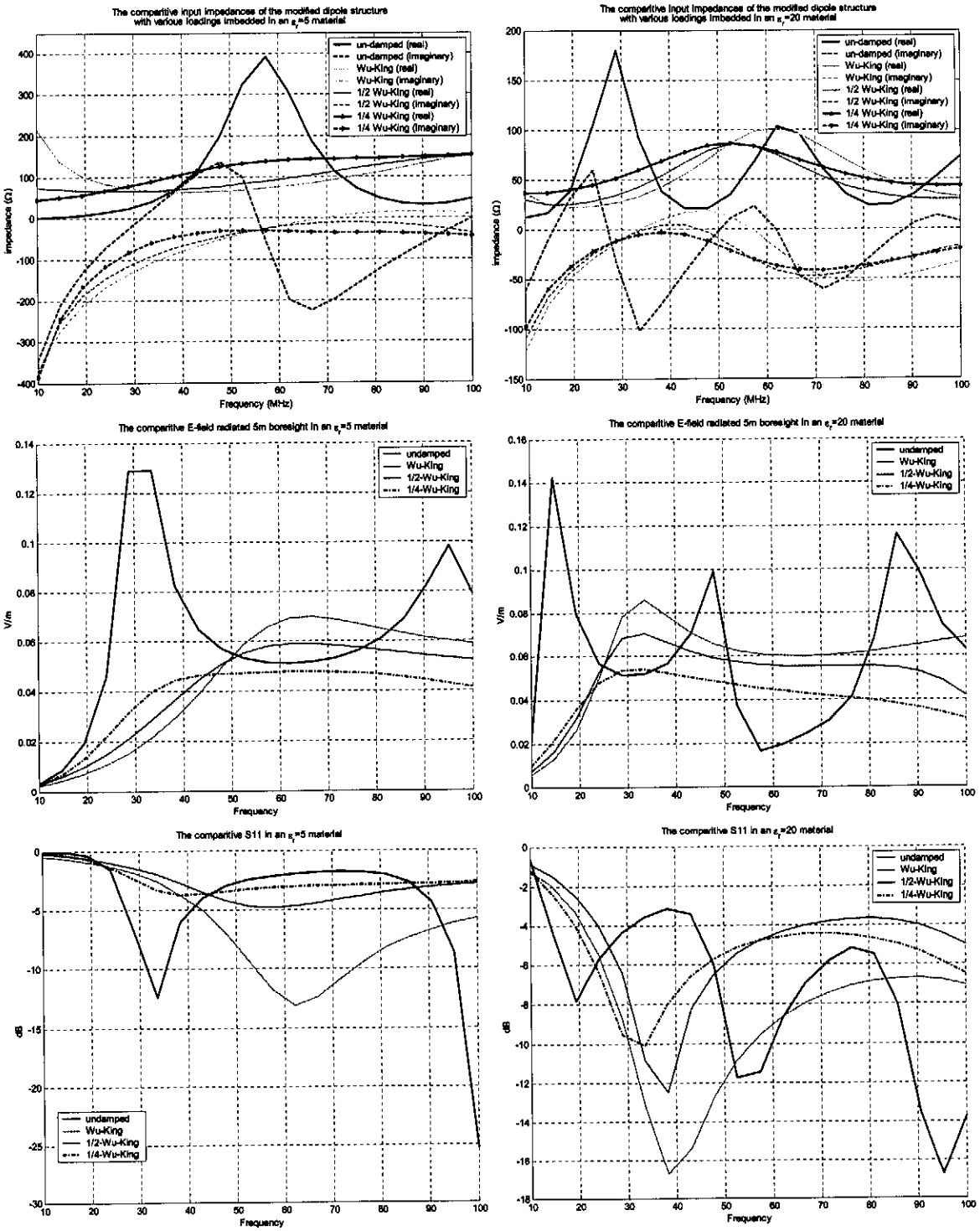

Figure 66 The comparative input impedance, E-field radiation and reflection coefficient of the modified dipole structures considered to this point with different loading percentages

The results shown in Figure 66 show clearly the consistent improvement over the bandwidth of interest for all the loading profiles applied to the modified dipole structure. A few points that must be noted are:

- There is a noticeable relative improvement of low frequency radiation efficiency in lower permitivity dielectric materials with a reduction in the loading profile.

- The pseudo-resonance observed on the modified loaded dipole structure seems to be more pronounced for heavier loading profiles. This effect can be explained in the time domain, by noting that there will be a percentage reflection of any travelling wave on the antenna at the first resistive element. For the standard loading, this reflection will have little or no effect in the frequency band of interest as an element spacing of well below $\lambda/4$ at the highest frequency of interest is employed. By modifying the loading however, and shifting the first resistive element away from the feed point, the reflection will begin to play a role within the frequency range of interest. Simplistically, the observed damped resonance can be seen as the resonance of the central, unloaded section, damped due to the loaded structure instead of free space at the end of the unloaded section. By reducing the loading of the structure, the reflection at the loading interface, and thus also the effect and frequency point of the unloaded section resonance is reduced. The loading dependant central pulse reflection can be clearly observed in the currents on the antenna structures as shown in Figure 69. A very good idea of the effects of this type of reflection on time-domain radiation can be achieved by considering the currents on segments at equal spacing along the antenna arm, as shown in Figure 70 (segment 6 is the end segment of the antenna arm and the loading profile is applied form element 2 onwards).

- The radiated E-field results suggest that the general radiation efficiency of the structure drops off with a decrease in the loading, but the relative variation over the band decreases. This must be considered carefully in the time domain, to determine the pulse efficiency effects. Note that the insinuated drop in radiation efficiency may be largely related to the increase in the input reflection coefficient of the antenna with a decrease in loading.

Using the methods outlined in section 2.1.3, the time-domain pulsed operation of the modified loaded dipole antenna structures considered thus far was modelled. The results are shown in Figure 67.

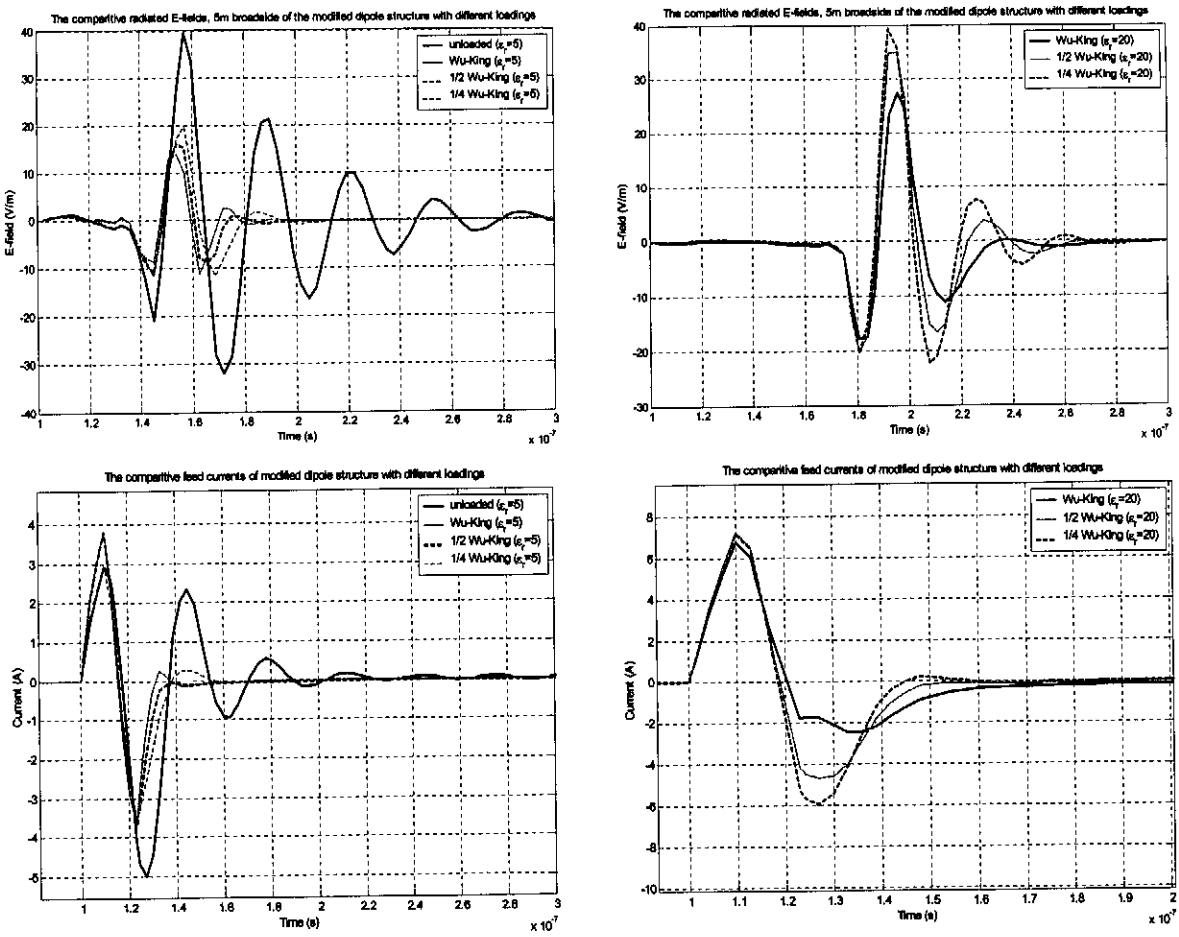

Figure 67 The radiated pulse forms and differential feed currents for modified dipole antenna structures with different loadings imbedded in different rock materials

If we consider the time related pulse efficiencies (defined in (2.9)) for the pulse forms of Figure 67, we get the results shown in Figure 68 and Table 5.

Property	No loading	Quarter Wu-King loading	Half Wu-King loading	Full Wu King loading
$\varepsilon_{shifted\text{-}pulse\text{-}form}(\varepsilon_r=5;\%)$	40.29	69.85	77.73	76.11
$\varepsilon_{shifted\text{-}pulse\text{-}form}(\varepsilon_r=20;\%)$	52.03	67.68	68.73	68.45
$\varepsilon_{pulse}(\varepsilon_r=5;\%)$	52.74	12.05	8.97	6.95
$\varepsilon_{pulse}(\varepsilon_r=20;\%)$	100	90.97	69.33	50.42

Table 5 The computed radiation pulse efficiencies of a few modified antenna structures imbedded in rock of different permitivity (Note that the pulse efficiencies are scaled to 100%)

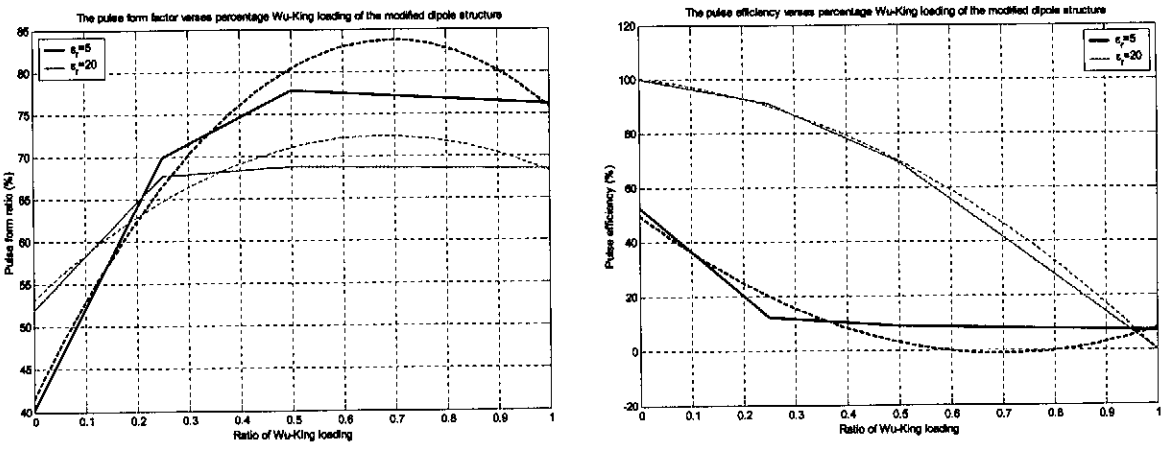

Figure 68 The pulse efficiency (scaled to 100%) and pulse form ratio verses the percentage loading on a modified dipole structure imbedded in rock

The improvement in the shifted pulse form with the addition of a loading profile is clear in both the ε_r=5 and the ε_r=20 cases. For the standard Wu-King resistive profile application, it is expected that the best pulse form radiation (i.e. the best broadband operation) will occur when the full profile is applied. Figure 68, however shows that for the modified dipole structure, this is not necessarily the case.

For the model considered (i.e. wire structures embedded in rock), it appears that minimal pulse deformation will occur with approximately 60% of the full Wu-King profile (this point can be roughly determined by fitting a 2nd order polynomial to the data as shown). It is important to note that this observation is only so for the specific model, and it is expected that in different environments the optimal loading point for the best pulse form will change.

As must be the case, the efficiency drops off with an increase in loading in both of the propagation materials considered. The form of the loading-pulse efficiency profiles for the two rock materials differ, however, with the efficiency reduction effect of small resistive loadings a lot more dramatic for structures embedded in lower permitivity propagation materials. The pulse radiation efficiency (for a 50Ω source) is generally better in higher permitivity propagation media.

The simulated currents on a few segments of a 25%, 50% and full Wu-King loaded modified dipole structures are given in Figure 69 (as was presented for an unloaded structure in Figure 40) and Figure 70. Notice that the pulse form assumed is an extremely large bandwidth pulse (650MHz), $\frac{\sin x}{x}$ function, so that the propagation of the whole pulse along the length of the antenna can be observed. Two major observations can be made with regard to these results.

- All of the loading profiles effectively damp the reflection of energy at the end point of the antenna structure for the excited travelling wave. This is clear when we compare the results of Figure 69 with those of Figure 40.

- The modification of the loading profile introduces a current reflection at the interface between the loaded and unloaded sections of the antenna (circled in the figure). The effect of this reflection is inversely dependant on the degree of the loading applied, as the mismatch reflection coefficient will drop off with a decrease in the value of the load resistor.

- The pulse propagation profiles of Figure 70 suggest that the pulsed radiation performance of the ¼-Wu-King loaded modified dipole is better than that of both the ½-Wu-King loaded structure, and the full Wu-King loaded structure, as both the midpoint and end point pulse reflections are extremely small.

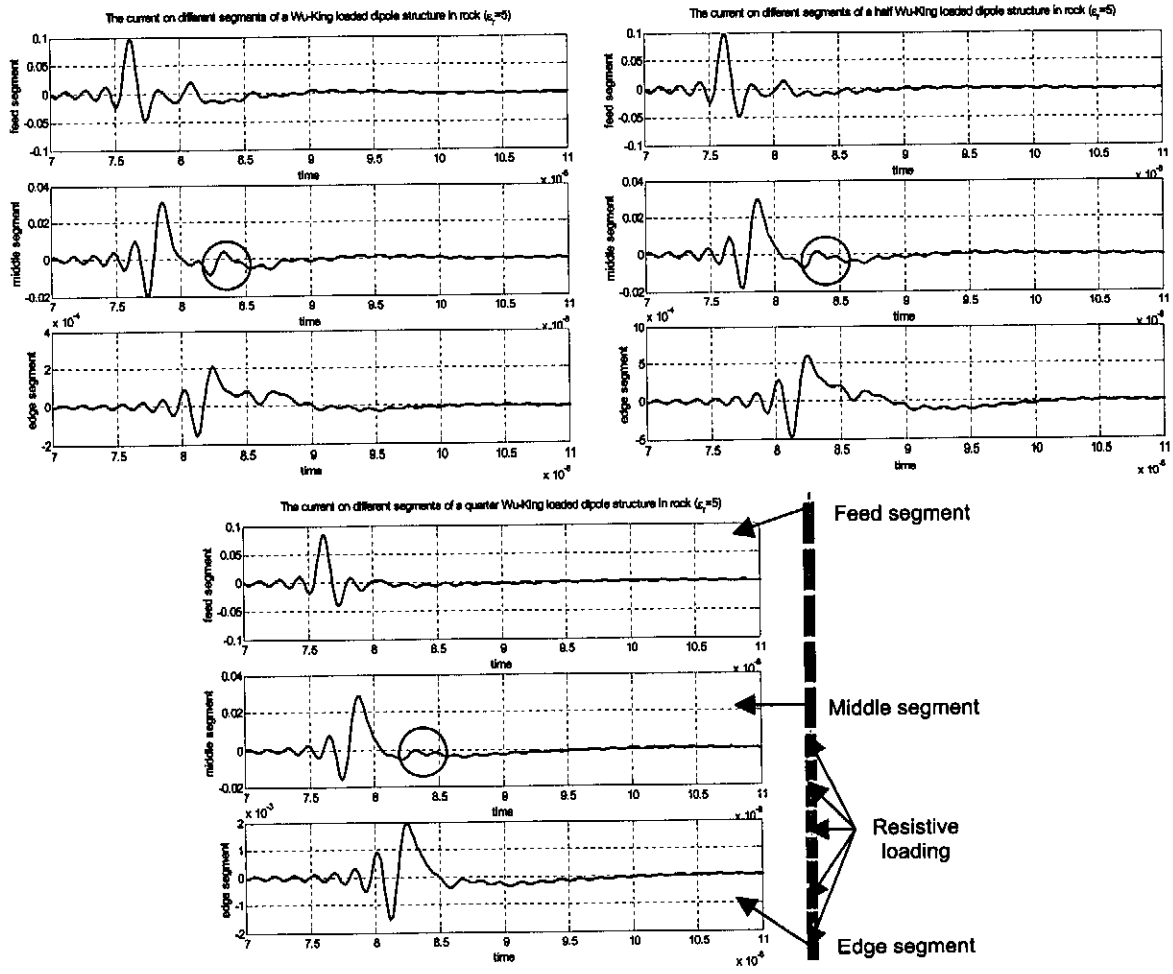

Figure 69 The FEKO simulated currents on the feed, middle and edge segments of a dipole with various percentage modified Wu-King loadings

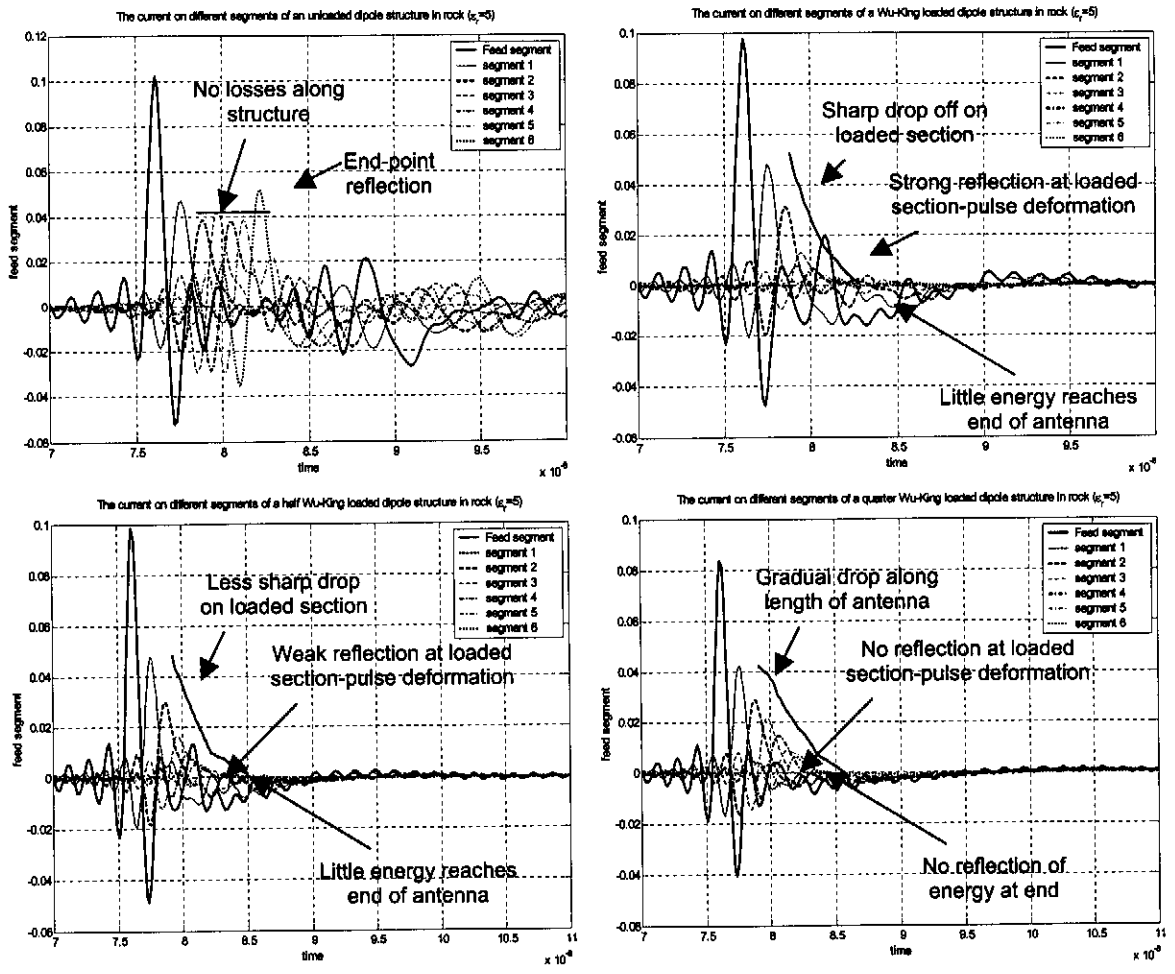

Figure 70 The FEKO simulated currents along the length of a dipole with various percentage modified Wu-King loadings, showing the time development of the currents on the structure

F. Loading profile investigation results using practical, realistic model structures

The results presented to this point give a good qualitative idea of the effects of resistive loading. A more detailed computational structure was used to verify and accurately quantify the results of the previous three subsections. The FEKO model is shown in Figure 71.

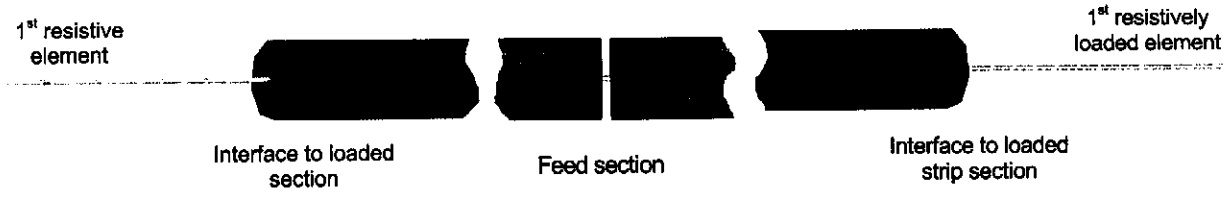

Figure 71 An accurate FEKO model of the physical structure of the modified, single strip loaded dipole antenna structure, embedded in rock

It was found that the use of a 20%-25% Wu-King loading on a structure with a 400mm-500mm un-damped hollow cylindrical centre section delivered good broadband radiation, with optimal efficiency. Although the reduction of the loading profile did show an improvement in the poor low frequency radiation characteristics of the antenna noted during consideration of the Wu-King profile, the lower side radiation is still relatively poor, despite the improvement in efficiency over the rest of the frequency band of interest.

The simulated characteristics of an accurate cylindrical-strip model structure, imbedded directly in rock (ε_r=7.5;tanδ=1/20) with a 20% Wu-King modified loading profile applied as shown in Table 4 are shown in Figure 72. The characteristics of an antenna structure used in the existing GEOMOLE BHR system (TX probe), and the thick-wire model approximation used in the previous section, under the same conditions are shown for comparison.

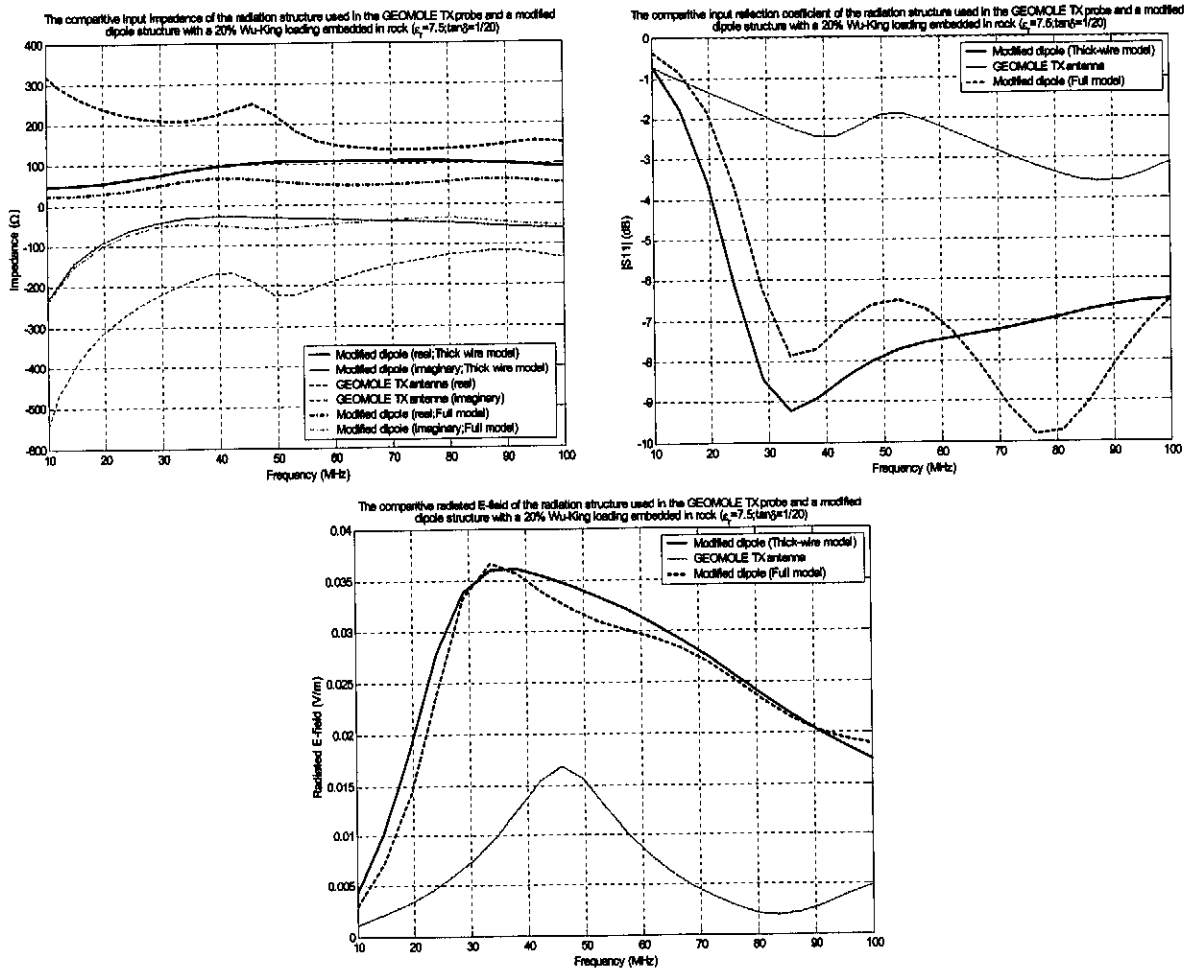

Figure 72 The comparative FEKO simulated characteristics of the GEOMOLE TX radiation structure and a modified 2m cylinder-strip dipole antenna structure with a 20% Wu-King profile loading imbedded in rock (ε_r=7.5;tanδ=1/20)

It is clear from the results of Figure 72 that the modified loaded symmetric dipole antenna has much better, efficient broadband radiation properties than the radiation structure used in the existing transmitter.

The results of Figure 72 assume that both of the structures are embedded in the rock, and do not include the effect of the probe housing and the borehole structure it self. Both of the computational models used to generate the results of Figure 72 are physically accurate (i.e. no physical simplification by using wire elements instead of the hollow cylinder structures etc.) and have been verified by measurement. It is thus possible to predict that even in a different environmental model, the modified dipole structure should perform better than the existing radiating structure. We will consider the environmental effects in the next section.

Time domain characterization of the two antennas characterized in Figure 72 was performed using the methods of section 2.1.3. The comparative results are shown in Figure 73.

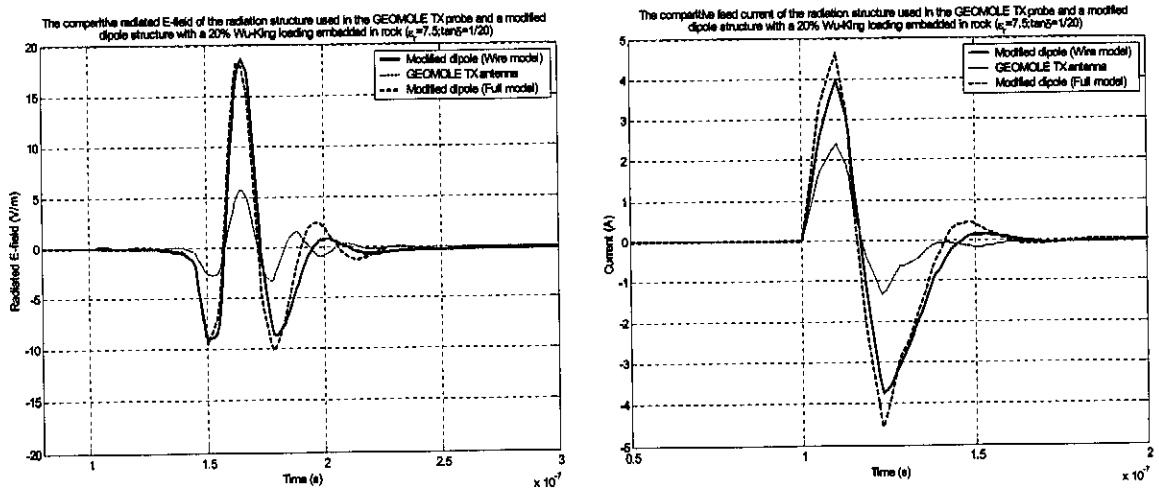

Figure 73 The ADS computed radiated E-fields and feed current for a modified dipole antenna with 20% and a 25% Wu-King loading and the GEOMOLE TX radiating structure in rock (ε_r=7.5;tanδ=1/20)

The pulse form ratio and pulse efficiency of the two radiated pulses shown in Figure 73 are;

- GEOMOLE transmitter antenna structure: $\varepsilon_{pulse\text{-}form}$=71.02% and ε_{pulse}=0.001137
- 20% loaded modified dipole structure: $\varepsilon_{pulse\text{-}form}$=70.34% and ε_{pulse}=0.01359
- 25% loaded modified dipole structure: $\varepsilon_{pulse\text{-}form}$=72.18% and ε_{pulse}=0.01294

The pulse efficiency of the 20%-25% loaded modified dipole structures is clearly better than the existing structure (around 10 times), and the pulse form ratio is the same as that of the existing structure.

Comparison between the simplified wire dipole approximation structure and the full antenna structure shows that all the antenna characteristics are very similar, except for the real input impedance, which is lower for the accurate model than for the wire dipole approximation. This discrepancy, however has very little effect on the ADS computation of the time-domain radiated pulse form, and is only really of interest when considering the interface between the antenna and the probe electronics, where optimal power transfer is desired (by conjugate matching of the electronics impedance to the antenna input impedance).

By alteration of the radiating structure to the full cylindrical form of model 2 in Figure 53, or by replacing the single loaded strip with multiple strips spaced equally around the circumference of the central cylinder, the difference between the tick wire model simulated real impedance, and the real impedance of the more accurate topologies becomes very small. It is important to note that the higher impedance case is generally more desirable for mono-static application, as it will improve the quality of isolation that can be achieved using the circulation topology of Chapter 4.

2.5.2.4. The length of the un-damped electronics housing

The length of the un-damped section of the radiating structure used to house the electronics and the battery pack will have an effect on the operation of the antenna. This effect will only be considerable in the case where the length of the unloaded section changes so much that a different number of elements of the loading profile must be used by the application policy of Table 4. A full, accurate model of the antenna structure, imbedded in an ε_r=10 medium was used to quantify the effect of a change in the length of the unloaded section. A typical result is shown in Figure 74, showing the effect of the increased damping implied by using a shorter un-damped section, and more resistive damping elements of the original standard Wu-King profile.

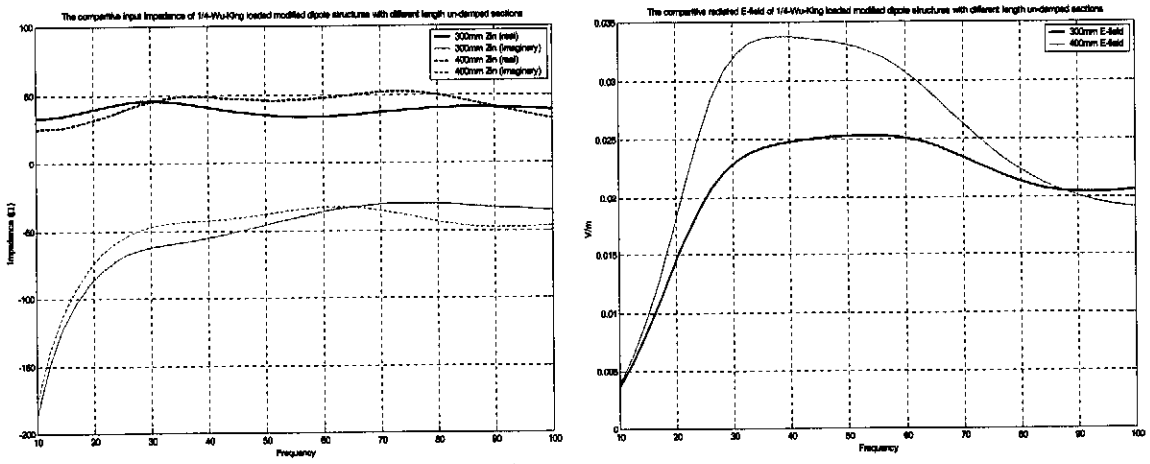

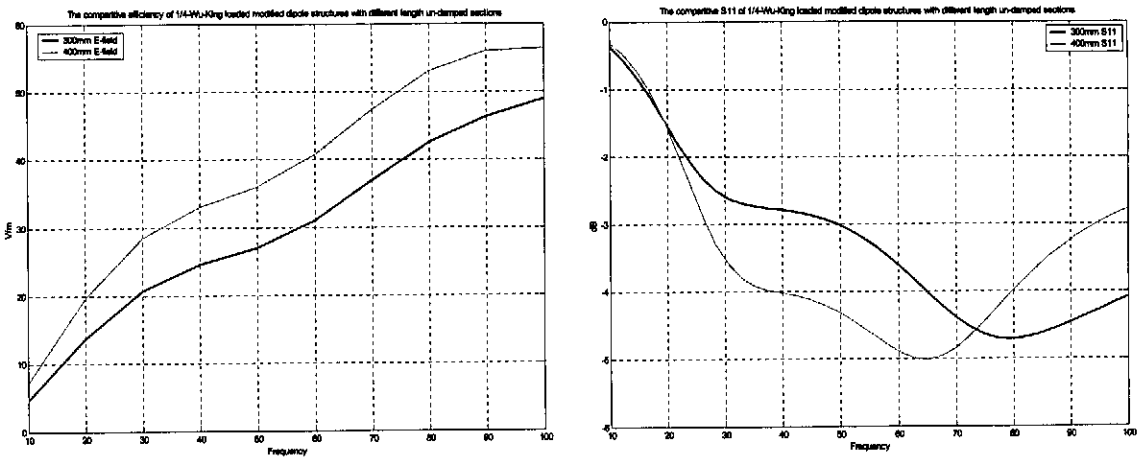

Figure 74 The effect of changing the length (and number of resistive elements accordingly) of the un-damped section from 400mm to 300mm for a modified ¼-Wu-King loaded dipole in a loss-less, ε_r=10 medium

The low frequency operation of the 400mm un-damped dipole is better, and the structure is generally more efficient (approximately 10% higher over the band of interest). The characteristics of the 300mm un-loaded structure do indeed suggest better bandwidth performance, except at the LF where the imaginary impedance is larger for the 300mm case. Results indicate that changing the length of the unloaded hollow cylindrical section in the range 100mm to 500mm in length, without changing the number of loading elements or their values and positions has little effect on the antenna operation. The space needed for the electronics and battery pack of a mono-static probe will not exceed 500mm. In such a case, the loaded arms may be shifted further away from the feed point, increasing the effective length of the probe, or, alternatively the loading profile may be altered on the shortened loaded sections to try and achieve the best possible characteristics. Generally, the total length of the damped sections of the antenna should not be less than half of the total antenna length, to be able to have a considerable damping effect on the structure.

The way in which the profile should be modified for application to a physical structure with different dimensions to the one considered in this report depends on the change made to the radiation structure geometry. We will only consider the case where the loading begins further than 500mm from the feed point for the specific design of a profile for such a structure performed during the development of prototype-mono-static radar for field-testing. This structure will be shortly discussed in section 2.6.2.

2.5.2.5. Environmental effects on antenna operation

In this section, the effects of the environmental geometry in which the BHR system is deployed, on the operation and characteristics of the antenna structure will be considered.

As discussed in section 2.2, there is a large variation in both the geometry and the physical properties of the materials in the BHR environment. In order to characterize the effects of the environment, we will thus consider the two extreme geometrical cases as depicted in Figure 37, with the variation of the material properties of Table 1.

The effects of four environmental factors must be considered.

- The PVC pipe in which the antenna is housed
- The borehole in which the antenna is deployed
- The effect of potting material used to give mechanical stability and robustness and improve the watertight sealing of the probe
- The effect of air in the probe structure in the case that potting is not used

Only the investigation results for the modified dipole structure shown in Figure 52 with two 400mm unloaded central sections, terminated with single resistively loaded strip sections, applied as described in Table 4 will be initially presented. Both simplified thick wire dipole models, and more complex computational models will be used. The introduction of alternative practical topologies that approximate the thick wire dipole case, as shown in Figure 53, will be considered toward the end of the study.

A. The effect of the PVC pipe housing (no borehole; with and without potting or an air gap)

We begin by considering the first extreme case (as defined in Figure 37), where the antenna structure is housed in a PVC pipe structure and imbedded directly in rock. The characteristics of the PVC pipe are taken as shown in Table 1, with a wall thickness of 2mm. The detail of the FEKO models used to simulate this situation, with and without potting material are shown in Figure 75.

FEKO input impedance simulation results assuming two extreme values of permitivity of the surrounding rock, for a few percentage Wu-King loadings are shown in Figure 76. The conductivity of the rock material is $\sigma=1x10^{-5}$ in all cases. Results with no PVC pipe, presented in section 2.5.2.3, are also shown for comparison purposes.

Note that the permitivity of typical material used for potting is between 3.6 and 4 (see [6] for measurement of the ε_r of potting used in the existing probes). The permitivity is thus almost identical to that of the PVC pipe, and for computational purposes, the pipe and potting can be defined as a single, homogeneous layer as shown in Figure 75.

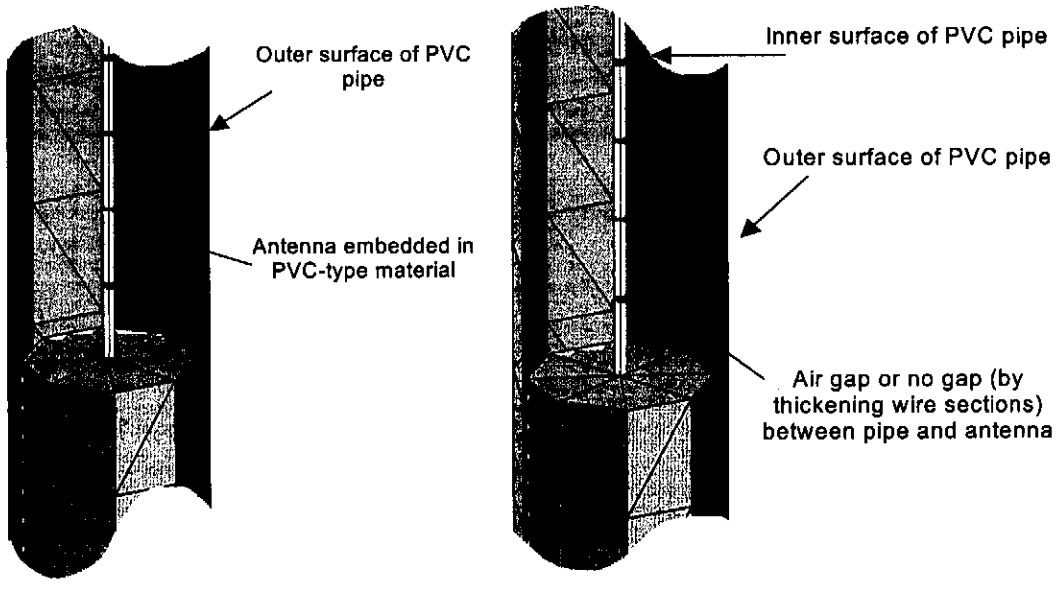

Figure 75 The form of two FEKO models used to model the effects of a PVC pipe structure, with and without potting material, embedded in rock on the operation of the antenna

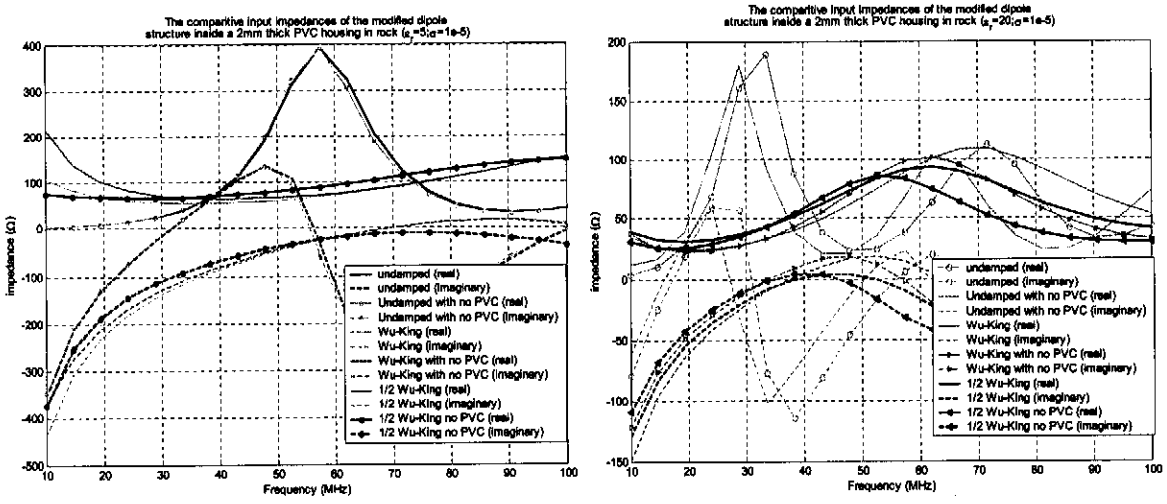

Figure 76 The comparative input impedances of a few antenna structures imbedded in rock, with and without a PVC pipe housing; no potting material or air gap effects included

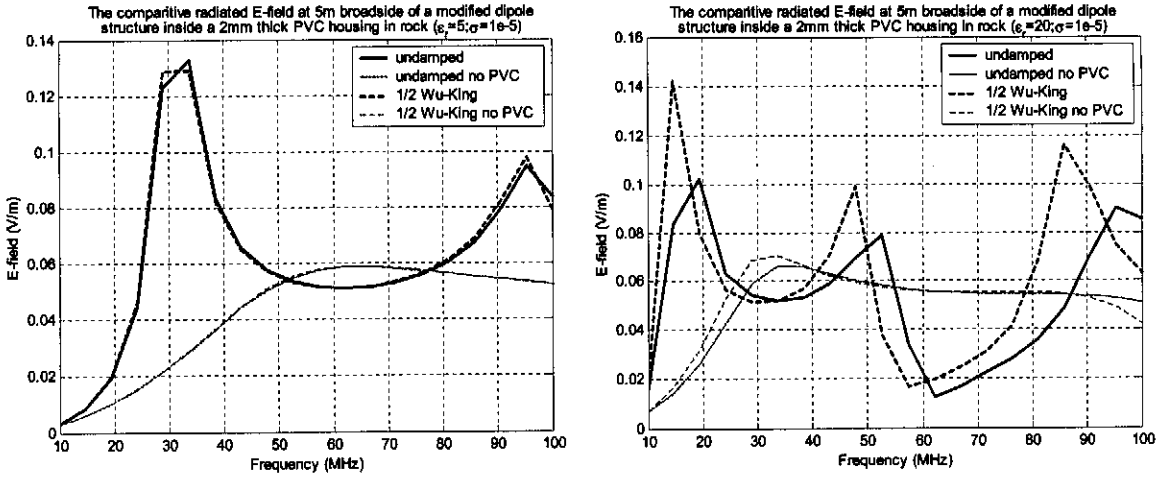

Figure 77 The E-field computed at a point 5m broadside of a few antenna structures with and without a PVC pipe housing; no potting material or air gap effects included

The effect of the PVC pipe layer alone is very small. The following observations can be made.

- For smaller values of ε_r of the rock material, or when the difference between the rock permitivity and the PVC permitivity is small, the PVC layer has very little effect. As the permitivity of the rock propagation medium begins to increase, the PVC layer begins to affect the antenna characteristics more markedly.

- Simulations show that the PVC isolation layer effectively frequency-scales the antenna properties, with little effect on the general magnitude or the characteristic form. The scaling effect is more pronounced at higher frequencies.

- The effect of the PVC isolation layer is independent of the antenna loading. The comparative E-field coupling (measured 5m broadside of the antenna structure) as shown in Figure 77 agrees with these observations and indicates that the antenna in fact couples better to a high permitivity rock if the PVC pipe layer is present.

Simulation results including the effects of a PVC-type potting material and an air gap in the probe structure, for a single loaded strip topology are shown in Figure 78 and Figure 79 respectively. A 20% Wu-King loading is assumed, and the results without potting, and with a 50% loading are shown for comparison, to show the effect of the potting, and of a change in the weight of the loading profile.

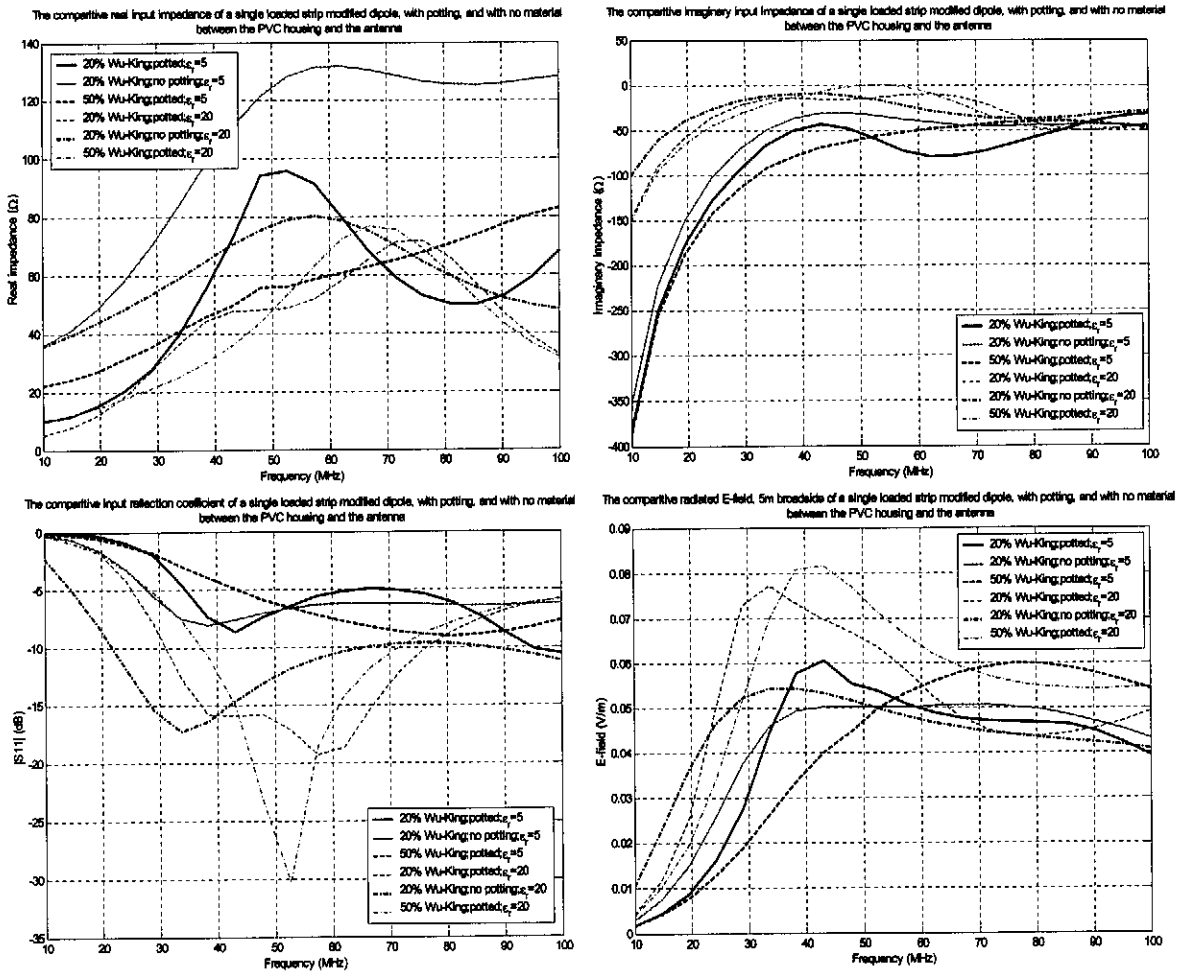

Figure 78 The comparative simulated characteristics of a single strip 20% and 50% Wu-King loaded modified dipole structure imbedded in rock, with a PVC pipe layer, and either with no gap between the pipe and antenna, or with potting material (ε_r=3.7) between the pipe and the antenna

It is apparent form the results of Figure 78 that the layer of potting material between the antenna structure and the PVC pipe probe housing has a marked effect on the operation of the structure, particularly with respect to its input impedance.

The wideband radiation of the potted structure is generally poorer at the LF side (below 30MHz), but the peak magnitude of the radiated E-field is higher in the potted antennas. The radiation magnitude indicates that the use of a heavier loading on the potted antenna structure will worsen the wideband operation. Direct comparison of the feed reflection coefficient of the 20% and 50% loaded potted antenna structures also clearly shows the improved wideband properties of the lighter loading in both ε_r=5 and ε_r=20 rock.

Consideration of the real input impedance of the structures of Figure 78 immediately shows the impedance scaling effect of the potting layer. This is particularly evident in the ε_r=5 case. Although the

potting layer does cause a general drop in the real impedance of a given structure, the scaling effect of change in the permitivity of the rock medium is effectively damped, with the real impedance of all the potted structures of Figure 78 varying around 50Ω. For the low permitivity material, the real impedance of the heavier loading seems better, as it show less global and local variation, and more importantly, does not drop off so steeply at the LF side. For the higher permitivity case, however, the lighter loading shows better real impedance characteristics. The low LF real impedance of all the potted structures is not ideal. Similar observations may be made concerning the imaginary impedance of the potted structures. Note that in the case of the high permitivity rock material, the heavier loading threatens to become resonant. This close to resonance operation is also clear in the radiated E-fields, and should be avoided.

In the case of an air gap, as shown in Figure 79, the structure shows more variation over the frequency band of interest than for the potted case. The LF operation of the air gap antenna in particular is a lot poorer than both of the potted and no gap cases.

Particularly, the results indicate resonant and close-to-resonant operation in the lighter damped structures, with large variation in antenna characteristics with frequency. The effects of the rock permitivity are again strongly damped by the air gap layer in the antenna structure, particularly as far as impedance scaling of the real part of the input impedance is concerned.

The results presented in this section suggest that by the inclusion of a potting layer with permitivity in the order of that of PVC, The operation of the antenna structure will become marginally poorer. This, however must be weighed against consideration of the reduction in the dependence of the antenna characteristics on the surrounding rock permitivity, as well as the mechanical robustness and protection that potting will afford. The presence of an air gap in the single strip antenna topology is detrimental to the antenna characteristics, and should be avoided by the addition of potting, or by employing a different structural topology that will be less affected by air gaps.

From the point of view of the realization of stable, robust mono-static isolation, the dependence on the antenna input impedance is critical. The results indicate that for monostatic application, it may be prudent to choose an antenna that provides the best impedance characteristic over a given range of environments, rather than an antenna that provides the best radiation properties. The effects of variation of the input impedance on the operation of a bi-static system are not so critical, and can generally be considered as secondary to the radiation performance.

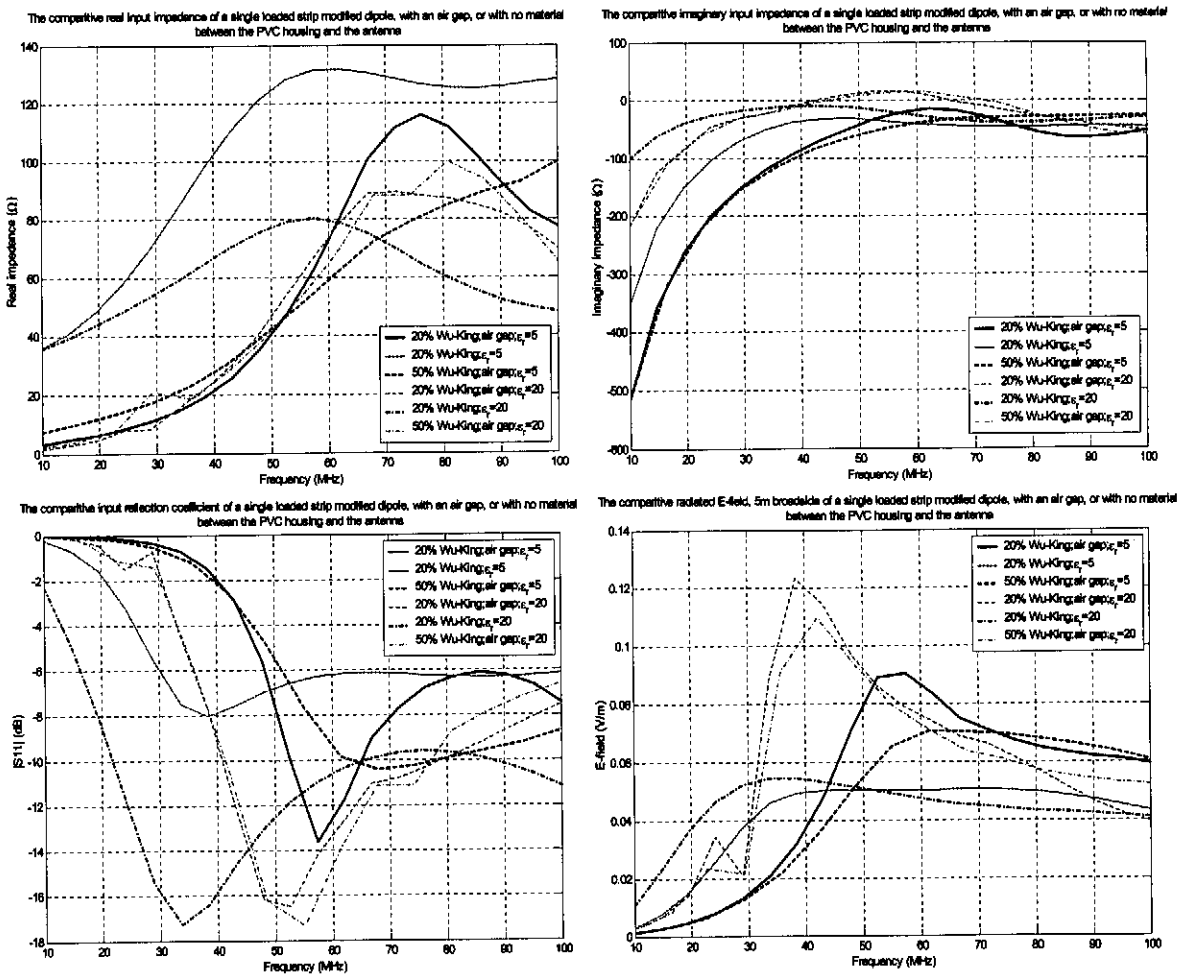

Figure 79 The comparative simulated characteristics of a 20% and 50% Wu-King loaded modified dipole structure imbedded in rock, with a PVC pipe layer, either with no gap between the pipe and antenna, or with an air gap between the pipe and the antenna

B. The effect of the borehole environment (including PVC pipe with no potting material or air gap effects)

The second extreme environmental model postulated in section 2.2 includes not only the PVC housing layer, but also the effect of the borehole, which may be filled with anything ranging from dry air to ionised or salty, conductive water. Coaxial location of the radiating structure is assumed, to simplify the simulation process.

Due to the large variation possible in the property parameters of the borehole material, only a few relevant results will be presented for three loading profiles of a single strip modified dipole structure of the form of Figure 52 with 400mm length unloaded central sections (loading profile applied as shown in Table 4). As discussed in Appendix B.3, the modelling of both the PVC layer and the borehole environment can be simplified for the case of the thick wire approximation model of the antenna structure (similar to model 1 of Figure 53), by defining the PVC pipe layer as a dielectric coating around

the wire elements. For the more accurate models, comprising both wire elements and cylindrical conducting structures, dielectric regions defined using ME/DI card pairs are employed.

FEKO simulation results of the characteristics of thick wire dipole models are given in Figure 81 to Figure 84.

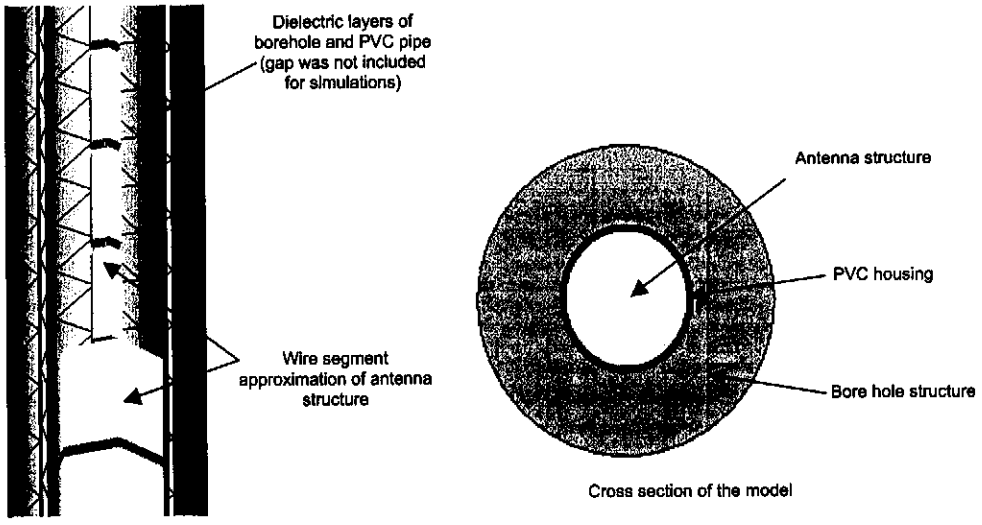

A variable thickness wire segment approximation of the antenna inside a PVC pipe in a borehole

Figure 80 The form of the FEKO model of a wire segment approximation of the antenna inside a PVC pipe, in a borehole, with no air gap between the antenna and the PVC pipe

We begin with an unloaded structure, and a Wu-King loaded structure in ε_r=5 and ε_r=20 materials respectively. Next, we will perform identical simulations, assuming structures with 50% and 25% of the assumed Wu-King loading.

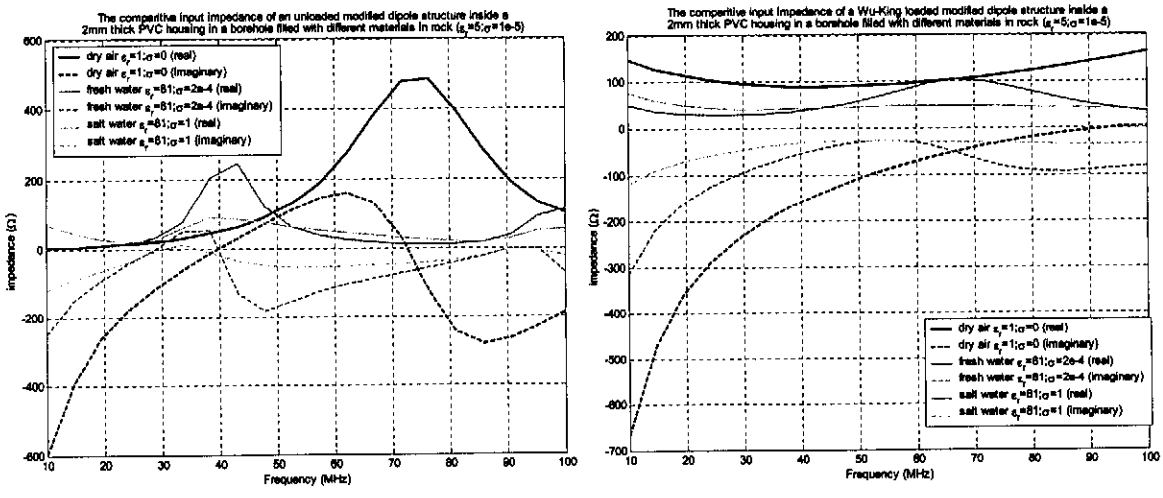

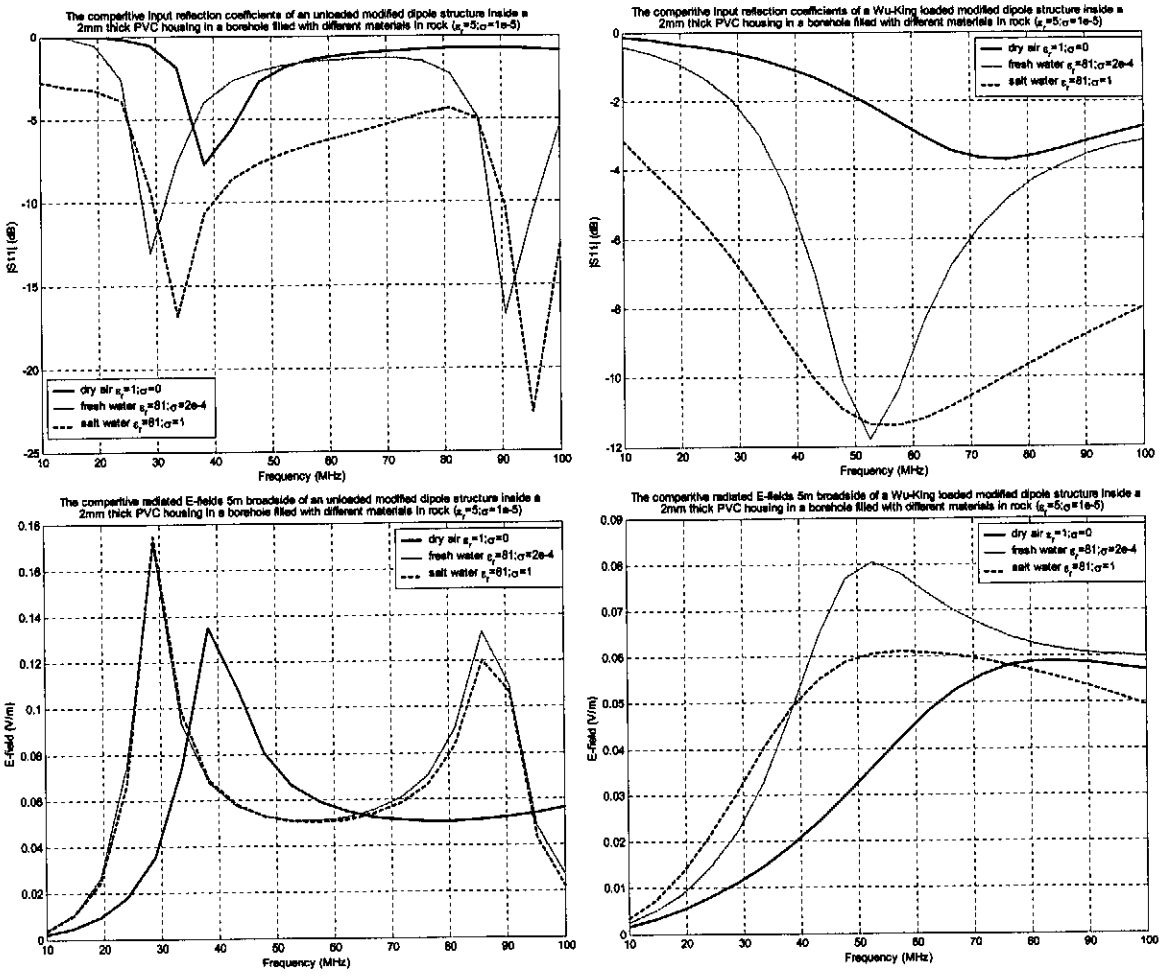

Figure 81 The comparative operational characteristics of an un-loaded and Wu-King loaded thick wire modified dipole structure in a PVC housing (no potting or air gap) centrally located in a borehole, filled with air, fresh water, and salty water respectively in rock with ε_r=5

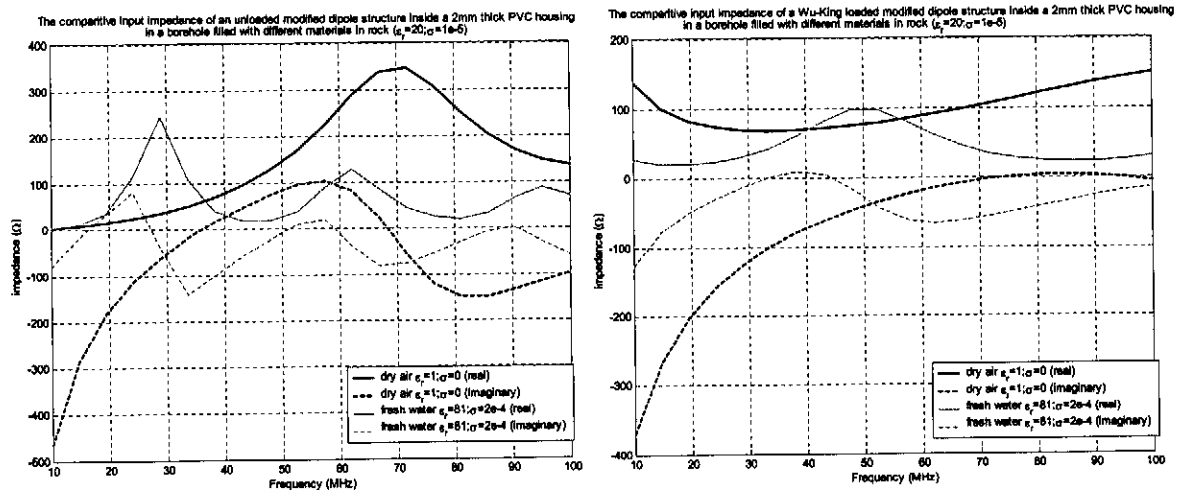

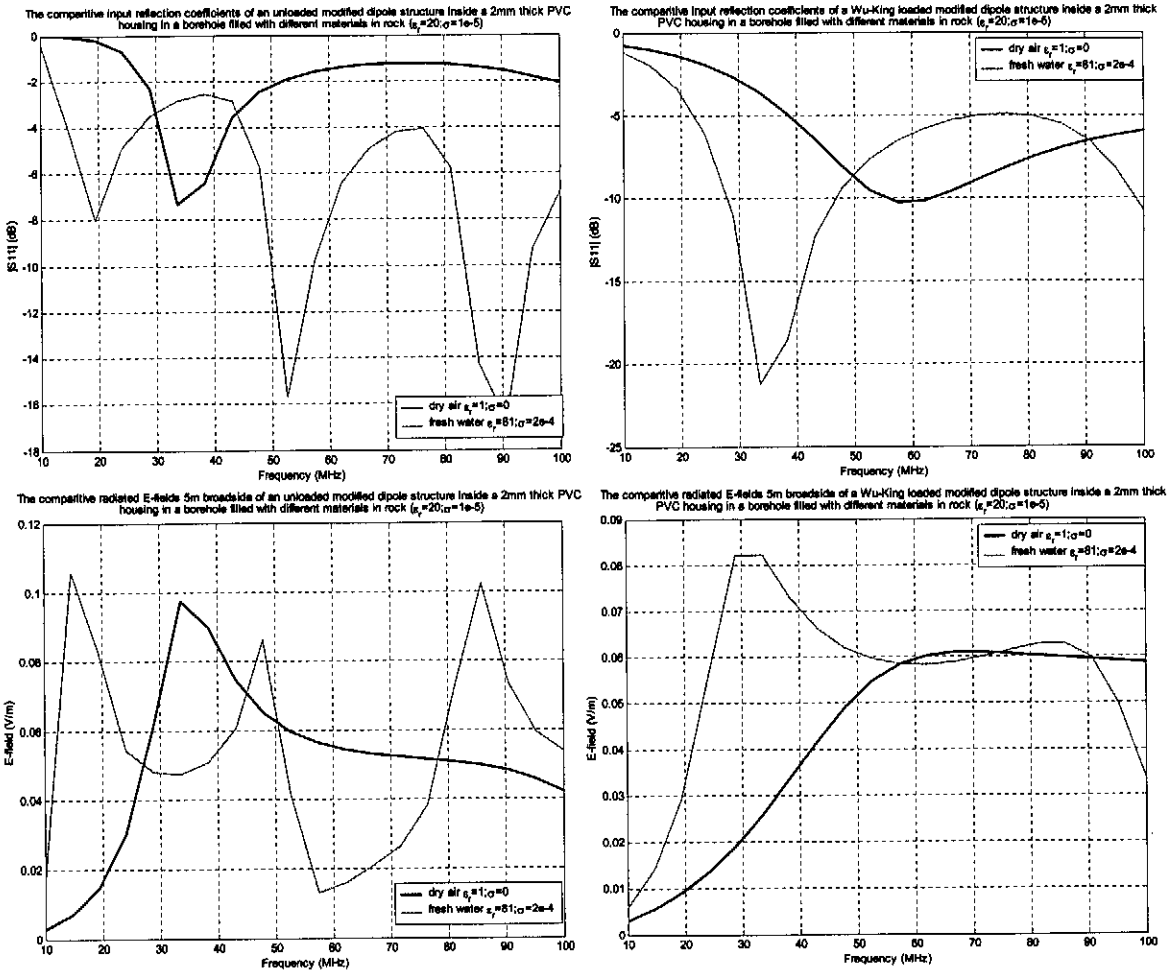

Figure 82 The comparative operational characteristics of an un-loaded and Wu-King loaded thick wire modified dipole structure in a PVC housing (no potting or air gap) centrally located in a borehole, filled with air and fresh water respectively in rock with ε_r=20

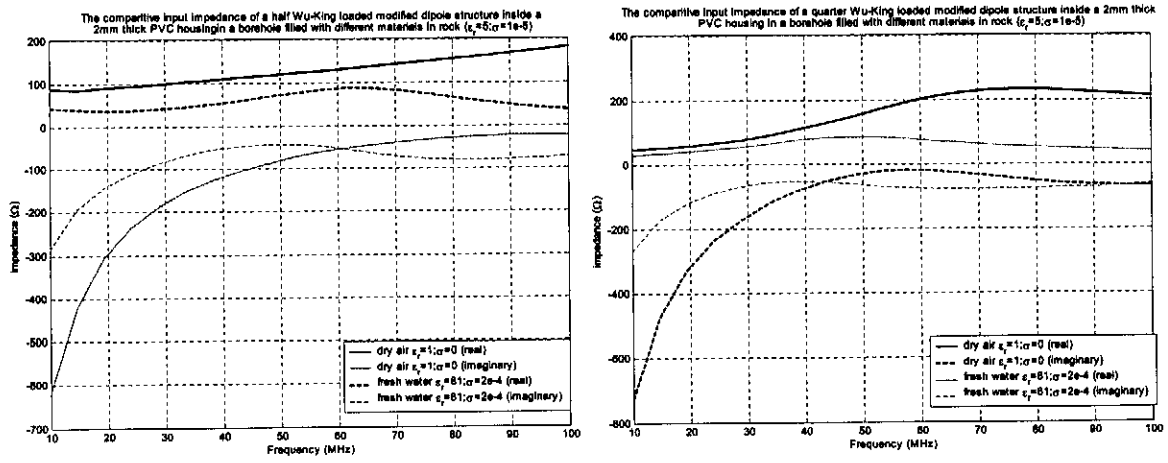

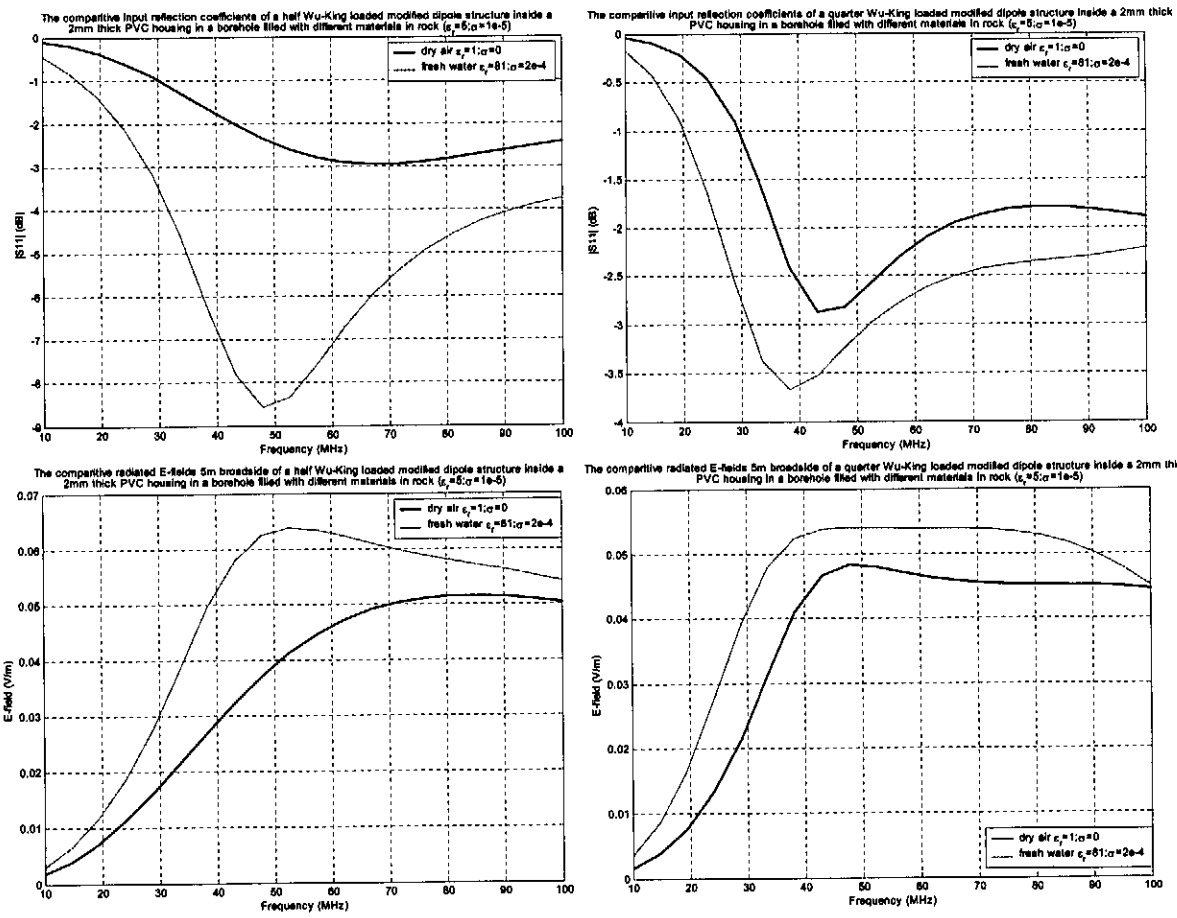

Figure 83 The comparative operational characteristics of a thick wire, half Wu-King loaded modified dipole, and a quarter Wu-King loading in a PVC housing (no air gap or potting), centrally located in a borehole, filled with air or fresh water respectively in rock with ε_r=5

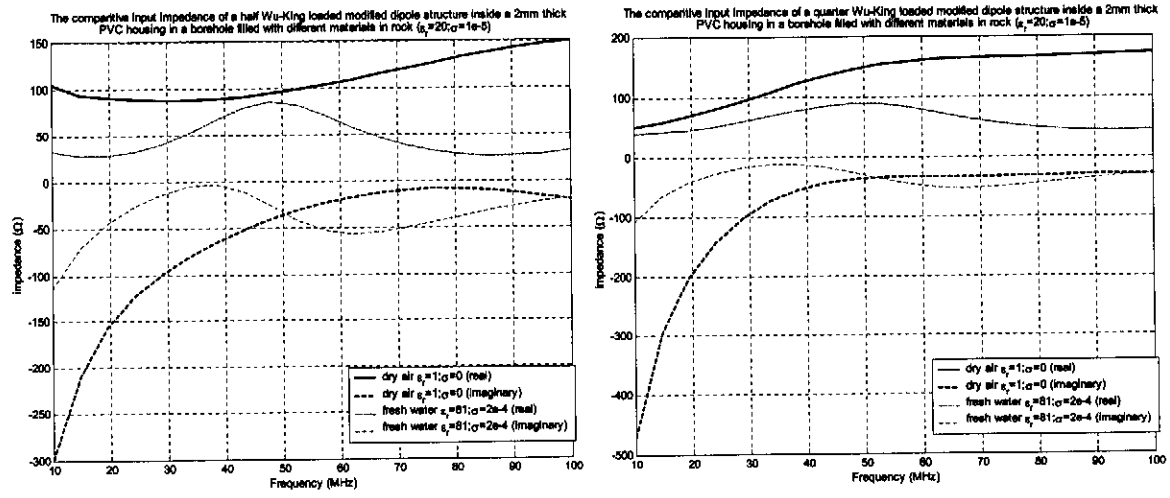

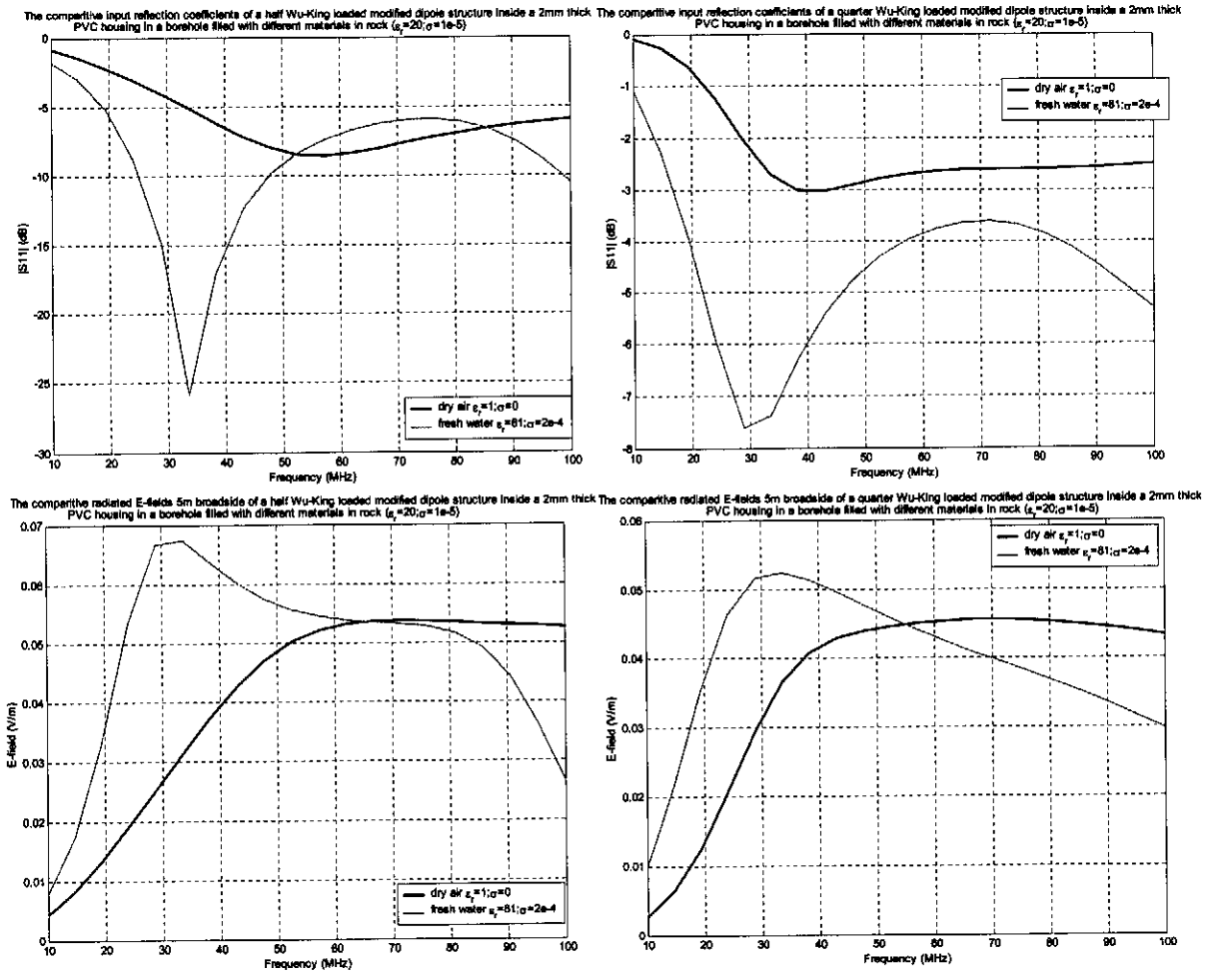

Figure 84 The comparative operational characteristics of a thick wire, half Wu-King loaded modified dipole, and a quarter Wu-King loading in a PVC housing (no potting or air gap) centrally located in a borehole, filled with air or fresh water respectively in rock with ε_r=20

The pulse forms radiated by the structures centrally located in various borehole environments are shown in Figure 85. The pulse efficiencies and pulse form ratios for the various pulses are computed as shown in Figure 86.

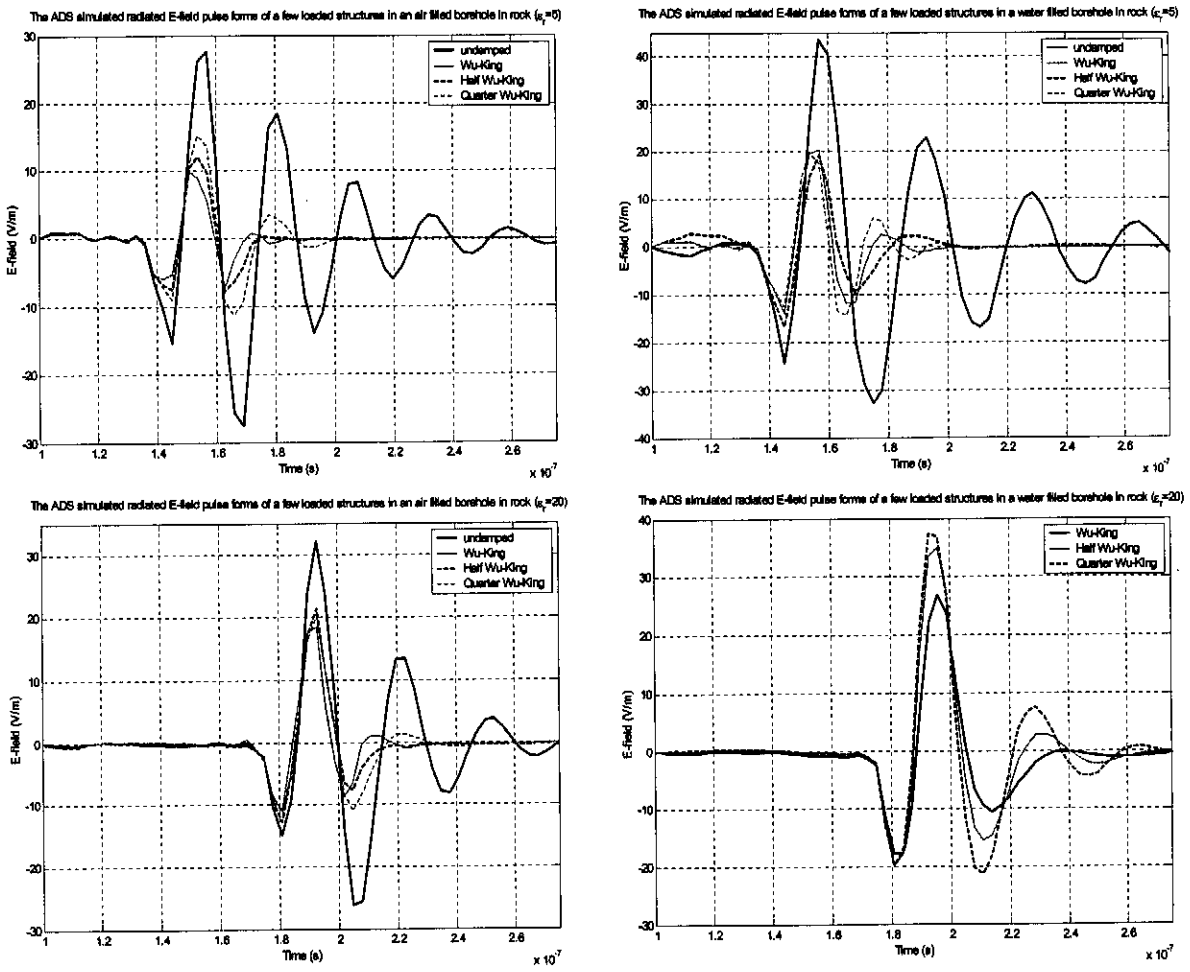

Figure 85 The ADS computed time-domain radiated pulse forms for a few loaded thick wire modified dipole structures simulated in a model of the full BHR environment, with no potting or air gap

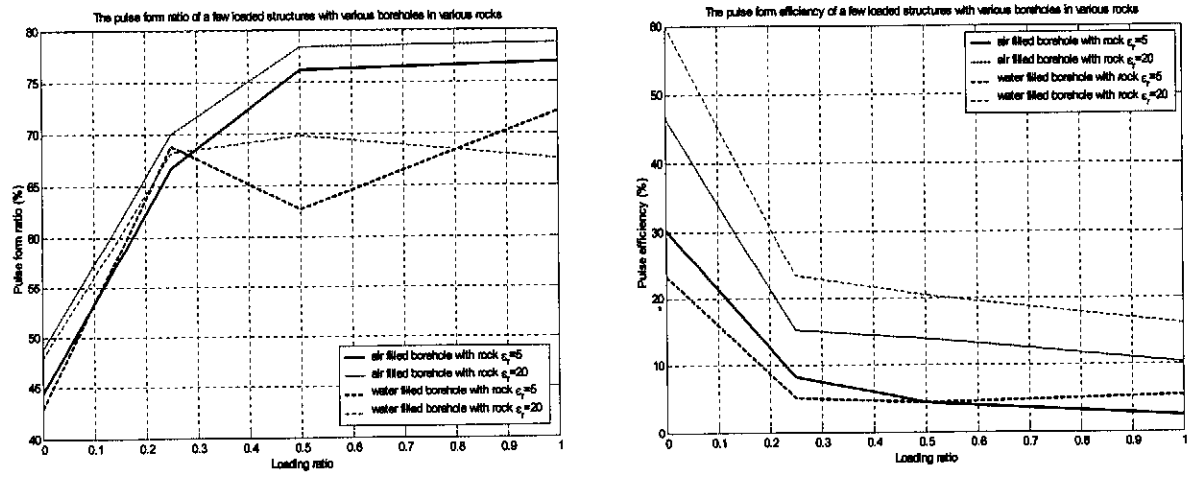

Figure 86 The computed pulse form factor and pulse efficiency of the pulses shown in Figure 85.

The simulation results presented in this section suggest a number of effects that can be attributed to the properties of the material in the dielectric-filled borehole layer around the probe structure. A few of these are:

General effects of the environmental factors

- In the case of a water-filled borehole, the coupling of energy to the propagation material is generally better, particularly on the low frequency side (higher pulse efficiency), but at the cost of a reduction in the quality of the coupled pulse form (lower pulse form factor)

- The high permitivity of the borehole layer in the case of a water-filled borehole causes an increase in the general permitivity of the material in the direct environment of the antenna. This has a frequency scaling effect on the antenna characteristics, and an impedance scaling effect on the load impedance presented by the antenna (lower real impedance; smaller capacitive load). This change in impedance implies a better radiating structure, but again the effect on the real impedance reduces the quality of isolation that can be achieved in mono-static application.

- The conductivity of the water in the borehole is critical to the operation of the antenna structure. For low conductivity water, the antenna operates well, and maintains good impedance and radiation characteristics. If the water becomes too conductive, however, the antenna radiation is extremely ineffective, and the load impedance becomes very small.

- The inclusion of a borehole in the environmental model largely damps the scaling effects of a change in the permitivity of the rock propagation medium. The inferred resonance point of a half Wu-King profile in a water filled borehole in rock with ε_r=5 is at approximately 62MHz, while in ε_r=20 rock, under the same conditions, the pseudo-resonance appears at 48MHz. As shown in the results of 2.5.2.5.A, we would expect the ε_r=20 case to have a pseudo-resonance at around half the frequency of the ε_r=5 case. The borehole damping effect is clear from this comparison.

Observations in regard to the impedance and radiation properties of different loading profiles

- For the case of a wet or dry borehole, and lower rock permitivities in the range considered, the quarter Wu-King loaded case exhibits the best wide band effective radiation. This is also true for the dry borehole case in high permitivity rock material, while in a water filled borehole environment, the heavier loading of the half Wu-King damping deliver better wideband radiation. These observations are supported by the time domain pulse form factor computations.

- Below 30MHz, the impedance of the quarter Wu-King antenna in a dry borehole is poorer (low real impedance and large capacitive imaginary part) than the heavier loading cases. Above 30MHz, the impedance of the quarter Wu-King case in a dry borehole, exhibits the best imaginary impedance, although the relative variation in the real part is still fairly large.

- For a wet borehole, the wideband impedance characteristics improve with a decrease in the antenna loading, irrespective of the surrounding rock permitivity. We note particularly that a heavy Wu-King loading will cause the antenna to become resonant in a wet borehole due to the increased effect of the pseudo-resonance on a heavier loaded modified dipole structure.

- The computed time-domain radiated pulses, and the pulse factors and efficiencies generally support the observations made thus far. Note particularly that the initial consideration of the FEKO computed radiated field magnitude with frequency indicates that the peak radiated fields for structures with heavier damping profiles is higher in all cases. The time-domain pulse radiation efficiencies however indicate that for pulsed applications, the structures with the best radiation bandwidth properties, rather than the best peak radiation magnitudes are most effective.

C. The effect of the borehole environment (Including both PVC pipe and PVC-type potting material)

We will now extend the computational model of the BHR environment used in 2.5.2.5.B, by the addition of a PVC potting material in the space between the antenna structure and the PVC pipe housing. The results presented in this section assume a single loaded strip topology, as shown in model 3 of Figure 53.

FEKO simulation results for the loaded antenna structures under consideration, employing un-simplified antenna- and environmental-models (shown in Figure 87) are presented in Figure 88 to Figure 91. The time-domain radiated pulse forms, 5m broadside of these structures, for the standard excitation defined in section 2.3.2.1 are shown in Figure 92. The pulse form factors and pulse efficiencies for the structures are plotted in Figure 93.

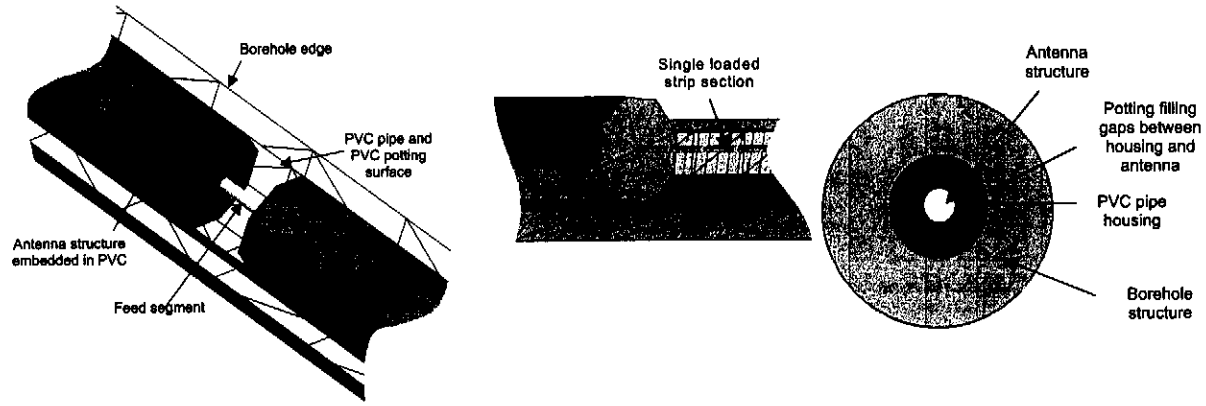

Figure 87 The form of the FEKO model used to characterize the single loaded strip modified dipole antenna structure inside a borehole, with both PVC pipe and potting effects taken into account

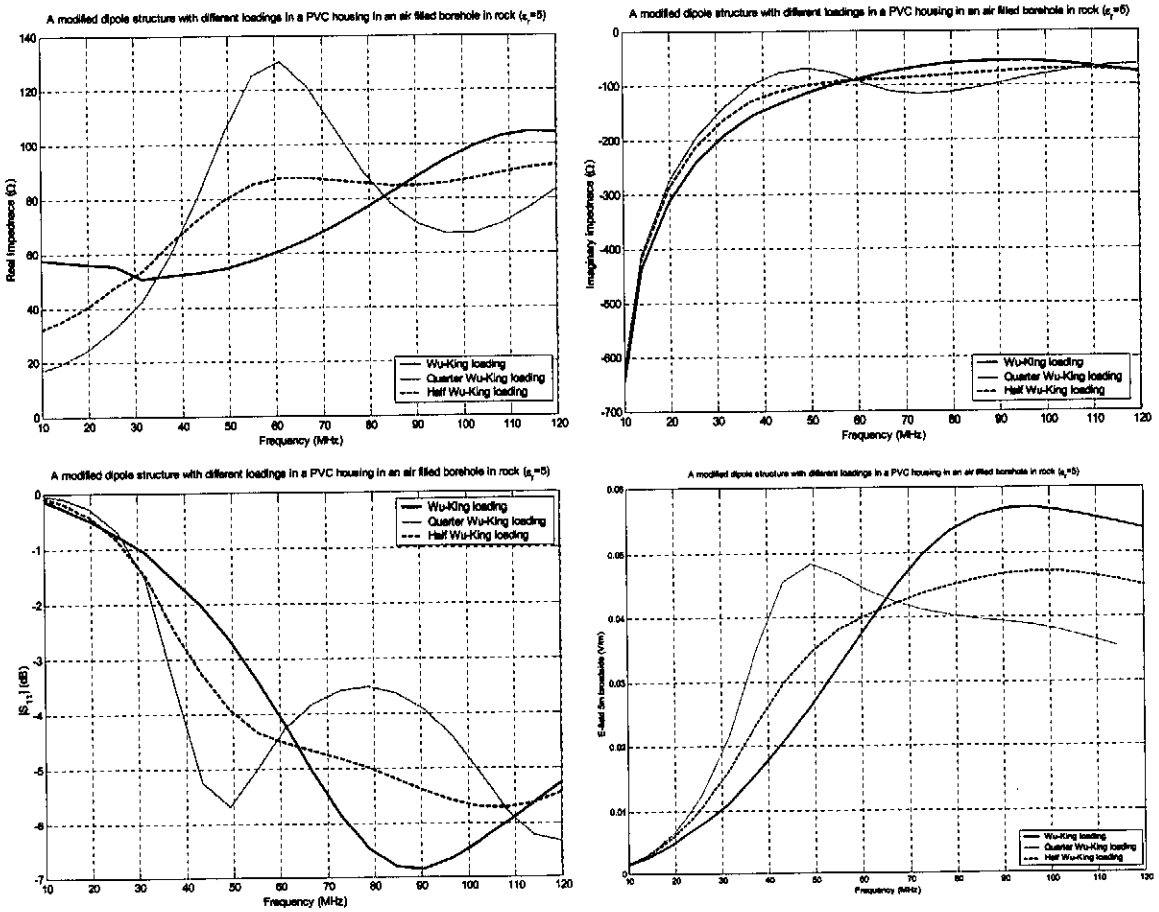

Figure 88 The FEKO simulated characteristics of a single-strip modified dipole antenna structure in a PVC pipe housing including the effects of PVC-type potting material deployed in an air filled borehole in rock (ε_r=5)

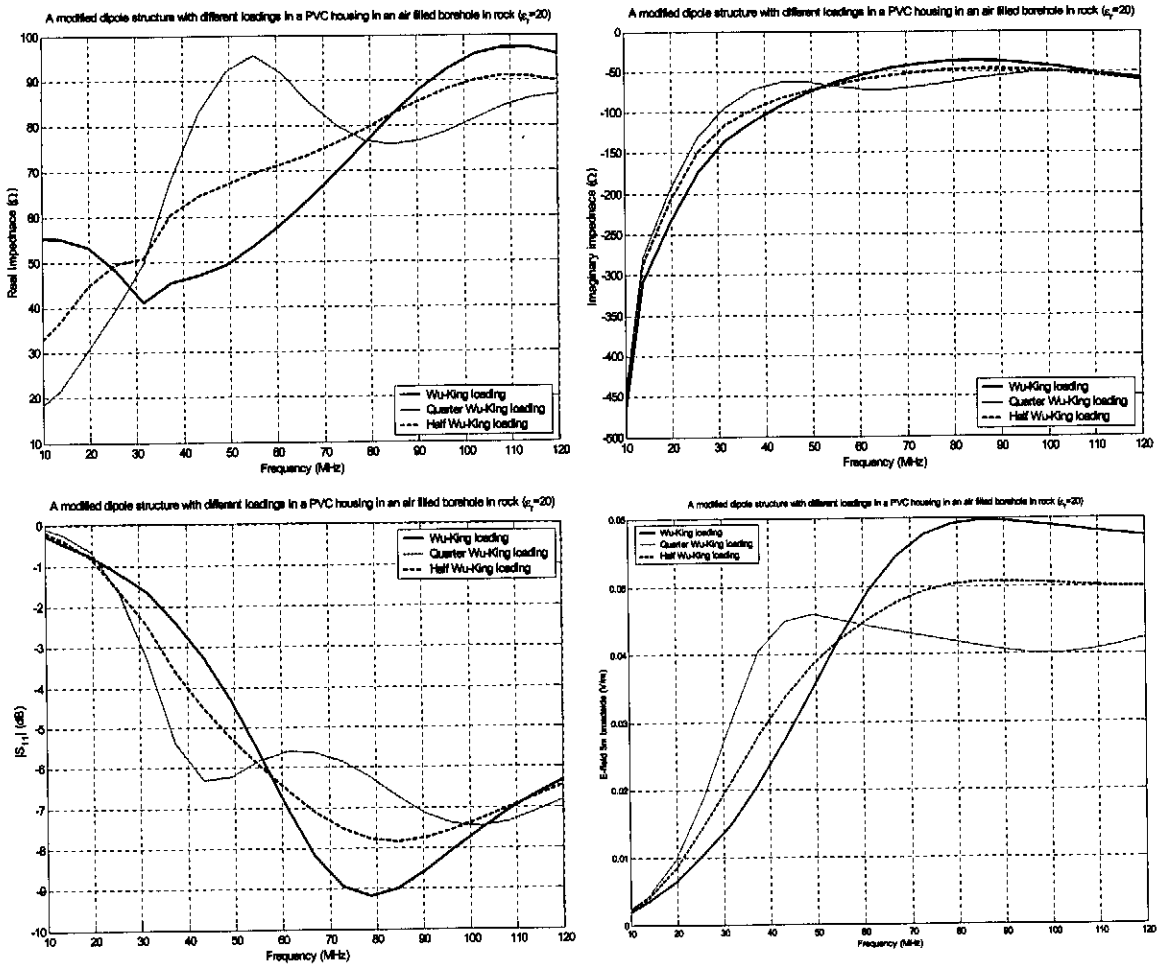

Figure 89 The FEKO simulated characteristics of a single-strip modified dipole antenna structure in a PVC pipe housing including the effects of PVC-type potting material deployed in an air filled borehole in rock (ε_r=20)

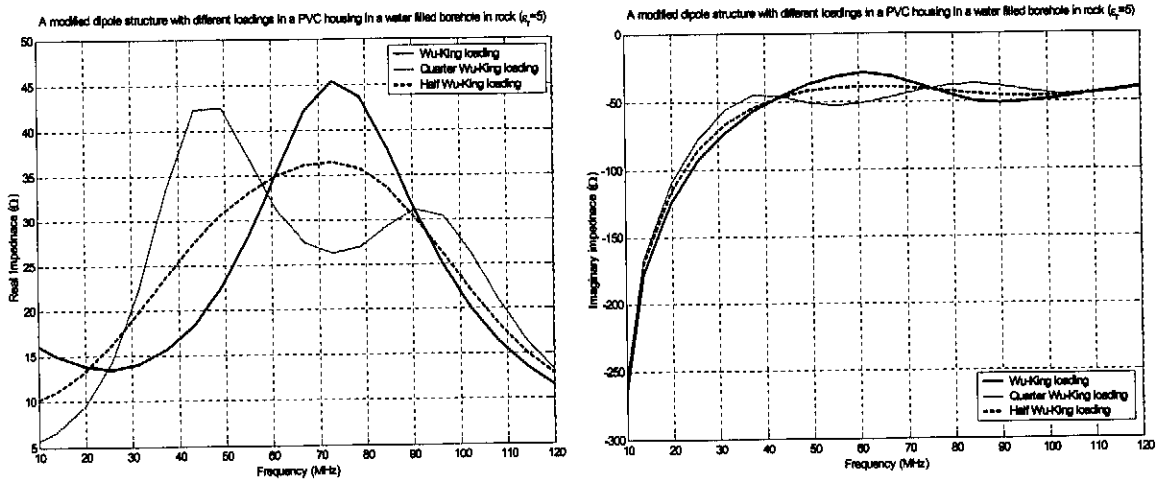

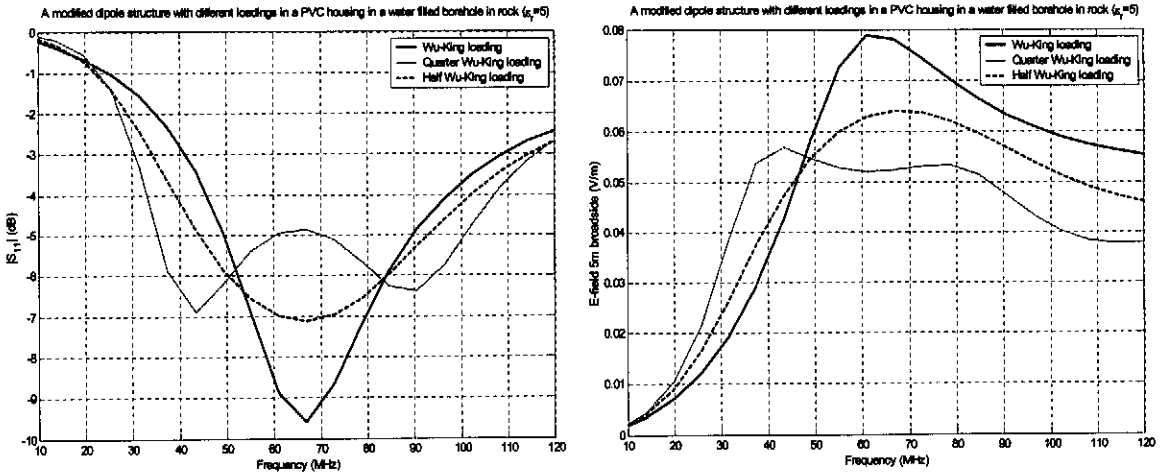

Figure 90 The FEKO simulated characteristics of a single-strip modified dipole antenna structure in a PVC pipe housing including the effects of PVC-type potting material deployed in a water filled borehole in rock (ε_r=5)

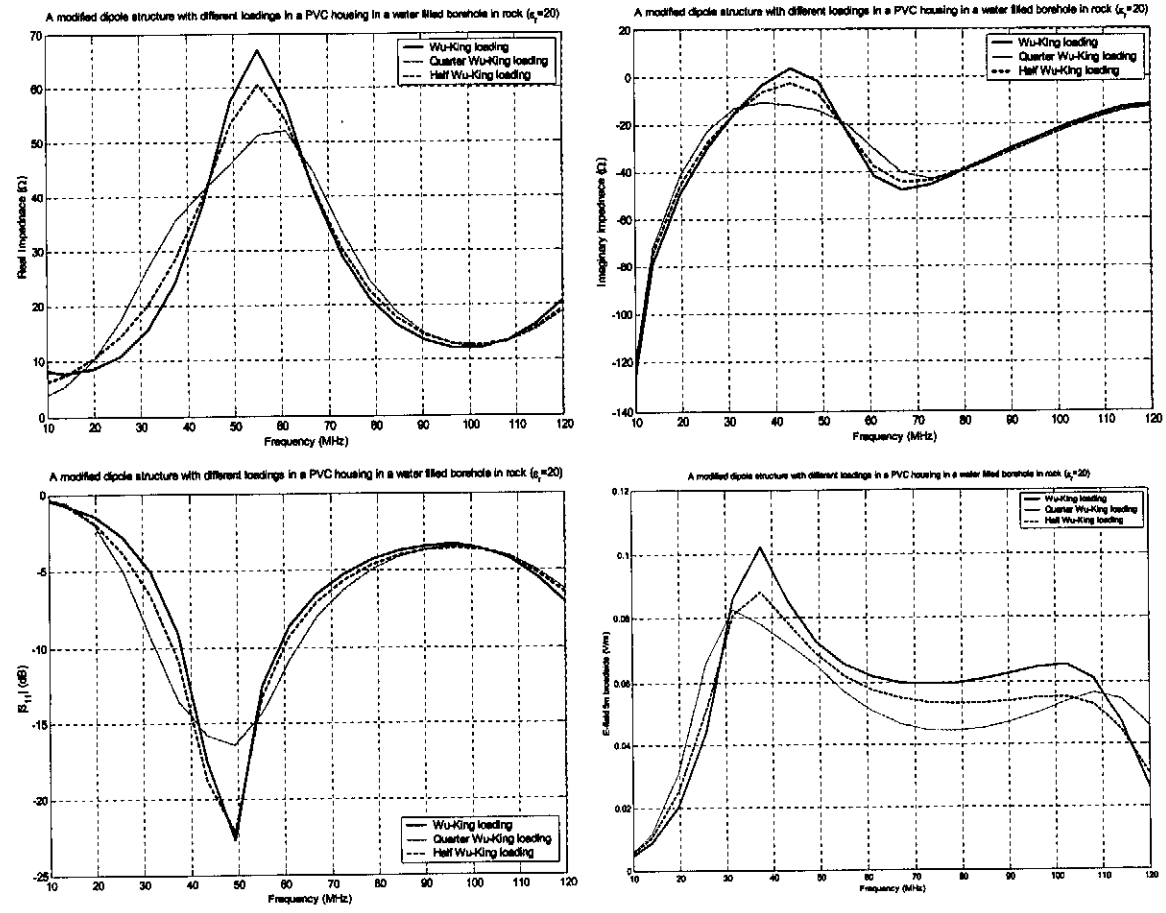

Figure 91 The simulation results for the FEKO characterization of a modified dipole antenna structure with a single central loaded strip with different loading profiles in a PVC housing model including potting (ε_r=3.7), deployed in a water filled borehole in rock (ε_r=20)

Once again, in the case of an air filled borehole, the impedance of the antenna structures is not affected very much be a change in the rock permitivity, other than a general decrease in the capacitive part of the impedance as the rock permitivity decreases. For the air filled borehole case, the radiation seems relatively independent of the rock permitivity, except for the slight effect of the change in capacitive impedance at the low frequencies. The effect of the potting material is evident if we compare these simulation results to those presented in the previous section. As was found during the consideration of the potting effects for the first extreme environmental topology postulated in section 2.2, the potting generally worsens both the impedance and the radiation characteristics of the antenna structure, particularly for lower frequencies. The potting seems to have a larger effect on the real part of the input impedance, reducing is dramatically from that of the case presented in B, effectively halving the impedance, and causing a slight shift in the pseudo-resonance's observed on the structures (downward shift for an air filled borehole, and an upward shift for a water filled borehole).

For ideal broadband radiation, the lighter resistive loading profile (25% Wu-King) performs best in all cases. From the point of view of impedance stability, a heavier loading (50% Wu-King) seems to be more ideal.

In the case of high permitivity rock and a water filled borehole, the impedance properties of the antenna structure are very poor for broad band operation, and the structure shows resonance characteristics particularly for heavier loading profiles. The realization of a good antenna for operation under these conditions proves to be very difficult, due to the high permitivity of all the materials in the environment compared to the materials in which the antenna is housed. An antenna deployed under such conditions will provide very poor broadband pulse radiation capabilities.

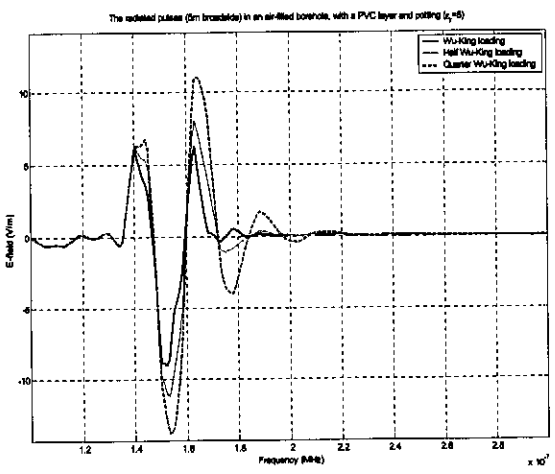

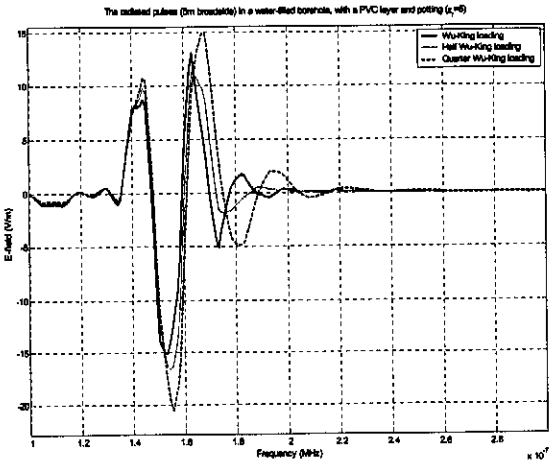

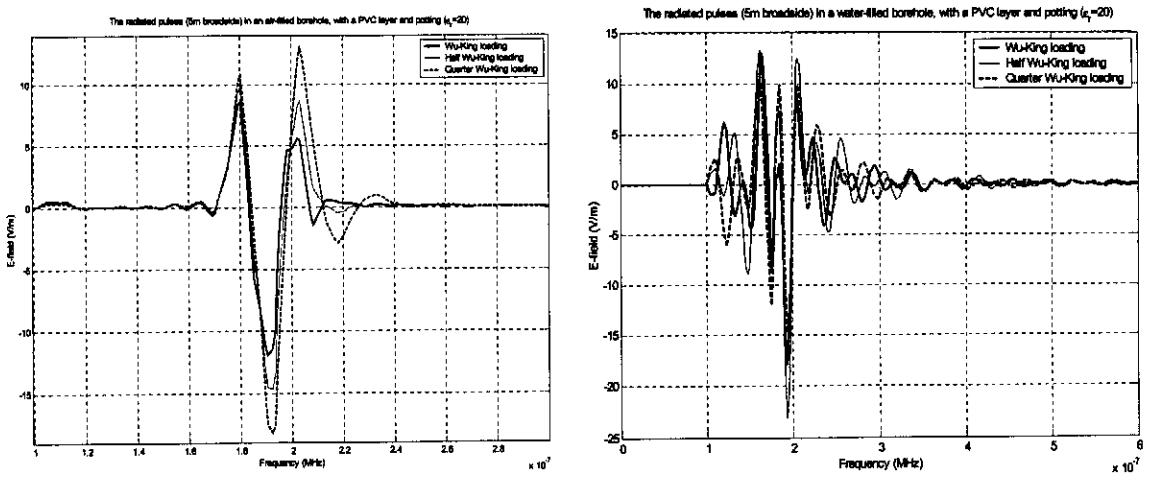

Figure 92 The simulated radiated pulse forms for full-model simulations of a loaded modified dipole structure with a single central loaded strip section deployed in boreholes in different rock materials including the effects of the PVC housing and potting material (ε_r=3.7)

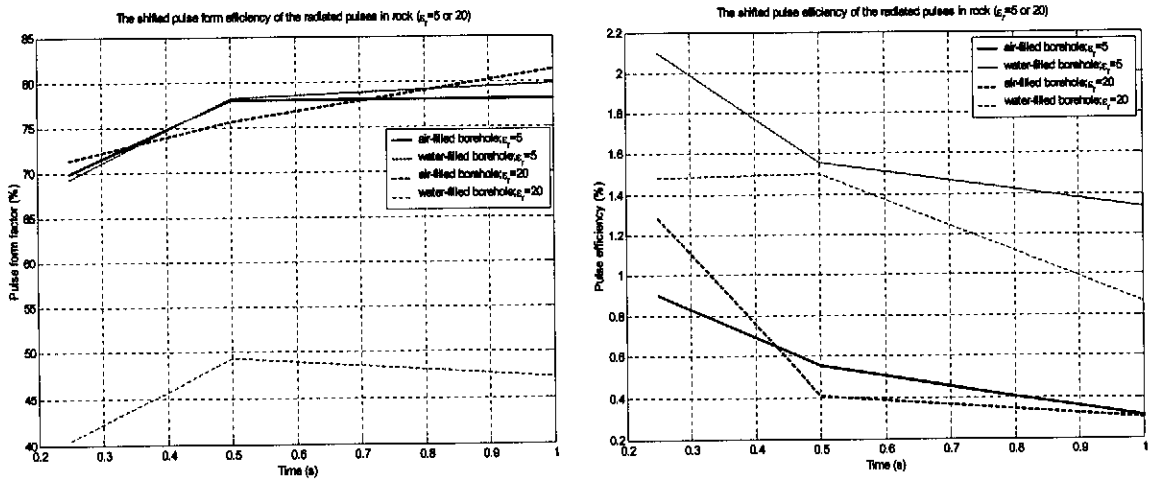

Figure 93 The shifted pulse form factors and pulse efficiencies computed for the pulses of Figure 92

An improvement in the pulse form factor, and drop in the pulse radiation efficiency is observed with an increase in the weight of the loading profile. The predicted resonant operation of the antennas in a water-filled borehole in high permitivity rock is clear in both the time domain pulse forms computed in ADS for this case, and also the very poor pulse form factor of below 30% for all the different loading profiles considered.

When we compare the results presented in this section to those of section 2.5.2.5.B, we find that for the single loaded strip topology under consideration, the operational characteristics of the antenna are generally worsened by the inclusion of a PVC-type potting layer in the probe structural model. (The same was noted for the first extreme environmental case considered in section 2.5.2.5.A).

There are 2 possible solutions to this. The first solution is to consider different potting materials to improve the antenna operation. The second solution is to alter the antenna topology by the addition of a number of loaded strip sections spaced around the circumference of the probe, just inside the PVC-pipe housing, or by adopting a cylindrical loaded topology similar to that of model 2 of Figure 53. These antennae can be accurately approximated using the thick wire dipole structures assumed in 2.5.2.5.B, and will have operational properties similar to those shown in the results of section 2.5.2.5.B.

D. The effect of the borehole environment (Including PVC pipe with an air gap)

A number of simulations were performed with an environmental model assuming an air gap between the antenna and the PVC pipe housing, with a borehole around the whole structure. This is an extremely complex model, and it was found that only some of the simulations delivered sensible results. These simulations show that, as was concluded during consideration of the first extreme environmental case of Figure 37, the operation of the potted antenna structure is generally better than that of a structure with air filling the gaps between the antenna and the PVC housing. This is particularly so on the low frequency side, where the air gap model becomes very capacitive with small real impedance. We will not present computational results generated with this model here. The FEKO model used for the computation of the full antenna structure with an air gap between the antenna and the PC housing is shown in Appendix B.3.

Due to the number of, and wide variation in the parameters in the complex environmental models described in 2.5.2.5.C and 2.5.2.5.D, presentation of all the possible cases would be impossible. Based on both the simulation results presented here and other observations made during the period of this thesis study, an attempt was made to determine and roughly characterize the effect of variation in the environment on the antenna operation and suggest a radiating structure that will operate well under most practical conditions that can be expected in the BHR environment.

In the next section, we will give a short summary of these observations and predictions.

2.6. Investigative conclusions

In this section, we will shortly summarize the observations and conclusions reached during the investigation presented in this chapter. We will then describe and attempt to fully characterize a radiating structure for use in a mono-static radar system, using accurate models of the suggested antenna topologies, in a detailed model of a typical BHR environment.

It is clear from simulation results that there are a number of factors that can be identified as critical in determining the operation of the BHR antenna structure. These factors are:

- **The dimensions of the structure**: For longer antenna structures, radiation is generally more efficient and the properties of the antenna are more stable over the frequency range of interest. For

pulsed applications, the radiated pulse form is however generally poorer. This agrees with intuitive predictions. For the modified dipole structure suggested in this report, the length of the resistively damped sections should be chosen as at least 50% of the total arm length of the structure, in order to effectively damp the radiation of ringing energy. (By shifting the interface between the unloaded and loaded sections further and further from the feed, the travelling wave reflection at the interface begins to play a more and more important role in the radiation of the structure.) The radius of the radiating structure should be chosen as large as spatially possible, both due to the improved intrinsic bandwidth properties of a thicker structure, to maximize housing space and allow effective shielding of the probe electronics by placing them inside the antenna structure.

- **The resistive loading:** It is clear from time-domain simulations that the addition of a resistive loading profile to an antenna structure improves that antenna's pulse radiation performance (transient phase response). The resistive loading also has implications on the radiation efficiency of the structure, but the time-dependant efficiency implications are not as pronounced as the effects on the general efficiency defined independent of time. The ideal loading of the antenna structure for general pulsed application will be less than that ideal theoretical loading for a CW system, as it is the transient response of the antenna that is of importance for pulsed application, rather than its steady-state characteristics. Consideration of the time-evolution of the currents on the chosen antenna topology for a pulsed excitation confirms this. The loading profile must be chosen taking both the pulse form and the time-radiation efficiency of the antenna operating in the expected operational environment, as well as the load impedance characteristics into account.

- **Environmental effects:**

  - **Extreme environmental case 1:** In the first extreme case defined in Figure 37, the following factors are of importance, and directly affect the operation of the antenna structure.

    - **The permitivity of the propagation rock material:** Simulations indicate that the permitivity of the rock material in which the radar system is deployed has an effect on both the radiation and impedance characteristics of the antenna structure. The change in permitivity causes a frequency scaling and impedance scaling of the characteristics of the antenna.

    - **The PVC pipe housing of the antenna structure:** The PVC-pipe housing of the antenna structure has a minor, loading independent, effect on the impedance and radiation characteristics of the antenna. It does cause a slight frequency shift in the antenna load characteristics. The effect is larger at higher frequencies, and for rock materials that have much larger permitivities than the PVC pipe. The major effect of the PVC pipe is that it provides electrically isolation of the antenna from its environment.

- **Dielectric materials between the antenna structure and the PVC housing:** Potting material or an air gap has a surprisingly large effect on the antenna operation. The real impedance of the antenna drops with the addition of standard potting materials (ε_r<4), while the input capacitance decreases. Both of these effects are undesired, and negatively affect the bandwidth and operation of the antenna. The negative effect of an air gap on the antenna operation is similar, and much pronounced than that of potting material, particularly on the LF side. The choice of an antenna topology that operates as a thick structure that fills the whole space inside the PVC pipe largely negates the negative effects of the air gaps or potting materials. Thick-wire-approximate structures may be realized by either a continuous loaded cylindrical structure, or a multiple loaded strip configuration instead of the single strip topology.

- **Extreme environmental case 2:** The operation of an antenna in the second extreme environmental case defined in Figure 37 is affected in the following ways by the following factors

  - **The permitivity of the propagation rock material:** The effects of change in rock permitivity are the same as for case 1, but are not as marked when a borehole structure is included in the environmental model.

  - **The PVC pipe housing of the antenna structure:** As in the case of the embedded antenna model, the effect of the PVC-pipe housing on the properties and performance of the antenna structure is minimal.

  - **Dielectric materials between the antenna structure and the PVC housing:** The inclusion of a dielectric material in the gaps between the antenna structure and the PVC-pipe probe housing has a large, generally undesirable effect on the antenna characteristics and operation. By assuming a distributed multiple strip of loaded cylinder topology, the effects can be greatly reduced.

  - **The borehole-filling material:** The material in the borehole (between the probe and the rock) is the environmental factor that has the largest independent effect on the operation of the antenna. This is generally due to the extremely large variation in both the permitivity and conductivity properties of the materials that can be routinely expected. The most important factor for mono-static application, employing the isolation strategies described in section 4.2 is the effect of the borehole filling material on the impedance of the antenna. This effect is not so critical in existing bi-static systems, as isolation is achieved by spatial separation, rather than pulse comparison. The general radiation efficiency of the antenna improves with an increase in the permitivity of the borehole filling material, but for materials

with considerable conductivity, the coupling of energy to the rock may be severely impaired.

- **The design of environmentally tolerant antennas:** For mono-static applications, the antenna characteristics must be extremely tolerant to environmental conditions to allow for good isolation under all practical conditions. The investigations during the period of this report suggest that the pulse-form radiation properties of the investigated antenna structures are fairly tolerant to environmental variation, although the radiation efficiency may be influenced (this is not so in the case where conductive water is present in the borehole, as very little or no effective coupling to the rock is possible). The environmental dependence of the antenna impedance is of larger concern, and shows more variation for different environments. Environmental impedance variation is to a large degree related to the impedance scaling inferred by a change in the permitivity of the environment. It is difficult to damp this effect by antenna loading, and the possibility of using different antennas for different environments, and adjusting the isolation electronics accordingly must be considered to achieve acceptable and stable mono-static isolation.

2.6.1. Suggested radiating structure/s based on computational simulation results

Based on observation of the computational investigation into the radiating structure of the BHR system, with particular interest in the development of a structure that can be implemented in a mono-static radar probe, the following radiating structure design was determined. It is important to note that the investigation described thus far in this chapter suggests that the design of different antennas for application in different environments is prudent, and generally necessary to facilitate the necessary isolation for mono-static application. The antenna structure presented in this section is designed to give good impedance characteristics and pulse radiation characteristics in different environments. The structure is, however, not environmentally tolerant in the sense that it will present the same impedance and radiation characteristics under all practical environmental conditions, as the realization of such an antenna is not possible if the amount of possible variation in the operational environment is considered. The application of this antenna structure will thus have to be accompanied by careful calibration of the mono-static electronics based on the operational characteristics of the antenna in the expected environment that the system would be deployed. This calibration is performed by extraction and implementation of a lumped element approximation as a dummy load for the internal estimator of the transmitter circuitry.

We will consider the operation of three alterative topologies, based on the same design. Results are presented in both of the extreme environmental models postulated in section 2.2. The computational results suggest that the second topology is the most environmentally tolerant and stable topology for application in a mono-static system.

The geometry of the structure of Figure 52 can be used as an acceptable antenna topology that conforms to the spatial and operational requirements for a BHR radiating structure. The dimensions of the structure are chosen as shown in Figure 94.

The total effective discrete resistive loading profile applied to each of the loaded sections is designed as shown in Table 6. (In the case of a multiple strip application, a multiple of this profile must be applied to each strip, so that the parallel combination of the resistor values is that of Table 6.)

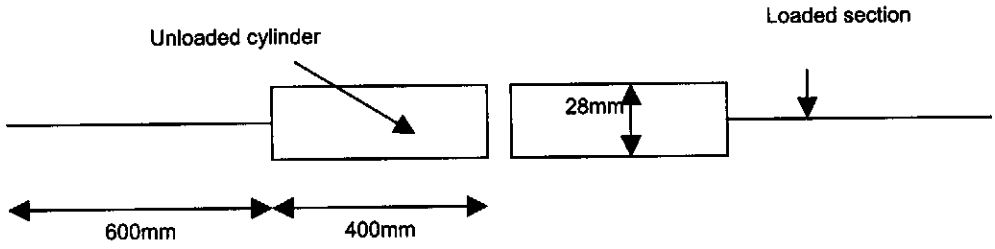

Figure 94 The structural dimensions of the final radiating structure developed during the period of this report

Position (mm from feed point)	500	611	722	833	944
Value (Ω)	26.5	33.4	44.8	68	146.6

Table 6 The loading profile applied to the final radiating structure designed during the period of this report

2.6.1.1. Topology 1: A single strip loaded modified dipole

The first antenna topology that we will characterize is a single, central loaded strip topology, as used in existing antennas, and shown in model 3 of Figure 53 Simulations indicate that this is not the ideal case, as the negative effects of potting or an air gap are considerable.

Computational characterization of the single strip structure, using FEKO, with a full model of a practical BHR environment, including ε_r=3.7 potting material, is shown in Figure 95. The model used to generate these results is identical to the one shown in Figure 87.

The single strip structures show large variation in impedance in the frequency band of interest, particularly for the case of an air filled borehole. These impedance properties, particularly on the low frequency side are poor. The radiation of the structure however is good, and relatively independent of the environment.

The poor relative impedance of the structure can largely be ascribed to the effects of the potting layer, which are large for the single strip topology.

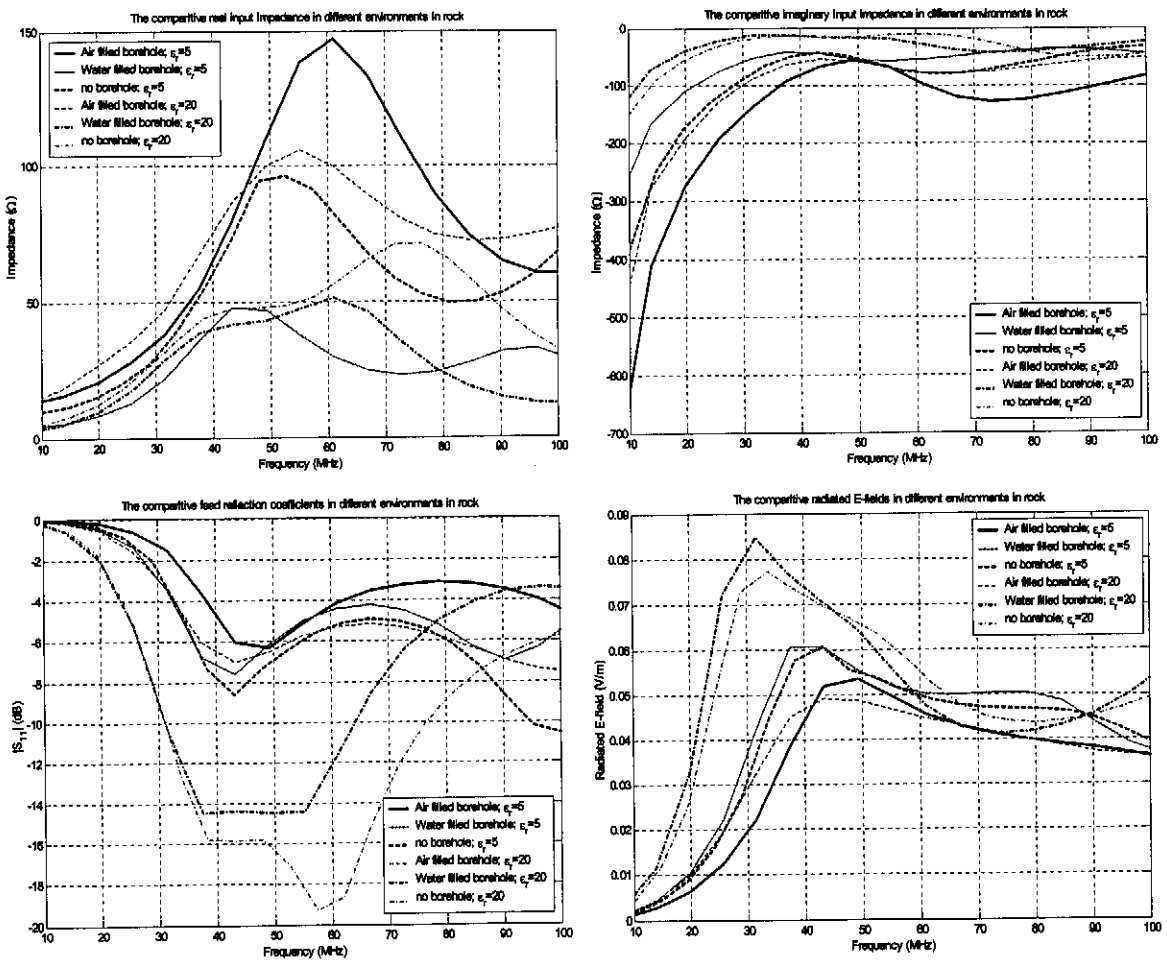

Figure 95 The FEKO simulated characteristics of the final radiating structure suggested in this report, assuming a centrally located single loaded strip and ε_r=3.7 potting, in various extreme environments

The radiated E-field pulse forms 5m broadside of the antenna structure under various environmental conditions and the radiation pattern at a few frequencies are shown in Figure 96. The radiated pulse forms and radiation efficiency of the structure is good under all environmental conditions. The radiation pattern of the structure is broadside, and just begins to show the beginning effects of side lobe formation at the high frequency side.

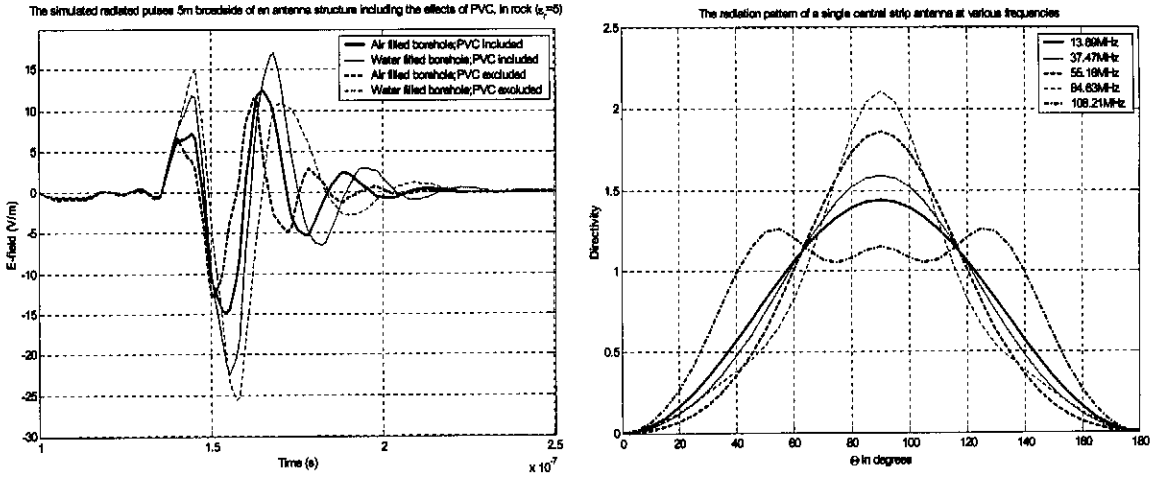

Figure 96 The ADS simulated radiated E-fields of the pulsed final antenna structure assuming a single centrally located loaded strip section, in a potted probe (ε_r=3.7) in a few different operational environments; the radiation pattern of the single loaded strip structure

2.6.1.2. Topology 2: A multiple strip loaded modified dipole

The second antenna topology is realized by spacing a number of loaded strip sections around the edge of probe housing circumference, instead of one centrally located strip. This realization approximates the case where the antenna is build of solid conductor sections that fill the whole cross sectional area of the probe housing.

The characteristics of the 4 loaded strip topology, including an ε_r=3.7 potting material, is shown in Figure 97. The FEKO model used to generate these results is also shown.

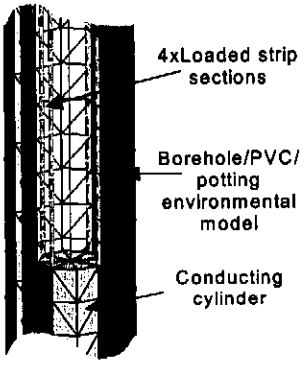

Multiple loaded strip antenna model in a practical BHR environment

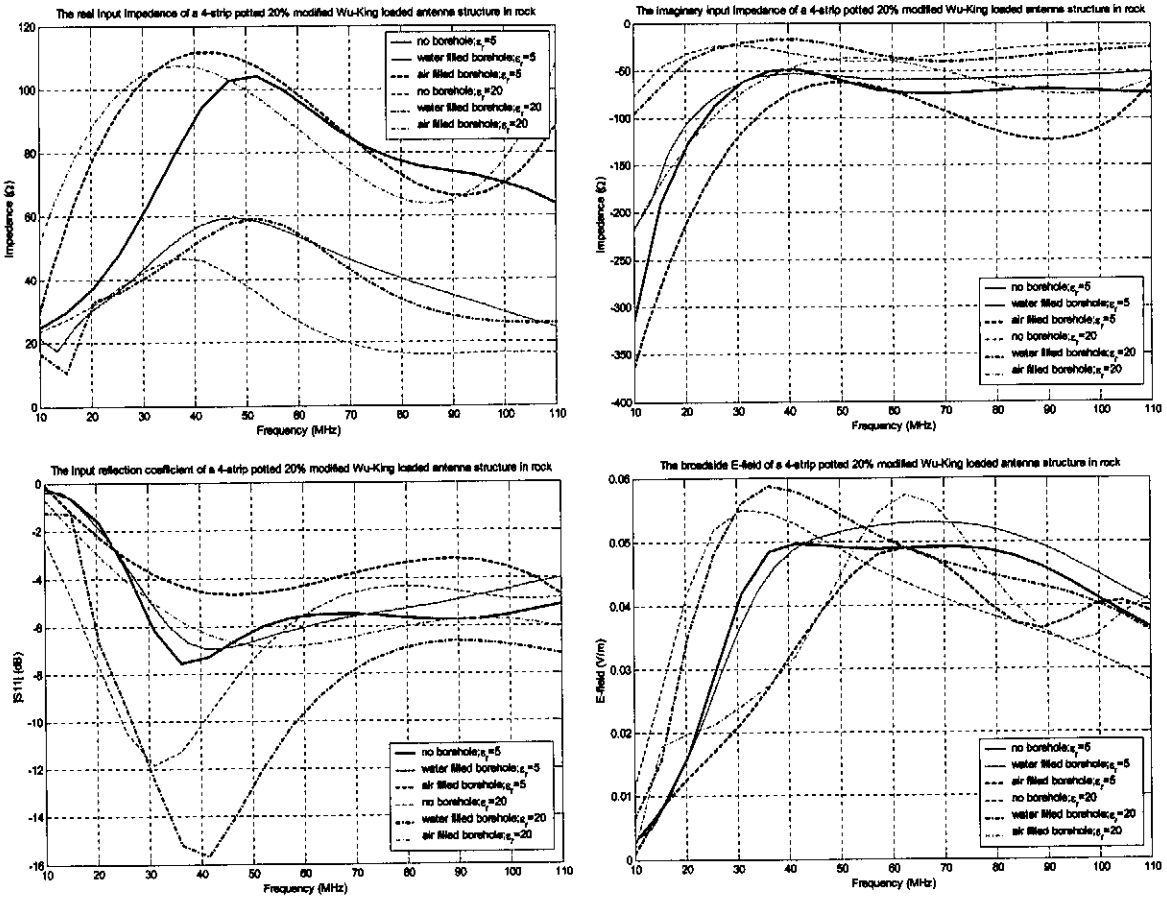

Figure 97 FEKO model of a 4-loaded strip antenna model in an operational BHR environment, and a few results of FEKO simulations

ADS computed radiated pulse-forms, pulse form factors and the radiation pattern at different frequencies for the antenna structures of Figure 97 are shown in Figure 98.

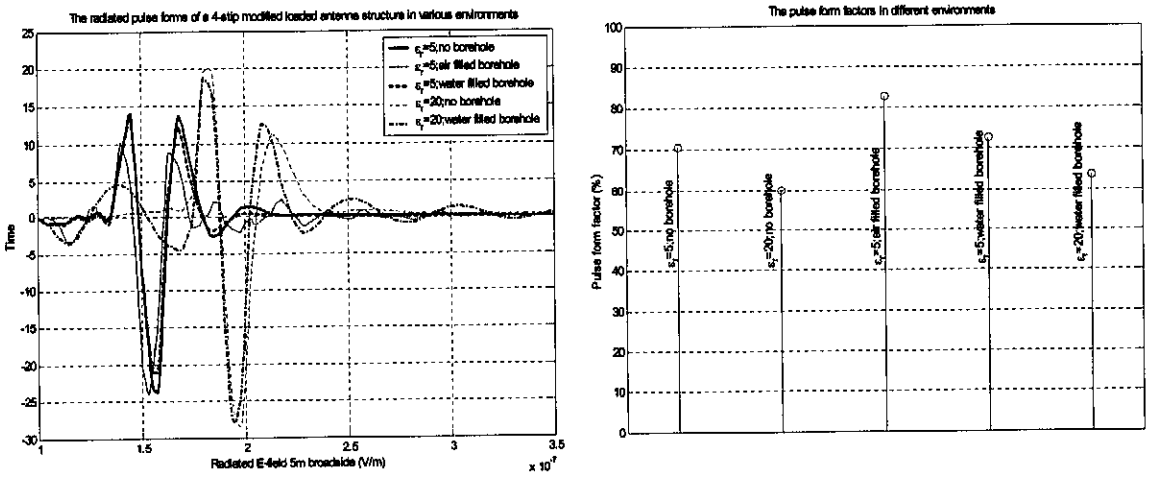

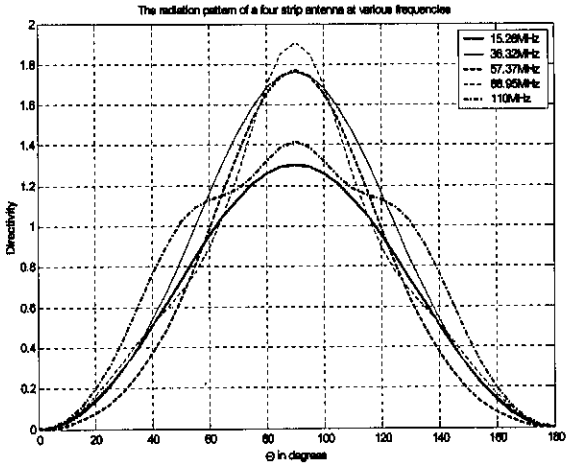

Figure 98 ADS simulated radiated pulse forms for the antennas of Figure 97 and the pulse form factors of the different pulse forms; the radiation pattern of the topology in a BHR environment

The 4-strip loading topology clearly performs better than the single strip structure for the same loading, under all the postulated extreme environmental conditions. The radiation pattern is more stable, the low frequency impedance is improved, there is less variation in the impedance properties over the frequency range, and the radiated pulse forms and efficiency are good. Note that the radiated pulse forms of this structure are very tolerant to the operational environment, as to a large degree are the impedance characteristics, which maintain a similar form, but exhibit impedance scaling properties as the permitivity of the rock material changes.

2.6.1.3. Topology 3: A cylindrical loaded modified dipole

The operation of an antenna structure, assuming the same loading profile, but with a cylindrical loaded structure, potted in an ε_r=3.7 potting material are shown in Figure 99. The FEKO model used to generate these results is also shown. (Note that no results are shown for the air filled borehole case, due to difficulties experienced during simulation of this case).

The cylindrical structure provides very good broadband radiation properties, although it does threaten to become resonant for the environmental assumption of deployment in a water filled borehole in high permitivity rock material. The pulse form factors of the pulses radiated in all the environments considered are extremely good, and the pulse radiation efficiency is exceptionally high, particularly for the case of a water filled borehole. The impedance of the cylindrical structure is not as tolerant to changes in the environment, or as stable over the frequency range of interest. The radiation pattern of the structure exhibits characteristics very similar to those of the multiple strip antenna radiation pattern.

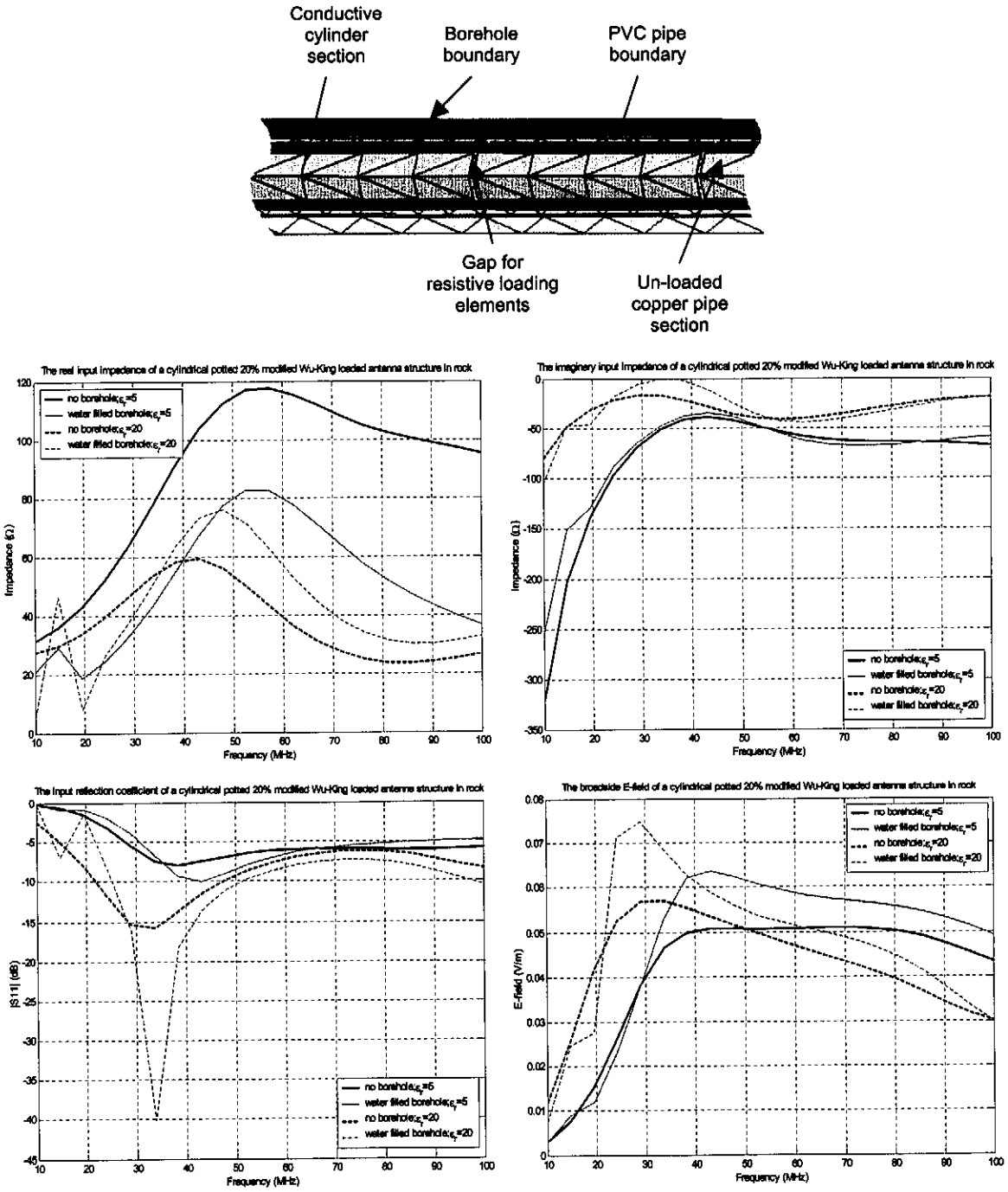

Figure 99 The FEKO model and simulation results for a 20% Wu-King loaded cylindrical modified dipole antenna structure (no results shown for air filled borehole)

The ADS computed radiated pulse forms 5m broadside of the antennas of Figure 99, and the computed pulse form factors are shown in Figure 100.

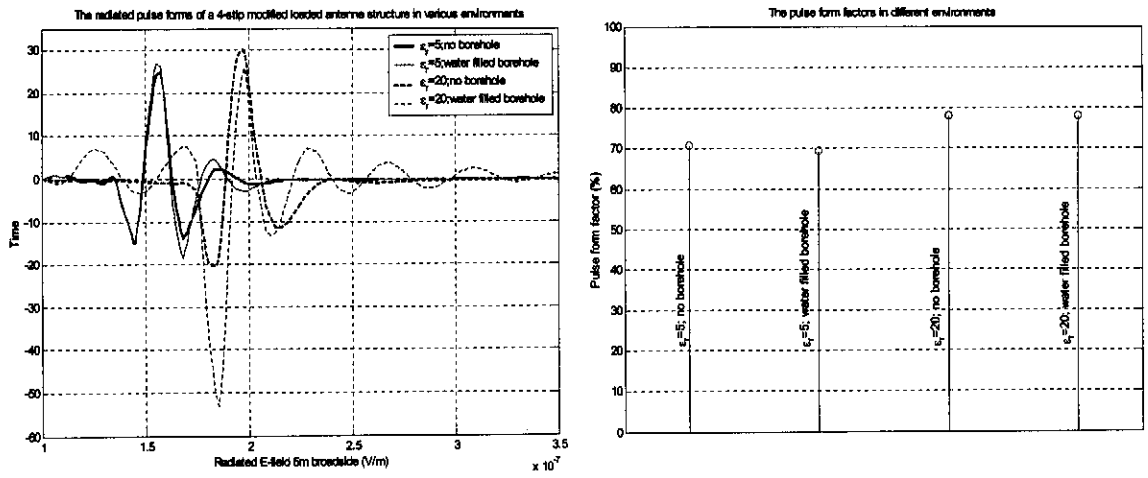

Figure 100 ADS simulated radiated pulse forms for the antennas of Figure 99 and the pulse form factors of the different pulse forms

2.6.2. An analysis of a radiating structure used during prototype testing

A radiating structure was used during the course of this thesis for prototype testing purposes. The structure employs the same geometrical form as described in Figure 52, but the unloaded central sections were lengthened to 600mm. The length of the outer loaded sections was 580mm, giving the radiation structure an arm length of 1.18m. The resistive profile loading used is shown in Table 7. The profile was chosen based on observation of computational simulation results in a simplified BHR environment. Later consideration of the structure in a more detailed model of the BHR operational environment unfortunately showed that this antenna is not a very good choice for BHR, and in particular mono-static BHR, application. We will present a short characterisation of the antenna, using an accurate antenna model in a detailed BHR environment. These results will thus accurately predict the operation of the assumed structure.

A detailed FEKO model of the structure is shown in Figure 101.

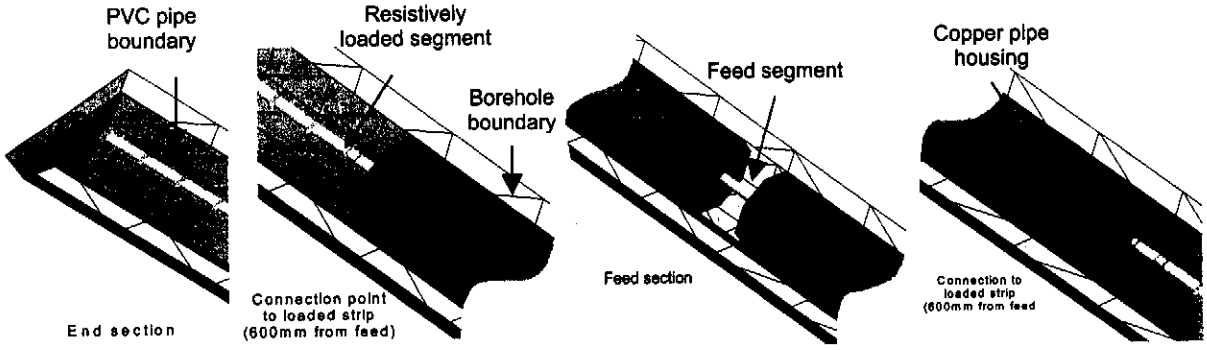

Figure 101 The FEKO model used to characterize the lengthened antenna structure used for prototype investigations

Position (mm from feed)	600	611	722	833	944	1055
Resistor value (Ω)	27	12	16.5	23	33	75

Table 7 The loading profile used for the modified dipole radiating structure with 600mm unloaded central sections

FEKO simulation results for the chosen profile in a borehole, in rock (ε_r=5 or 20) are shown in Figure 102.

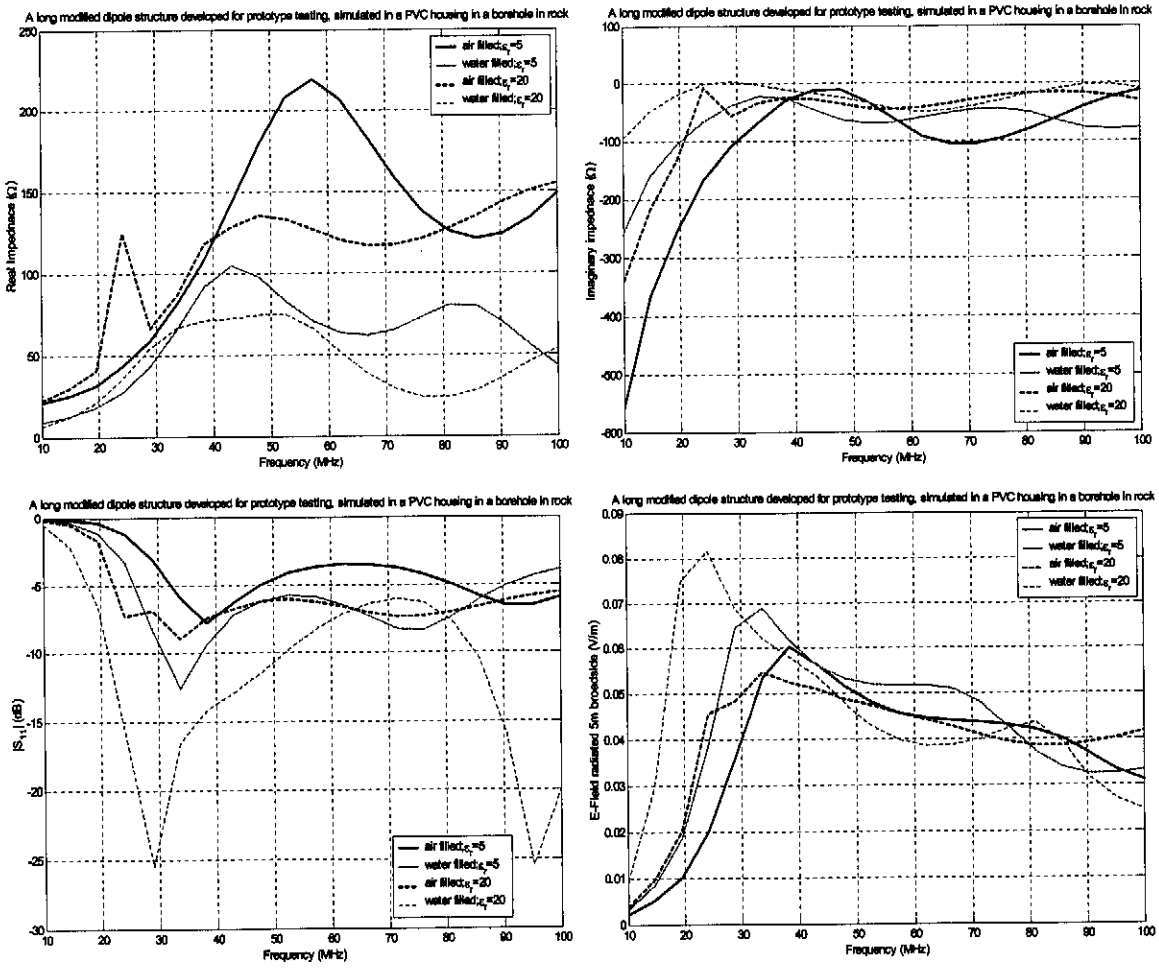

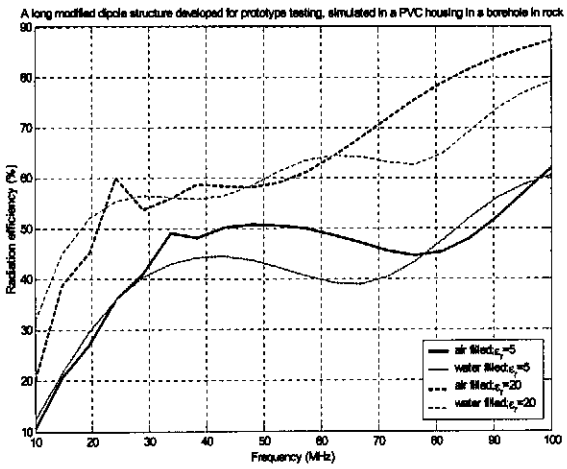

Figure 102 The FEKO simulation results of the long prototype antenna structure, simulated in a full BHR environment (loss less propagation) with potting material present (ε_r=3.7)

ADS computation of the pulse response of this structure delivered the results shown in Figure 103.

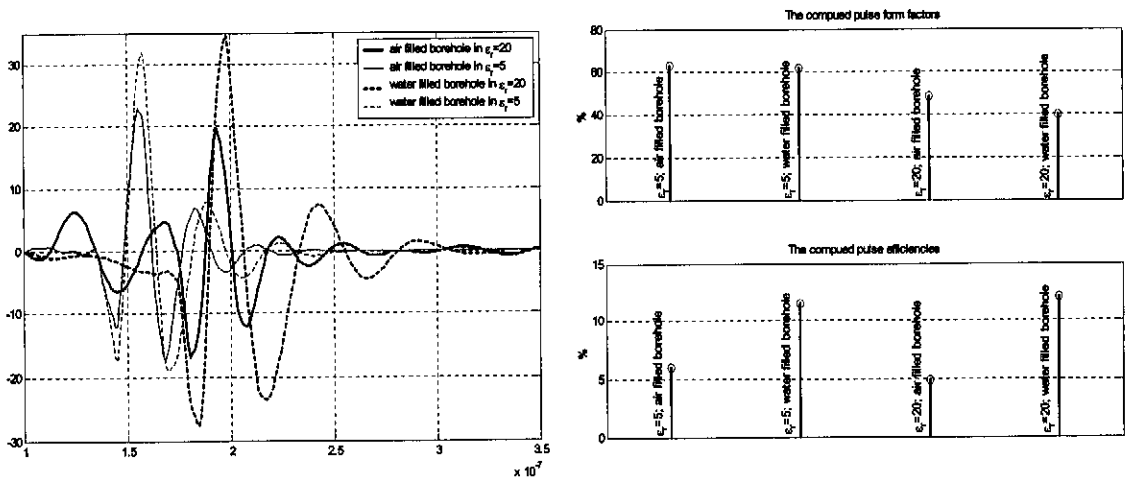

Figure 103 The form of the feed current and E-field pulse radiated by the 600mm unloaded section prototype antenna in an ε_r=5/20 loss-less propagation medium with ε_r=3.7 potting material; $\varepsilon_{pulse\text{-}form}$ and ε_{pulse}

The results of Figure 103 indicate that the long antenna structure is very efficient, but the radiated pulse forms are relatively poor in comparison with those achieved using shorter structures. In the case of the high permitivity rock, the pulse form factor of the antenna radiation drops below 50%, and the structure will thus provide very poor resolution data due to the marked pulse expansion.

In the case of the antenna with no potting material, but with an air gap between the antenna structure and the PVC pipe, the following FEKO and ADS simulation results are extracted.

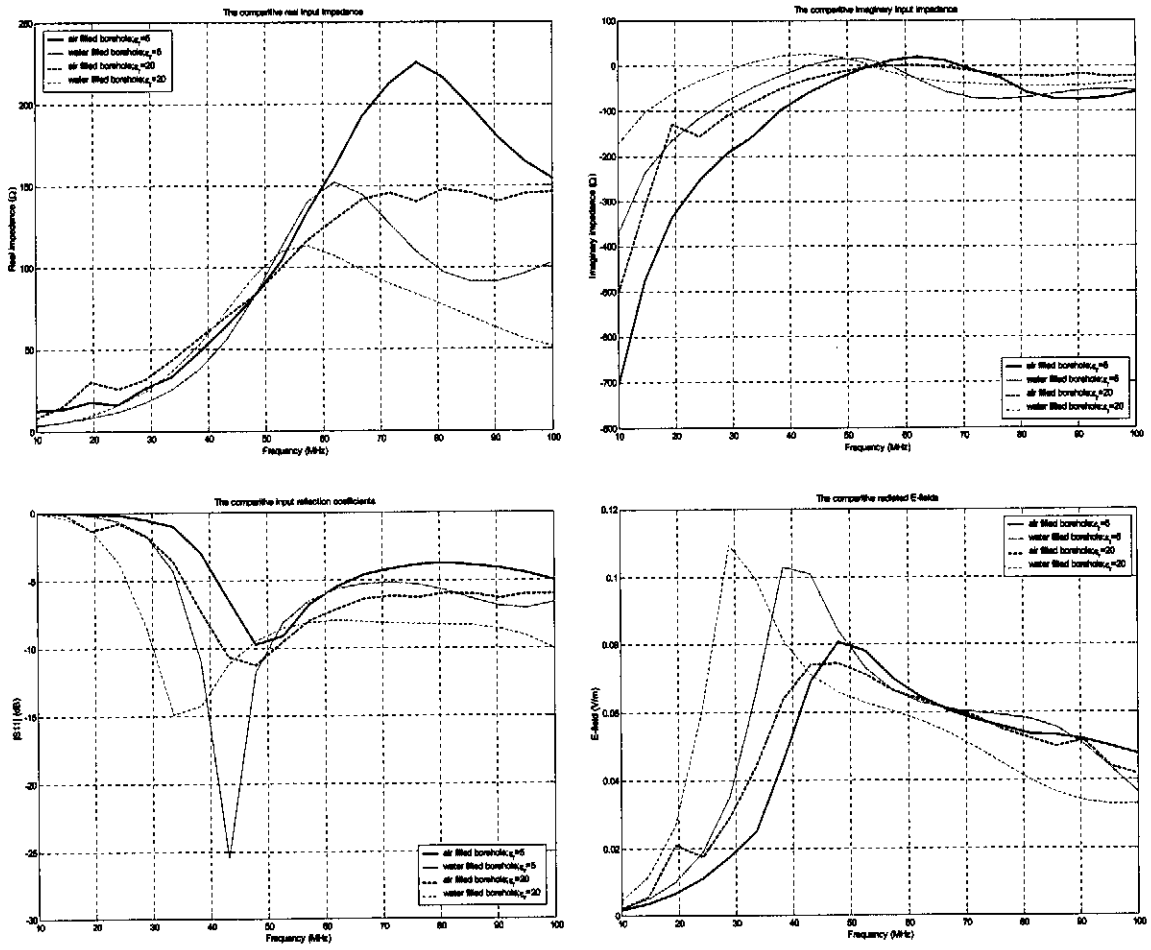

Figure 104 The FEKO simulated characteristics of a 1.2m arm length modified dipole structure with 600mm resistively loaded single strip sections

It is again clear that this structure is not ideal for mono-static application, particularly due to the high probability that the structure will exhibit resonant effects that will cause extreme deformation of the pulse form and spreading of the pulse energy. (This effect will be even more marked for the un-potted antenna than for the potted structure of Figure 101.)

The results of prototype testing, using the antenna with no potting material, but rather a single loaded strip section, with an air gap will be discussed in Chapter 6. The resonant effects of the prototype antenna can be seen in the acquired data.

Chapter 3 Receiver electronics

In this chapter, we will consider the receiver electronics for the mono-static BHR probe. We will begin by outlining the required characteristics of a BHR receiver. Next, we will in detail consider the operational characteristics of the critical components used in existing BHR receivers. The existing receiver chains will then be critically analysed. In the final section, a new receiver will be designed, implemented and tested.

3.1. Receiver requirements

In this section we will consider the basic requirements placed on the electronics for a BHR receiver. The characteristics of importance will be defined and discussed shortly from the perspective of a BHR application.

The purpose of the receiver chain of the mono-static BHR probe is to accurately amplify the pulse reflections received by the antenna structure, to a level that can be detected, digitised and stored for later analysis. The receiver must be able to perform this function for a great variation in signal levels, or pulse magnitudes. In order to determine how well a given circuit will perform these functions, there are a number of characteristics and factors that must be considered.

3.1.1. Receiver gain

Gain can be defined as a measure of the ratio of the output power to that of the input power of a component or system. Gain may be expressed in a number of forms; the most common of these is given in (3.1).

$$Gain = \frac{Power_{output}}{Power_{input}}$$
$$Gain(dB) = 10 \times \log\left(\frac{Power_{output}}{Power_{input}}\right) = Power_{output}(dB) - Power_{input}(dB) \quad (3.1)$$

Unless otherwise noted, log will refer to the base 10 logarithmic function

This definition may be expanded to include a number of cases. For the applications of this report, we will make the following definition for the peak-voltage pulse-gain of a system.

$$Gain_{peak-voltage}(dB) = 20 \times \log\left(\frac{\text{Peak signal voltage in output pulse}}{\text{Peak signal voltage in input pulse}}\right) \quad (3.2)$$

In order to compute the approximate amplifier gain that is required for accurate digitisation of the received signal in a given BHR operational environment, we must consider the noise component of the received signal. As the signal level drops , it approaches the noise floor, until after a given period of

time, the signal level is below the noise floor, and it cannot be detected. If we consider the case where a receiver is used in a medium of temperature T, the antenna noise figure is T_a, the receiver noise figure is N, and the signal is to be digitised by an n-bit converter, then the computation of the optimal amplifier gain is as follows.

We want the noise signal to toggle the last bit of the n-bit digitiser (if this is so, then the received signal can be 'lifted' out of the noise by stacking of the stored data). We thus want to amplify the noise, until it has a level of $\frac{V_{digitization}}{2^n}$ volt. The computation is as shown in (3.3).

$$N = kT_A B$$

$$gain_{required} = 20 \times \log\left(\frac{V_{digitization}}{2^n}\right) - 10 \times \log\left(NR_{rad}\right) - NF_{amplifier}$$

where $V_{digitization}$ is the voltage level of the most important bit

k is Boltzmann's constant (3.3)

B is the system bandwidth of interest

T_A is the noise temprature in Kelvin at the antenna feed

R_{rad} is the antenna radiation resistance

$NF_{amplifier}$ is the noise figure in dB of the amplifier chain

As an example of this computation for a typical system in a BHR environment we can take general values of the given parameters to calculate the optimal gain needed as shown in (3.4). We take the antenna efficiency as 40%, the ambient temperature as 310K, the antenna temperature as 300K, the noise figure of the receiver chain as 2dB and the digitisation voltage as 1V, with 8 or 12-bit digitisation.

$$N = kT_A B = \left(1.38 \times 10^{-23}\right)\left(0.4(310) + (1-0.4)(300)\right)\left(100 \times 10^6\right) = 419.5 fW$$

$$gain_{8-bit} = 20 \times \log\left(\frac{1}{2^8}\right) - 10 \times \log\left(419.5 \times 10^{-15} \times 10\right) - 2 = 63.6 dB \quad (3.4)$$

$$gain_{12-bit} = 20 \times \log\left(\frac{1}{2^{12}}\right) - 10 \times \log\left(419.5 \times 10^{-15} \times 10\right) - 2 = 39.5 dB$$

This computation gives a good idea of the maximum useful gain in an n-bit system. The advantage of using a larger number of digitisation bits is clear, as the total gain needed in the amplifier chain drops off with an increase in n, without a loss in data capturing capabilities.

3.1.2. Bandwidth

The bandwidth of a system is related to the frequency region over which the specified operational gain is applicable. Bandwidth is usually defined with respect to the point where the gain drops below a

certain level. The 3dB bandwidth of a system or component is thus the frequency range over which the gain is at least 3dB below the quoted or peak gain.

$$BW = f_{high}(\text{3dB below peak gain}) - f_{low}(\text{3dB below peak gain}) \quad (3.5)$$

For the BHR applications under consideration in this report, the approximate operational bandwidth of interest is between 10MHz and 100MHz. We would generally like the bandwidth of the receiver electronics to be marginally wider than this, so that the receiver characteristics can be flat over the operational bandwidth, and the pulse response of the electronics can be as good as possible, even for the pulsed spectral content outside of this band. The bandwidth must, however not be too large for noise-power limiting purposes.

3.1.3. Saturation and recovery

There are two main kinds of saturation, both of which have similar effects. The first form of saturation occurs when a component cannot drive the output beyond its voltage rails. In such a case the top and/or bottom of a signal will be clipped off. This form of saturation is generally referred to as clipping, and does not necessarily occur due to the power in the input signal, but rather to the magnitude of the signal. The effect of clipping is shown in the time domain and in the spectral domain for a typical pulse (assuming immediate recovery) in Figure 105.

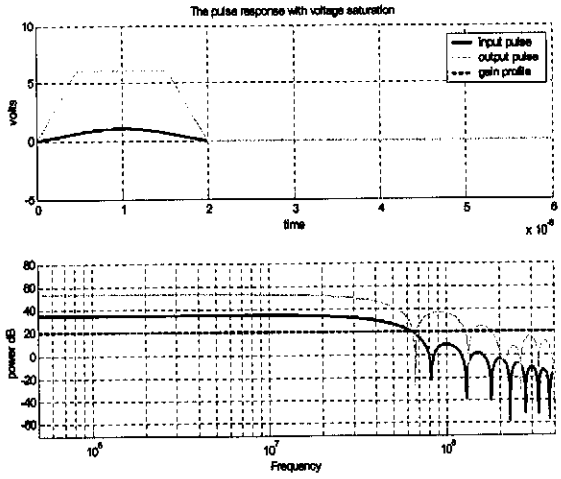

Figure 105 The effect of voltage clipping on a pulse form in the time and spectral domain

A second form of saturation occurs when a component cannot deliver the power required to maintain its expected gain if the input power to the component or system exceeds a certain level. In this case, the output signal is not necessarily clipped, but will indeed be deformed according to the maximum power delivery capabilities of the component. The 1dB compression point is defined as the point (generally in terms of the output power) at which the gain falls 1dB below the expected gain.

The general effects of both clipping and power saturation are that the gain drops, the output signal becomes deformed, and the percentage harmonic content of the output increases.

A certain amount of energy or capacitive charge retention occurs during saturation, and once the input signal level falls, this charge must dissipate before the system can return to normal operation. This dissipation time is generally referred to as the saturation recovery time of the system. Generally, this effect is more pronounced for clipping saturation than for power saturation.

3.1.4. Noise and the noise figure

There are two forms of noise that are of interest in general GPR and BHR applications. The first type of noise is noise that is received by the antenna itself, and the second type is noise that is generated by the active electronics. Received noise consists of thermal noise (as will be discussed in the following paragraph) and also radar 'clutter' noise, due to the environment in which the system is deployed. This form of noise is dependant on the type and texture of the propagation medium, the operational frequency band of the system and the polarization of the radiated EM waves. The amount of 'clutter' noise that can be expected in a given propagation medium can be determined by the volume clutter constant, based on measurement of the radar-cross-section clutter constant of the medium.

The BHR environment is relatively quite from an RF noise perspective, with only thermal or Nyquist noise (defined in (3.6); see [10] pp.550-551) making a considerable contribution.

$$\begin{aligned} \text{noise power}=N_{thermal} &= kTB \\ \text{rms noise voltage}=v_n &= \sqrt{4kTBR} \\ B = \text{system bandwidth, T=temperature in K, k=Boltzmans constant} & \end{aligned} \tag{3.6}$$

The gain of the antenna structure affects how must of this noise is fed into the system. The antenna structure itself also has an intrinsic noise figure. The received noise at the antenna feed point is dependant on the antenna gain, the environmental noise temperature, and the antenna noise temperature, cascaded as shown in (3.8).

The environmental and antenna thermal noise sources are external to the system operation, and are factors that cannot be controlled by design. We will now consider the internal noise characteristics of a general active BHR receiver system.

The noise figure of a system can be defined as the ratio of the input SNR to the output SNR. It is thus a measure of the reduction in signal to noise ratio as a signal passes through a system (see [10] p 555).

$$\text{Noise Figure=NF=}\frac{\left(\text{Signal power}/\text{Noise power}\right)_{input}}{\left(\text{Signal power}/\text{Noise power}\right)_{output}} \geq 1 \qquad (3.7)$$

By keeping the noise figure of the receiver chain as low as possible, the additive output noise is reduced, thus improving the output signal to noise ratio, and the sensitivity/dynamic range of the system. The noise figure of a cascade of components is computed as shown in (3.8) ([10] p558).

$$NF_{cascade} = NF_1 + \frac{NF_2 - 1}{G_1} + \frac{NF_3 - 1}{G_1 G_2} + \ldots \qquad (3.8)$$

Where NF_1 and G_1 are the noise figure and gain of the first stage in the cascade, and the following stages are numbered in ascending order. From (3.8), it is clear that the noise figure of the chain is very dependant on NF_1 for any considerable value of G_1. For this reason the front-end component of the chain must be chosen as a low noise component to keep the chain noise figure as low as possible, and improve the receiver dynamic range.

3.1.5. Dynamic range

The dynamic range of the receiver is critical to the operation of the BHR system. Dynamic range can be defined as in (3.9), and as depicted in Figure 106 ([10] p549). In the BHR environment, the ambient environmental noise floor is due mainly to the operating environmental temperature. In order to maintain an acceptable output SNR, the noise figure of the receiver electronics must be limited.

$$DR = 10 \times \log\left(\frac{\text{Amplifier compression power}_{\text{output}}}{\text{Noise floor}}\right) \qquad (3.9)$$

From this definition it is clear that for a BHR application we want a large dynamic range to cater for a large variation in signal levels with respect to the noise floor power.

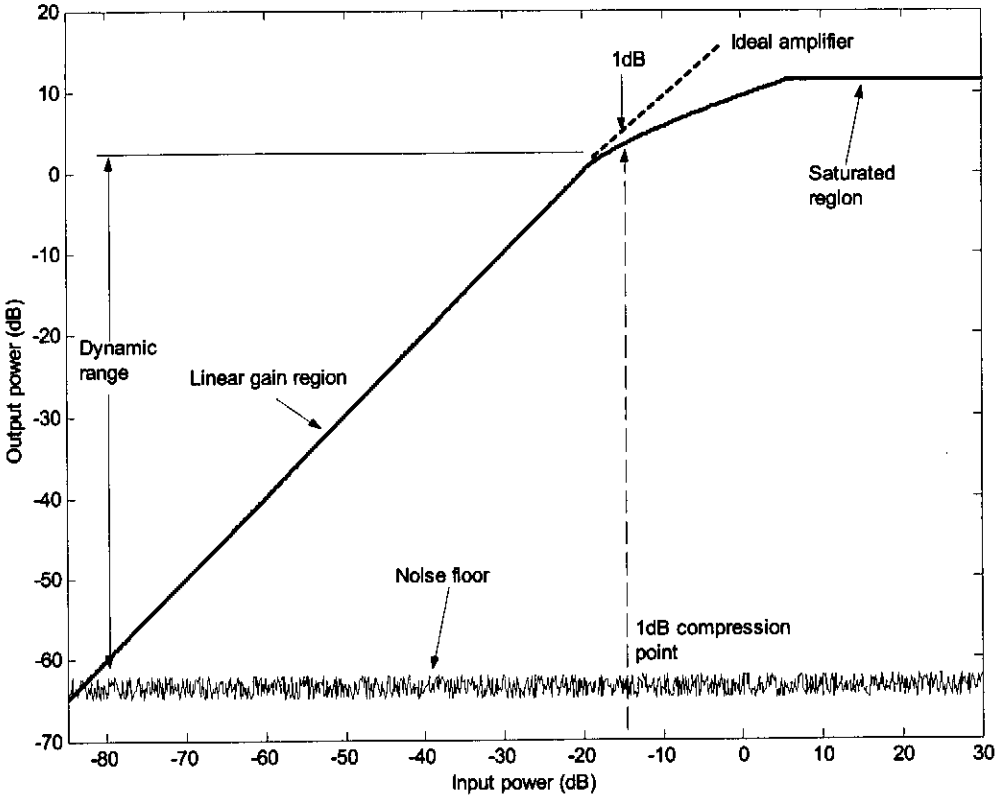

Figure 106 The definition of the dynamic range, saturation and 1dB compression point of an amplifier

3.1.6. Pulse response and recovery time

The BHR system is a pulsed radar system, and the operation of the electronics for pulsed inputs is more important than the standard power-related definitions used to define the operation of most systems. We can divide the pulse transfer effects or response of a system into two categories. The first category includes the amplitude and pulse form effects, and the second the relative timing of the output response to an input pulse.

The ideal pulse shape and spectral content for a BHR system were discussed in the previous chapter. The variation in the system characteristics over the whole frequency range of the pulse spectral content affect the pulse response of the system.

In section 3.1.1, equation (3.2), we postulated a definition of the peak-voltage pulse-gain of a system. This value is not necessarily the same as the power gain of the system as defined in (3.1). If the spectral content of the pulse falls within the linear gain bandwidth of the system, then the output pulse magnitude will be a scaled version of the input pulse. (This is only true if the input pulse is not large enough to drive the system into saturation or clipping). Any variation in the gain of the system at a frequency where the input pulse contains considerable spectral content will cause a deformation in the pulse shape. In order to demonstrate these effects, we will compute the effects of various systems on

an ideal pulse form. If we assume an ideal system, with infinite bandwidth, and a pulse gain of 20dB, then the time-domain pulse response of the system will be as depicted in Figure 107.

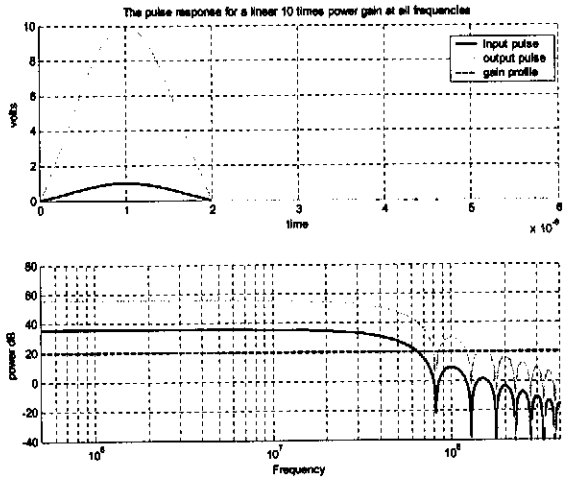

Figure 107 The pulse response of an ideal, infinite bandwidth amplifier with no saturation

If, however we assume a finite bandwidth system, in the frequency range of interest (while maintaining linear phase), the pulse response is as shown in Figure 108. The LF cut-off of the finite bandwidth system causes a shift in the average value of the pulse, as the DC component is damped. The HF cut-off causes a rounding of the pulse edges.

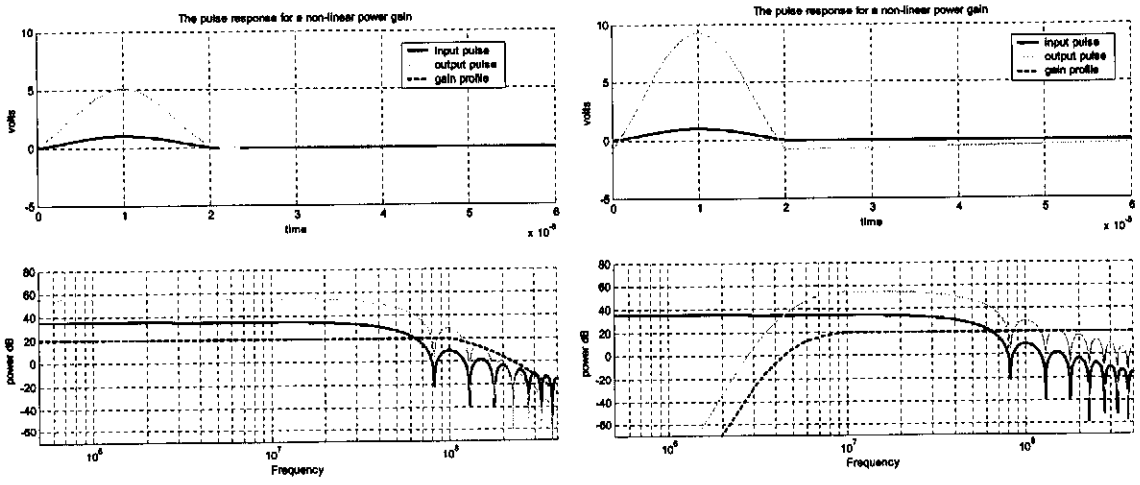

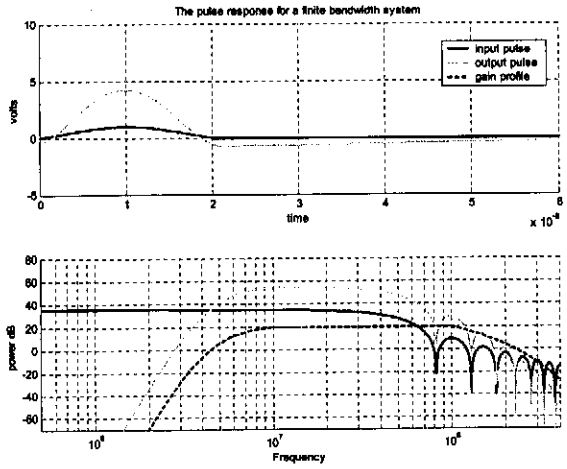

Figure 108 The ideal pulse response of various finite bandwidth, linear phase amplifiers

In order to determine the factors that affect the timing of the pulse response of a system, we must not only consider the magnitude of the spectral transfer function, but also its phase. In order to do this, we must introduce a non-zero phase response as was assumed in the plots of Figure 108. The effect of non-linearity in the phase response of the amplifier system is depicted in Figure 109. A linear phase change over all frequency merely causes a time shift in the pulse, but when any non-linearity is introduced, a change in the form of the pulse occurs. This is due to the non-linear phase and group delay characteristics of the component. Phase and group delay are generally defined for a system as shown in (2.10).

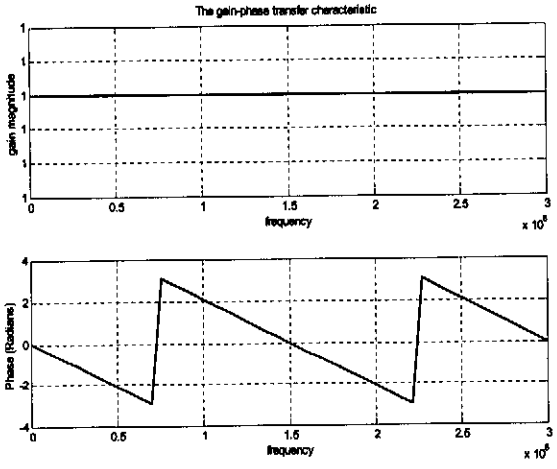

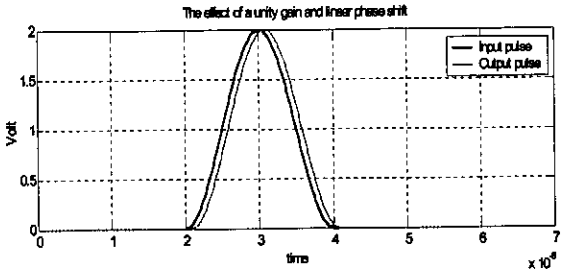

A unity gain, linear phase transfer function

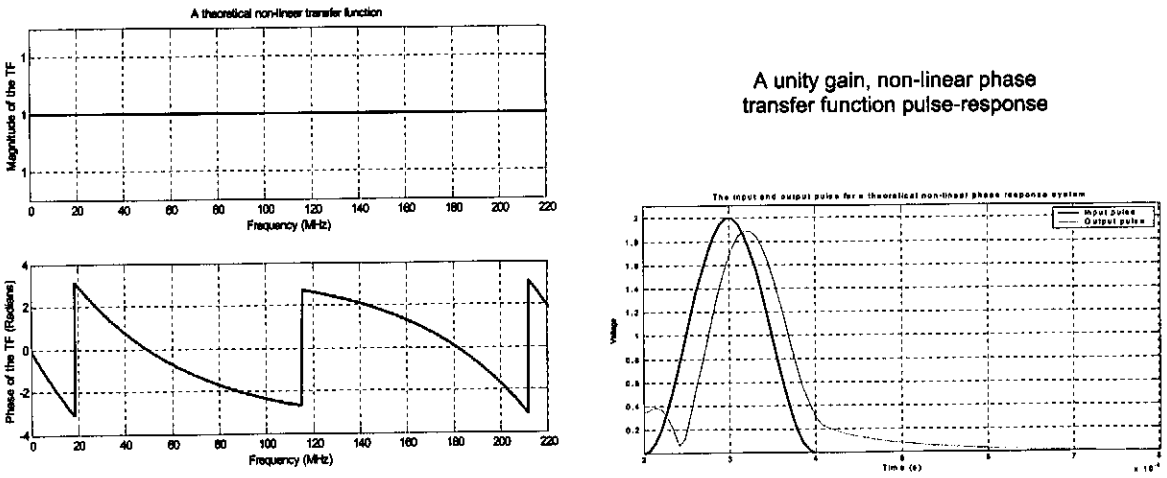

Figure 109 The effect of a non-zero linear phase change in the transfer function of a system, and the effect of any non-linearity's in the phase of the system of a pulse form

It is clear form these theoretical considerations that we require a linear phase response, constant gain system, over the whole frequency range of interest.

3.1.7. Spatial and environmental considerations

During the development of the electronics for a BHR receiver the spatial limitations must be carefully considered. The electronics must be fully housed inside a cylindrical conductive pipe section, which forms part of the radiating structure of the probe. The length of the electronics must also be such that it can be easily housed along with any other components in the interior of the pipe structure. The total space for electronics, and the approximate space allowable for the receiver is shown in Figure 110.

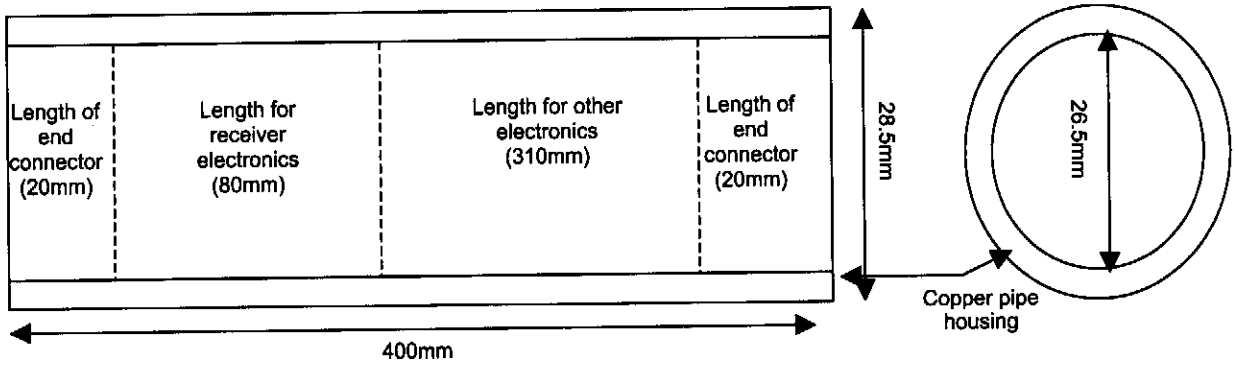

Figure 110 The space available inside the electronics housing structure

3.2. Measurement methods to determine the relevant characteristics of a component or system of interest

In this section we will consider the measurement methods used to practically determine the characteristics of interest of a component or device, with a view to determining its relative suitability for

application in a BHR receiver. Most characteristics can be extracted from measurements in either the time or frequency domain. As far as possible, we will shortly consider both methods.

3.2.1. Transfer function measurements

The measurement of the spectral transfer function of a system or component is one way of determining the component characteristics, including its gain, bandwidth, gain compression power and phase response. The general method used to determine the frequency domain transfer function is by using a calibrated network analyser (NA) to measure the S-parameters of the component, from which the transfer function can be extracted.

Measurement of the transfer function in the time domain is also possible, by determining the relative output (magnitude and phase) of the component for discrete excitation at a number of frequency points.

The gain and bandwidth of a system can easily be determined by considering the amplitude of the forward transfer function (S21) in dB.

When the input power of the measurement is increased to such a level that the measured component gain over the bandwidth of interest drops off by 1dB, the output power will then be the 1dB compression point.

We can compute the phase and group delay of a component by considering the phase of the transfer function. Phase and group delay are defined in (2.10), and give a good idea of the pulse deformation characteristics of a system. For an ideal system, both the phase and group delay would be flat over the band, and equal to zero. For a practical system, with a good pulse response, however, we require that both the phase delay and group delay be small and relatively flat over the band of interest.

3.2.2. Noise figure measurements

Noise figure measurement of a component is done using a calibrated noise figure meter at various frequency point in the range of interest. The measurement employs the 'Y-factor' noise measurement method [10], [24], as shown in Figure 111. The 'Y-factor' method employs the measured output power of the device under test (DUT) for two known noise sources in a shielded, low noise environment. If the effective noise temperatures of the two known noise sources are T_1 and T_2 respectively, and the noise temperature of the DUT is T_e, then the power measured in each case will be as given by (3.10), where G is the DUT gain, B is the bandwidth of the system and k is Boltzman's constant.

$$\begin{aligned} P_1 &= GkT_1B + GkT_eB \\ P_2 &= GkT_2B + GkT_eB \end{aligned} \tag{3.10}$$

From these two measurements we can then determine Y, and extract the noise temperature of the DUT as shown in (3.11).

$$Y = \frac{P_1}{P_2} = \frac{T_1 + T_e}{T_2 + T_e}$$
$$\therefore Te = \frac{T_1 - YT_2}{Y - 1} \qquad (3.11)$$
$$and$$
$$NF = 1 + \frac{T_e}{T_o}$$

The measurement is made using a noise figure meter that executes the algorithm of Figure 111. The meter is calibrated based on a comparison of the ENR table of a known noise source, and the measured output power of the noise source at different frequencies of interest in the measurement set-up, with the DUT removed. More detail about the noise figure measurement procedure and the operation of a noise figure meter may be found in the literature [24].

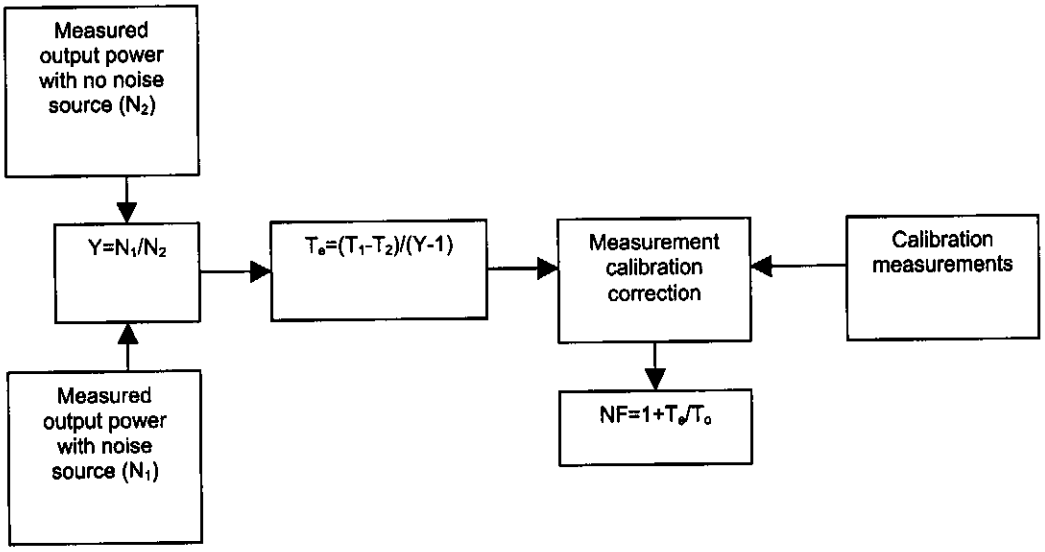

Figure 111 A flow chart of the noise figure measurement procedure

3.2.3. Reflection coefficient measurements

The reflection coefficient measured at the input or output of a component is an indication of the percentage power transfer that occurs at the interface of interest. The reflection coefficient is generally measured in the frequency domain using a calibrated NA. The reflection coefficient in a 50Ω system can be directly extracted from the S11 or S22 measurements of the NA. This reflection coefficient can then be used to determine the reflection coefficient in any other impedance system. Alternatively, by

transforming the reflection information into the impedance domain, the input/output impedance of the component can be computed directly. The reflection coefficient definition and Z-parameter conversion procedure are shown in (3.12) (see [10] p.66).

$$\Gamma = \frac{Z_{in} - Z_0}{Z_{in} + Z_0} = S_{nn} = \frac{V_{reflected}}{V_{incedent}}$$
$$\rightarrow Z_{in} = Z_0\left(\frac{1+\Gamma}{1-\Gamma}\right) \qquad (3.12)$$

3.2.4. Measurement of the spectral content of a signal

The spectral content of a signal can be directly measured using a spectrum analyser (SA). There are a number of factors that will influence the accuracy of this direct measurement. These include the IF bandwidth, the video bandwidth, the input impedance (must be matched to 50Ω), the sweep time, etc. Detail around the factors influencing SA measurements may be found in the literature [25].

Alternatively, by taking the Fourier transform of a time-domain measured signal, the spectral content over a given frequency range can be determined. This bandwidth of this technique is however limited by the sample rate of the digitisation of the measured pulse before the Fourier transform is performed, as described by the Nyquist condition of general sampling theory [20].

3.2.5. Pulse response

The pulse response of a component is critically important for BHR application, and a number of factors are of importance to determine the adequacy of a component for application in a BHR system.

The main factors of the spectral characteristics of a component that will influence the pulse response are the bandwidth and the phase response of the transfer function. Both of these characteristics can be determined in by spectral measurement, using a calibrated NA, and considering the S21 transfer function of the component. The bandwidth and phase- and group-delay can then be extracted according to their definition as given in section 2.3.2.4.

In the time domain, the pulse response can be measured directly by comparing the time domain input and output pulses of a pulsed system, on the same time base. Care must be taken to consider the loading effects of measurements that may affect the circuit operation.

3.2.6. Saturation and recovery times

Spectral domain measurement of the S21 characteristic of a system using a calibrated NA for various input power levels can be used to determine the general gain saturation characteristics of a component.

No differentiation between power saturation and clipping saturation can be made directly, using this method.

The response to a time-domain pulse that drives the component into saturation can be considered, in order to determine the time-saturation recovery characteristics of the component, again by direct comparison of the input and output pulses of the component on the same time base. The type of saturation (clipping or power) can be determined by directly considering the output pulse form.

3.3. Analysis of the operation of the existing receiver chains

3.3.1. The ST-probe receiver chain

In section 1.3.4 a basic description of the ST-type receiver probe was given. We will perform a critical analysis of the ST-probe receiver electronics based on measurements using the techniques and definitions outlined in the previous sections.

The input reflection coefficient (|S11|) and transfer function (S21) of the full un-saturated electronics chain was measured in a 50Ω system as shown in Figure 112. The system is well matched to 50Ω input impedance, with a slightly capacitive imaginary component (due mainly to the input coupling capacitor). The noise figure of the chain is measured as 2dB over the frequency range of interest. The mean gain over the band 10MHz to 100MHz is 46.503dB, with a peak gain of 46.951dB at 12MHz, and a minimum gain of 46.056dB at 91MHz (0.447dB variation over the band). The lower 3dB cut-off of the receiver electronics is measured as 3MHz and the gain climbs to 50dB at 380MHz before dropping off. The 1dB compression point is measured as 11.795dBm, also shown in Figure 112. This compression measurement was made by varying the input power to the chain, for 50MHz excitation, with a variable attenuator (1dB steps).

The phase response of the chain is relatively linear over the frequency band of interest, with only a slight non-linear response at frequencies below 25MHz, and we thus expect a good pulse-form response, with a short response delay, and some LF ringing. The group and phase delay, as defined in section 2.3.2.4 are computed for the receiver chain as shown in Figure 112.

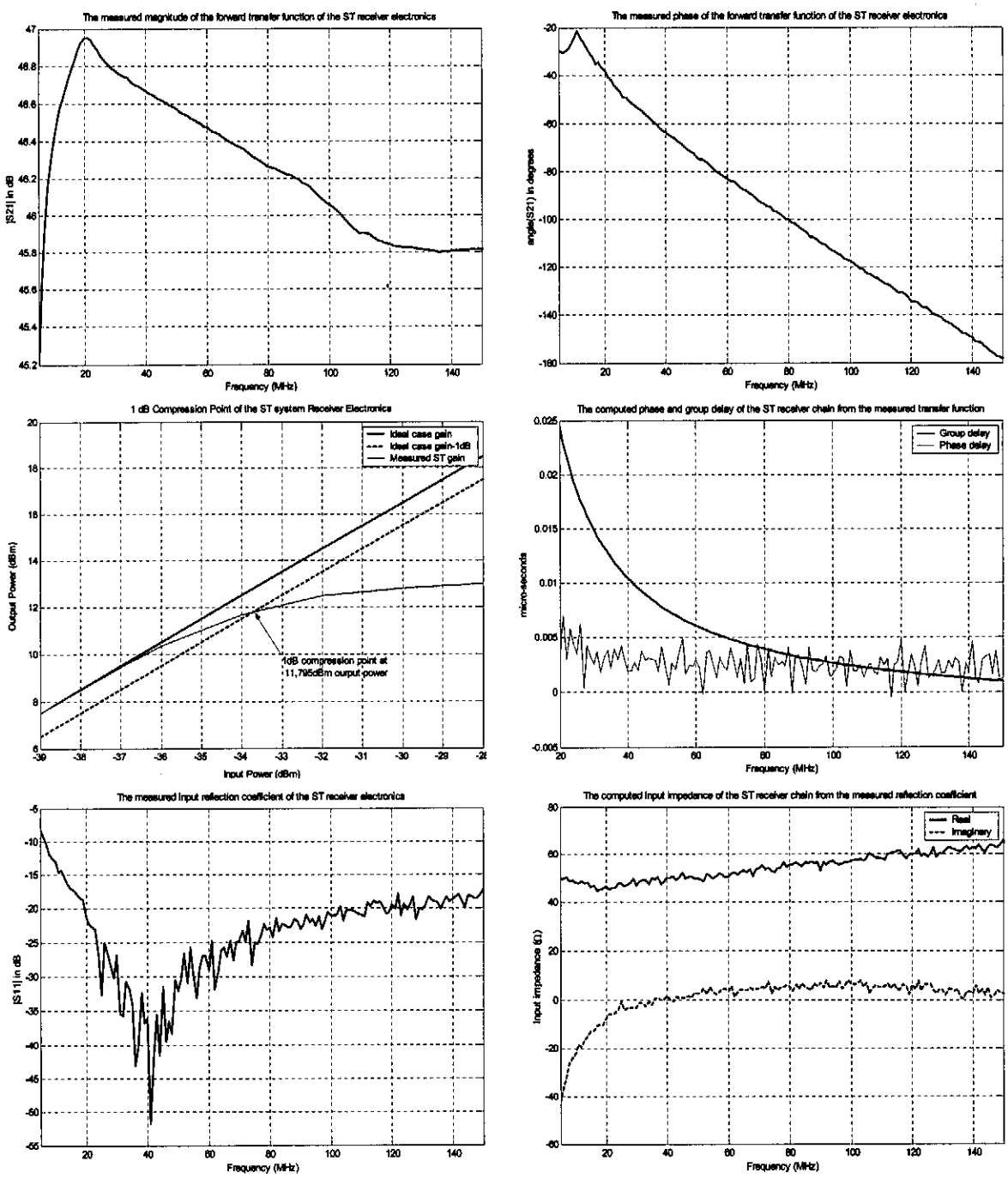

* The transfer functions shown here are extracted from data measured by P. Herselman[7]

Figure 112 The measured forward transfer function, input reflection coefficient, input impedance and 1dB compression point of the ST receiver electronics

Time domain analysis of the chain response was performed using the measurement set-up of Figure 113. The results are shown in Figure 113 and Figure 114. It is clear that the receiver chain does have a good pulse response for the shown excitation, and the short response delay predicted by the computed phase delay is measured as approximately 3nS. The LF response delay is evident in the slow settling

time after the pulse. The effect of the LF cut-off can be seen in the time domain pulse form, and the computed gain. For larger magnitude pulse inputs, the saturation and recovery of the chain takes the form of a slow RC pulse recovery, and a dead time in the case of heavy saturation. The saturation effects are particularly evident in the spectral representation of Figure 114. The chain begins to show clipping saturation at an output voltage level of 800mV (input peak voltage of 3.1mV). It is immediately obvious that this clipping characteristic of the ST receiver chain will render it inappropriate for mono-static application.

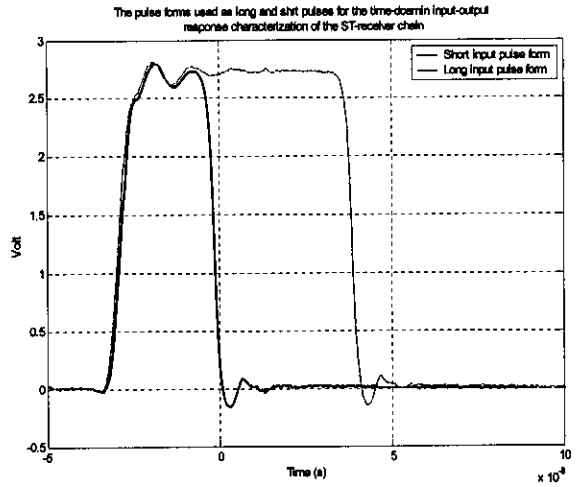

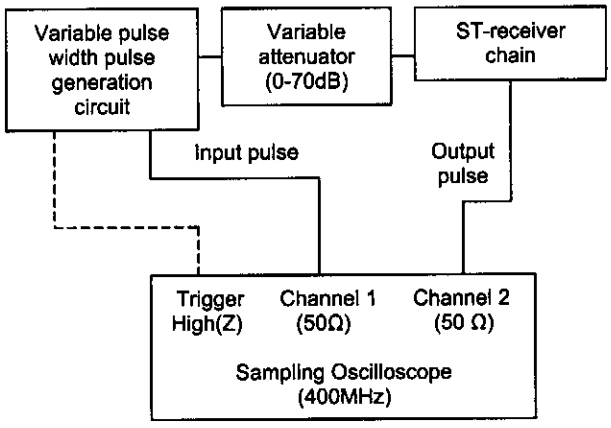

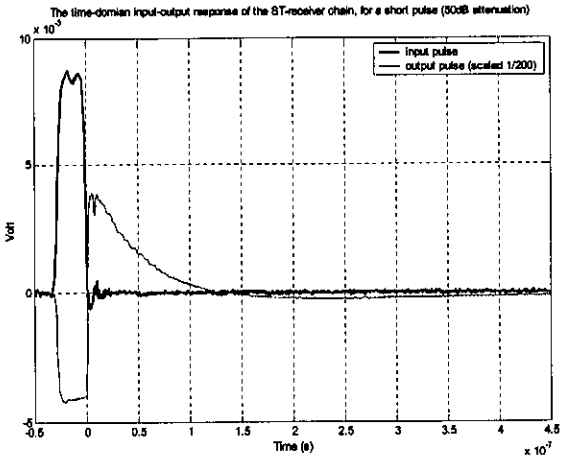

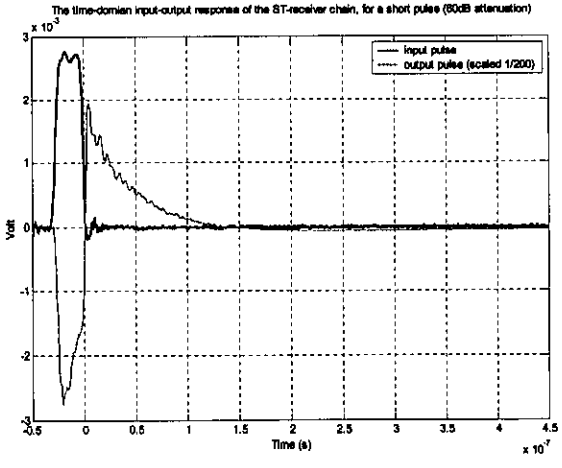

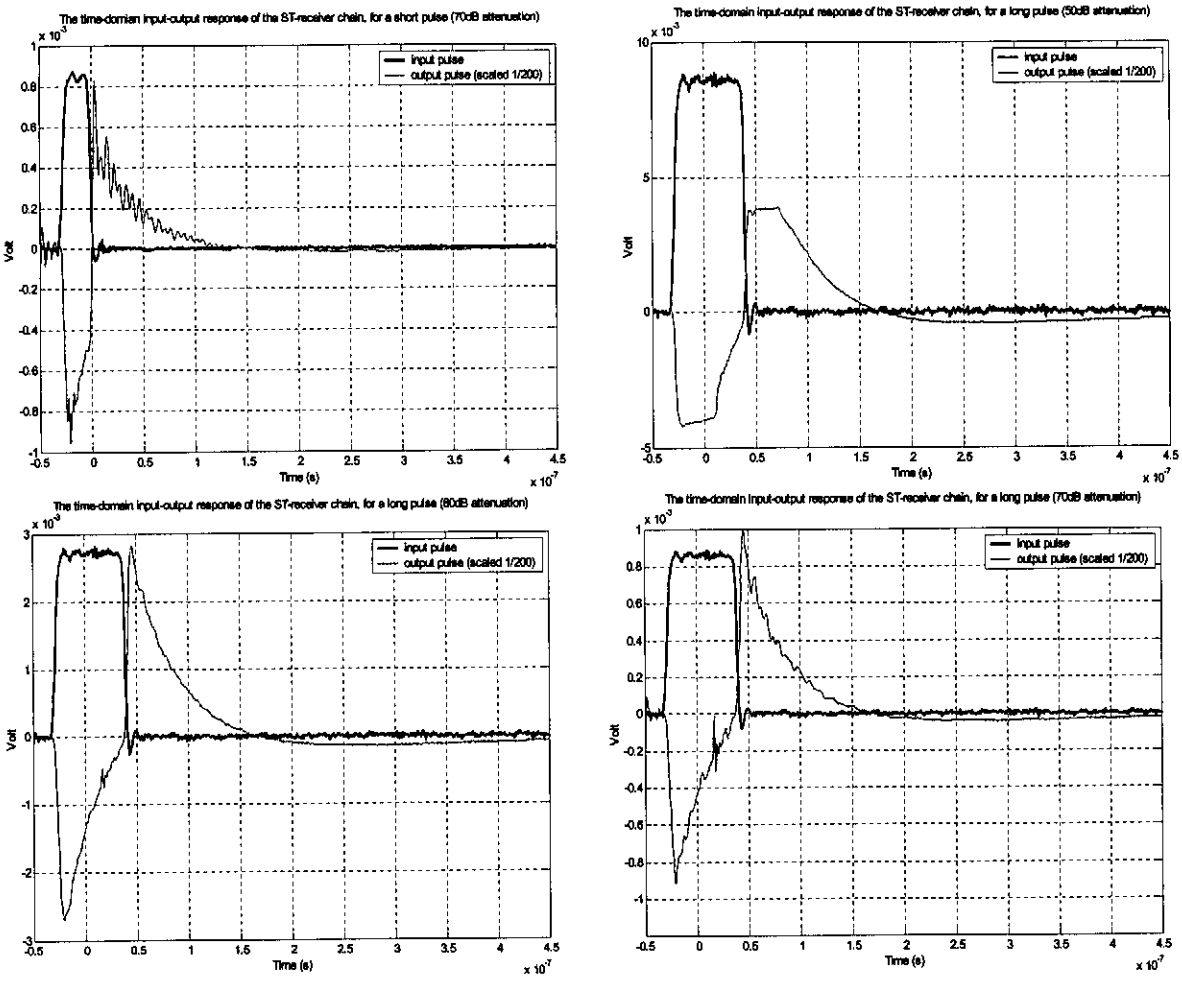

Figure 113 The time-domain measurement set-up and measured input-output pulse response of the ST-receiver electronics measured for a long and a short input pulse

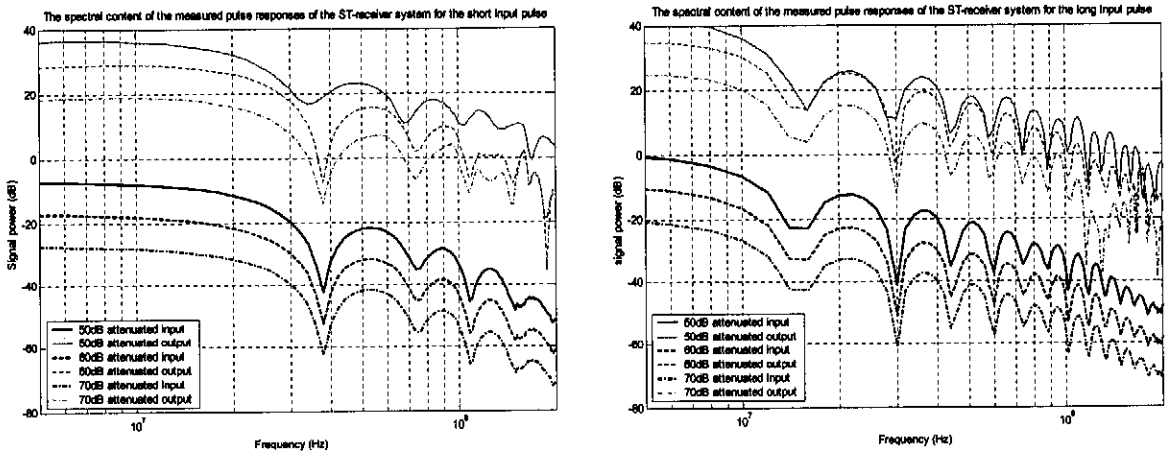

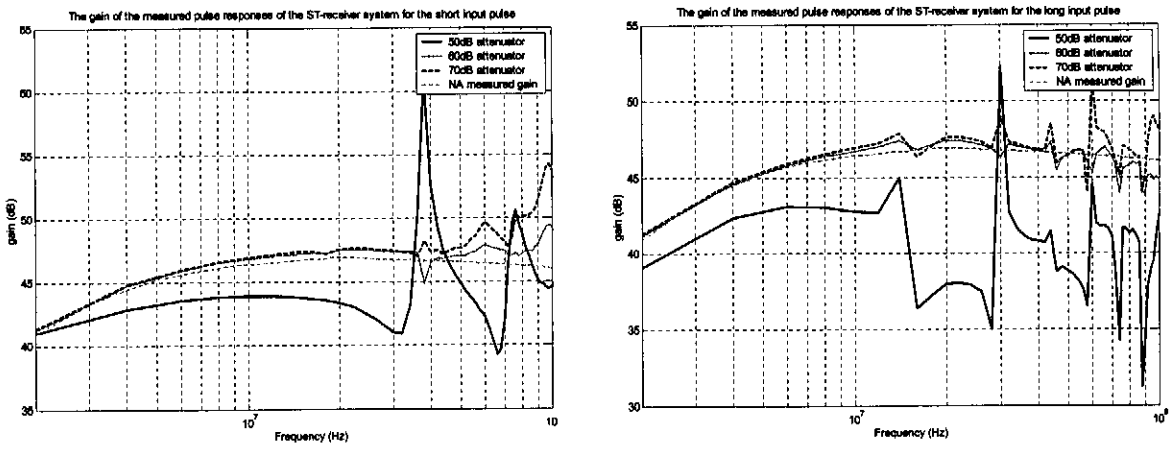

Figure 114 The spectral content of the time domain measured pulse responses and gain of the ST system receiver for a short and long excitation pulse (see Figure 113)

This receiver chain operates well, except for the large LF artefacts that are observed after the pulse edges. The clipping-saturation point is low, and recovery to large pulses is slow.

3.3.2. The Marius van Wyk receiver chain

The receiver design suggested by Marius Van Wyk in his thesis [6] introduces a few different possibilities for the receiver electronics. In this section, we will discuss and critically analyse this design based on measurements and practical observation.

The major operational difference between the ST-receiver chain and the Van Wyk chain is that the Van Wyk chain employs a high impedance buffer as the first stage in the chain (voltage probe), while the ST-chain is designed as a 50Ω power amplifier. The basic topology of the receiver chain is shown in Figure 115.

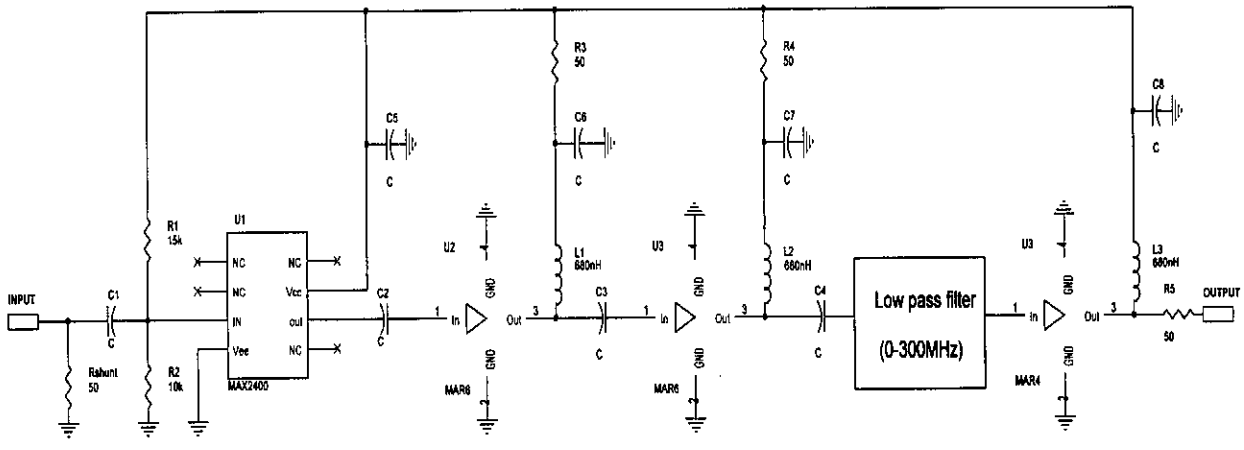

Figure 115 The topology of the M Van Wyk receiver chain

The input reflection coefficient (|S11|) and transfer function (S21) of the full un-saturated electronics chain was measured in a 50Ω system as shown in Figure 116. The system is a high input impedance receiver, and a 50Ω shunt-impedance was included at the input to match the receiver to the 50Ω measurement system. The 50Ω shunt resistor input topology introduces a ~6dB loss in the first stage of the chain. This, coupled with the noise figure of the MAR amplifiers gives the receiver chain a very poor noise figure, measured as 12dB over the band of interest. (The shunt input resistance is also the reason for the excellent observed |S11| characteristic). The mean gain over the band 10MHz to 100MHz is 44.75dB, with a peak gain of 45.17dB at 149MHz, and a minimum gain of 40.59dB at 10MHz (4.58dB variation over the band. This is mainly due to the sharp cut-off at lower frequencies - the gain is still 44.19dB at 20MHz, which is a 0.83dB variation). The lower 3dB cut-off of the receiver electronics is measured as 10.43MHz and upper cut-off point is above 300MHz. The 1dB compression point is measured as 16.25dBm.

The phase response of the chain is relatively linear over the frequency band of interest, with only a slight non-linear response at frequencies below 25MHz, and we thus expect a good pulse-form response. The group and phase delay, as defined in section 3.2.1 are computed for the receiver chain as shown in Figure 116.

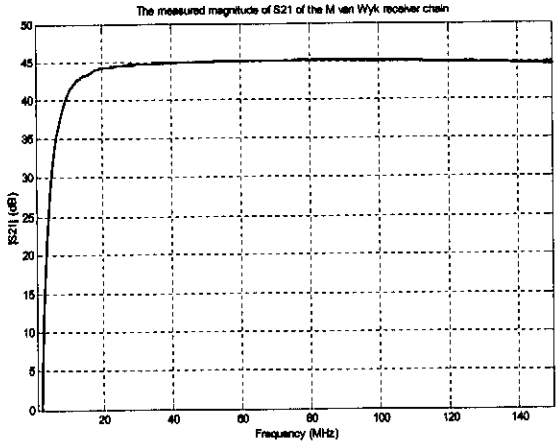

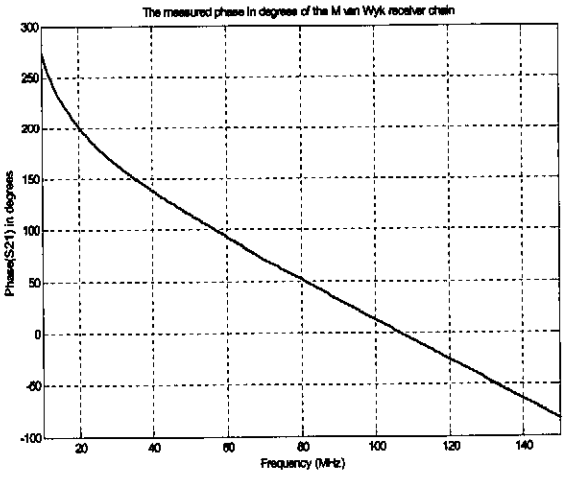

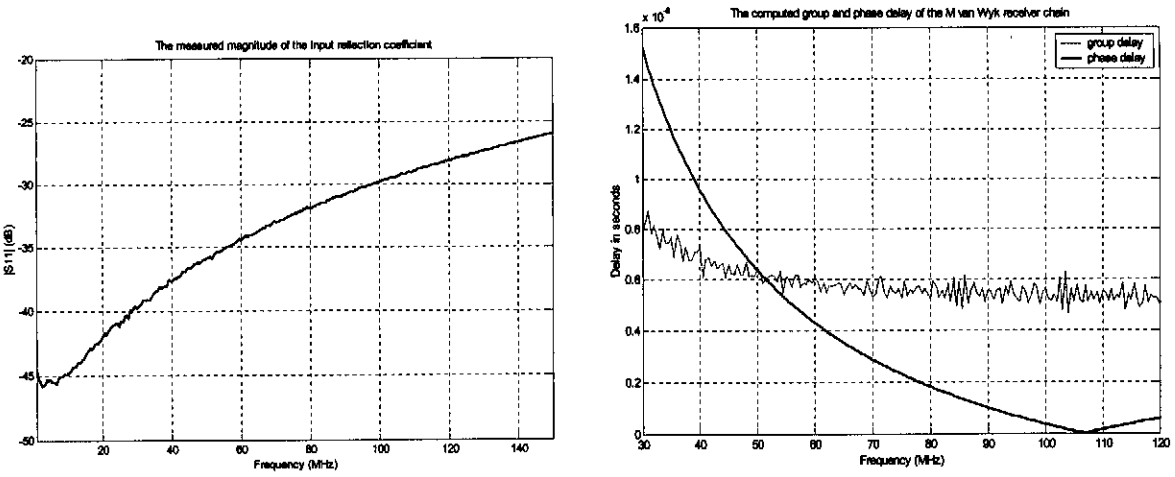

Figure 116 The measured forward transfer function, input reflection coefficient, phase and group delay of the M Van Wyk receiver chain

Time domain measurement of the pulse response of the Van Wyk chain is shown in Figure 117, with the spectral representation of these measurements in Figure 118.

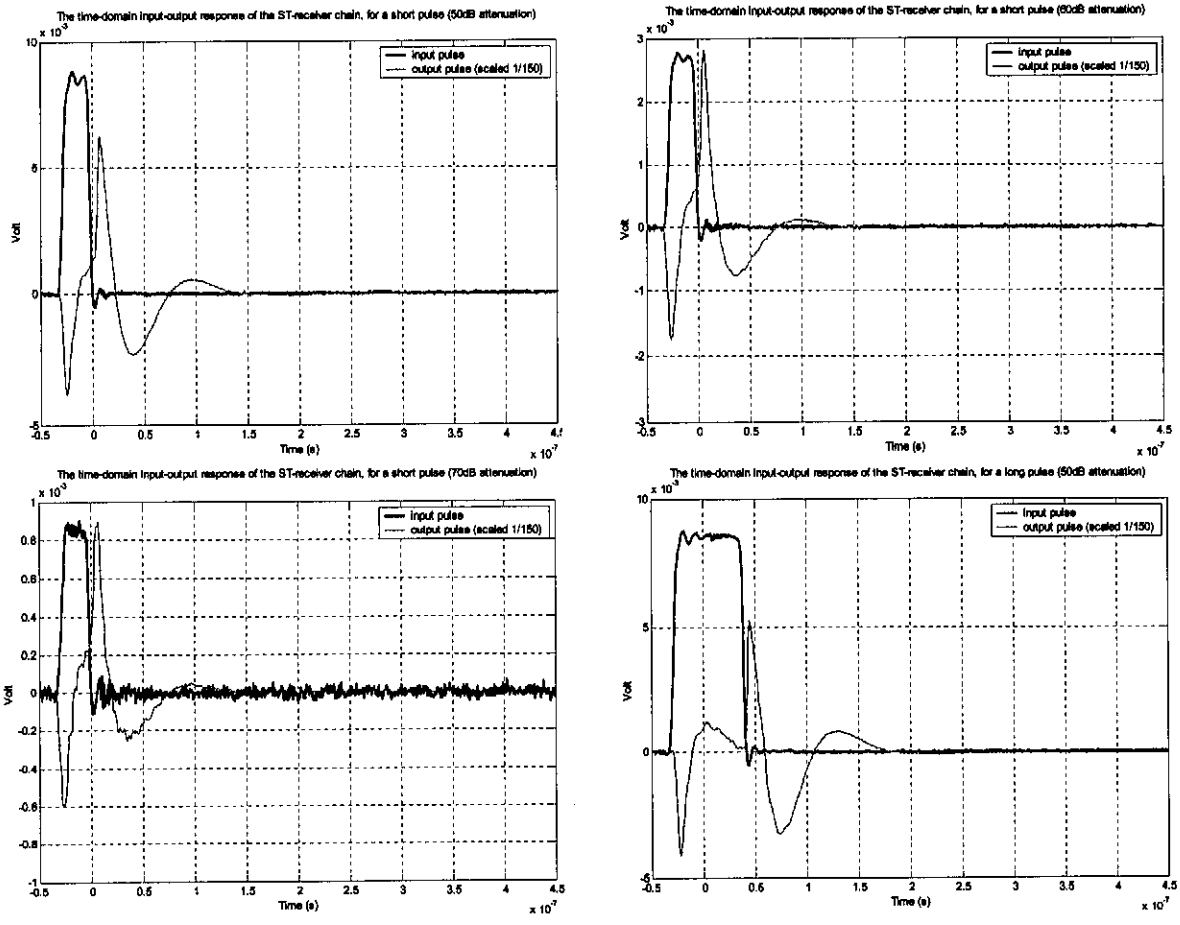

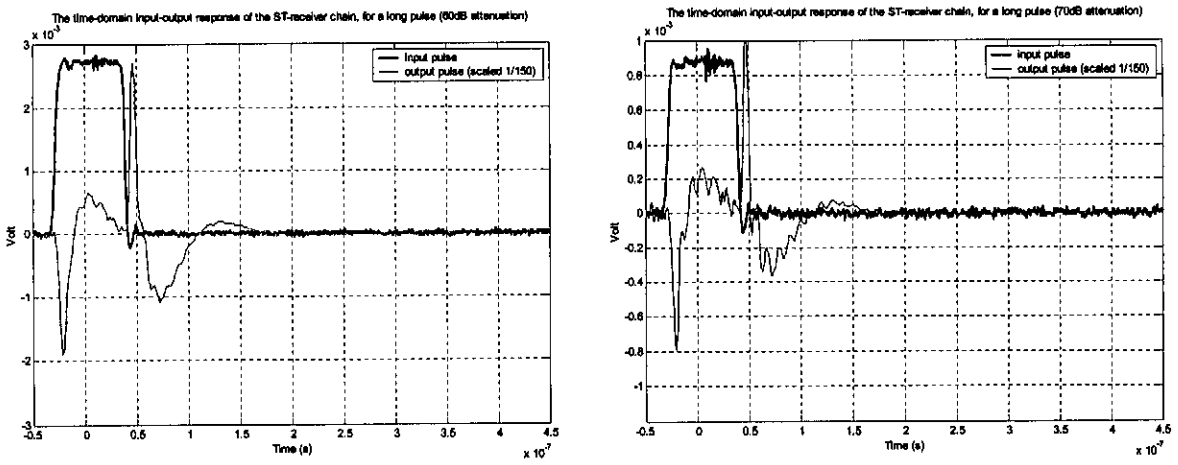

Figure 117 The time-domain measured input-output pulse response of the receiver electronics designed by Marius Van Wyk, measured for a long and a short input pulse

The sharper low frequency cut-off in the response of the system, when compared to that of the ST-system receiver is immediately obvious in both the time and frequency domain representations of the pulse response measurements. The LF increase in the phase delay is clear in the 'ringing' after the pulse form. The clipping-saturation point of the chain is a lot higher than that of the ST-system, and the saturation recovery characteristic is better, despite the observed recovery overshoot.

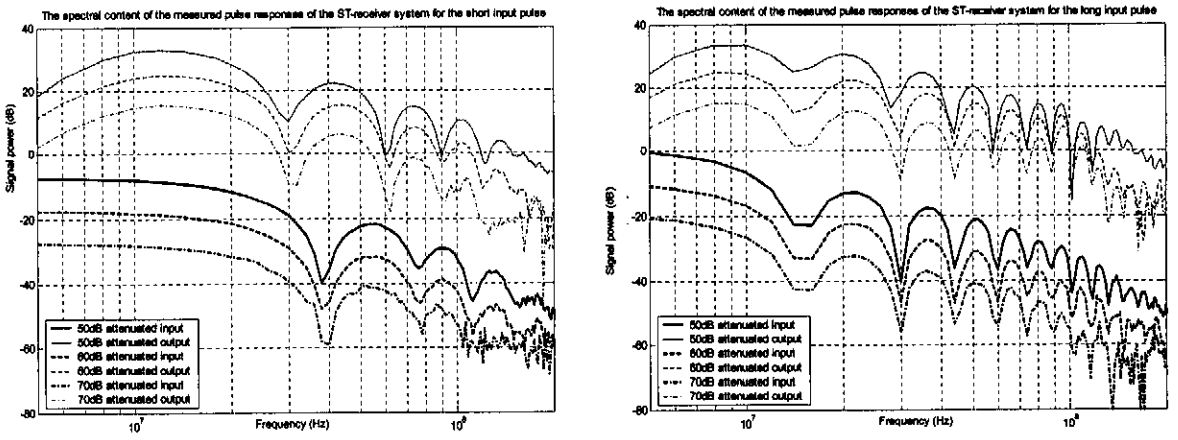

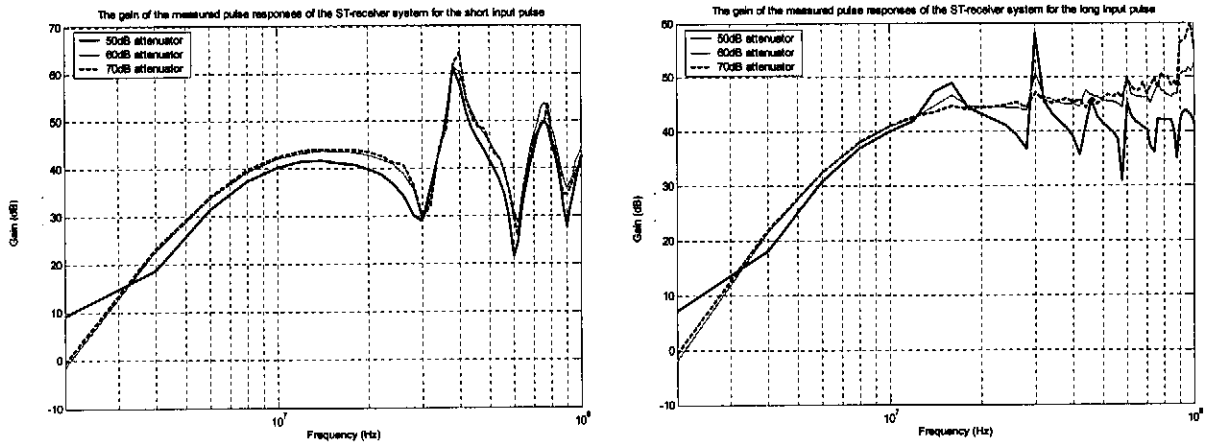

Figure 118 The spectral content and gain of the time-domain measured pulse response of the receiver designed by Marius Van Wyk (see Figure 117)

3.3.3. Summary

Although the pulse response, and saturation characteristics of the Van Wyk chain are generally better than those of the ST-receiver chain, the noise characteristic of the Van Wyk chain is very poor. The bandwidth of both systems is good, with a flat response over the band of interest, although the ST-receiver does cut off slowly on the LF side. This slow cut-off seems to affect the pulse response of the system, introducing a substantial LF recovery component. The effective gain of both chains is similar, but according to the computations of (3.4), about 15dB below the optimal gain required for an 8-bit digitisation system. The ST-receiver is well suited for operation in a 50Ω-matched system. The Van Wyk receiver's high impedance input stage, however makes it a poor choice for a 50Ω feed, as will be the typical case in a mono-static system (see Chapter 4).

3.4. Design, simulation and testing of a receiver chain

We will outline the design of a basic receiver chain that is acceptable for application in a mono-static system. Results presented in the previous section suggest that although the receiver chains considered adhere to all the requirements placed on a general BHR receiver circuit, the saturation and clipping characteristics will render them unacceptable for co-located, mono-static implementation. This issue will receive specific attention in section 3.4.3, where methods of improving the operation of the basic chain designed in 3.4.1 will be considered and implemented. In the final part of this section, we will consider issues related to the integration of the mono-static receiver chain with the other subsystems of a mono-static system, defined in section 1.5.

3.4.1. Design of the basic receiver chain

In section 3.1, we stated that the purpose of the receiver electronics is to accurately amplify the received signal to a level that can be digitised. In order to design a receiver chain that can do this, we

need to consider both the gain, as discussed in section 3.1, the additive noise figure of the electronics, the pulse response for a given input pulse, and particularly for the mono-static application, the saturation and recovery characteristics of the chain.

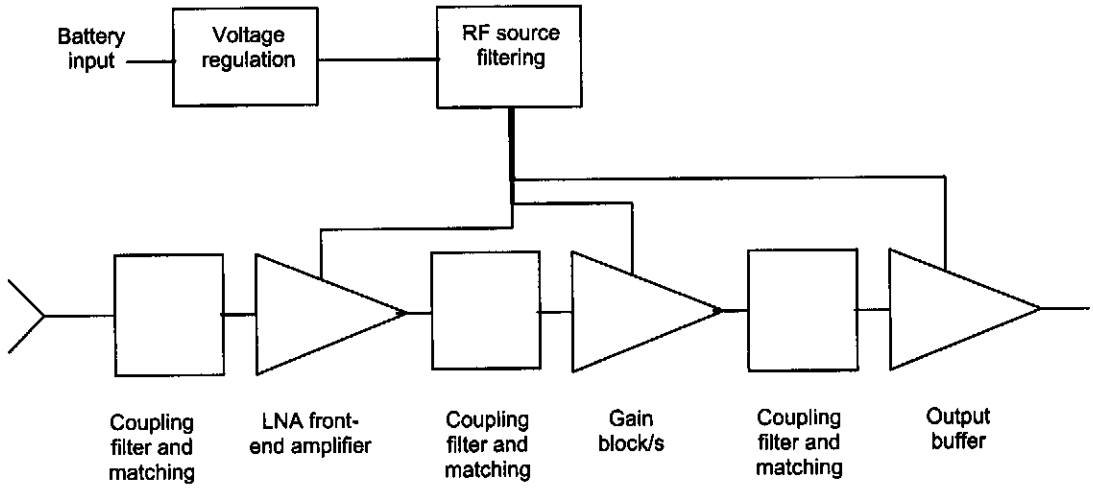

Figure 119 A functional schematic of the basic receiver chain

A functional schematic of a basic amplifier chain is given in Figure 119. We will consider each of these blocks separately.

3.4.1.1. The LNA front end

As discussed in 3.1.2, the front-end component plays a critical role in the determination of the intrinsic noise characteristics of the receiver chain. The first stage amplifier must have a very low noise figure, with a medium to high gain. The effect of the saturation characteristics of the LNA on the chain is also very important. Based on consideration of a few available components, the Amplifonix TN7111 was chosen. This component was chosen above a similar higher gain LNA (the TN7101) to improve the input peak voltage handling capability of the chain.

The TN7111 amplifier is an integrated hybrid amplifier, designed to be used in a 50Ω system, with a quoted noise figure of 1.4dB and a nominal gain of 12.5dB (see Figure 120). The TN7111 was characterized using the circuit shown in Figure 121. The S-parameters (magnitude and phase), measured on a calibrated network analyser for the TN7111 are shown in Figure 122. The LF filter effect of the coupling capacitors used on the operation of the stage is obvious if the S-parameters for 100nF and for 470pF coupling are considered.

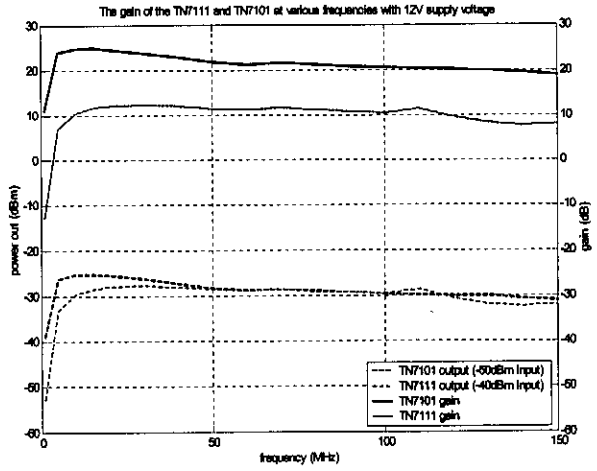

Figure 120 The comparative SA measured gain of the two components considered for LNA front-end application (TN7111 and TN7101)

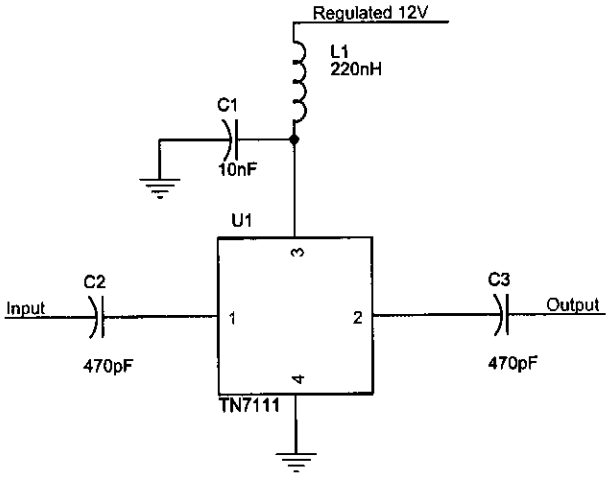

Figure 121 The circuit used to characterize the LN7111 LNA amplifier front-end component

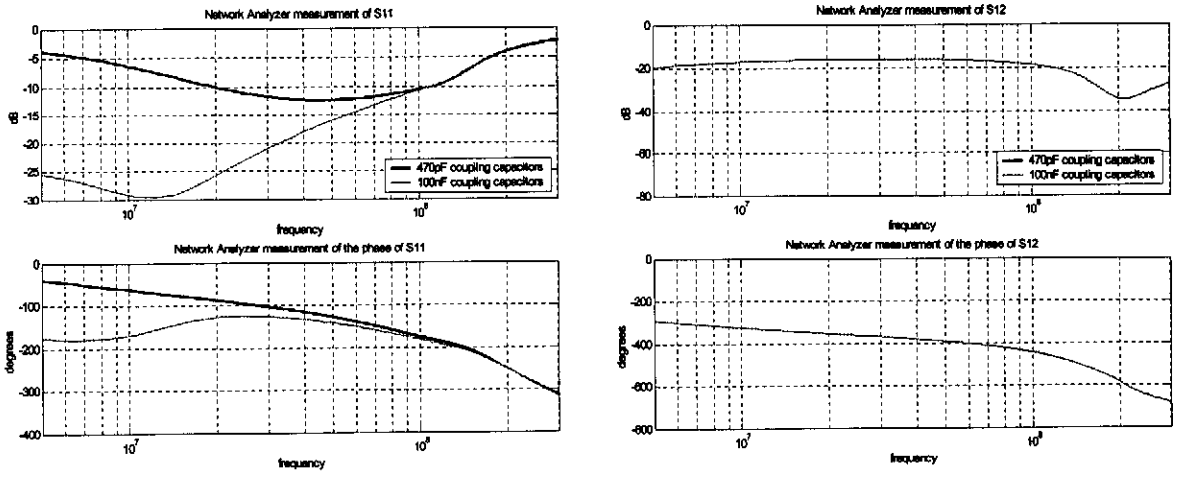

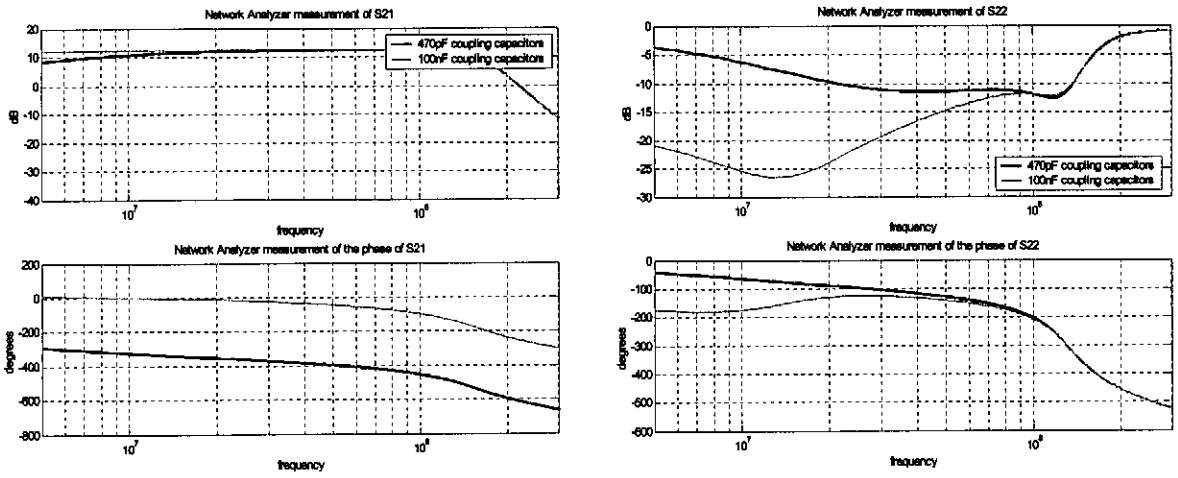

Figure 122 The measured S-parameters of the TN7111 LNA component

Time domain measurement of the pulse, recovery and saturation characteristics of the amplifier for a few input pulses was done using the set-up shown in Figure 123.

The results with component values chosen as shown in the circuit diagram of Figure 121 for a few input pulses are shown in Figure 124. The peak pulse gains, as defined by (3.2) are also shown.

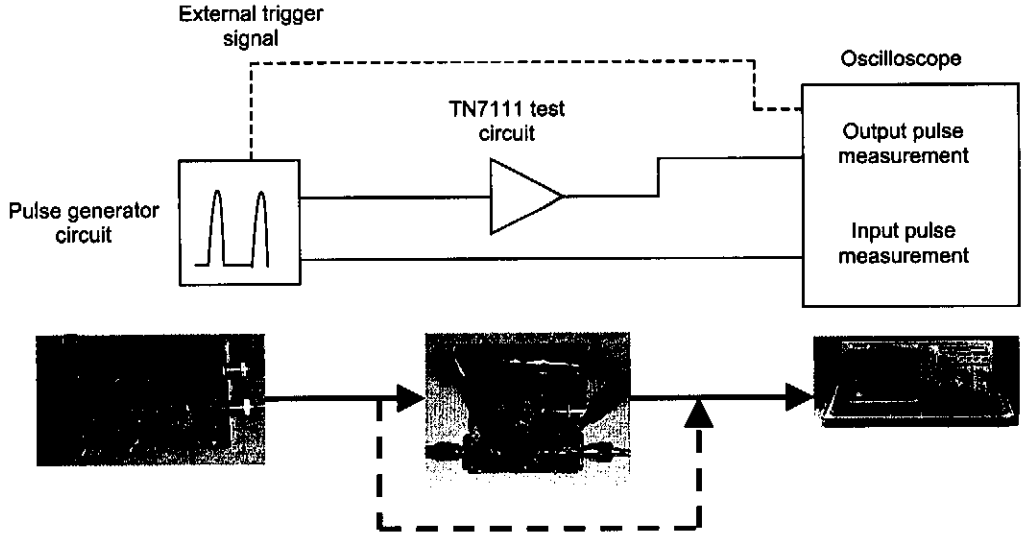

Figure 123 The measurement set-up for pulse response characterization of the TN7111 LNA front-end component

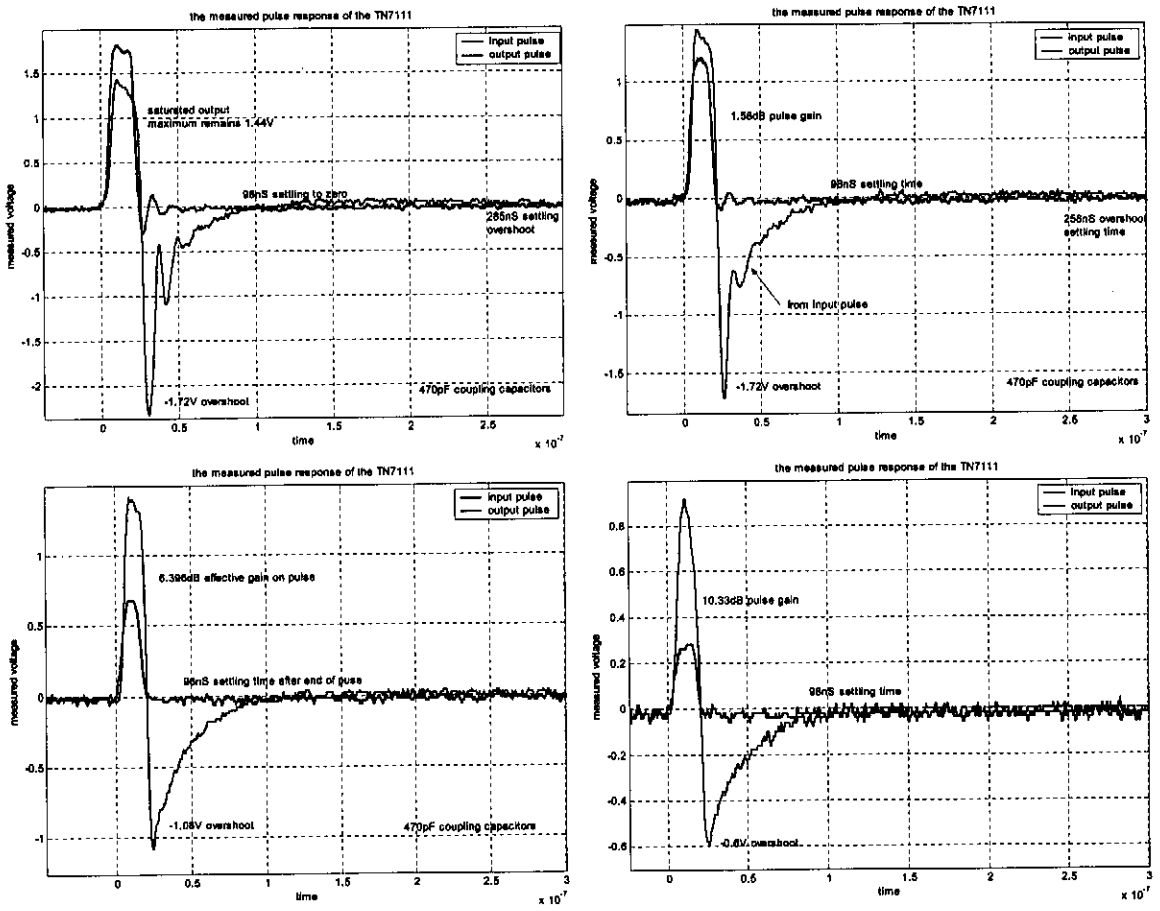

Figure 124 A few measurements of the pulse response of the TN7111 with 470pF coupling capacitors

From the measurements of Figure 124, we can note a number of things. The amplifier performs extremely well in accurately reconstructing the pulse form at the output. This is expected, due to the very linear phase in the frequency range of interest as shown in the S12 measurement of Figure 122. The delay over the frequency range of interest is calculated as shown in Figure 125.

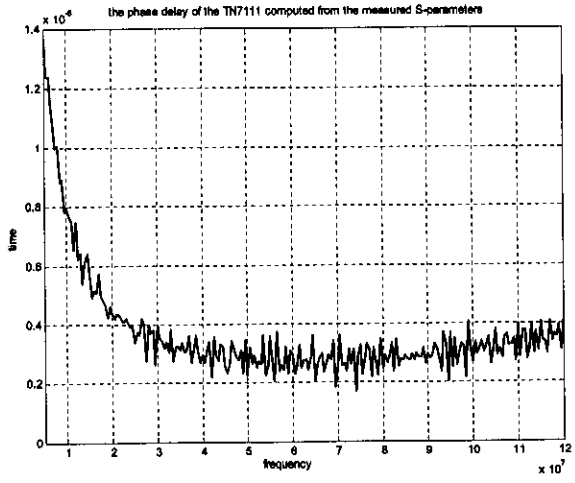

Figure 125 The group delay of the TN7111 computed from the measured S-parameters

The group delay of the amplifier is clearly very good above 40MHz, but the delay measured below 40MHz increases steeply. The cause of this characteristic can be attributed to the small coupling capacitors (470pF) used in the measurement. Similar measurements were made using 100nF coupling capacitors. The pulse response measurement results are shown in Figure 126, and the S-parameters and computed phase delay is plotted in Figure 122 and Figure 127 respectively.

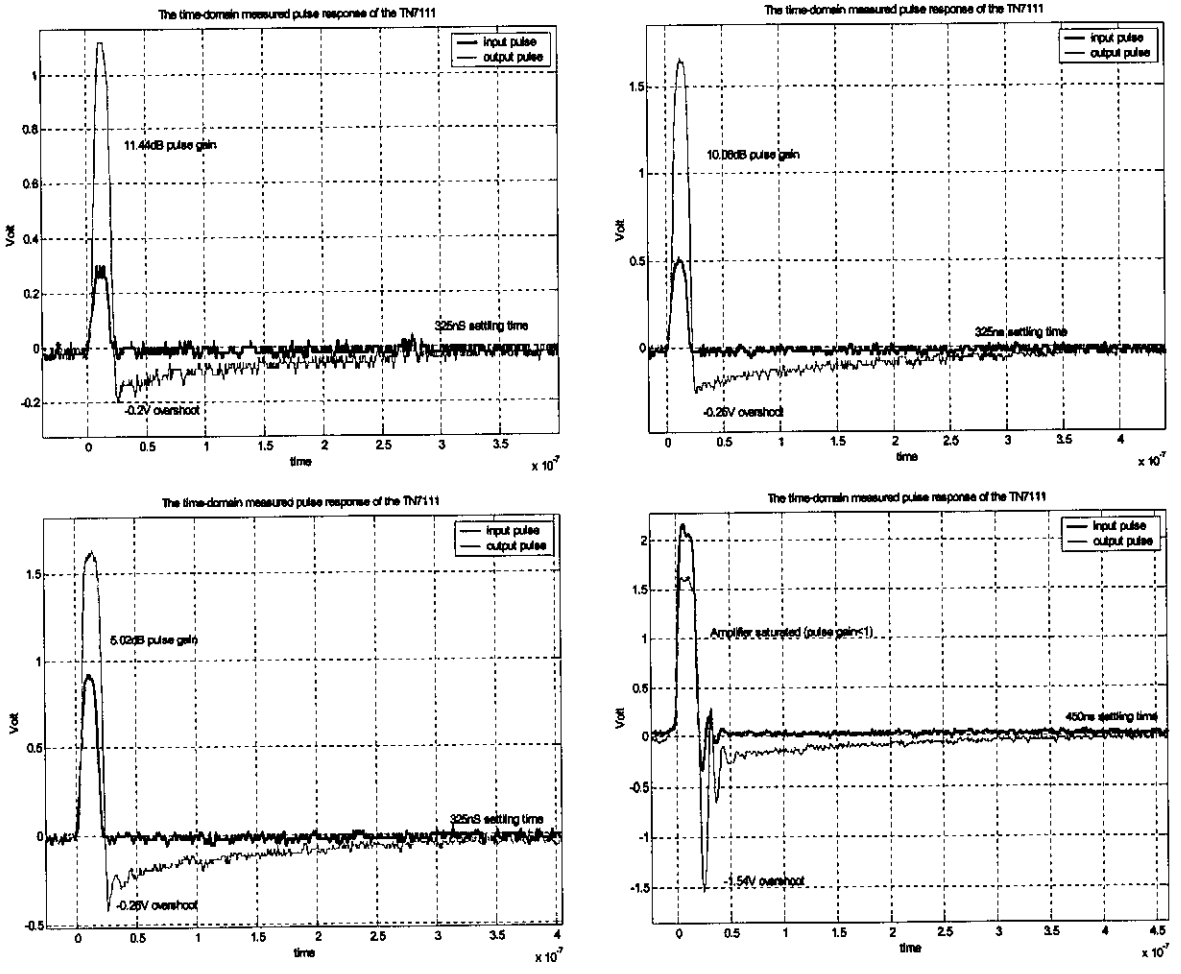

Figure 126 The time-domain measured pulse response of the TN7111 with 100nF coupling capacitors

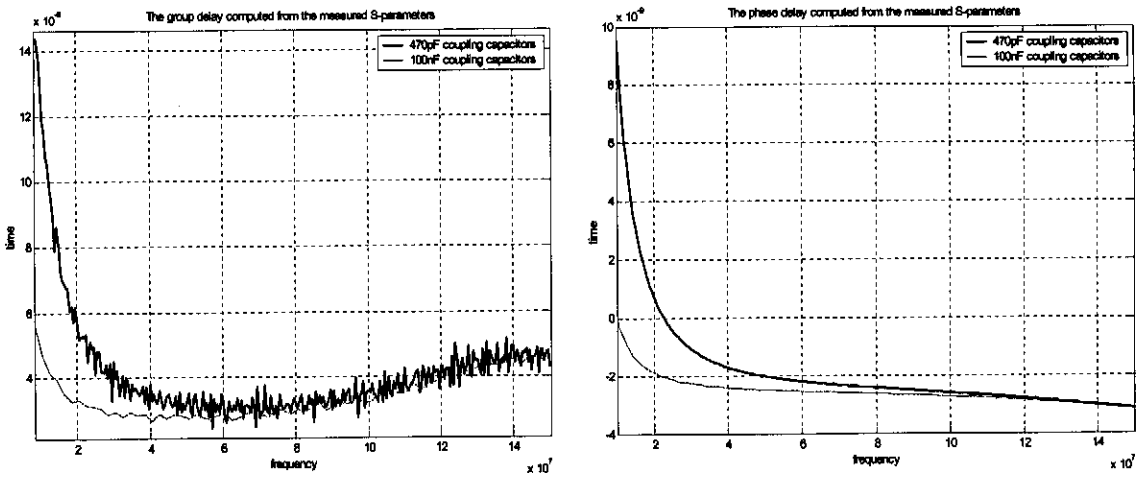

Figure 127 The comparative delay with 470pF coupling capacitors and 100nF coupling capacitors

The improvement in the low frequency response of the system is clear. The exponential recovery time is dependant on the coupling capacitors only (approximately 98nS for a 470pF coupling, and 325nS for a 100nF coupling). The low frequency delay for the 100nF coupling is a lot less than for the 470pF coupling, thus the better pulse form. Measurements made with a 100nF capacitor at the TN7111 input, and a 470pF capacitor at the output show a setting time of around 140nS.

The output voltage clipping point of the amplifier is measured at around 1,5V, but the component maintains a good recovery response (less than 30ns overshoot recovery time) for peak input voltages up to approximately 2V. This is very good, and suggests that the Amplifonix stage in the ST-system is not responsible for the low chain output clipping voltage measured in Figure 113.

The noise factor of the TN7111 over the band of interest was measured as below 1.6dB. This agrees with the values quoted by the manufacturer. The power gain compression of the TN7111 was measured as shown in Figure 128. The 1dB compression point is at 18.33dBm.

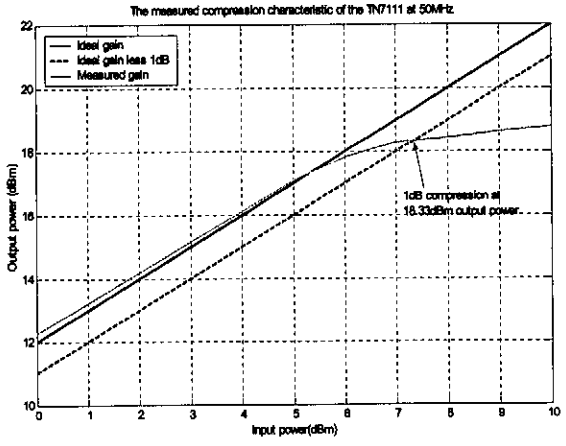

Figure 128 The measured compression characteristics of the TN7111

The measured characteristics of the TN7111 LNA stage are summarized in Table 8.

Property	Measured value
Bandwidth	8-105MHz
Gain	12dB
Noise figure	1.6dB
1dB power compression point	18.33dBm (output)
Peak output voltage clipping point	1.51V
Maximum group delay	7nS@10MHz

Table 8 The measured characteristics of the Amplifonix TN7111 hybrid low noise amplifier

3.4.1.2. The gain block

The Mini-circuits hybrid MAR-6 amplifier block, and the TN7101 LNA block were considered for application as amplifier gain blocks in the mono-static BHR chain. The application of both components is fairly simple, and requires only a simple bias network. The application circuit for the MAR-6 is shown in Figure 129, and for the TN7101 in Figure 130.

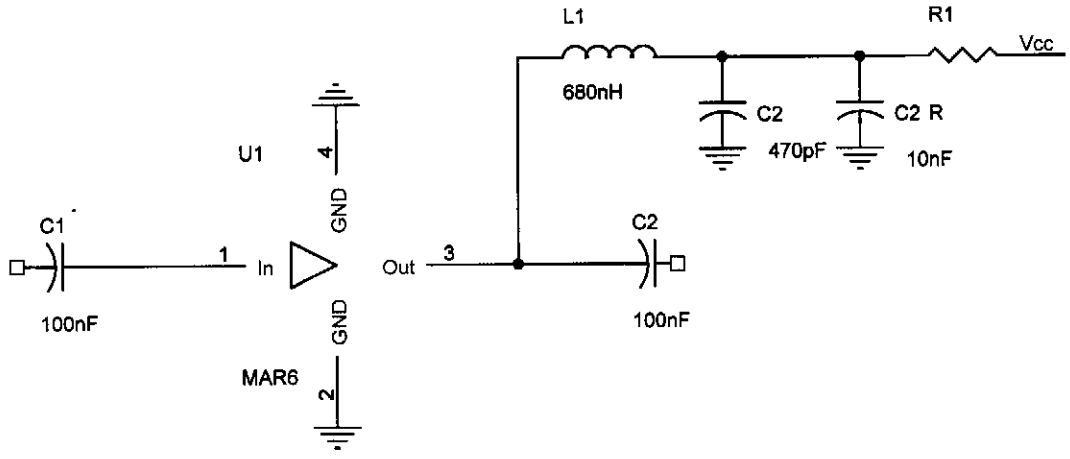

Figure 129 The application circuit of the Mini-circuits MAR-6 gain block

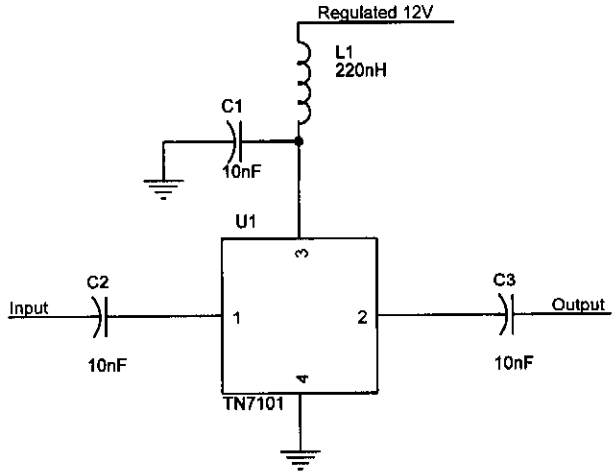

Figure 130 The application circuit of the TN7101 LNA gain block

The comparative S-parameter measurements for the two components are shown in Figure 131.

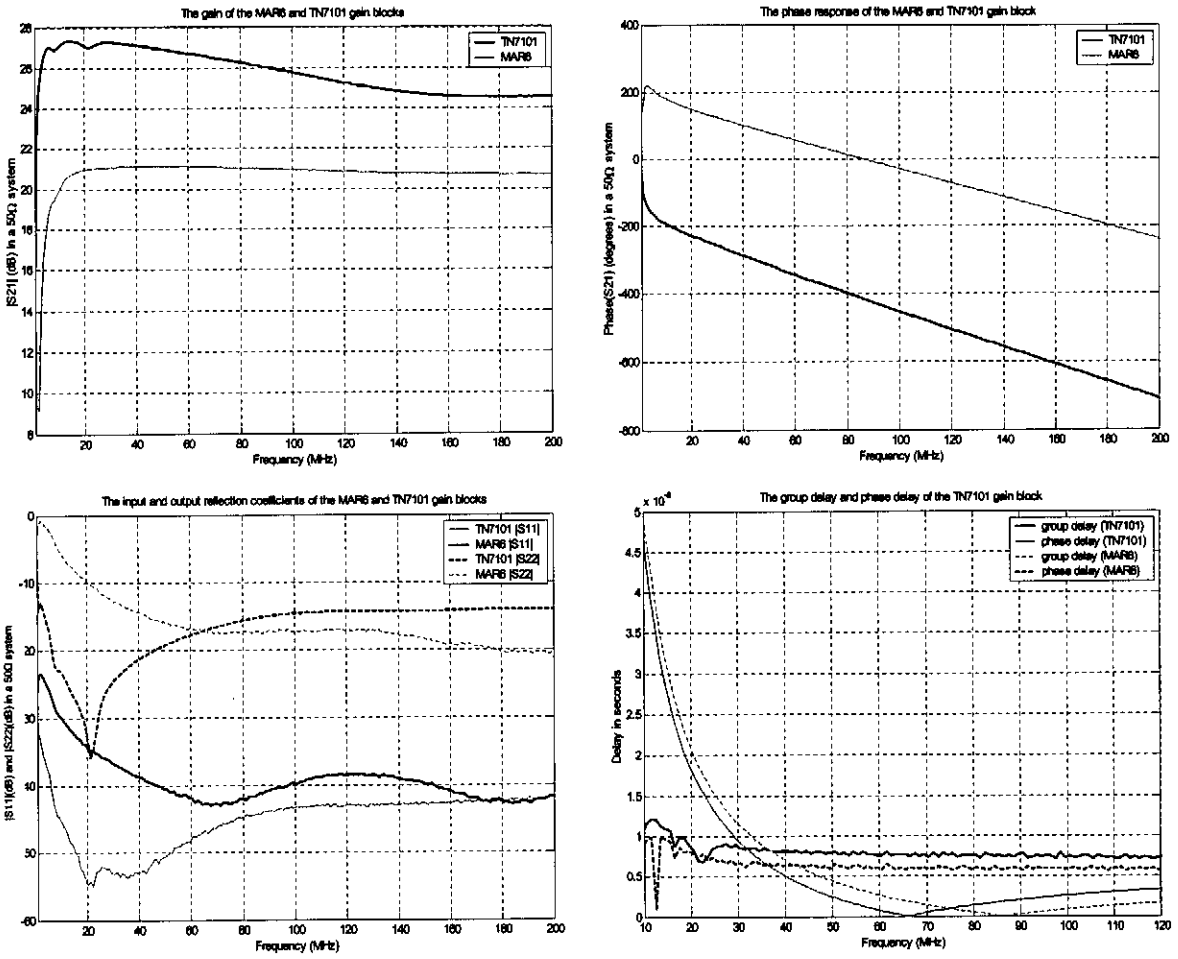

Figure 131 The comparative NA measured S-parameters and computed delay of the MAR6 and TN7101 gain blocks

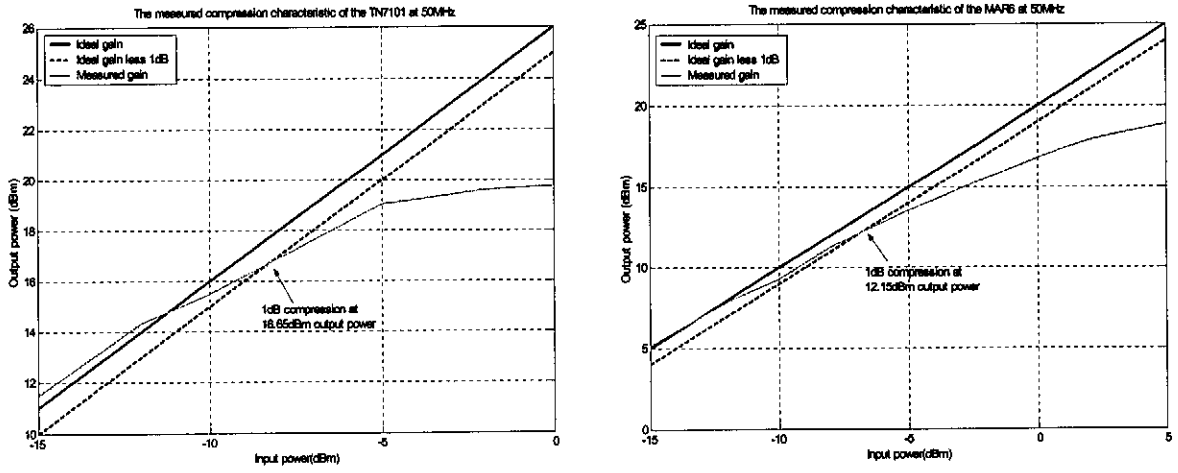

Figure 132 The measured compression of the TN7101 and the MAR6

The gain of the TN7101 and MAR6 are relatively flat over the frequency band of interest, and the MAR6 cuts off on the LF side quite sharply. The average gain over the frequency range of interest is 21dB (1.44dB variation) for the MAR6 and 26.72dB (1.53dB variation) for the TN7101. The 1dB compression point of the MAR6 was measured as 12.15dBm (10dBm above that quoted in the data sheet), and the compression point of the TN7101 as 16.65dBm. The phase response characteristics of both of the amplifiers are good over the whole band, except at lower frequencies, where a considerable delay begins to occur. We thus expect that the time domain pulse response of both components will be good, with a delay in the LF components. A few time domain measurements of the pulse responses of the MAR6 and TN7101 are shown in Figure 133.

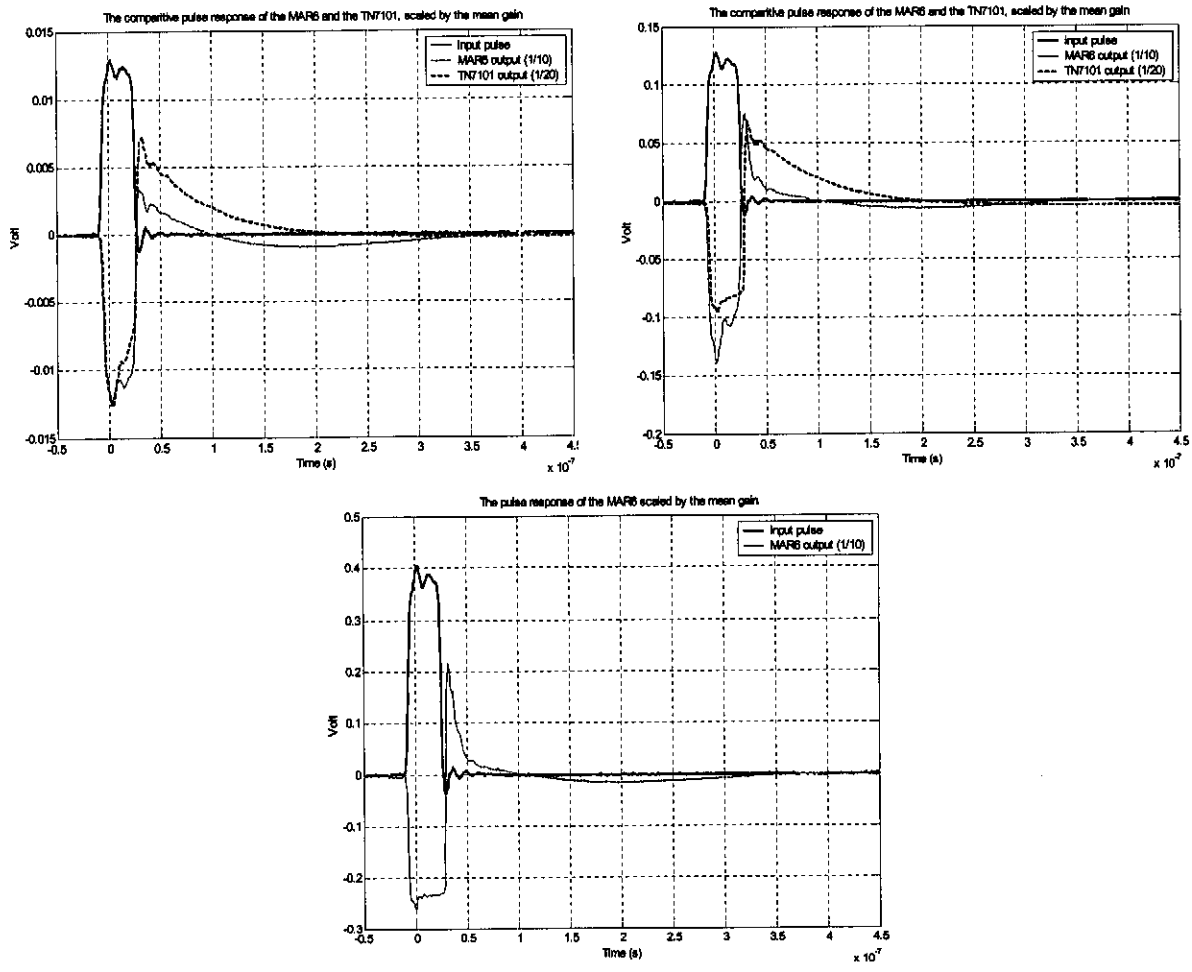

Figure 133 The time domain response of the MAR6 and TN7101 for a few input pulses of different magnitudes

Both of the components are inverting, and accurately reproduce the input pulse form at the output. Both components show voltage saturation at a certain point, but the pulse timing remains good above the voltage saturation point for both of the components. Only when the peak input voltage exceeds a certain level does the effective output pulse width begin to widen. This pulse-widening effect can be

seen for the TN7101 with a 120mV peak input pulse, and for the MAR6 with a 380mV peak input pulse in Figure 133.

The LF delay in the phase of the response of both components is clear in the slow rolling observed after the initial pulse-period has passed. The recovery of the MAR6 from saturation is generally faster, and it saturates at a higher voltage level.

The noise figure of the TN7101 was measured as 2dB, while the MAR6 has a noise figure of just over 3dB over the band of interest.

The comparative measured properties of the two components are shown in Table 9.

Property	TN7101	MAR6
Bandwidth	2 to +200MHz	5 to +200MHz
Gain	26dB	21dB
Noise figure	2dB	3.1dB
Peak output voltage clipping point	1.6V	2.2V
1dB compression point	12.15dBm	16.65dBm
Maximum group delay	Approximately 3nS	Approximately 5nS

Table 9 The comparative measured properties of interest of the TN7101 and the MAR6

Both of these components shown very good operational characteristics, and could both conceivably also be employed as replacements for the first LNA stage. The saturation effects of both of these gain block following the front-end component considered in the previous section, will be the limiting factor on the saturation of the resultant chain, as neither component will be able to handle a peak output voltage at the clipping level of the LNA stage before saturation.

3.4.1.3. The output buffer

The receiver designed in this report must be compatible with the DAQ employed in the existing BHR system. The later inclusion incorporation of an onboard acquisition system is also possible, but a buffer stage is still necessary to drive the DAQ input, and prevent excessive loading on the amplifier chain.

Two buffer components were considered for the output buffer stage; the MAX4200 from MAXIM and the BUF601 from Texas Instruments. Both components are relatively simple to use, and have very similar operation. Comparative measurement of the spectral transmition (|S21|) characteristics of both components using a calibrated NA is shown in Figure 135, using the application circuits of Figure 134 (note the 50Ω series output resistors employed in both circuits, introducing a 3dB transmition loss in the 50Ω measurement system).

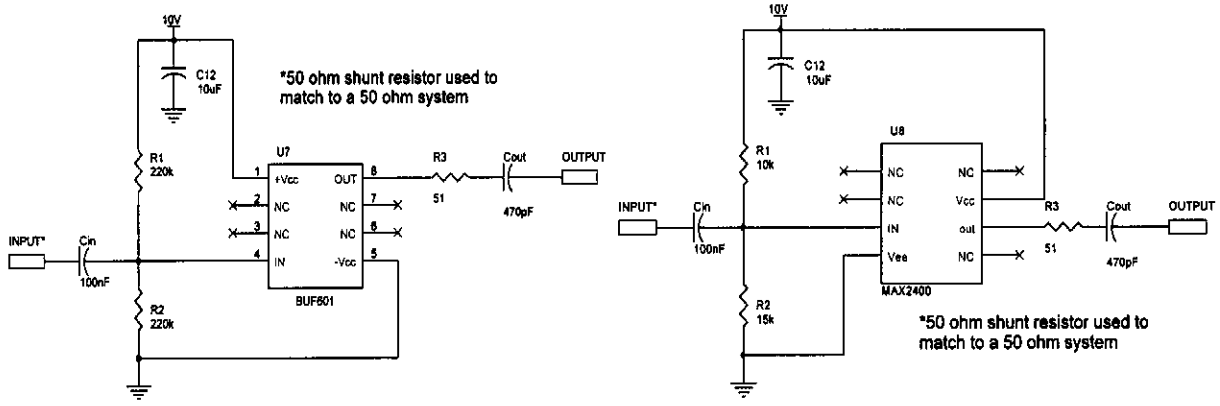

Figure 134 The application circuits of the BUF601 and the MAX4200

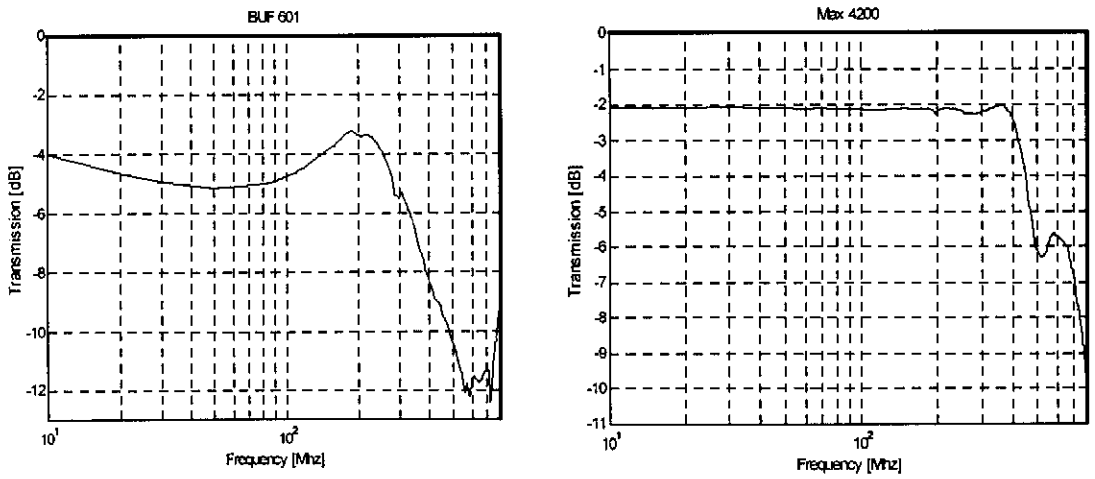

Figure 135 The comparative transmission (S21) of the BUF601 and the MAX4200

Time domain pulse measurements of the components are shown in Figure 136 and Figure 137. (Note that for these measurements, a 100Ω load was used, thus the actual voltage at the output pin of the components was measured. We thus expect the gain to be 3dB above the gain measured for the circuits of Figure 134 in a 50Ω NA measurement system, with a 50Ω series resistor at the output pin.) The computed gain is in the order of –1dB over the band for the BUF601 and 1dB for the MAX4200. This agrees with the predictions. The BUF601 begins to clip at an output voltage level of 3V, but operates well under saturation conditions. The MAX4200 does not saturate for the shown pulses, and also operates very well, even for large input pulses.

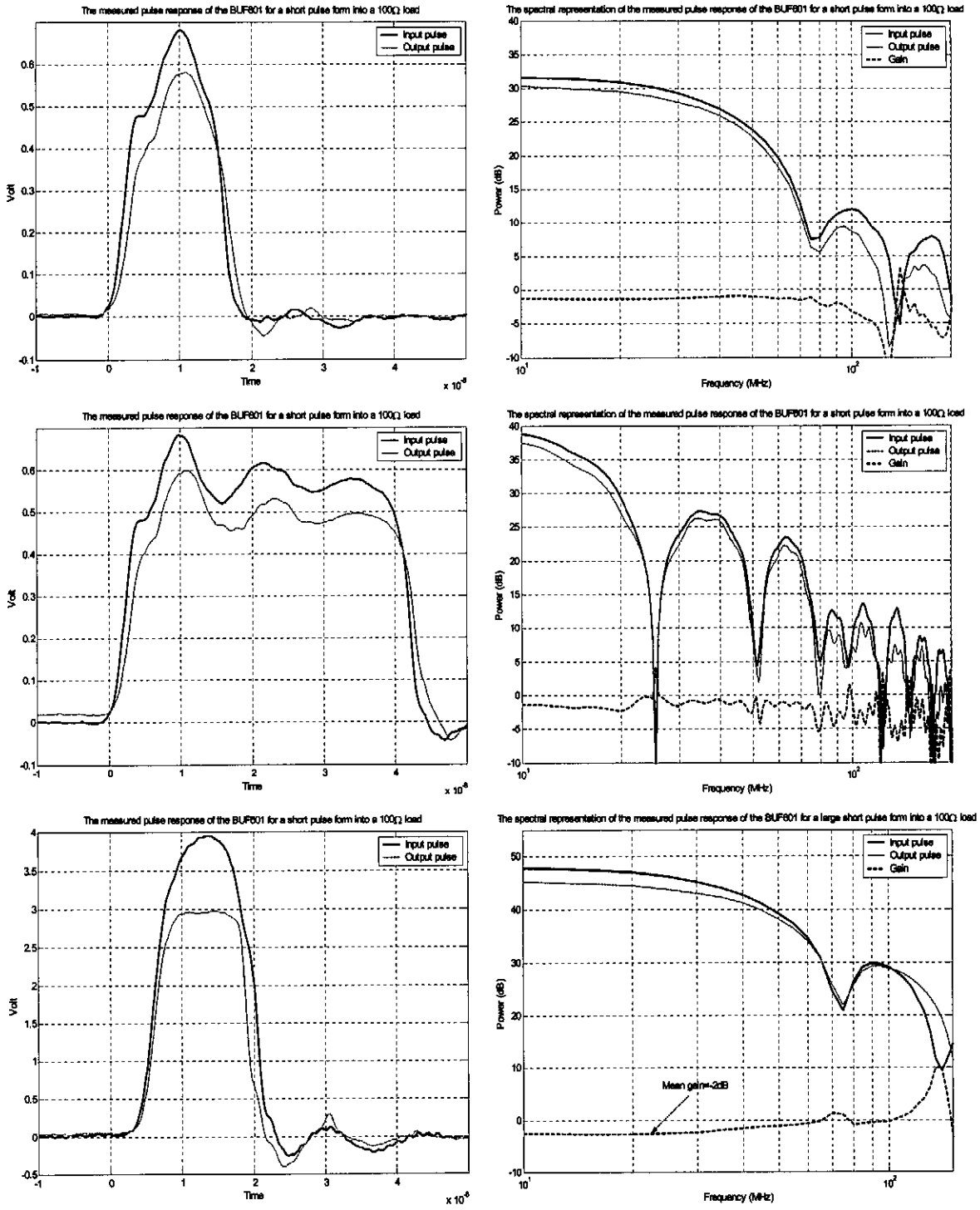

Figure 136 Time domain measurements of the pulse response of the BUF601 (effective output voltage at the output pin of the component)

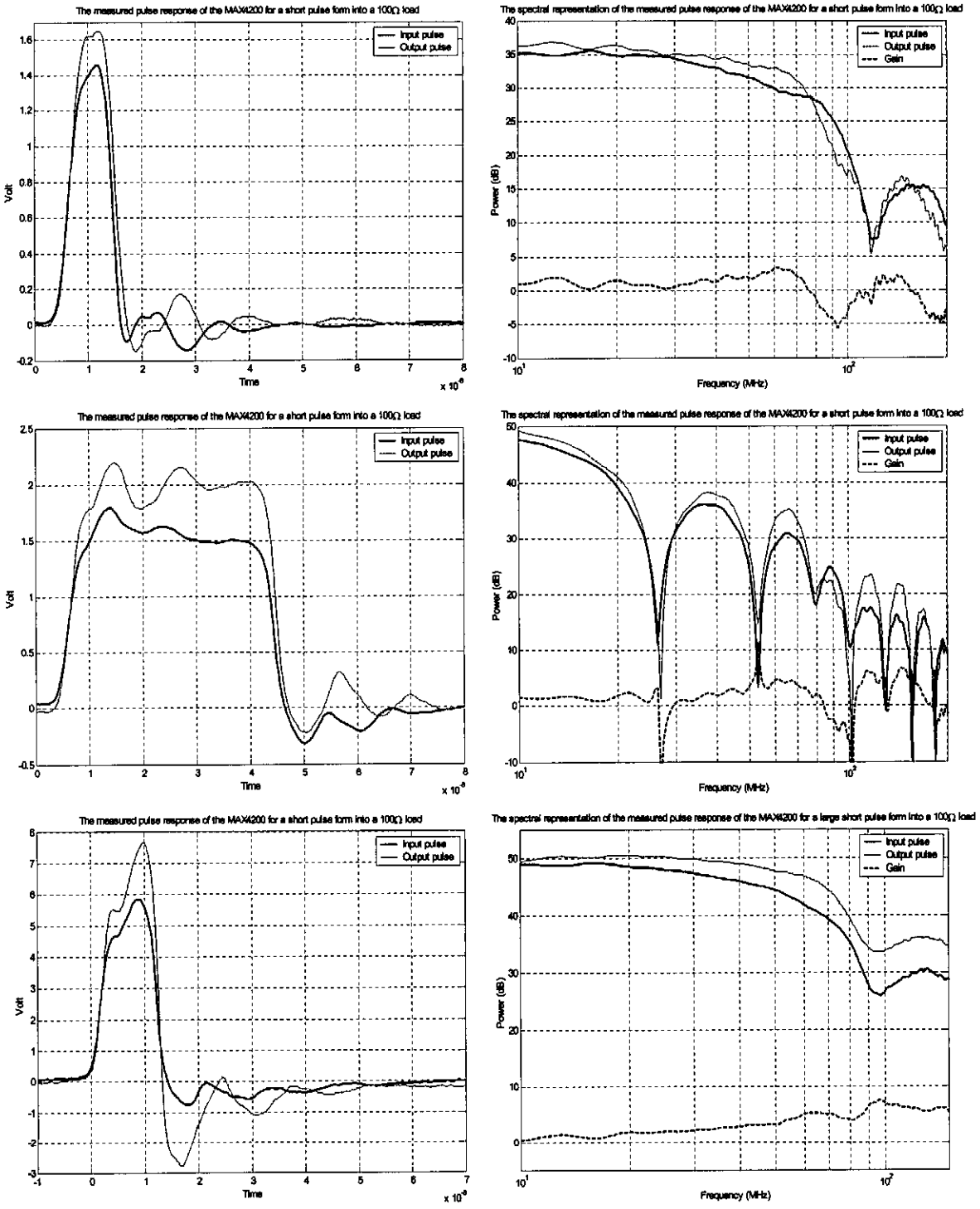

Figure 137 Time domain measurements of the pulse response of the MAX4200 (effective output voltage at the output pin of the component)

Both of these components are acceptable for the final buffer driver stage, to drive either the optical transmitter or the input of the DAQ directly. The BUF601 was chosen for application in the receiver designed in this report due to availability considerations. The pulse response measurement results

performed on both buffer components show that they will not limit the operation of the chain designed thus far, as the output of the gain block will begin to clip before clipping effects of the buffer stage come into play.

3.4.1.4. The optical driver

The analog optical connection to the surface located DAQ of the existing system was designed as shown in Figure 138. The optical transmit diode is biased at a quiescent point of 65mA, which is approximately in the centre of the linear region of the diodes current-voltage characteristic. A choke inductor is included to damp any source coupling. Comparative measurement of the full chain, including and excluding the output buffer and optical channel will be considered in the next section.

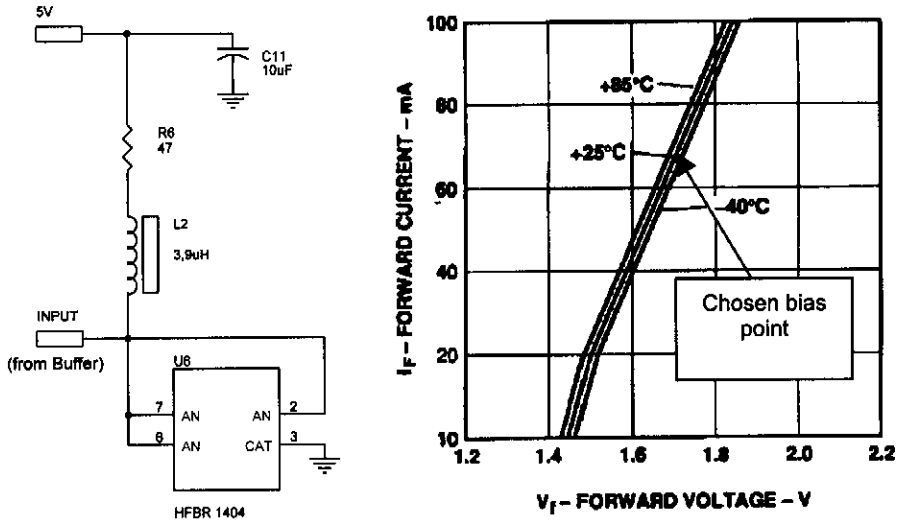

Figure 138 The application of the optical diode used to drive the DAQ connection and the current-voltage characteristic of the optical diode specified in the component data sheet.

This was found to operate well. More detailed analysis of the performance of the optical link will be performed during the characterization of the final amplifier design.

3.4.2. Summary of the full basic receiver chain

Up to this point, we have briefly described the operation of the components of a basic receiver chain, laid out as shown in Figure 119. We can quantify the expected ideal operation of such a chain, by considering the additive effects of each of the stages. The typical characteristics of interest of two typical chains are shown in Table 10.

Property	LNA component	Gain block/s	Gain (dB)	Noise figure (dB)	1dB compression point (dBm)	Peak voltage clipping point
RX chain 1	TN7111	2 x TN7101	63	1.9	Output: 12.15dBm Input: -51.85dBm	Output: 1.6V Input: 1.01mV
RX chain 2	TN7111	2 x MAR6	53	2	Output: 16.65dBm Input: -37.35dBm	Output: 2.2V Input: 4.93mV

Table 10 The theoretical characteristics of two typical chains, based on practical measurement of the separate components

Both of the chains described in Table 10 promise to perform well in a BHR application. The mono-static requirement that the receiver be able to perform well for relatively large peak input pulses in the order of 1V-2V is, however clearly not met by either of the two chains. We must consider methods of altering the receiver chain, in order to meet this requirement.

A number of possible solutions are possible, including the use of limiting amplifiers, or switching elements. A third solution is the use of a time variable gain, to improve the peak pulse voltage capabilities of the chain.

3.4.3. Introduction of gain control into the receiver chain

In order to limit the effect of saturation and clipping on the operation of the receiver chain, the possibility of introducing a time dependant gain was considered. Generally, time dependant gain implementations have poor noise figures. In order to minimize the effect of this, variable gain will be considered at the gain block stage of Figure 119.

After consideration of a number of components, gain control was implemented using the AD8367 variable gain amplifier component from Analog Devices. The component is specified to offer a maximum gain sweep between –2.5dB to 42.5dB. We will consider replacing both of the constant gain blocks in each of the receiver chains of Table 10 with this single component. Both automatic gain control (AGC) and sensitivity time control (STC) application of the component are considered.

3.4.3.1. The AD8367 variable gain amplifier

The application circuit used to characterize the AD8367 is shown in Figure 139.

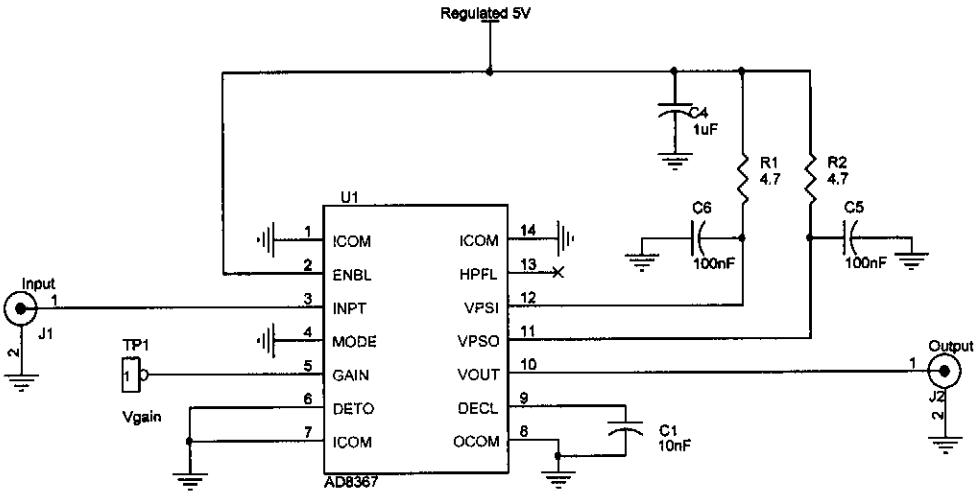

Figure 139 The application circuit used to characterize the AD8367 variable gain amplifier component

A. Interface considerations

The input impedance of the AD8367 is specified as around 200Ω in the frequency range of interest. An impedance transformer was thus used to match the 50Ω output impedance of the LNA front end to the 200Ω AD8367 impedance. A 4:1 (impedance ratio) Mini-circuits impedance transformer was chosen. The transformer was measured on a calibrated network analyser as shown in Figure 140. The computed primary input impedance with a 200Ω load on the secondary is close to 50Ω over the frequency band of interest (R_{in}=46.15Ω to 58.8Ω between 10MHz and 100MHz), and the imaginary input impedance component also remains small (I_{in}=j7.8Ω to –j12.8 between 10MHz and 100MHz). The impedance transformer will thus effectively transform the 200Ω input impedance of the AD8367 to match the 50Ω output impedance of the previous stage.

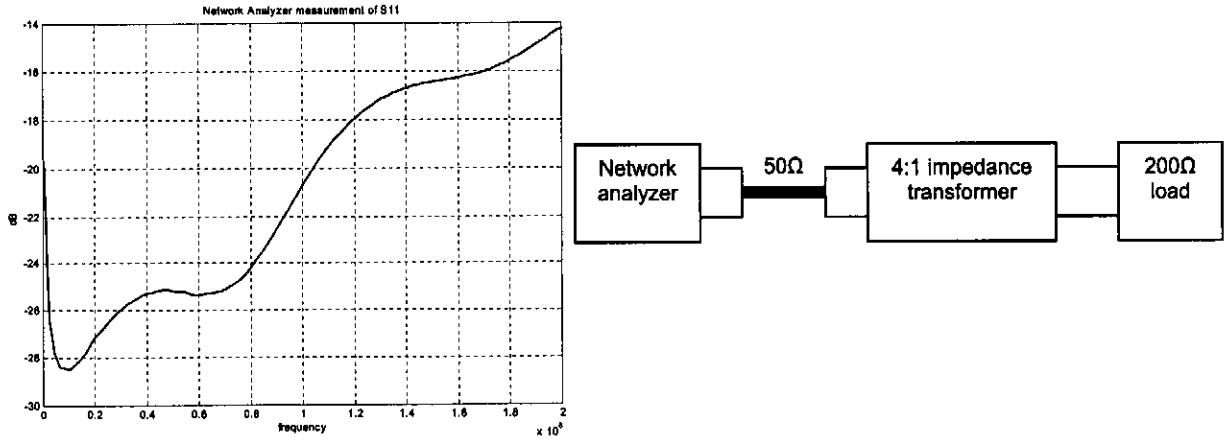

Figure 140 The measured S11 magnitude of a 4:1 impedance ratio Mini-circuits transformer with a 200Ω load on the secondary

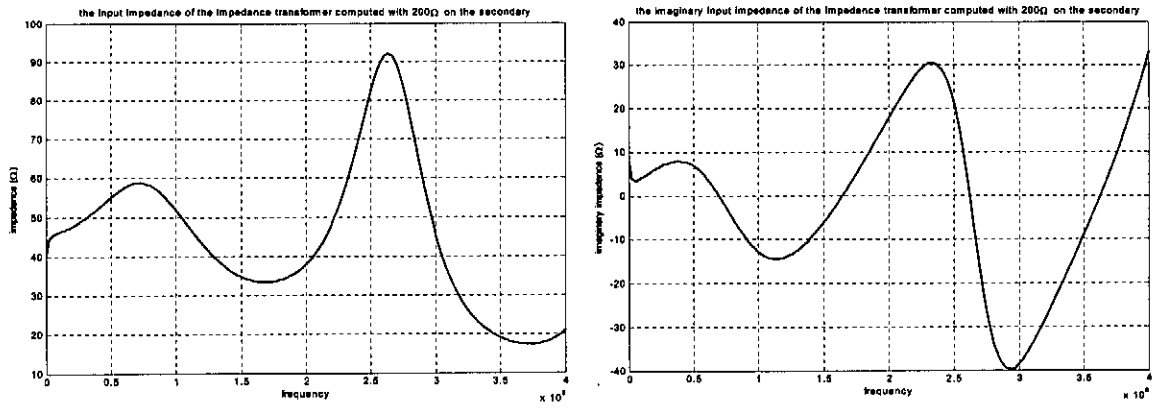

Figure 141 The computed input impedance of the impedance transformer with a 200Ω load on the secondary

The time-domain pulse response of the Mini-circuits 4:1 impedance transformer was measured for to pulse forms as shown in Figure 142. The measurement was made with a 50Ω source, and a 200Ω load on the secondary. The voltage gain due to the impedance transformation is clear in the time domain pulse forms, but if we consider the spectral power, taking the primary and secondary impedance bases into account, and scaling the pulses in the time domain accordingly, we see that the output power is in fact slightly less than the input power. This power loss can be quantified by considering the input and output spectral power. The pulse power losses over the frequency range of interest are measured as less than 1dB.

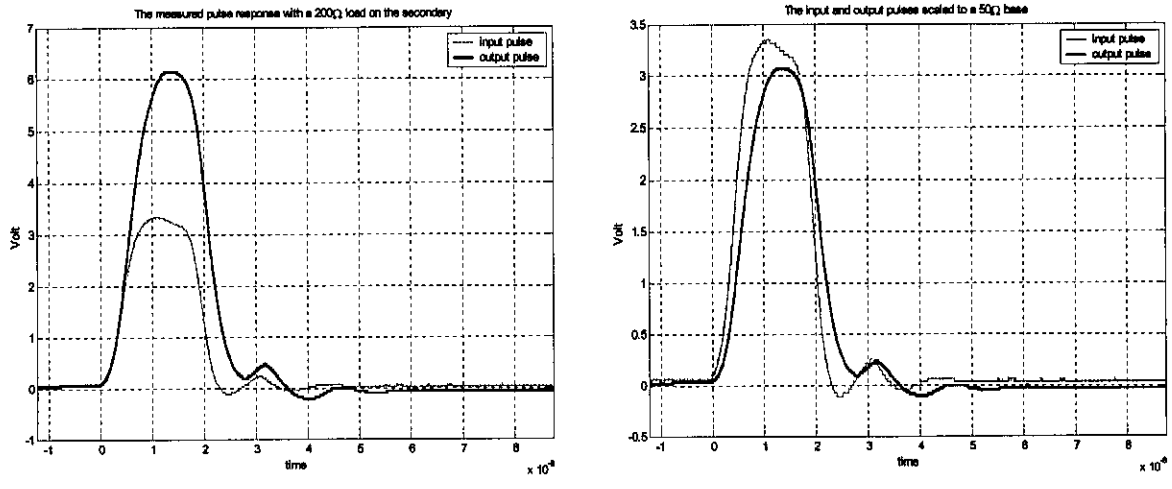

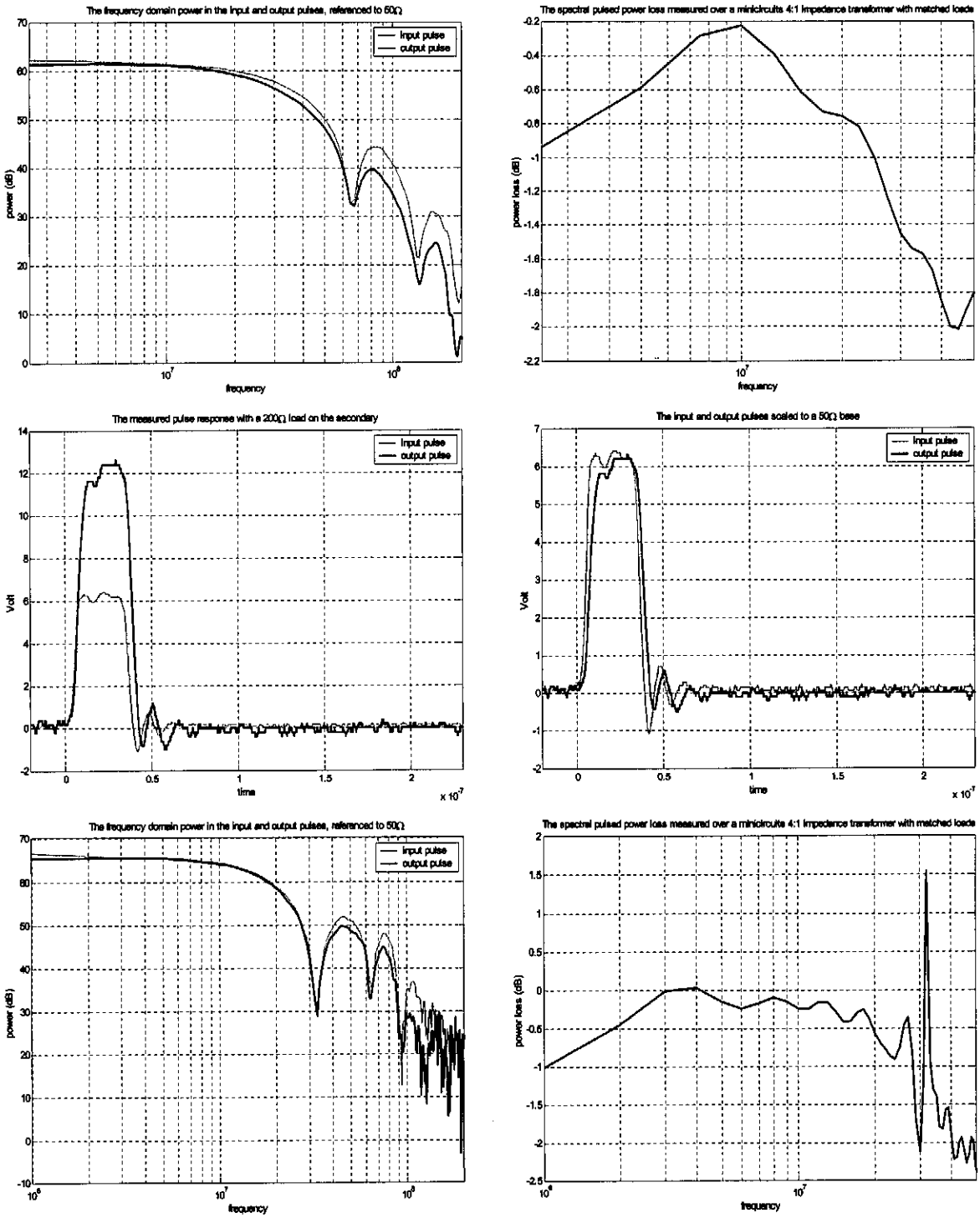

Figure 142 The measured input-output pulse response of a Mini-circuits 4:1 impedance transformer

The output impedance of the AD8367 is also designed to operate in a 200Ω system. Because the output of the AD8367 will drive a high impedance buffer, however, this requirement can be simply achieved by the addition of a 200Ω shunt resistor. (During testing of the receiver chain, it was found

that the AD8367 was capable of directly driving the high impedance buffer, but the addition of the 200Ω shunt resistor was found to be necessary to prevent oscillation of the amplifier at high gain settings)

B. Variable gain amplifier application

The gain of the AD8367 circuit is varied by altering the voltage at pin 5 (Gain) between 0 and 1 volt, to achieve a gain, linear-in-dB-proportional to the control voltage. The sign of the linearity can be set positive or negative by strapping the mode pin to V_{cc} or ground respectively. Network analyser measurement of the application circuit of Figure 139, with a 4:1 ratio impedance transformer employed to match both the input and output to the 50Ω network analyser impedance for a few gain control voltages and the gain vs. control voltage at a few frequency points, with the mode pin strapped to ground are shown in Figure 144. It is clear that the circuit performs well, and that the gain-control voltage relationship is as predicted by the manufacturer. The drop off in measured gain below the expected gain level for gain control voltages below 200mV is due to compression of the output of the amplifier at high gain.

The noise figure of the AD8367 component is of particular importance, if we consider the theory of operation of the component. The gain control mechanism of the component can be schematically represented as shown in Figure 143. The component is a voltage-variable 0-45dB attenuation network, followed by a constant gain 42.5dB amplifier. The noise figure of the component is dominated by the attenuation network, given by $NF_{attenuator}(dB) = loss_{attenuator}(dB)$ under normal conditions. This implies that at maximum gain, the noise figure will be approximately equal to that of the output buffer amplifier (7.5dB) and at minimum gain, the amplifier will have a noise figure of approximately 45dB+7.5dB=52.5dB. This is clearly a very poor noise performance, and underlines the need for a LNA before this stage can be implemented, to reduce the additive noise effects of the dynamic range of the system.

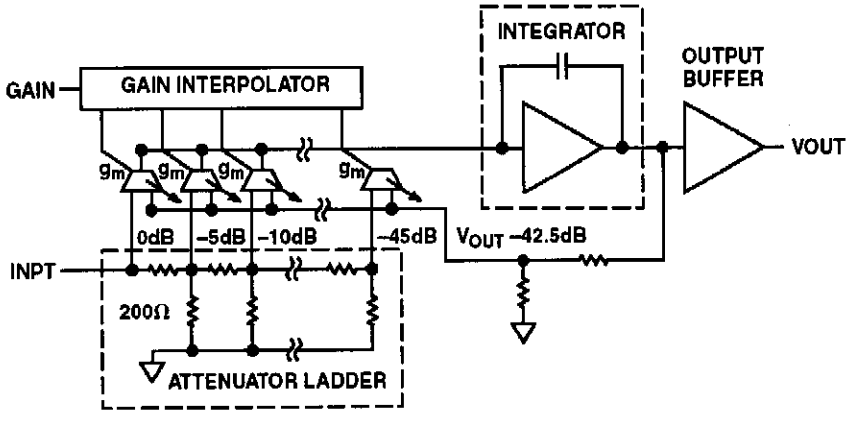

Figure 143 The simplified architecture of the AD8367, showing its principle of operation

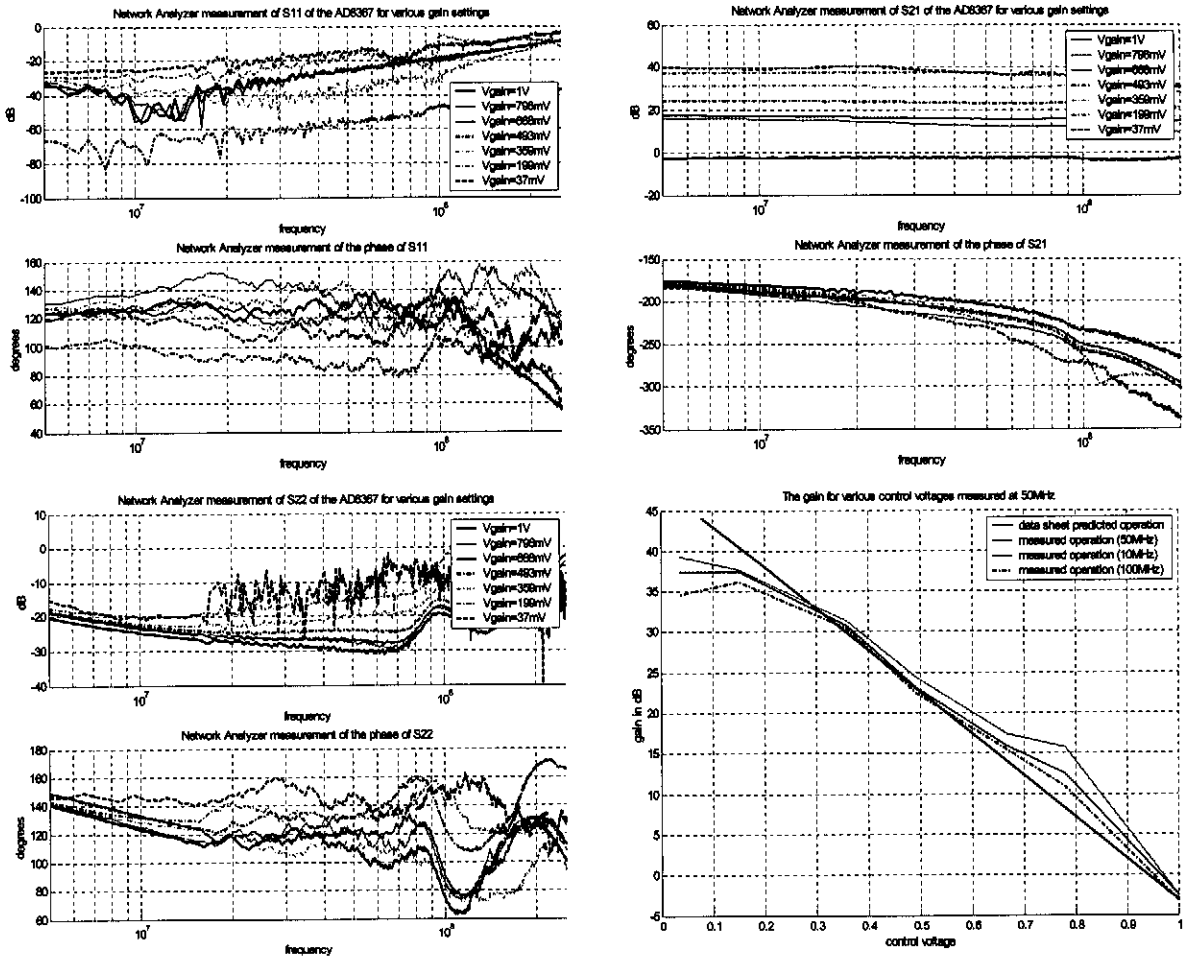

Figure 144 The S-parameters, and gain for a few control voltages of the AD8367 application circuit, matched to the 50Ω NA using 4:1 impedance transformers at the input and the output ports.

Time domain measurement of the pulse response of the AD8367 was performed. Some results are shown in Figure 145.

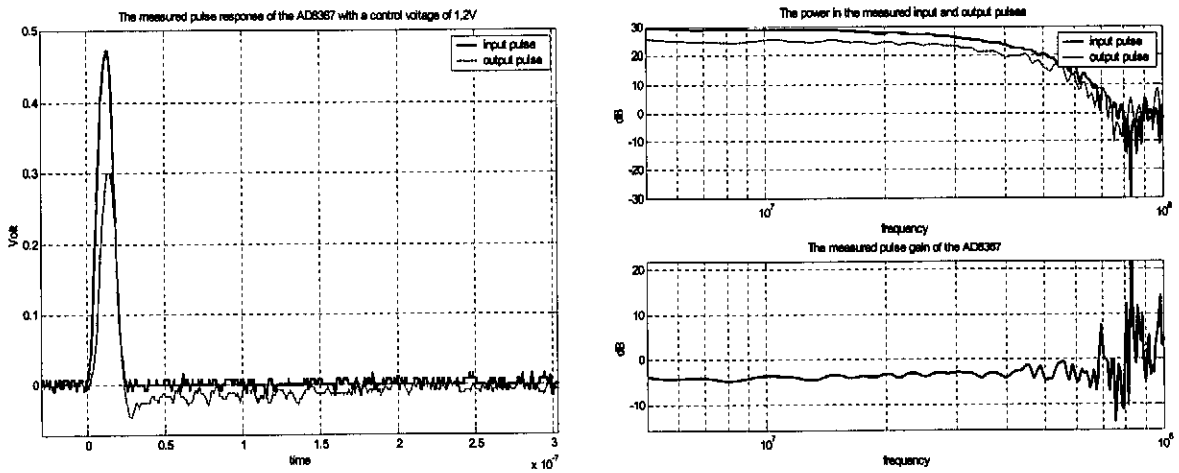

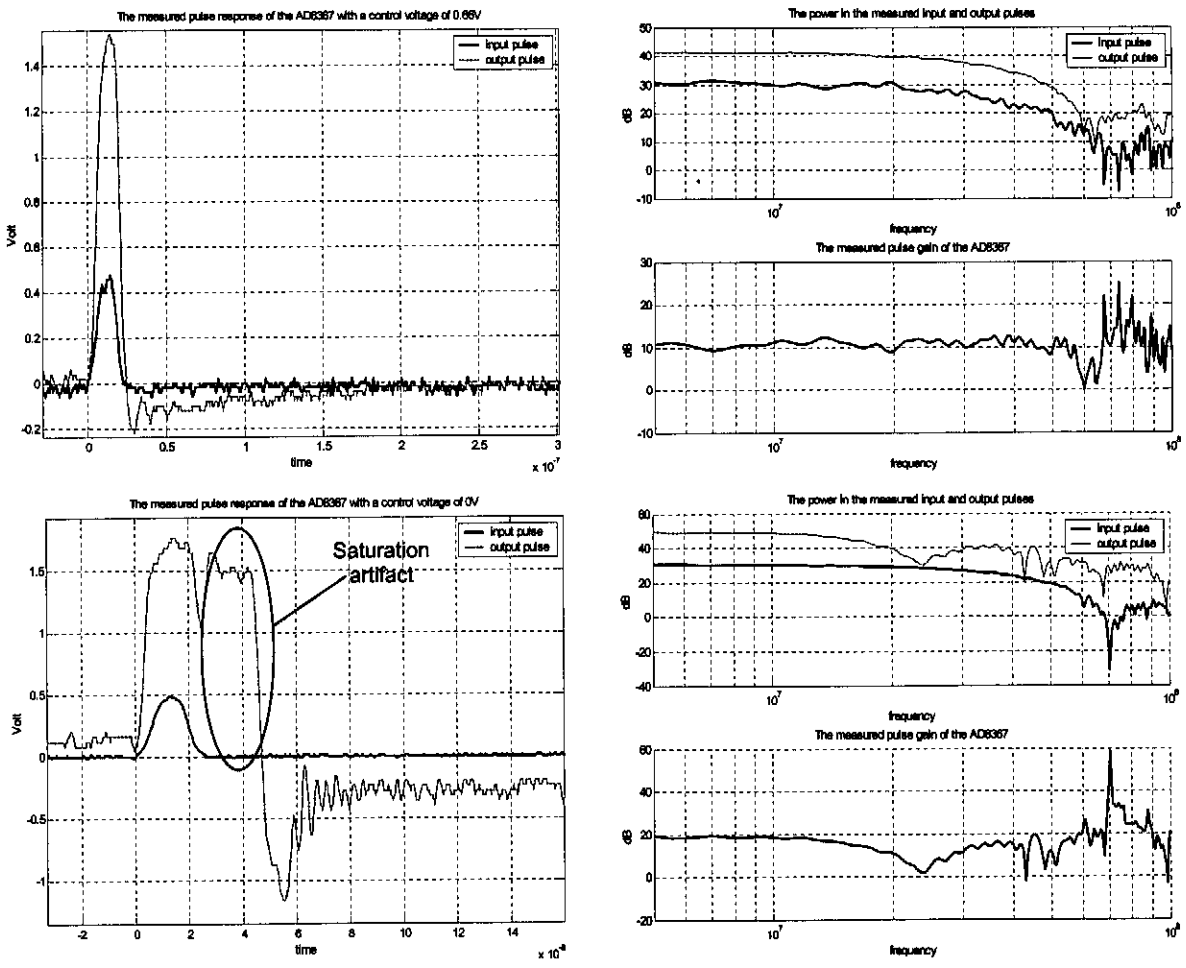

Figure 145 The time domain measured pulse response of the AD8367 matched to a 50Ω system using impedance transformers, for a few control voltage settings and the computed spectral gain for each case

It is apparent from the results of Figure 145 that the peak output voltage clipping level of the AD8367 is approximately 1,5V. This translates to a 2V peak input voltage at the specified minimum gain of the component, and an 11.24mV peak input voltage at the maximum specified gain of the component. At minimum gain, the Amplifonix LNA front-end component will saturate and clip before driving the AD8367 into saturation. The theoretical maximum peak input pulse that the TN7111-AD8367 cascade will be able to accept before clipping is thus 380mV (based on the measurements of section 3.4.1.1). This is clearly a drastic improvement on the peak voltage properties of the chains considered in section 3.4.2.

3.4.3.2. Automatic gain control implementation

AGC is an 'intelligent' method of controlling the gain level of an amplifier chain by feeding back and integration of the output or input signal power levels, comparing the result to a predetermined power

level and varying the gain accordingly. This method is commonly used in communication and radar systems, where large variation in received signal levels (large dynamic signal range) is expected.

In order to implement AGC, the response time and bandwidth of the feedback loop must be considered very carefully. The AD8367 features an on chip square law detector that can be used to measure the rms output voltage. This voltage is compared to the rms value of a $1V_{pp}$ sine-wave (354mV) which can then be directly used to charge/discharge a capacitor connected to the gain pin, thereby generating a gain control voltage based on the output power, and realizing closed loop AGC control. If the on-chip detection loop is employed, then the output will be maintained at $-9.02dBV_{rms}$. The response timing of the internal AGC control loop is dependant on the value of the capacitor used to integrate to the desired gain voltage level, introducing a single-pole time constant type response. The AGC circuit to employ the internal control loop, the stable gain point computation, and primary timing factors are described in Figure 146 and equation (3.13).

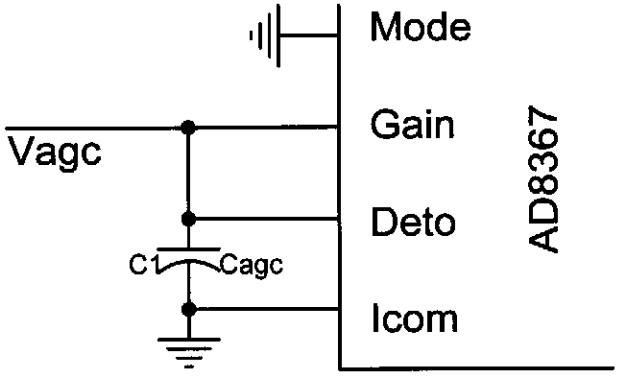

Figure 146 The basic connection of the AD8367 control pins for AGC control using the on-chip square law detector

$$V_{out}(dBV_{rms}) = -9.02 \Rightarrow V_{in}(dBV_{rms}) = -54.02 + 50 \times V_{DETO}$$
$$\tau_{AGC}(\mu S) = 10 \times \left(C_{AGC}(nF) + 5\right) \qquad (3.13)$$

The properties of the AGC loop can be altered by using an external detector and feedback mechanism.

AGC is generally very useful for continuous wave systems with high dynamic ranges. The application to a pulsed system is more complex, however. The main reason for this is that the sudden changes in signal levels demand an extremely fast response, but by the same token, we do not want the gain response time to be in the order of the pulse width, so that the gain changes dramatically during the pulse period. The single-pole type gain change response does not respond so fast as to cause difficulties of the second type, but the response to a sudden pulsed change in the input level is delayed, and thus ineffective, as the pulse has passed by the time that the control loop adjusts the gain accordingly. Typical AGC operation in a pulsed system is shown in Figure 147. It is clear that the AGC

is going to have very little effect on the gain during first pulse period due to the AGC response delay. When no more reflections are received, the AGC loop will settle back to maximum gain, and only respond again after the first received pulse.

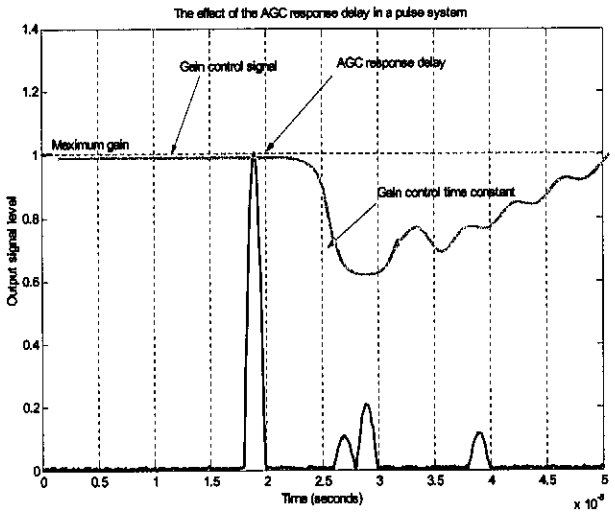

Figure 147 A representation of a typical causal AGC response in a pulsed system

Although continuous wave consideration of the continuous AGC operation showed that the AGC feed back can be very effective, with AGC response times in the order of 500nS, pure AGC was found to be very ineffective in the case of a pulsed system, due to the phenomenon depicted in Figure 147. Another difficulty with pure AGC control is that the gain control signal must be stored in some way for use during post processing. As an alternative, sensitivity time control (STC) was considered for application in a pulsed system.

3.4.3.3. Sensitivity time control implementation

Sensitivity time control (STC) is implemented based on the expected, rather than the measured time behaviour of the signal input to the amplifier, and relies on a predetermined profile rather than the real-time feedback of the signal power level. In order to design a time-gain profile that is applicable to the BHR case, we must consider three main time periods during the acquisition period. The first period is the period during which the transmitter is fired. During this period the signal at the receiver feed will be at its largest, and we thus require minimum gain to limit saturation of the receiver components. During the second period, after the transmitter has fired, the received signal will still be relatively large, but will begin to die away exponentially, as the radiated energy propagates away from the receiver. During this period we would like the gain to gradually increase as the received signal dies away. After a time, the propagating wave will be far from the receiver, and the received reflections will be very small. During this period the receiver gain should be at a maximum so that it is sensitive enough to detect the small reflected signals. Based on these considerations, the basic form of the time-gain profile is shown in Figure 148.

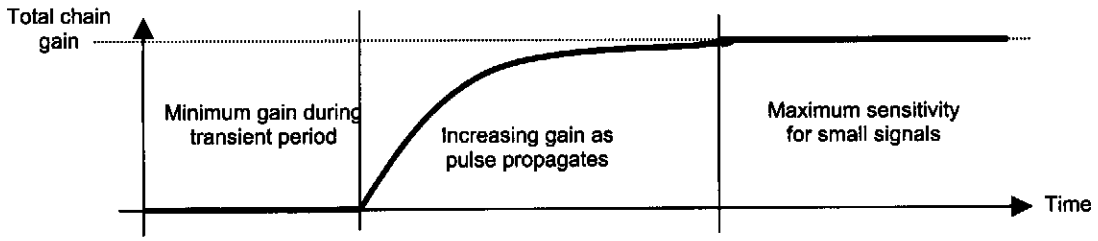

Figure 148 The approximate form of the desired STC profile for a general BHR system

This gain profile should be followed during each of the acquisition cycles, beginning at the time of the transmitter firing. In order to achieve the correct timing, the gain sweep should be initiated by the trigger signal from the transmit electronics.

The STC control electronics to achieve the gain profile of Figure 148 are shown in Figure 149. The input is a 5V square wave, with the falling edge at the transmitter trigger point. Figure 150 shows ADS simulation results demonstrating the operation of the STC control circuitry for the shown values. Note that for in this implementation we have chosen an exponential gain sweep with a typical RC time constant.

The gain control circuit was built and measured. The results, along with ADS simulations are shown in Figure 150. The timing of both the simulated and measured responses is very similar. The slight difference in the voltage from which the sweep begins is due to a number of non-idealities of the components, including lumped element value tolerances.

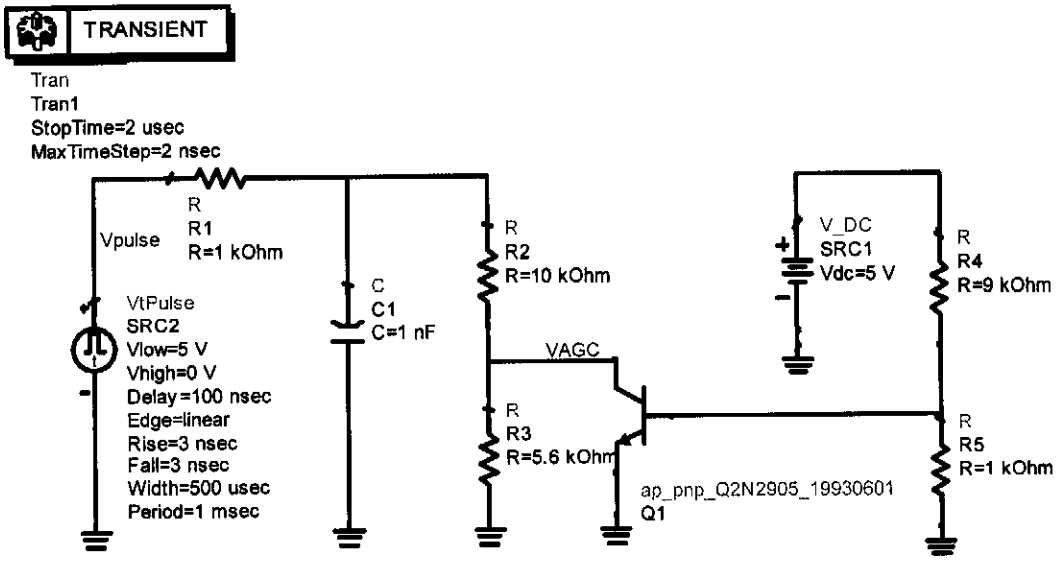

Figure 149 The control circuitry used to generate the STC profile from a 5V square wave

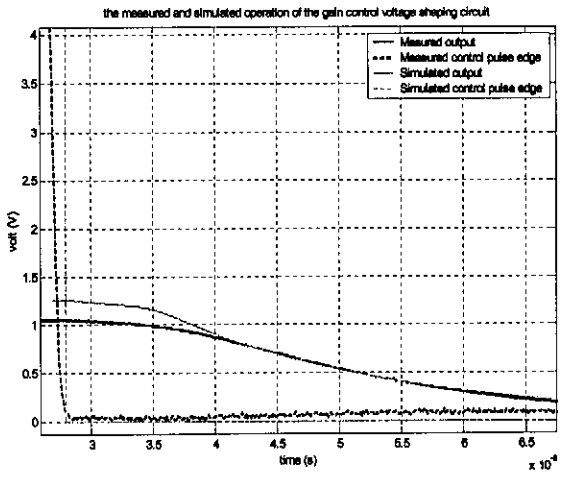

Figure 150 The comparative simulation and measurement results for the gain control circuitry

One critical issue that must be considered in the application of STC in a BHR system relates to the large gain sweep that is required in a short period, due to the fast drop off in the received signal levels with time. The total acquisition period, in which detectable data can be received (lifted above the noise level by stacking and various signal processing methods) is generally less than 2μs. The ideal gain sweep time from minimum to maximum gain after the pulse transient period has passed is thus in the order of hundreds of nanoseconds. The STC application must be able to realize this fast sweep.

The AD8367 component chosen for the STC application is specified to be able to sweep from 0dB to 30dB gain or visa versa in 300ns. If we assume that this is a linear response, the maximum gradient of the gain change signal should be kept below $\left|\frac{dV}{dt}\right|_{\max} \simeq \frac{|V_{0dB} - V_{30dB}|}{t_{30dB-step}} = \frac{|0.93-0.34|}{300\times10^{-9}} = 2\times10^{6}\,V/s$. The maximum gradient versus the total fall time (1V to 0.2V) is shown in Figure 151. It is clear that the minimum fall time, assuming the topology of Figure 151 that can be used is around 1μs if we do not wish to exceed the specification of the variable gain component. The operation of the amplifier with this higher-than-rated sweep gradient must be considered. In order to prevent the peak sweep gradient causing a problem, the gain sweep profile may need to be redefined to a more linear sweep, thus reducing the peak gradient of the sweep.

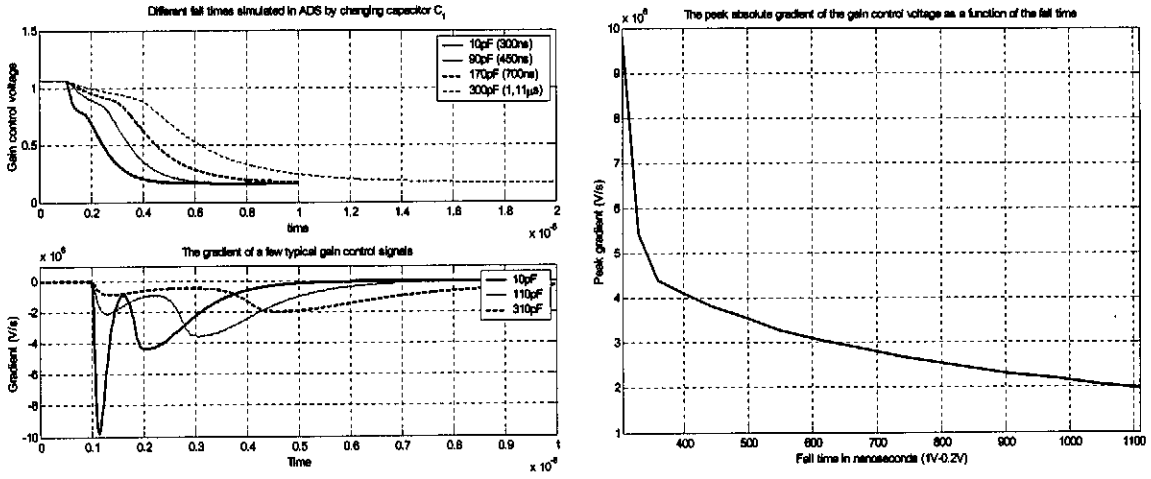

Figure 151 The peak simulated gain control signal gradient for different fall times (1V-0.2V) using the circuit topology of Figure 149

Measurement of the operation of the AD8367 in the time domain indicates that the effect of sweeping the gain at a gradient exceeding that specified is the introduction of transients at the output of the receiver at regular gain levels. According the manufacturer, these transients are related to the inability of the gain interpolator feedback loop and the output centring mechanism to compensate for the irregularities and transients generated as each of the 5dB attenuator blocks are switched in or out of the transfer path [28]. The typical transients observed for a steep gain sweep are measured at the output of the AD8367 as shown in Figure 152. Seven of the nine transients caused by the switching of the nine attenuator blocks can be seen for the chosen sweep. The final two 5dB attenuation blocks switch out smoothly, as the gradient of the gain-control signal is within the specified range at that point. It is important to note that the position and form of each transient is constant for a given sweep profile, and can be easily filtered out during post processing of the data. This is however clearly not ideal.

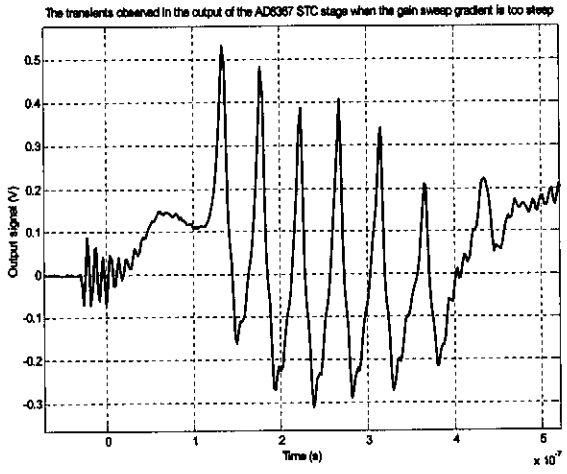

Figure 152 The form of the typical transients generated at the output of the AD8367 when the gain sweep gradient exceeds the specified value ($2x10^6$V/s)

From the results presented in this section, it is apparent that the saturation capabilities of a BHR receiver can be greatly improved by the inclusion of an STC gain sweep policy. The actual realization of such a gain sweep is possible, but is limited by the operational characteristics of the variable gain component. The implementation of a chosen VGA as discussed in this section shows that the timing limitations of the component make it non-ideal for Mono-static BHR application, but we have shown that variable gain application is an effective method of overcoming saturation sensitivity in a BHR receiver.

3.4.4. Interface considerations and receiver layout

The receiver must be able to interface with the antenna in a bi-static configuration, and must be compatible with the receiver port of the mono-static circulator in the mono-static configuration. In this section we will briefly define these interfaces. We will then consider the physical layout of the receiver or realization and testing.

The input of the first stage LNA amplifier is 50Ω, but simulations of the antenna structure suggest that the real impedance of the antenna structure will generally be larger than this. In order to match the input impedance of the LNA to the antenna, an impedance transformer was used. The 4:1 impedance ratio transformer discussed in section 3.4.3.1.A was chosen. This transformer serves both as an impedance transformer (transforming the input impedance of the receiver chain to 200Ω), but also as a feed balun, coupling the un-balanced receiver chain input to the balanced antenna structure. In a mono-static application, the connection between the antenna and the receiver will not be direct, but through the circulator connection to the transmitter. The balancing of the path between the receiver and the antenna feed is then performed as part of the transmitter circuitry.

The interface between the receiver circuitry and the mono-static transmitter consists of two lines. The first connection path carries the trigger signal, used to determine the gain-control sweep timing. The second connection path is the receiver port of the circulator, and carries the received signal output to the receiver.

In the BHR probe, a battery is used to supply power to the probe electronics. In general, such a battery can be modelled as a voltage source, with a very large parallel capacitor that will damp most source noise. The power feed lines, however may be relatively long, and care must be taken to isolate these lines from any RF signal coupling. This is of particular importance in the mono-static case, where the transmitter and receiver electronics share a common source, and any noise or RF coupling to the power lines from the transmitter will compromise the RX-TX isolation. RF choking of the power feed lines is considered as part of the probe design and construction discussed in Chapter 5

The full circuit of the receiver design, incorporating STC and allowing for an optical connection to the DAQ of the existing system is shown in Figure 153.

This general topology was laid out in ORCAD during the prototype period, and two separate PCB layouts were commercially manufactured. The first PCB incorporated both the transmitter and receiver electronics on the same board, while the second PCB included just the receiver electronics, as shown in Figure 153. The top and bottom layers of the 2-layer PCB receiver board are shown in Figure 154. The combined RX-TX PCB is shown in Figure 156

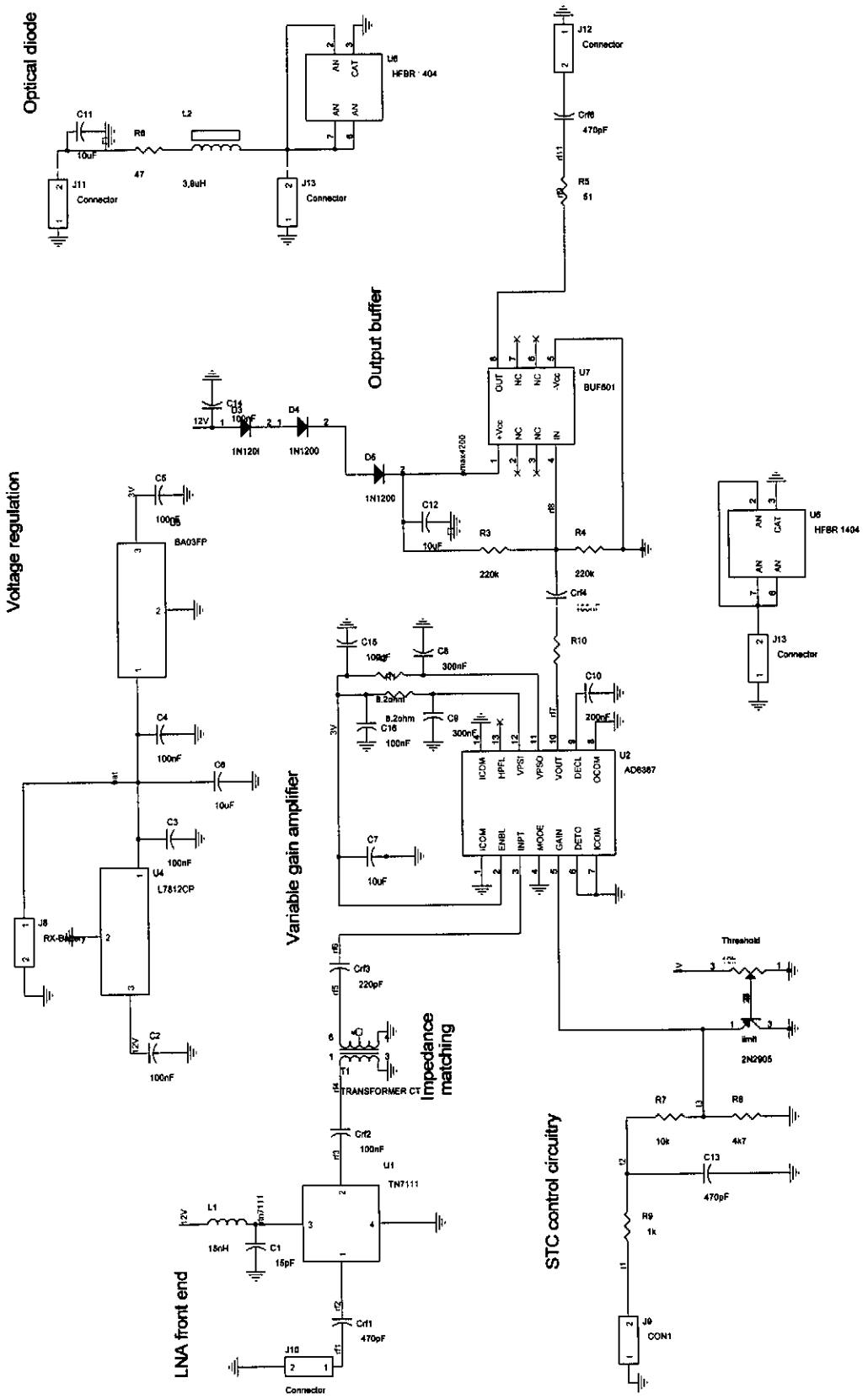

Figure 153 The circuit layout of the full receiver topology, incorporating STC and an optical driver

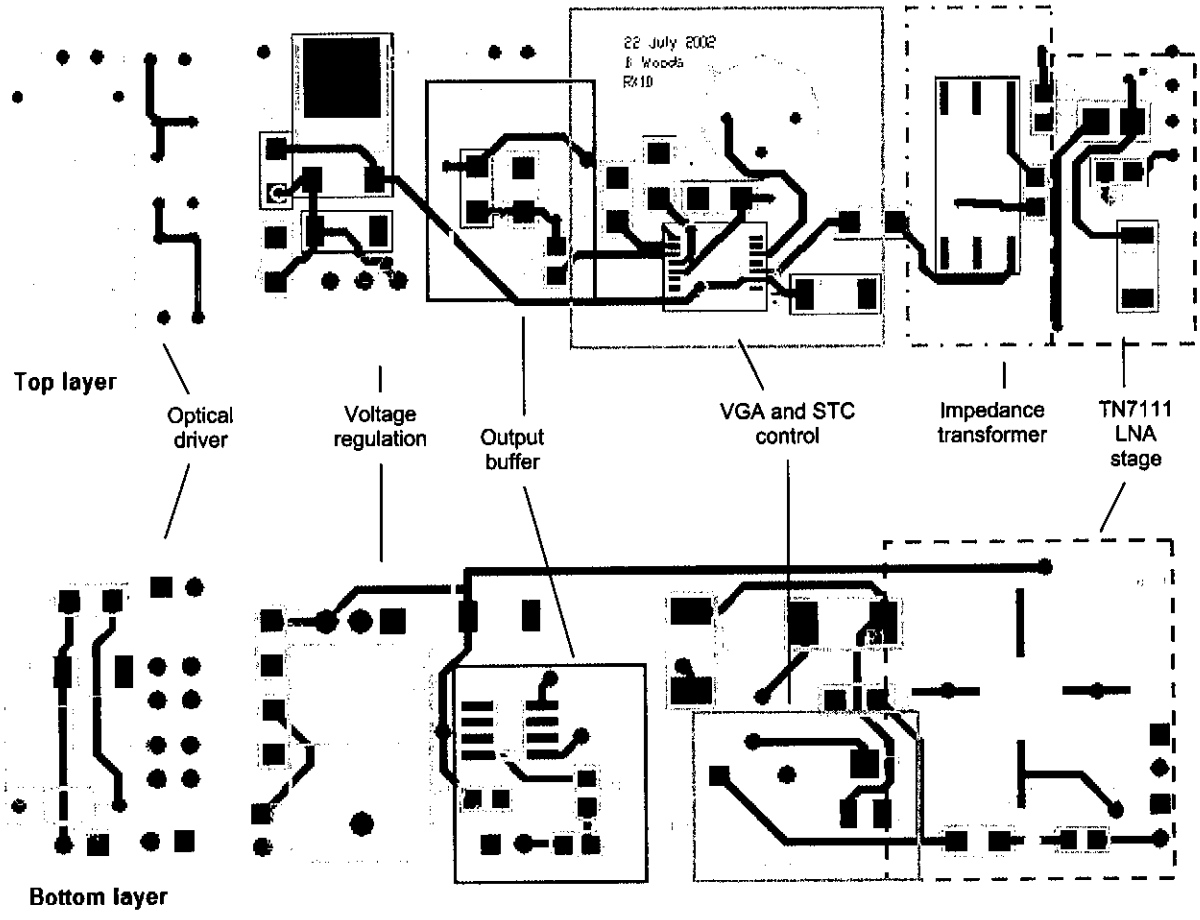

Figure 154 The top and bottom layers of a PC board layout of the prototype receiver circuit

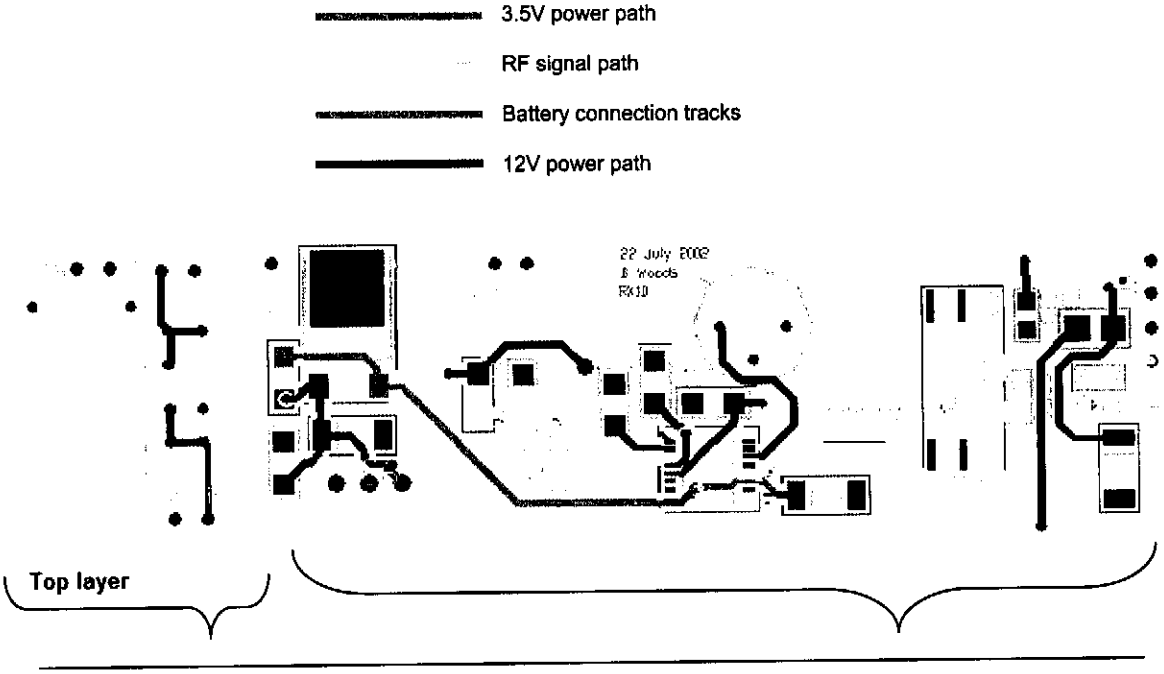

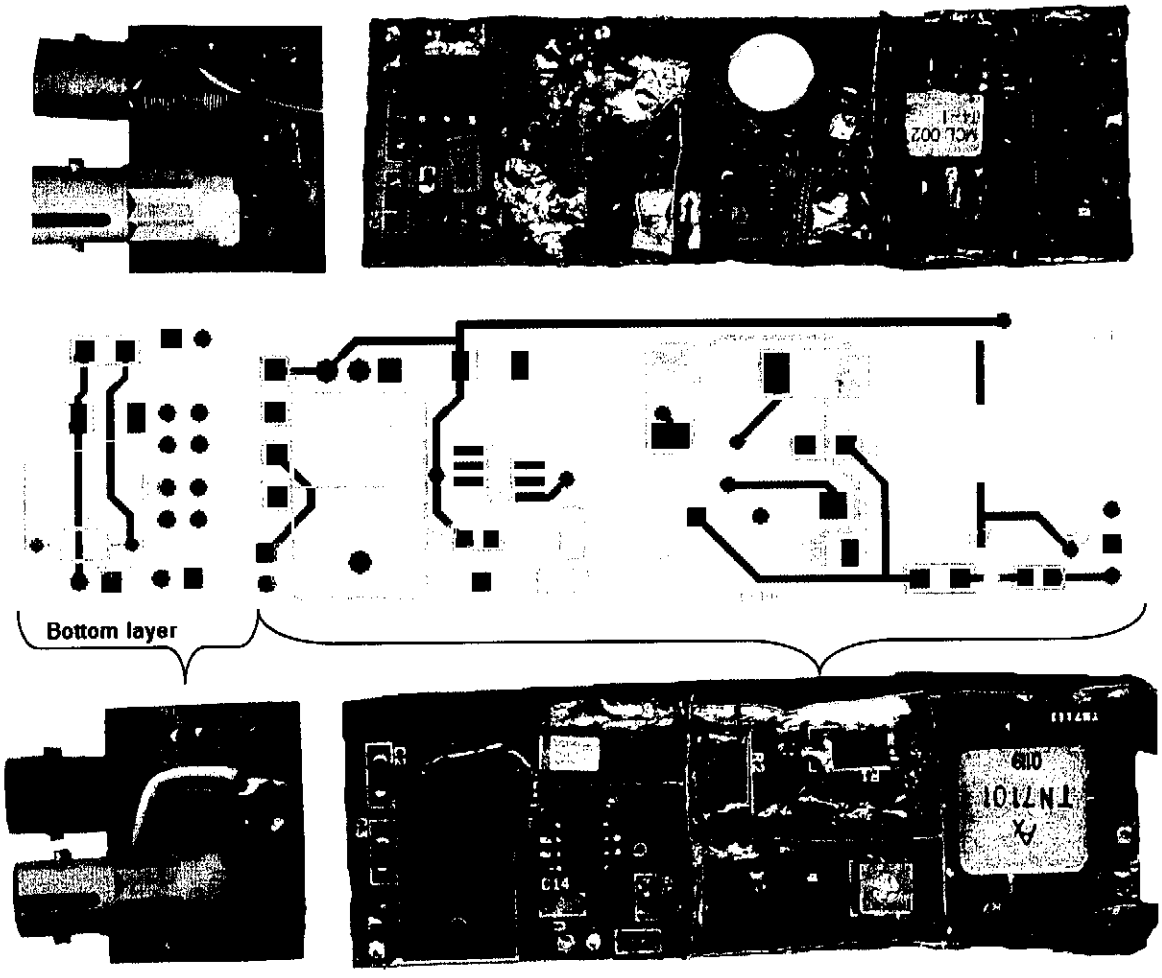

Figure 155 The receiver circuit board layout, showing the power tracks (3V and 12V), the battery connection, the RF path and the completed board

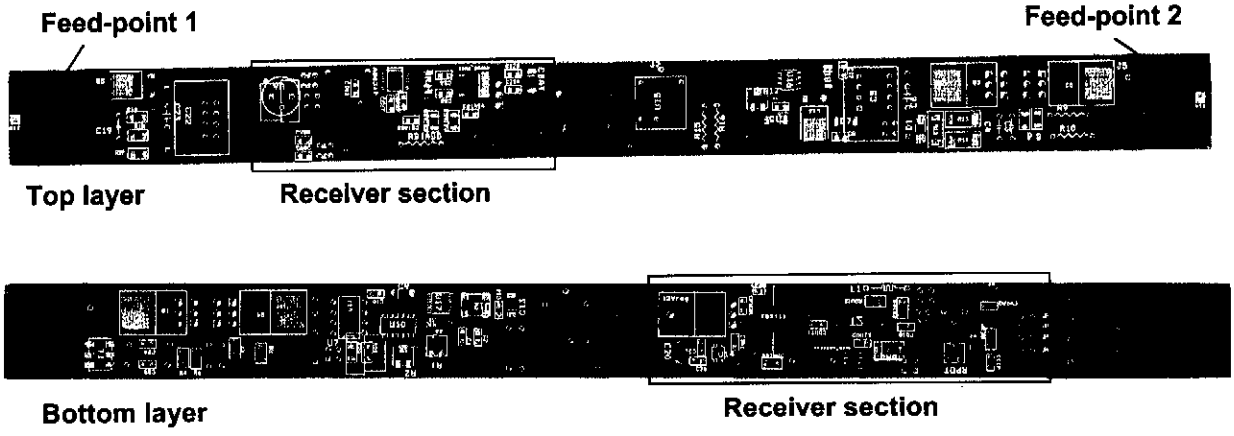

Figure 156 The layout of the receiver and transmitter electronics on the same PCB

3.4.5. Operational characterization of the receiver chain

3.4.5.1. Frequency domain characterization

The complete receiver chain of Figure 153 was built and tested. A number of difficulties were experienced with oscillations in the chain at higher gain settings. These problems were overcome by altering the source smoothing, and by shielding the tracks on the RF path. Detail of these changes will be given in chapter 6.

NA measurement of the chain, without the first LNA stage is shown in Figure 157. The same measurements made with a TN7101 front-end amplifier are shown in Figure 158. The irregular gain and phase response at maximum gain (V_{gain}=300mV) is due to saturation of the amplifier during the measurement. Both of these measurements show that the amplifiers perform well at all gain levels, with a very linear phase response, and a flat gain over the band of interest. The input reflection coefficient is below -8dB, at all frequencies of interest. The poor output reflection coefficient be ascribed to the mismatch between the mismatch between the 50Ω NA port and the low output impedance of the output buffer stage.

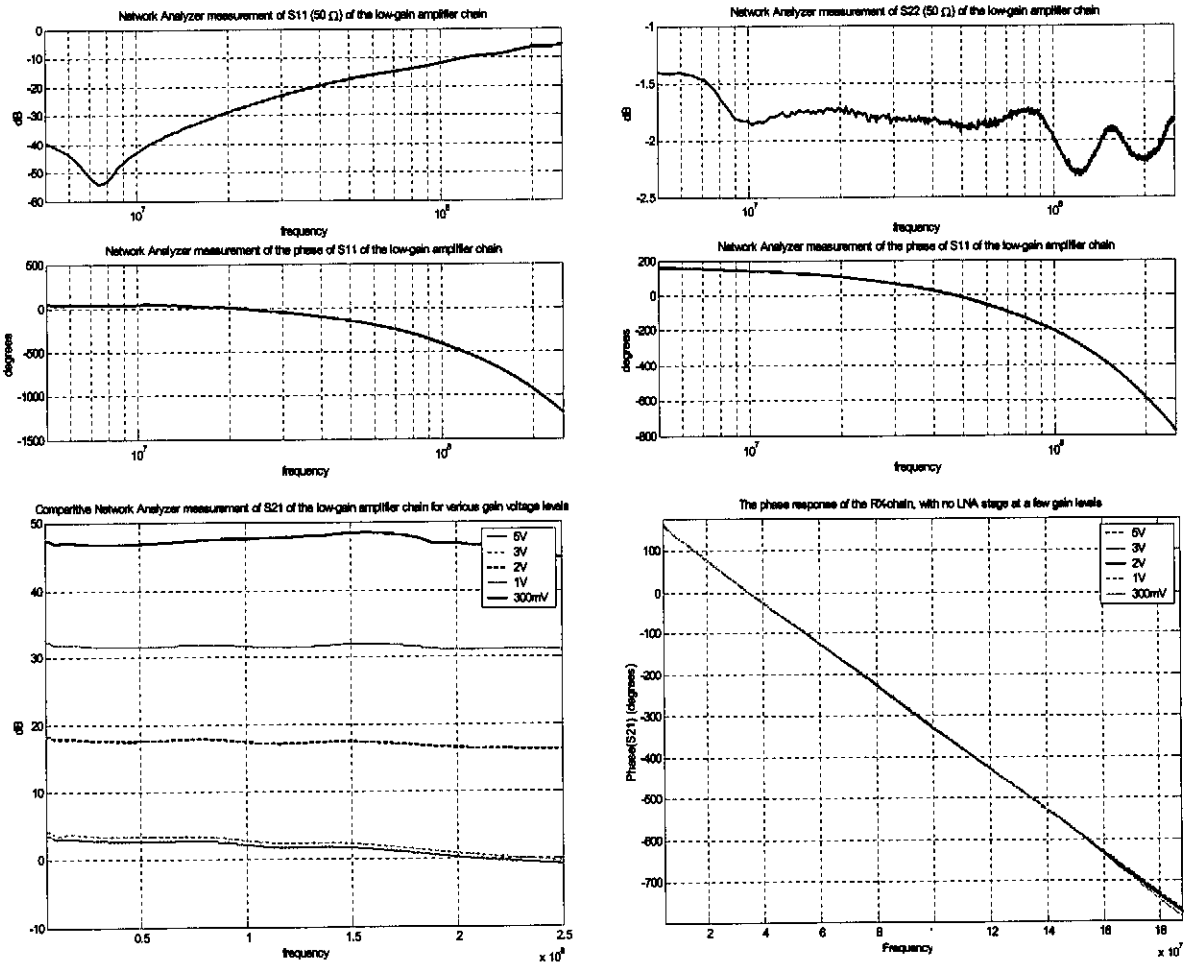

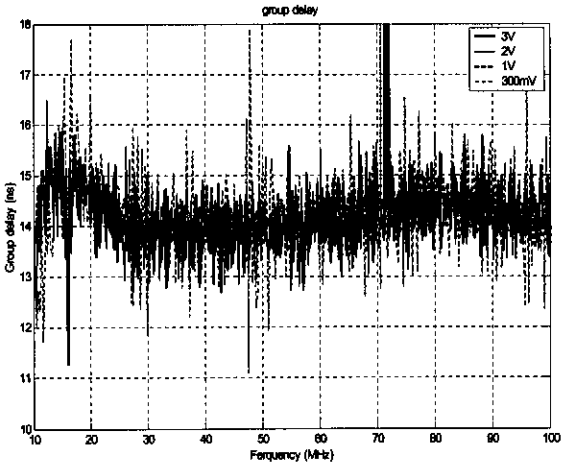

Figure 157 The NA measured S-parameters for various gain control voltages of the full RX chain without the first LNA stage

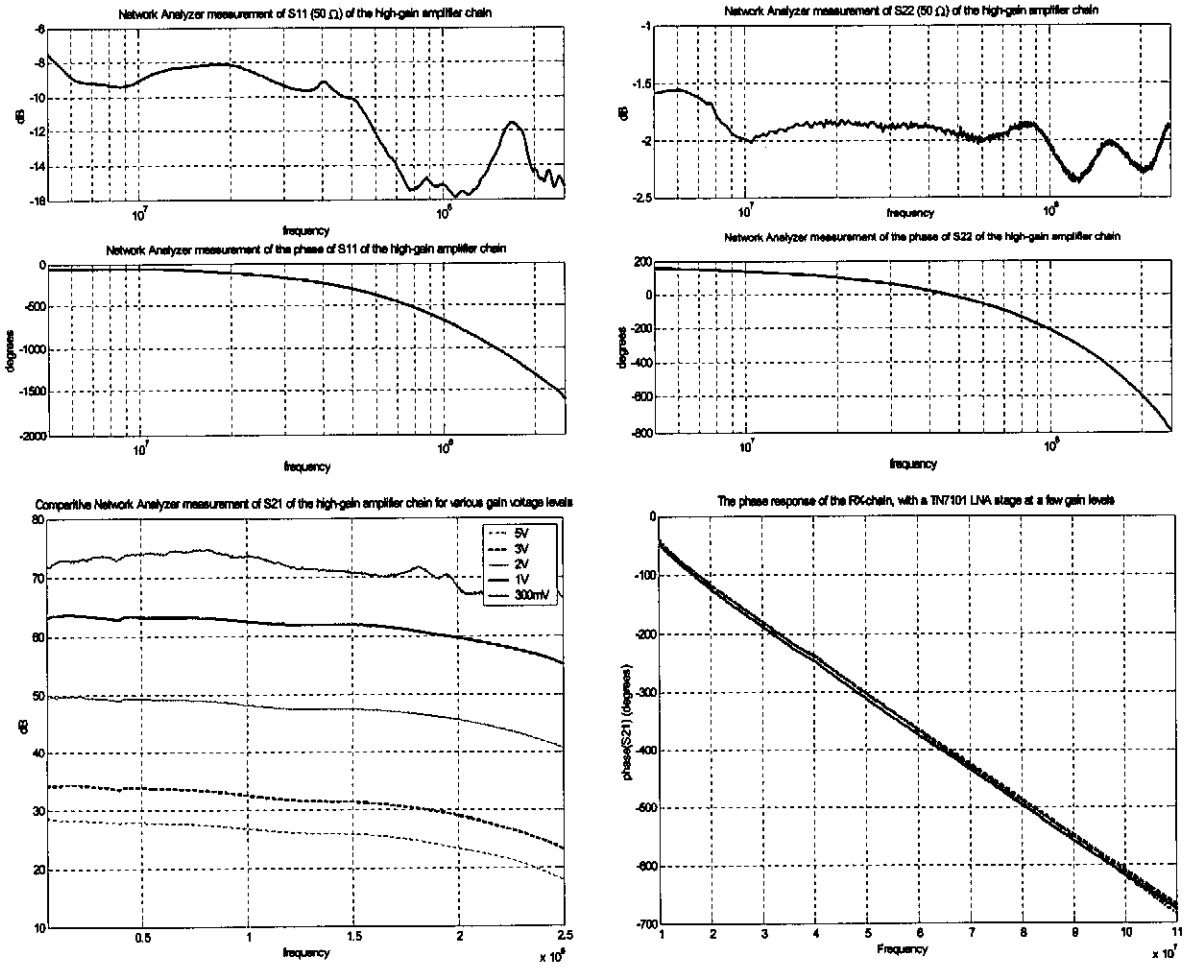

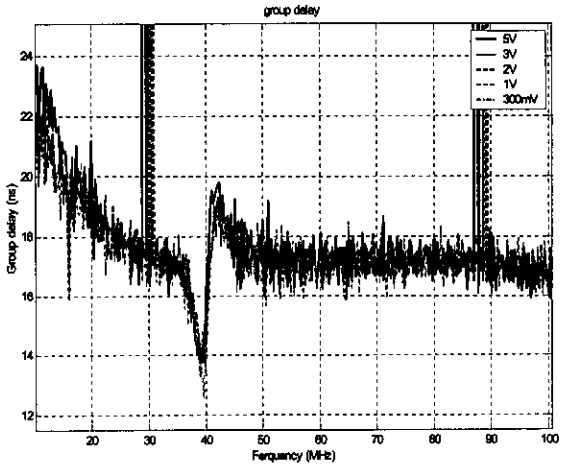

Figure 158 The NA measured S-parameters of the full receiver chain, with a TN7101 LNA front end for a few gain control voltages

3.4.5.2. Time domain characterization

Time-domain pulse response characterization of the final variable gain amplifier chain was performed using the set-up shown in Figure 159.

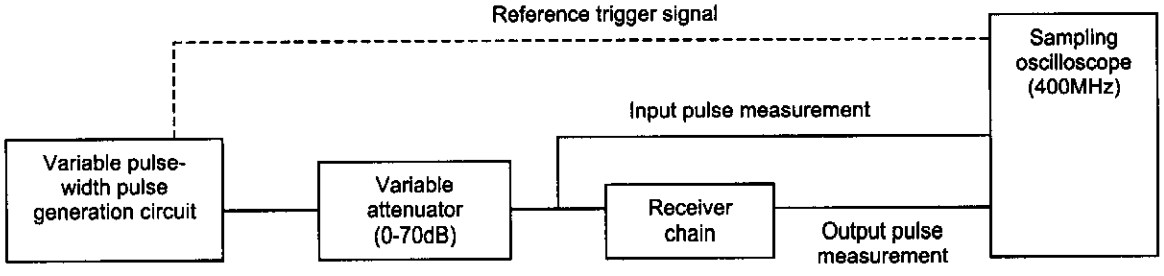

Figure 159 The measurement set-up used to characterize the time-domain pulse response of the RX receiver chain

A few typical measurement results for various pulse-width and amplitude pulses are shown in Figure 160 and Figure 161. The results show the pulse responses for both the case where no front-end component is present, and when a TN7101 LNA front end is used.

The measurements show that at minimum gain, the chain without the LNA clips at around 600mV output peak voltage for a positive-going pulse, and at –1V for a negative going pulse. At minimum gain, a 1.5mV peak pulse is easily visible above the noise at the output. When the gain is set to maximum, the circuit output clips much lower, but a 400μV input pulse is visible as a 100mV peak pulse at the output.

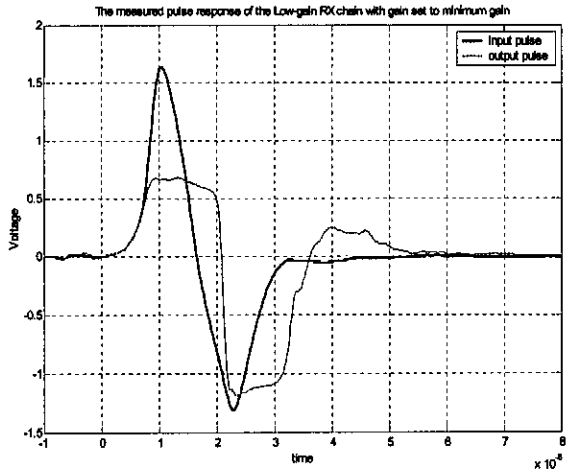
The measured pulse response of the Low-gain RX chain with gain set to minimum gain
input pulse
output pulse
Voltage
time
x 10^-8

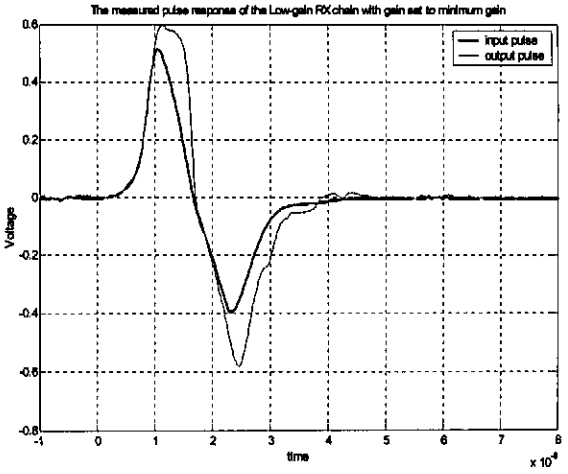
The measured pulse response of the Low-gain RX chain with gain set to minimum gain
input pulse
output pulse
Voltage
time
x 10^-8

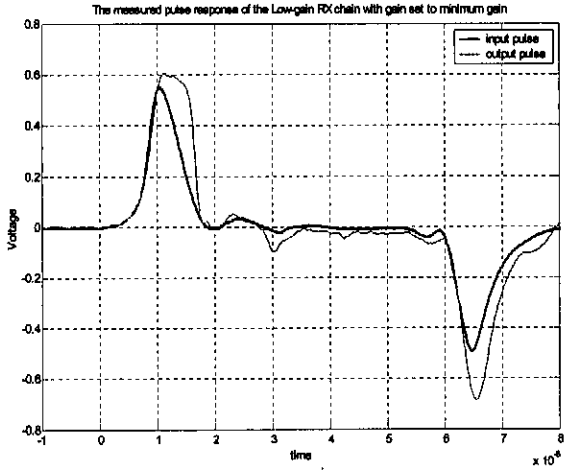
The measured pulse response of the Low-gain RX chain with gain set to minimum gain
input pulse
output pulse
Voltage
time
x 10^-8

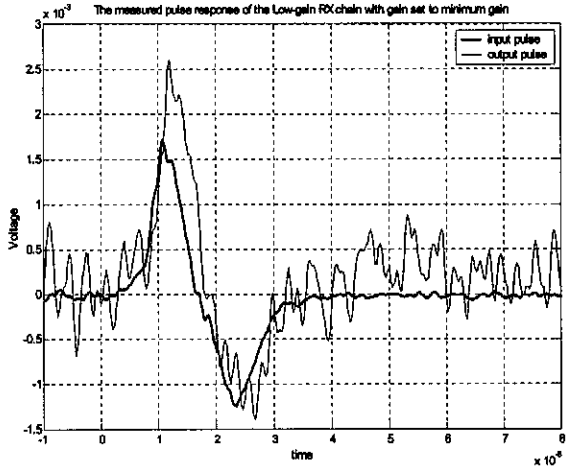
The measured pulse response of the Low-gain RX chain with gain set to minimum gain
x 10^-3
input pulse
output pulse
Voltage
time
x 10^-8

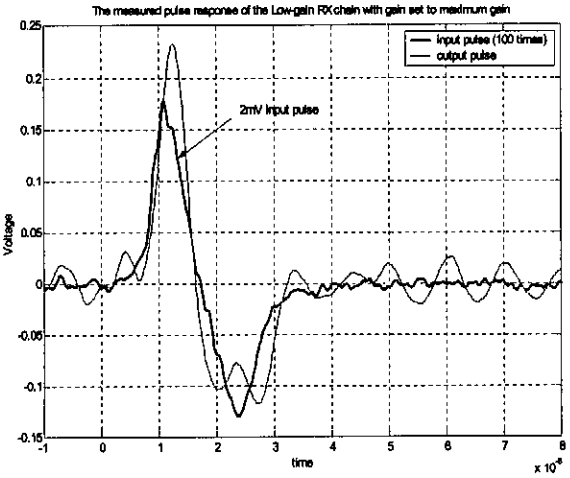
The measured pulse response of the Low-gain RX chain with gain set to maximum gain
input pulse (100 times)
output pulse
2mV input pulse
Voltage
time
x 10^-8

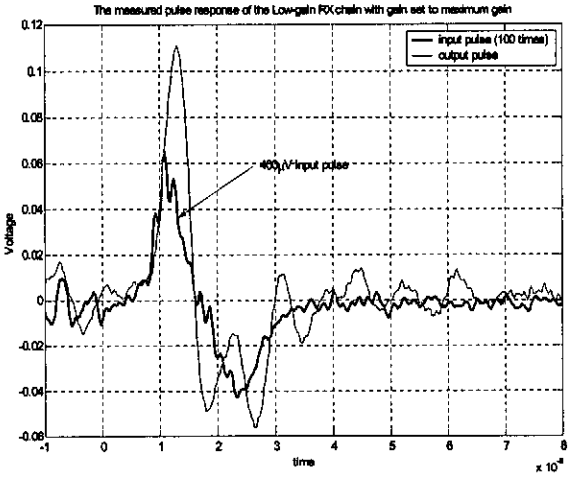
The measured pulse response of the Low-gain RX chain with gain set to maximum gain
input pulse (100 times)
output pulse
400μV input pulse
Voltage
time
x 10^-8

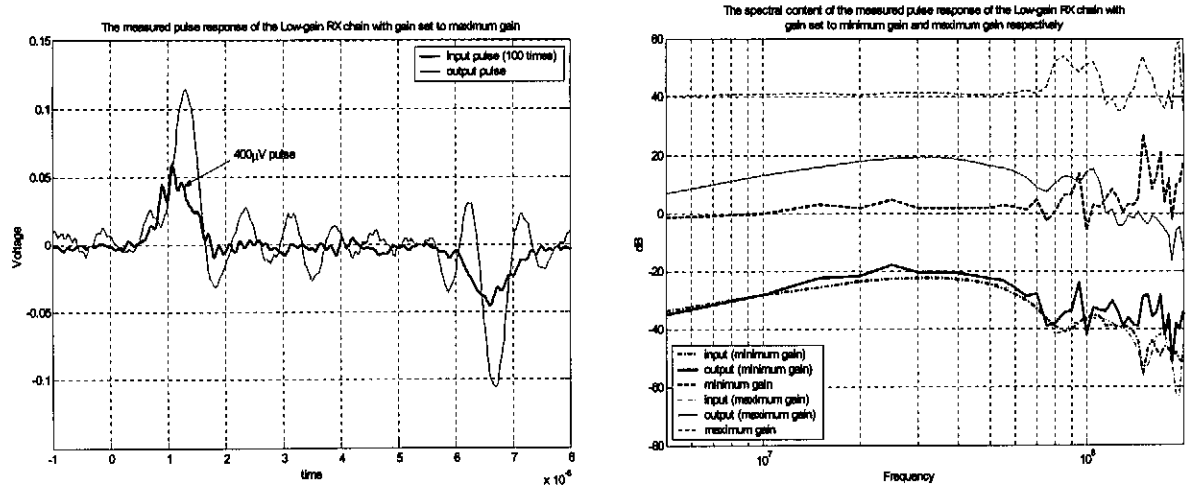

Figure 160 The time domain measured pulse response of the receiver chain with no LNA front end

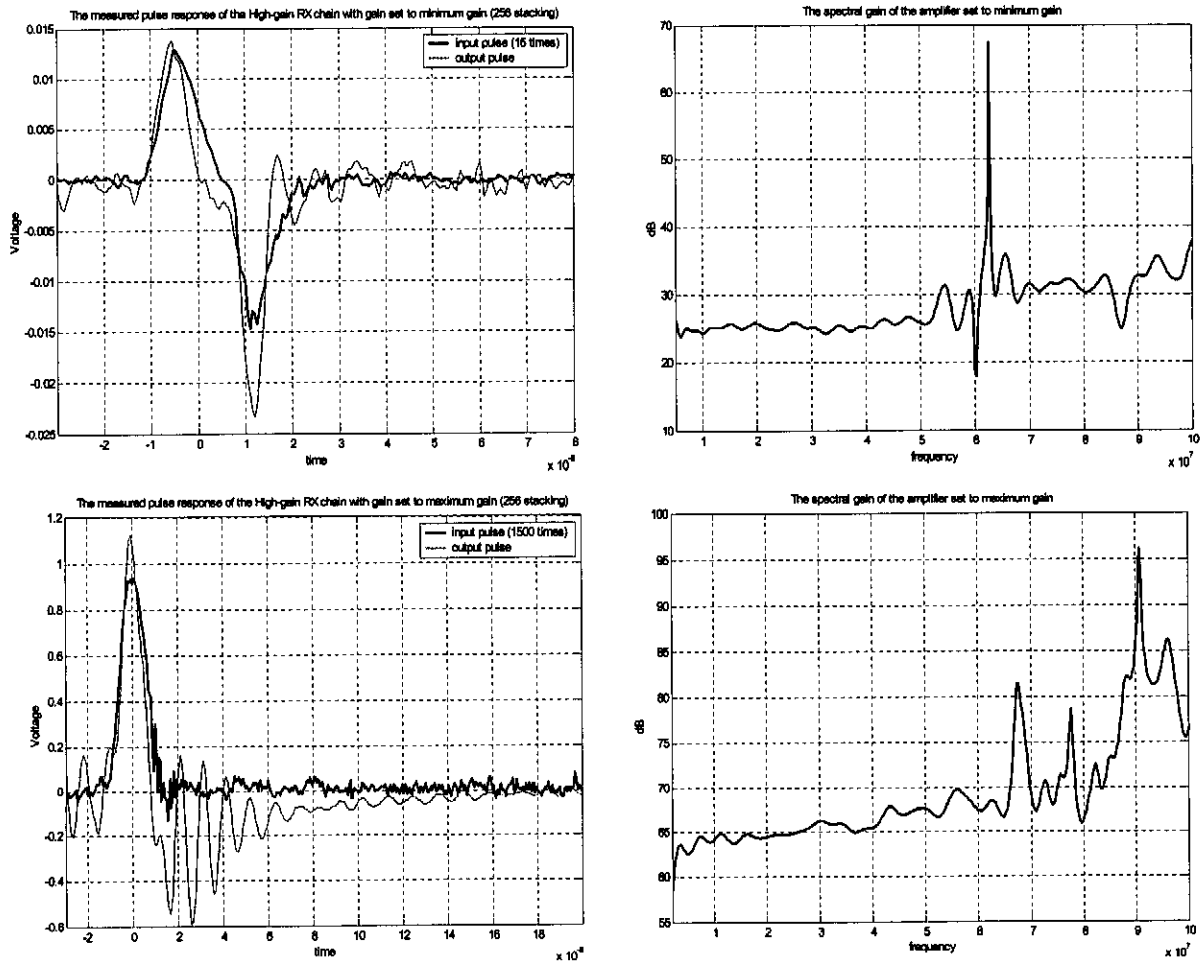

Figure 161 The time domain measured pulse form of the full receiver chain with the TN7101 LNA front end

For the chain with the LNA front end, the minimum gain is around 25dB, and the clipping point is relatively low. At maximum gain, the chain gain is in the order of 60dB, and a 600μV input pulse is accurately reproduced at the amplifier output as a 1V peak voltage pulse.

3.4.5.3. Mono-static characterization

In order to show the operation of the receiver circuit in a full mono-static system, a receiver chain was connected to the mono-static transmitter/circulator developed by Van der Merwe[9]. The bench set-up and a few measurement results are shown in Figure 162. The first result presented in Figure 162 shows the operation of the ST-receiver used in the existing BHR system in a mono-static environment. This result demonstrates the typical saturation problems that would be encountered when attempting to realize an operational mono-static radar with a general set gain amplifier. The ST amplifier remains in saturation 1.25μs, after which received signals can be observed superimposed on the ringing artefact of the chain saturation. The chain only recovers to stable operation more than 3μs after the beginning of the transmit pulse. Data capturing capability will be lost for almost the entire acquisition period.

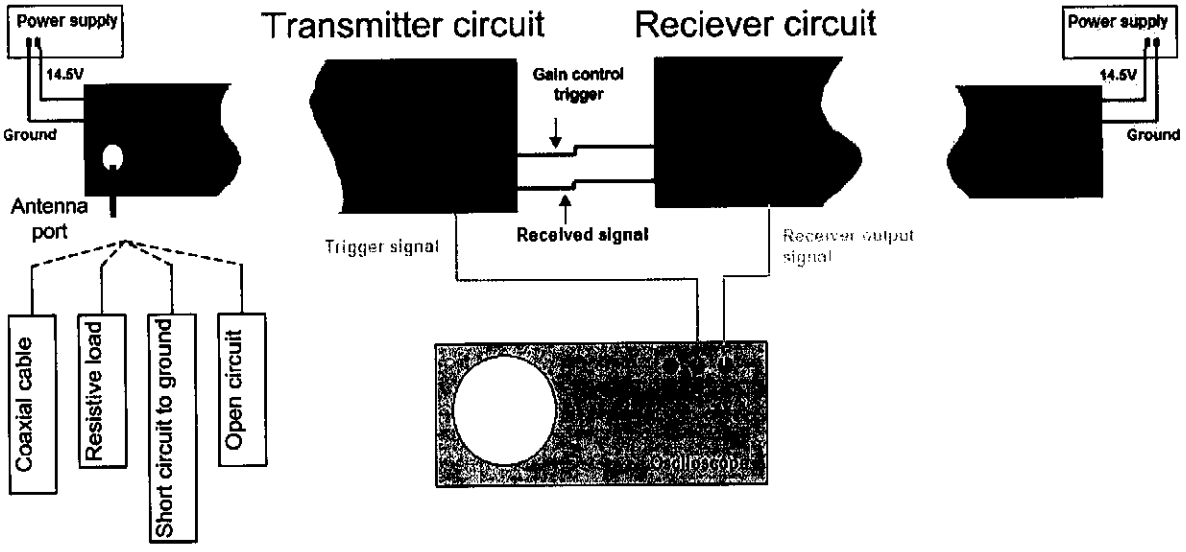

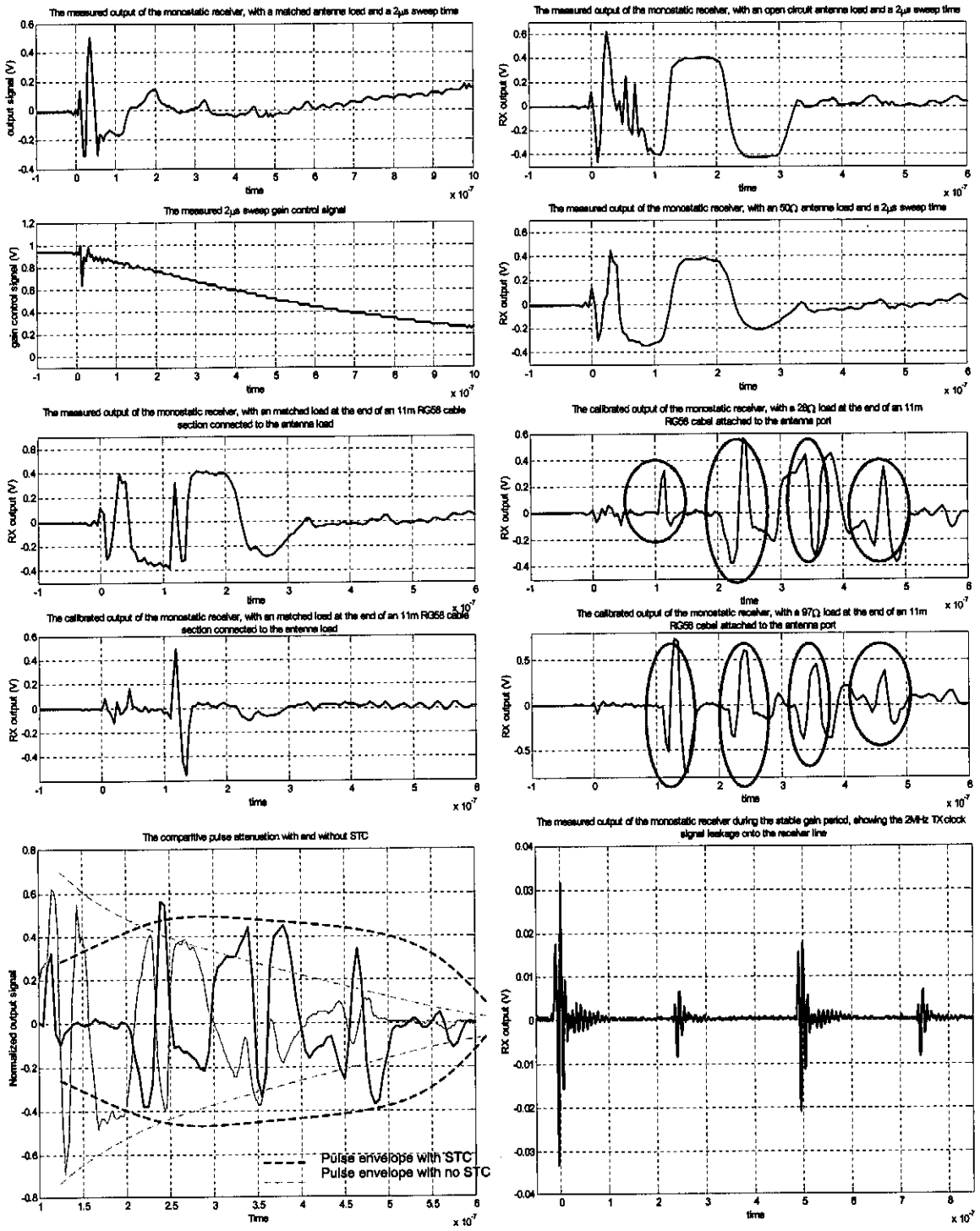

Figure 162 The measurement set-up used to measure the operation of the full mono-static system on the bench and a few typical measurements showing the performance of the system

The measurement results of Figure 162 include measurements performed under four antenna load conditions, as shown. The first two cases are trivial, with an open circuit or dead short at the port. The third case is when a resistive load is placed between the two differential terminals of the antenna port.

The last case has a coaxial cable section attached to he antenna port (for the measurements shown, an 11.05mcable was used). If a coaxial cable is attached to the antenna port, a travelling wave will be excited on coaxial cable during the transmit period, which will propagate to the end of the cable. A percentage of the propagating energy will be reflected at the end of the cable and propagate back towards the electronics. By varying a resistive load at the cable termination, the size and sign of the reflection can be controlled. This measurement effectively approximates an operational BHR system, and we can accurately predict the expected received pulses by considering the length, termination impedance and propagation properties of the coaxial cable.

For the 11,05m coaxial cable used in the measurements of Figure 162 (standard RG58, 50Ω coaxial cable), the propagation velocity and propagation time from the electronics to the cable termination and back are computed as shown in (3.14). We can therefore predict that the received pulses should be at multiples of this time.

$$\begin{aligned} c_{cable} &\approx 0.659 \times c_o = 197.677 \times 10^6 \, m/s \\ d_{propagation} &= 2 \times 11.05 = 22.10m \\ t_{propagation} &= \frac{d_{propagation}}{c_{cable}} = 111.74ns \end{aligned} \tag{3.14}$$

The results of Figure 162 clearly show the reflections measured at the receiver output (note that the reflections with the STC receiver do not die away exponentially as we would expect, due to the increasing gain with time). The time between the measured pulses (circled in grey) is measured as 111.76ns. This translates to an 11.04m length of RG58 cable (assuming the propagation velocity of (3.14)). The reflection pulses do indeed appear at the positions where we expect them. The final plot of Figure 162 shows a feature of the mono-static system that is noticeable when the measured data is closely considered. The receiver output shows regularly spaced high frequency 'glitches'. Careful consideration of these glitches indicate that the are due to coupling of radiation on the edges of the 2MHz clock signal generated using a crystal oscillator on the mono-static transmitter circuit to the receiver port of the circulator. This coupling is undesirable, and can be reduced by more careful layout of the transmitter board.

3.5. Conclusions

The following conclusions are made based on the results outlined in this chapter:

- A low-noise, linear phase-response amplifier with a bandwidth of 10MHz to 100MHz and a peak gain of approximately 60dB is required for an acceptable BHR receiver amplifier. Such an amplifier is realizable within the spatial and operational constraints of the BHR environment.

- The saturation properties of the receiver chain are critical for mono-static application. The receiver must be able to recover from a voltage input pulse of approximately 1V peak in times typically shorter than 100ns. The saturation recovery time of high gain amplifier chains for such an input pulse is generally too long

- Receiver topologies used in existing bi-static BHR radar systems were introduced and characterized. It was shown that although these receivers do generally adhere to all the requirements for general bi-static application, their pulse-saturation responses render them unacceptable for general mono-static application.

- A few low-noise gain blocks were considered and characterized with respect to their frequency-domain and pulsed time-domain operation.

- In order to overcome transmitter-leakage saturation limitations, the application of time-variable receiver gain was considered. It was shown that automatic gain control (AGC) is not effective for pulsed applications where a large initial leakage pulse must be catered for. Sensitivity time control (STC), based on the predicted variation in the peak received pulse magnitude with time, was identified as a more appropriate method of gain variation.

- A variable gain amplifier component was chosen for investigation of the application of variable gain in a BHR receiver chain. The component was implemented and characterized with respect to both its steady-state and pulsed frequency-domain and time-domain response.

- It was shown that STC implementation is possible in a BHR application. A number of weaknesses in the application of STC using the chosen component were identified. These weaknesses relate to the extremely fast sweep-time required in an STC BHR application and the high additive noise characteristics observed due to the principle of operation of the variable gain component.

- An operational prototype receiver design was completed and realized. The full receiver chain incorporated a low-noise front-end component, STC-stage application and an optical capability to interface with existing systems for field-testing purposes.

- The full receiver chain was characterized with respect to its frequency and time-domain performance.

- The mono-static receiver was successfully interfaced with operational mono-static transmitter and circulator circuitry. The operation of the receiver under typical operational mono-static conditions was measured and characterized in the laboratory. It was shown

that the receiver was able to operate satisfactorily with minimal data loss due to transmit-signal leakage onto the receiver port (valid data was observed approximately 80ns after the transmitter is fired).

- Four critical weaknesses were identified during characterization of the mono-static receiver system that make it non-ideal for BHR application. These issues need more attention to improve the operation of the receiver chain.

- The gain-sweep gradient required for effective BHR application exceeds the realizable sweep gradient of the receiver chain. Another component must be considered for application as a variable gain amplifier to correct this weakness, and to prevent loss of data due to spurious transients on the output signal of the receiver.

- The extremely high noise figure of the variable gain amplifier stage necessitates the use of a relatively high gain LNA front-end, and effectively worsens the chain noise figure, especially for low gain settings. The necessity of a high gain LNA also drastically reduces the large signal handling capabilities of the chain. Little can be done about the noise figure of the VGA, but the LNA must be carefully chosen to reduce the chain noise figure without compromising the large signal capabilities of the chain. Further study of available components, and methods of improving the front-end large impulse response, without worsening the noise characteristics of the system is necessary.

- The circulator isolation circuitry effectively introduces an attenuator loss between the antenna and the receiver feed. This signal attenuation has a large effect on operation of the receiver (particularly in terms of SNR) and the dynamic range of the system, and must be minimized.

- The leakage of transmitter signals onto the receiver port is undesirable, and compromises the integrity of the output signal and the intrinsic isolation of the circulator. The transmitter clock signal observed on the receiver output suggests that careful consideration of the internal signal coupling to the receiver port is necessary to improve the integrity of acquired data, and also the RX-TX isolation.

Chapter 4 The transmitter and mono-static isolation

In this chapter, we will consider the mono-static transmitter, and the problems associated with achieving the necessary isolation between the transmitter and the receiver in the co-located, mono-static configuration. Unless otherwise indicated, this chapter contains a summary of work done by Van der Merwe in his thesis titled '*The design of a monostatic ultra wide band VHF pulsed radar for detection of close-in targets*' [9].

We will begin by considering the mono-static transmitter theory of operation. Next, we will consider the incorporation of this transmitter into a circulator-based isolation topology, and finally operational measurements of the realized transmitter/circulator circuitry will be presented.

4.1. The basic transmitter topology

A functional block diagram of the transmitter designed by Van der Merwe is shown in Figure 163.

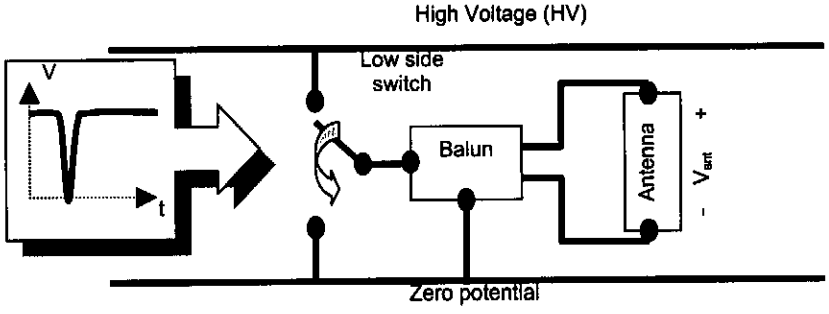

Figure 163 A functional block diagram of the mono-static transmitter circuitry

The balanced antenna structure is driven through a balun that is realized by the probe structure itself (see [9] and section 5.1.4). The antenna arm in which the probe electronics is housed is chosen as the zero potential point, while the other arm of the balanced structure is kept at a nominal voltage of 370V. During the transmit period, the high-voltage antenna arm is jerked down to ground potential, and back to 370V in a total time of approximately 20ns, thus exciting a short, high voltage pulse on the antenna structure. In order to realize this functionality, a carefully designed MOSFET-based switching topology is employed, in conjunction with a high voltage step-up DC-DC converter block. The functional circuit of the transmitter is shown in Figure 164. (Note that no component choices are shown on this schematic)

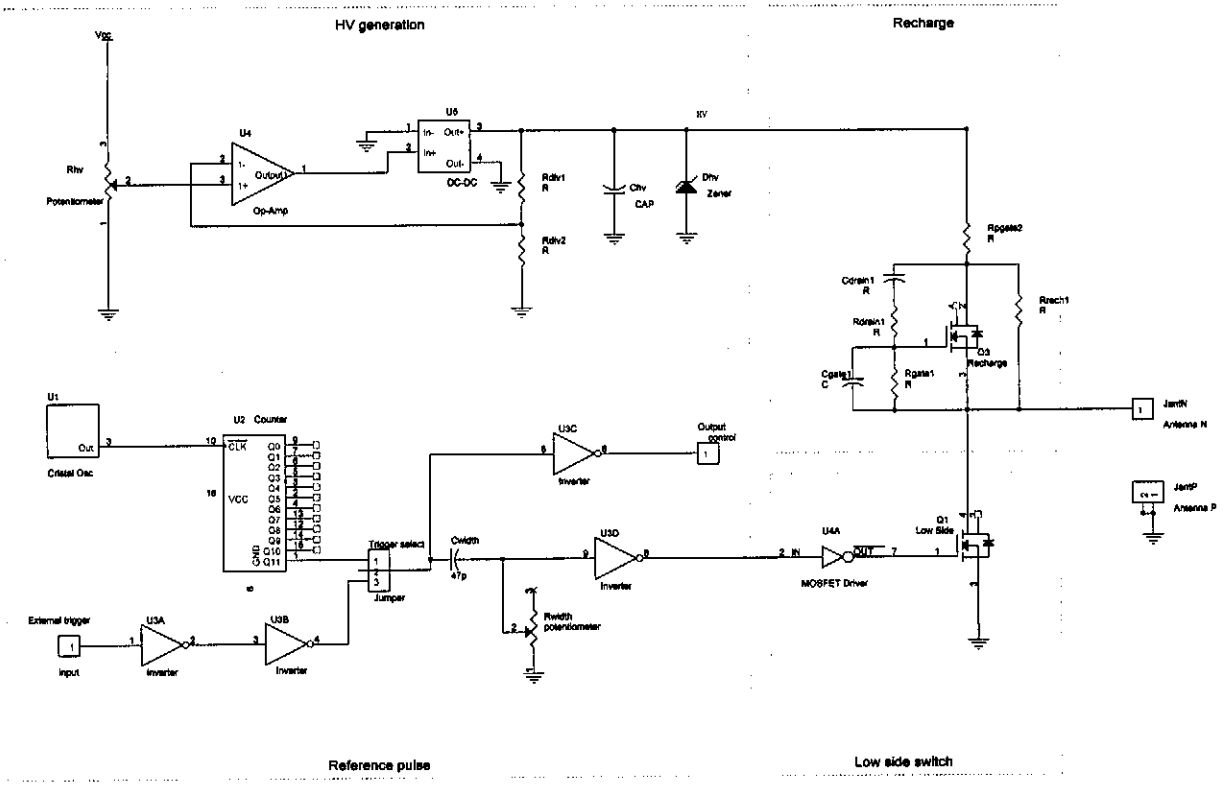

Figure 164 The circuit diagram of the transmitter topology chosen for mono-static application

4.2. The isolation strategy

The isolation strategy employed in the mono-static BHR radar system is arguably the most critical and most important factor in the successful realization of an operational system. The purpose of this strategy is to realize a method of effectively isolating the high-voltage pulses generated by the transmitter circuitry and the sensitive receiver circuitry, while maintaining a concurrent signal path from the transmitter to the common antenna and from the common antenna to the receiver. A number of theoretical methods can be postulated in order to achieve such isolation, including switching mechanisms, limiter chains, etc. For BHR mono-static application, Van der Merwe chose a circulator-based strategy. A functional block diagram showing the chosen concept is given in Figure 165.

The operation of the circulator concept is based on the differential comparison of the transmitter pulse form with an internally generated approximation of the same pulse. This differential signal is then fed to the receiver port.

During the transmit period, if the internally generated pulse (estimator pulse), and the feed pulse at the antenna port are identical, then no leakage of the transmit signal will occur. This is only true in the ideal case, where the 'dummy load' used to generate the estimator pulse presents an identical load impedance to that of the mono-static antenna. Any difference between these two loads will result in a differential miss-match between the antenna pulse and the estimator pulse, and a reduction in the

effective isolation. A lumped element network at a stable point can approximate the load impedance presented by the antenna, but this impedance will change as the environment of the antenna changes, resulting in an inconsistent, variational isolation. The circulator topology must be realized so as to be as tolerant as possible for such variation.

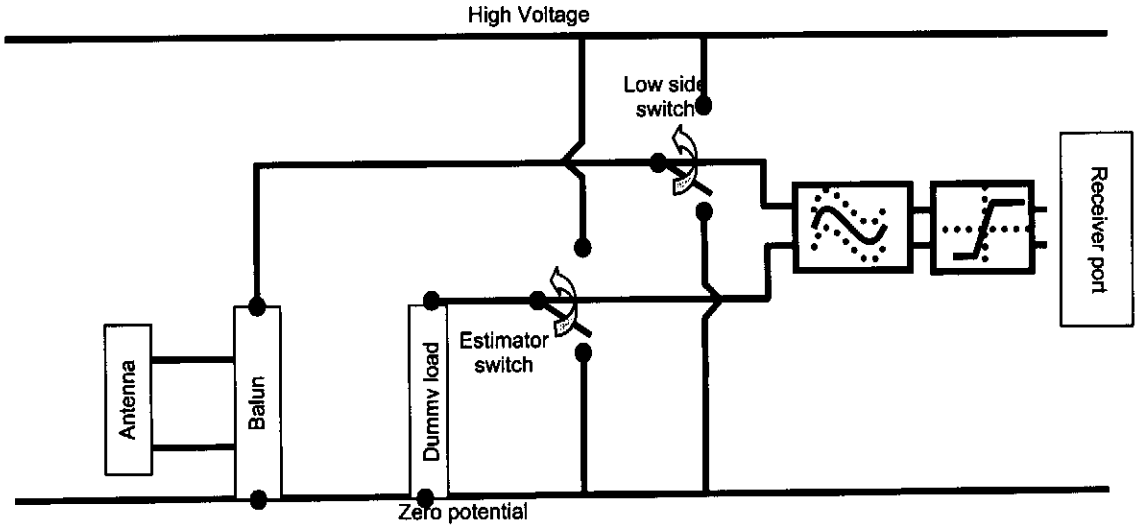

Figure 165 A functional block diagram of the circulator concept used to realize isolation between the transmitter and receiver in a mono-static configuration

During the receive or acquisition period, no signal will be present on the estimator side of the differential receiver feed, but any received reflections on the antenna will induce a signal at the antenna port. The differential feed to the receiver will thus ideally be exactly the signal received at the antenna feed point. Losses in the receiver feed path musty therefore be minimized, to allow for maximum power transfer to the receiver port, and to minimize the additive noise of the receiver feed path. The full circuit realization of the transmitter and circulator electronics is shown in Figure 166.

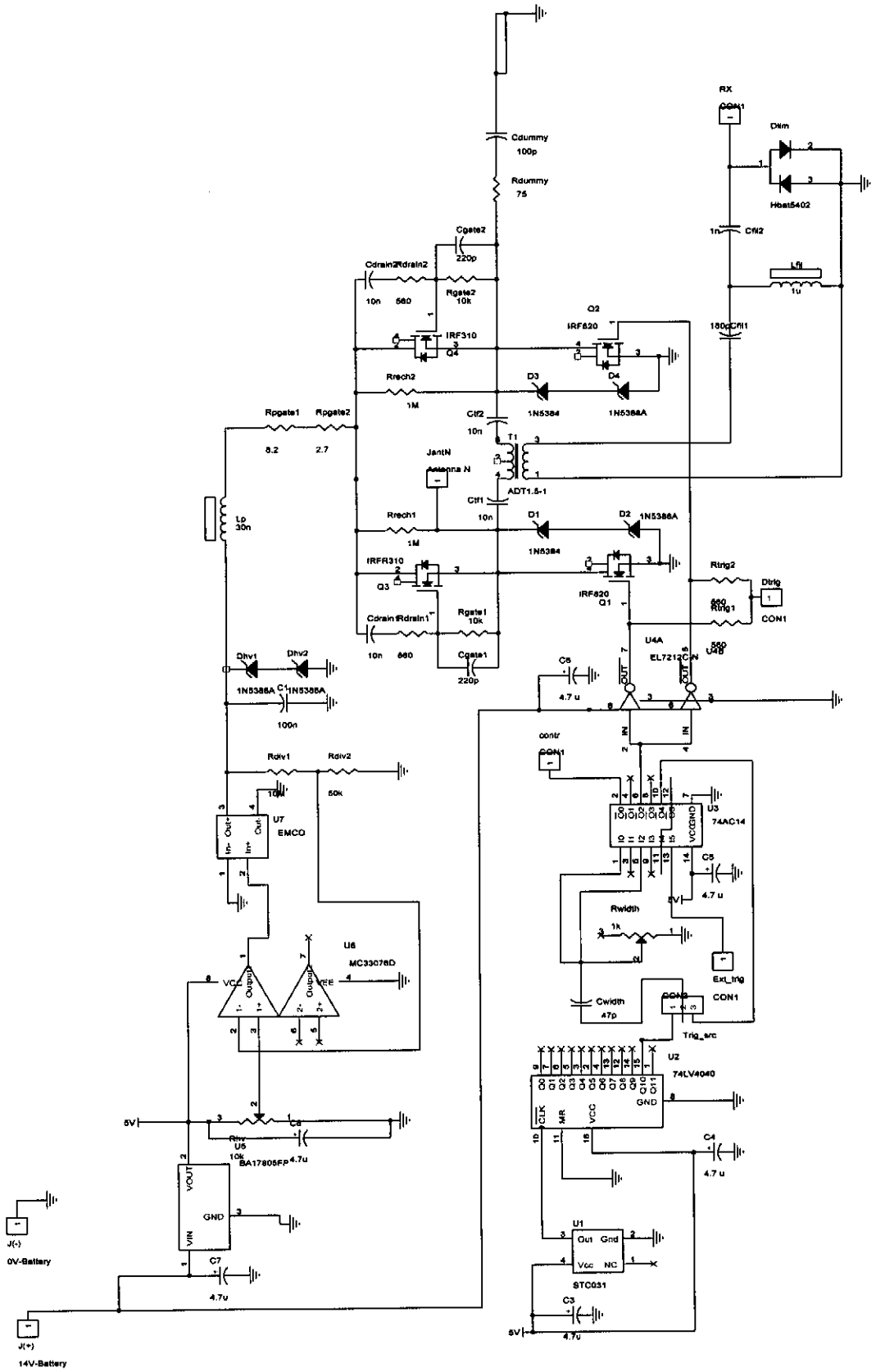

Figure 166 The full circuit diagram of the realization of the transmitter and circulator electronics

4.3. The layout and measurement of the operational circuitry

In this section, we will present a few measurements of the operation of the transmitter and isolation circuitry described in the previous section.

The PCB layout of the transmitter and circulator is shown in Figure 167.

Top layer

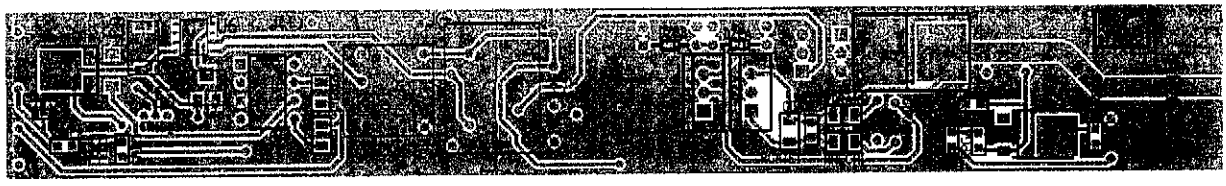

Bottom layer

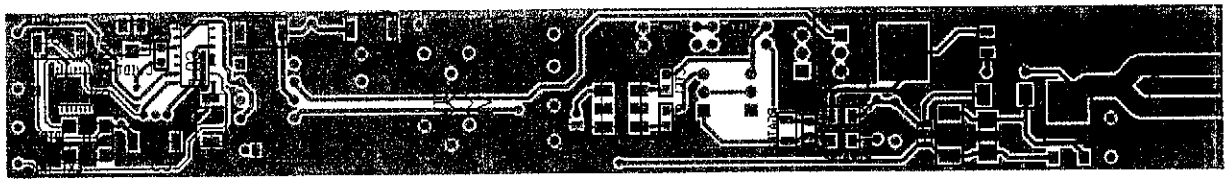

Figure 167 The PC-board layout of the mono-static transmitter and circulator topology

The estimator and antenna feed pulses, with a non-ideal approximation of the simulated antenna load impedance at the antenna port, is shown in Figure 168, along with the direct differential signal generated due to the load mismatch (before the filter and clamper circuitry).

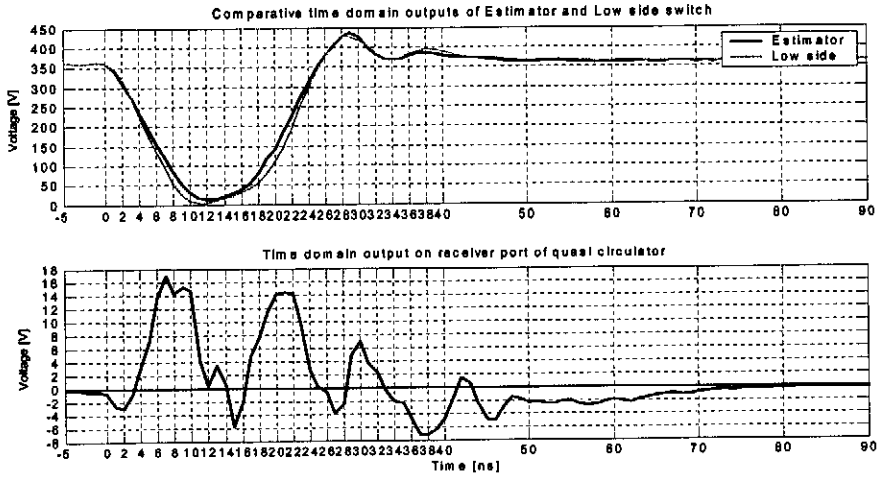

Figure 168 The measured estimator and antenna feed pulses, and the differential signal generated due to load mismatch

The typical peak differential leakage is in the order of 16V (approximately 27dB initial isolation). This is clearly still too large for the sensitive receiver circuitry. In order to improve the isolation, a filter and clamping limiter were added in the receive path. The time-domain effect and final output isolation achieved after these blocks is shown in Figure 59. The final isolation achieved is in the order of 55dB, with ~1V peak leakage to the receiver port.

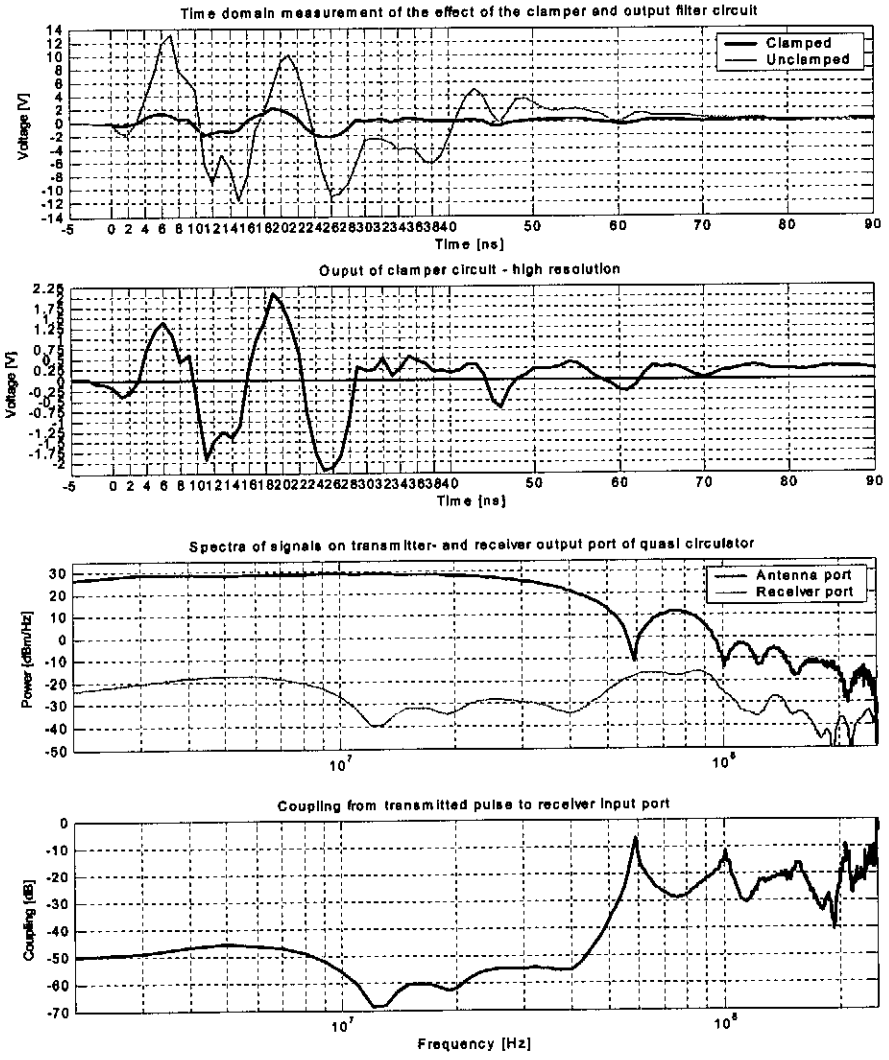

Figure 169 The final clamped and filtered leakage signal, fed to the receiver port, and the measured effective transmitter-receiver isolation

The measurement results presented in Figure 169 clearly show the need for the output filter and clamping circuit.

The final critical factor that must be considered in the characterization of the isolation scheme is the undesirable losses in the received signal path. These losses will have a large effect on the sensitivity of the system, and more importantly on the noise figure and dynamic range of the receiver. The measured

transmition between the antenna and the receiver port is shown in Figure 170. Losses in the received path signal are measured as approximately 8dB to 10dB over the band of interest. Three causes of these losses can be identified by consideration of the circuit layout.

- The output capacitance of the off-state MOSFET is in parallel with the antenna load during the receive period. This impedance effectively shunts the differential antenna feed, introducing losses.
- The 'dummy' impedance of the pulse estimator circuitry is effectively in the receiver path. For this reason, the dummy impedance must be chosen as small as possible, without compromising the isolation.
- The filter and clamper circuit introduce a small amount of loss into the receiver path, but their effect is very much secondary to the other two loss mechanisms.

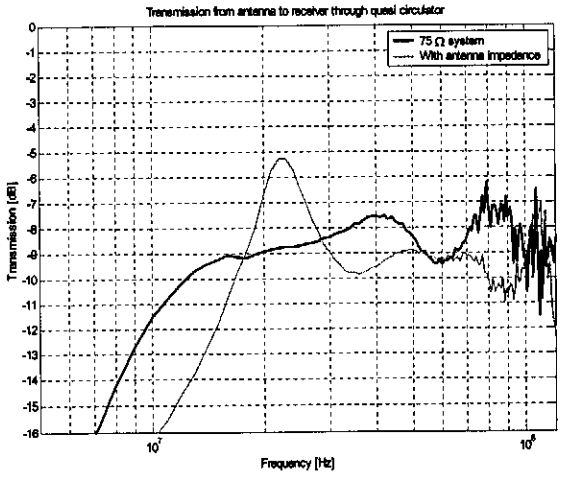

Figure 170 The measured transmition from the antenna port to the receiver port of the circulator circuit, showing the RF path losses introduced by the filter and clamper blocks

These receiver path losses will clearly be one of the most significant limiting factors in the operation of the mono-static system, damping the achievable dynamic range of the system dramatically.

Chapter 5 Design and layout of a prototype mono-static borehole radar system

In this chapter, we will consider the mechanical structure and electronic layout of a prototype probe developed during the course of this thesis. We will begin by outlining the mechanical design and then look at the electronic layout and practical realization and testing of the probe.

5.1. The mechanical design of the prototype probe

We will begin by considering the basic constraints on the physical probe structure that must be taken into account during the design. Based on these constraints, we will consider the external layout of the probe.

5.1.1. Considerations to be made during the probe design

The first obvious consideration when looking at the structure of the probe is the spatial constraints placed on the probe by the environment in which it will operate. The approximate borehole diameter that the radar is designed to be deployed in is around 48mm. The borehole radar probe must be housed inside a structure that can easily be inserted and moved up and down in the borehole, even if debris narrows the effective borehole radius at places.

The nature of the environment in which the BHR system will operate introduces a number of criteria for the probe packaging. The first and most obvious of these is that the packaging must be fully waterproof, and must protect the electronics inside the housing, even when the probe is fully submerged. Any interface connections must also function well, despite submersion. The probe packaging must be robust, and able to protect the internal electronics even when the probe is treated roughly, while maintaining reasonable probe weight to the limit the strain on the surface connecting cables. The packaging and all the connections must be able to handle the temperature variations expected in the mining environment. Any connections must be protected from dirt, and easy to clean in the event that they do get dirty.

At all stages of the BHR probe design, the cost and complexity of the probe must be considered. An attempt must be made to keep both of these to a minimum, in order to minimize the financial and replacement-time implications of loosing a probe while it is down hole, and to improve reproducibility during construction. The on site preparation and assembly of the BHR system during a survey must be kept as simple and repeatable as possible to simplify the identification of the source of system failure encountered during a survey (poor connections etc.).

5.1.2. Mechanical structure of the probe

In order to facilitate easy insertion manoeuvrability of the probe in the borehole, we will keep the external diameter of the probe structure the same as that of the existing BHR probes (that is, 32mm). This affords a clearance of 8mm on all sides in a standard 48mm borehole. The length of the probe structure will be limited to 2m in total, and can be sectioned into two sections to facilitate easy transportation of the probe in the mine environment. The external structure of the probe is sketched in Figure 171.

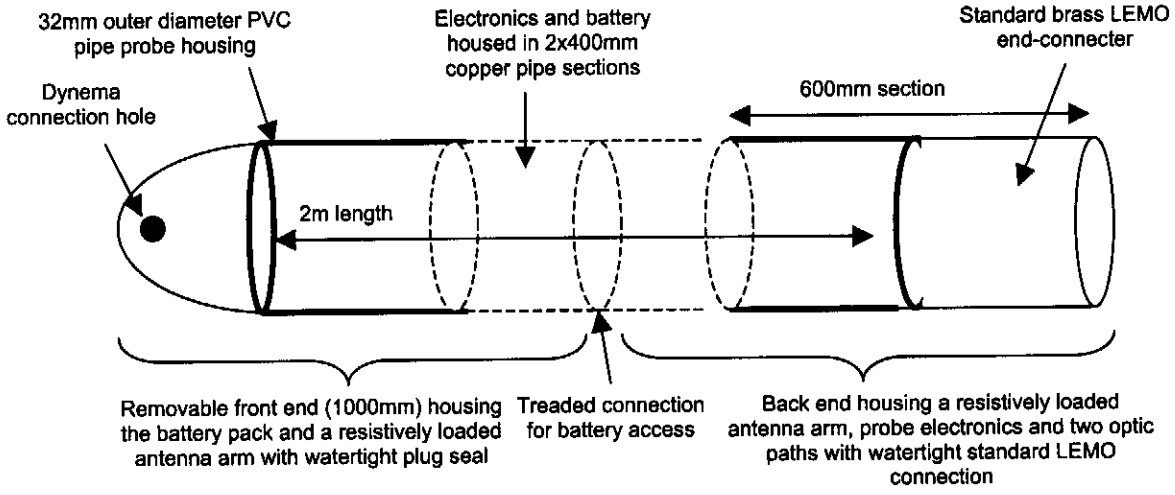

Figure 171 The external structure of the prototype probe

The first section of the probe structure houses the battery pack (inside a 400mm copper pipe section) and a 600mm resistively loaded, centre located strip section, connected to the battery housing. The end of this section is sealed with a PVC plug. The second arm houses the probe electronics, again inside a 400mm copper pipe section, terminated with a 600mm centrally located loaded strip. Two optical paths also run parallel with the loaded strip section, to carry the trigger and received signal to the brass LEMO fitting used to interface to the existing DAQ system.

5.1.3. General internal layout of the probe

The internal layout of the probe is shown in Figure 172. The two side sections contain the resistively loaded arms of the antenna structure, the battery pack and the means of connection to the up-hole DAQ (this surface connection will become redundant once the onboard digitisation and storage have been implemented and included in the probe). The transmit and receive electronics are housed in a separate copper pipe housing, which forms a common ground for the electronics. There is a removable joint between this pipe, and the removable arm housing the battery pack.

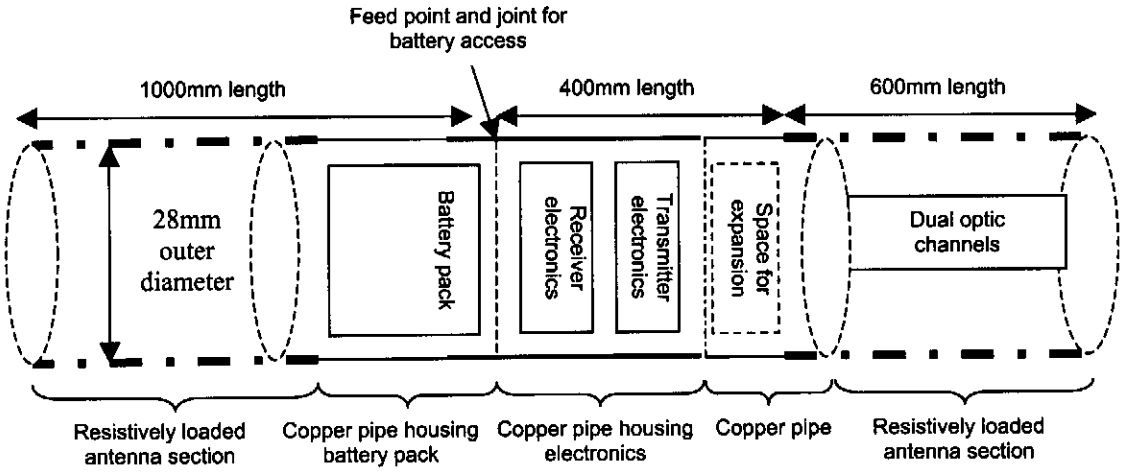

Figure 172 The internal layout of the probe

5.1.4. The antenna feed structure and RF isolation of the DC power feed

The antenna employed in the probe structure is a centre-fed, symmetrical structure, designed in Chapter 2. The electronics and battery pack of the probe are located on either side of the antenna feed point, and the feed structure must thus be designed to provide for three factors.

- The structure must provide a balanced RF feed path for the electronics.
- The structure must provide a DC path for current to flow from the battery pack to the probe electronics on the other side of the feed section.
- The RF and DC paths must be isolated, and not interfere with each other in any way.

The detail of the feed section designed to provide for these three requirements[29] is shown in Figure 173.

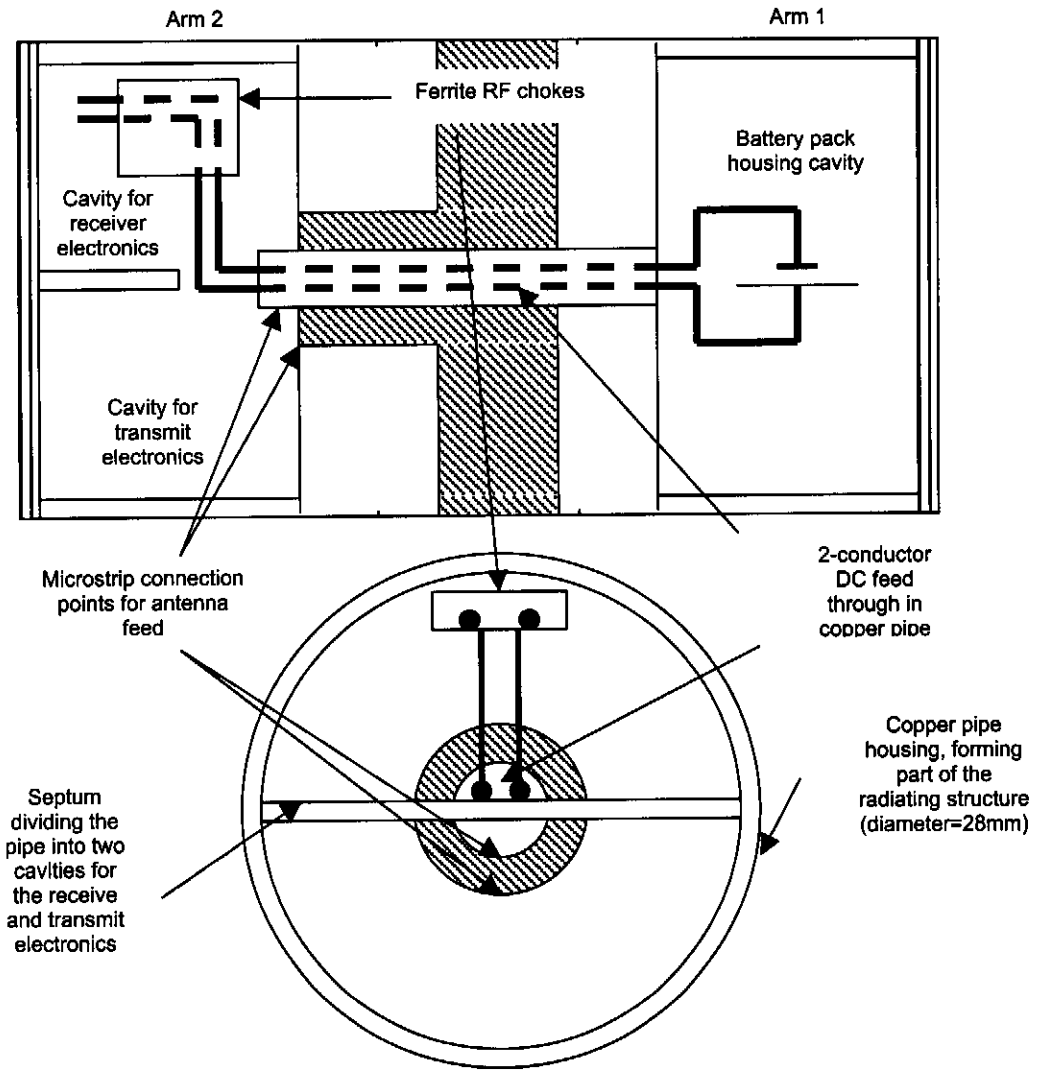

Figure 173 The detail of the feed section and the DC feed through (axial and radial cross sections)

We can simplify Figure 202 to show the RF paths in the feed structure as shown in Figure 174. Path 1 Shows the RF path for the feed of arm 1 of the antenna. The RF current travels along the microstrip feed structure, onto the copper housing for the DC feed through, and onto the arm of the radiating structure. Path 2 shows the return current path through arm 2. The current flows along arm 2 and onto the ground plane of the microstrip feed structure. Path 3 shows an alternative path for RF energy, along the DC feed wires. This path must be made high impedance for RF energy to prevent current following this path. This is done using ferrite chokes, as shown in Figure 202. The form of the RF fields in the dielectric structures are shown as arrows.

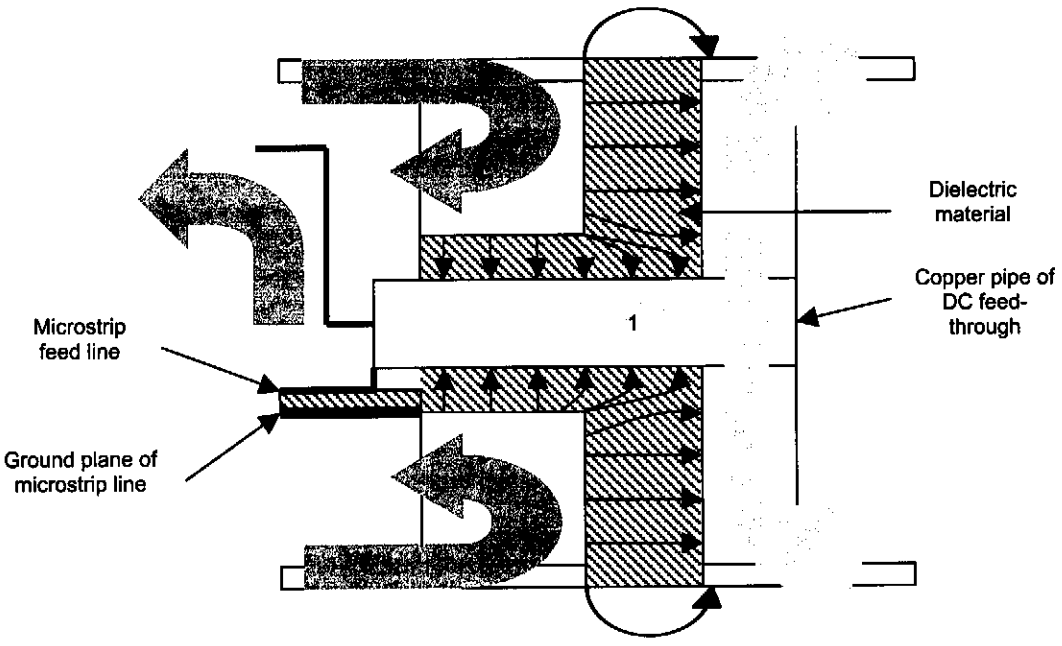

Figure 174 The RF paths at the feed section

The only path for DC current is along the one insulated conductor in the DC feed-through copper pipe, and back along the other insulated conductor.

The ferrite chokes must be chosen so that the RF impedance on path 3 is high at all frequencies of interest. This implies that the ferrite choke impedance at all frequencies of interest must be larger than the real impedance of the antenna structure (assumed as below 200Ω) and the input impedance of the receiver front-end (approximate maximum of 1kΩ). The impedance of the ferrite choke depends on the material and geometry of the bead, the number of turns used in the structure and the frequency under consideration. The choke must be designed so that the ferrite material will not become saturated at any time by the DC current that passes through it, and thus loose its inductive impedance characteristic. A number of ferrite materials were investigated. Measurements were performed to determine the operational impedance, and saturation currents of the structures at frequencies in the band of interest. Measurements made on the ferrite choke that was chosen are shown in Figure 175. The bead shows good impedance over the whole band of interest. In order to determine the flux level at which the ferrite material will saturate, and thus no longer operate, a set-up was used as shown in Figure 176. The measured inductance for the single turn, as the DC flux/current was changed is also shown.

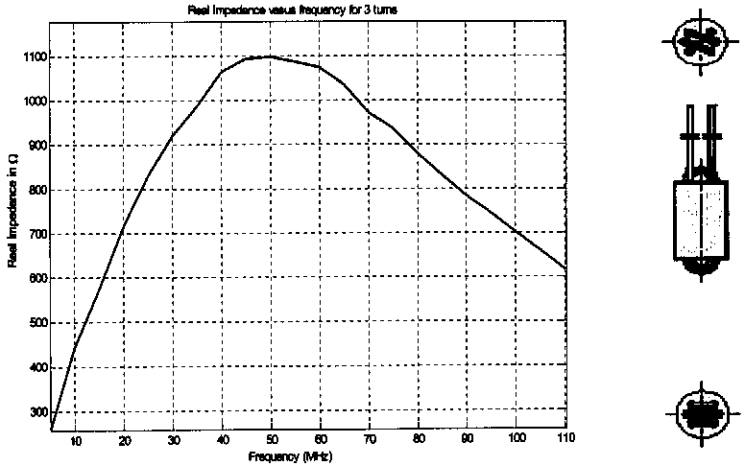

Figure 175 The network analyser measured real impedance of the shown ferrite bead structure (3-turns)

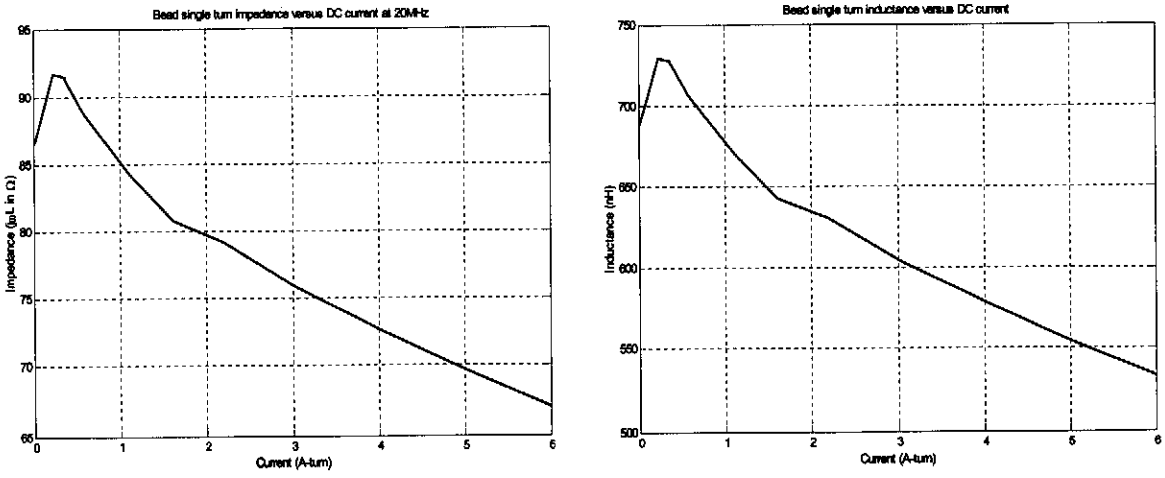

Figure 176 The measured saturation (inductance and impedance for a single turn at 20MHz for various DC currents per turn) of the ferrite bead

The measurements indicate that the ferrite does begin to saturate at around 400mA-turn, and that the inductance and impedance of the structure drops away as the DC flux increases above this point. The impedance of 1 turn drops 20Ω as the DC flux-inducing current increases to 5A-turn (it was observed that the ferrite begins to get warm for a DC current of around 5A-turn). The expected peak DC current that will flow in the DC path is between 1A and 1,5A. The effect of such currents on the ferrite inductance and impedance is not too large for a single turn, but if 3 turns are employed, as used in the measurement of the ferrite impedance, the peak A-turn current will be between 3A and 4,5A, which will have a larger effect on the effective ferrite RF impedance.

Other methods of employing the ferrite choke were considered. The results of one promising structure, as shown in Figure 177 are given. The main advantage of this structure is that both of the DC

conductors can be wound around the same ferrite bead. If the current direction in the conductors is opposite, the DC flux saturation problem can be eliminated, as the same DC current flows on the return and forward paths. The cross-sectional area of ferrite around which the wire is wound is smaller, so that the effective impedance will be around 200Ω smaller over the whole band.

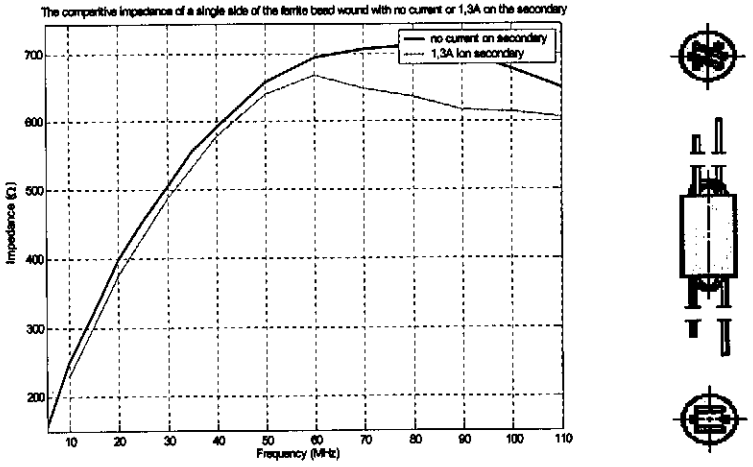

Figure 177 The measured characteristics of a second bead configuration

A model of the feed section was built to be used as a measurement jig, in order to determine the RF isolation and coupling between the three possible RF paths on the feed structure, identified in Figure 203.

The feed jig structure is sketched in Figure 178. The three measurement ports are numbered from 1 to 3, and NA measured coupling between the three ports at various frequencies is shown in Figure 179. For the measurements between ports 1 and 2, port 3 was connected to ground with a dead short. For the measurements between ports 1 and 3, port 2 was connected to a perfectly matched load (the network analyser matched load standard). These simulate the ideal RF operational conditions of the actual DC feed-through structure, where the antenna RF input impedance is taken as 50Ω and the DC power supply is a low RF impedance path to ground.

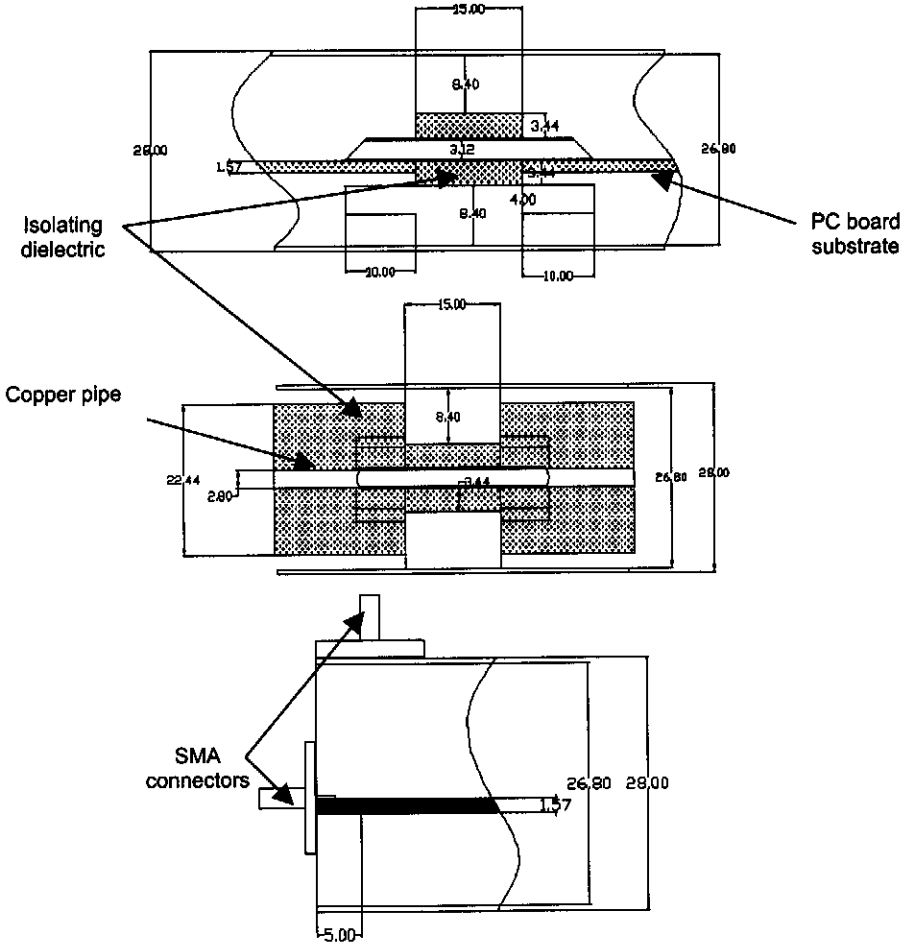

Figure 178 The structure of the feed test jig

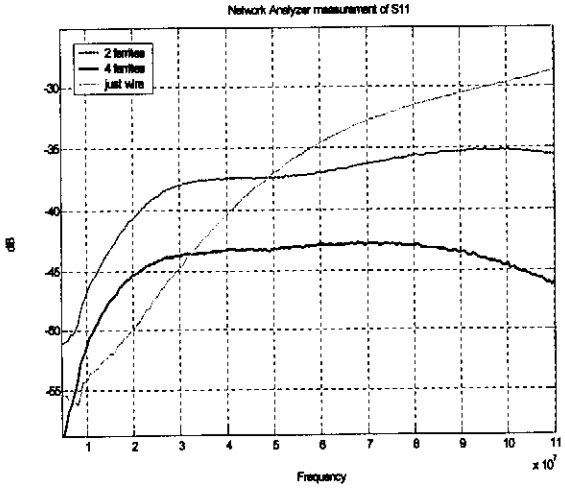

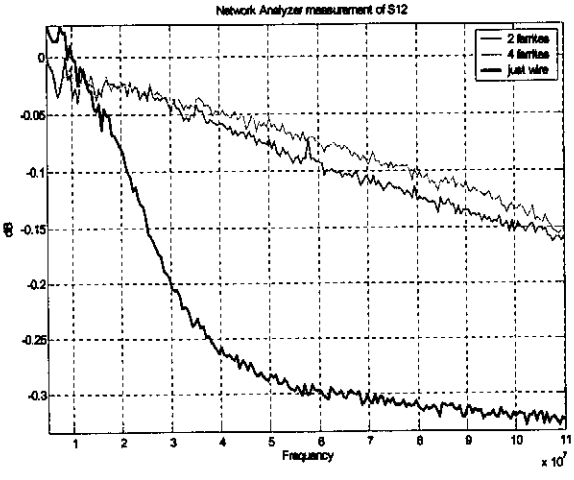

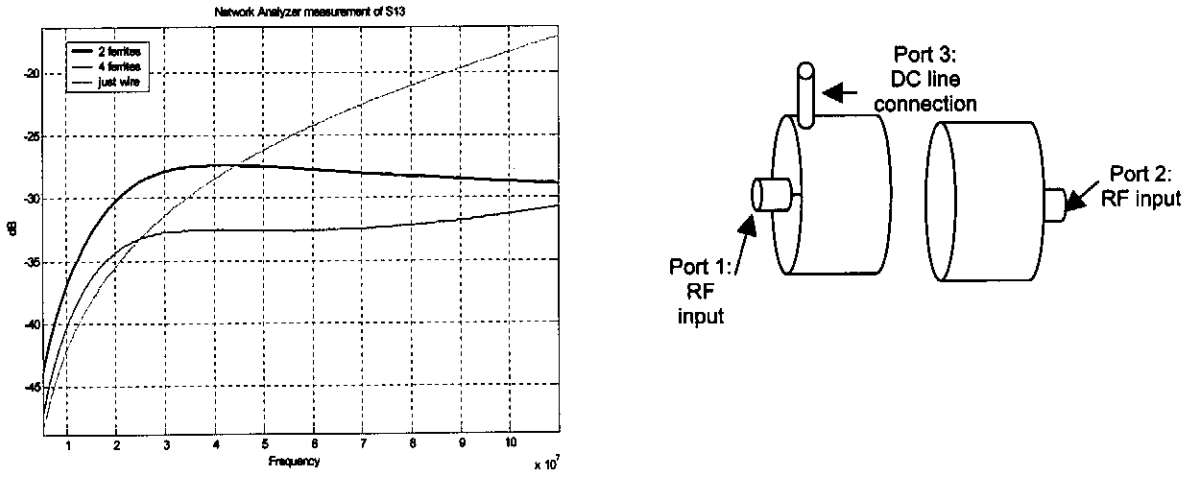

Figure 179 Network analyser measurements of the coupling between the three ports as defined in the sketch

The measurements suggest that the direct coupling between the RF and DC paths, without any ferrites on the DC path is around –17dB, and by the addition of ferrites, an isolation level of around –27dB to –33dB over the frequency range of interest can be achieved. The coupling between port one and port 2 is very good, with less than 0.3dB losses due to mismatch and leakage into the DC path. The measurements of Figure 179 show that when the ferrites are added, the isolation remains relatively constant above a certain frequency. To explain this, we must consider a lumped element model of the feed section. Referring to Figure 180, the model of the coupling between the DC and RF paths is modelled as a capacitor, and the RF path to ground as an inductor comprising the wire inductance and the added inductance of any ferrite structure on the DC path. In order to determine the magnitude of the coupling capacitor between the RF and DC paths, we must consider the measurement without any ferrite structure in the DC path.

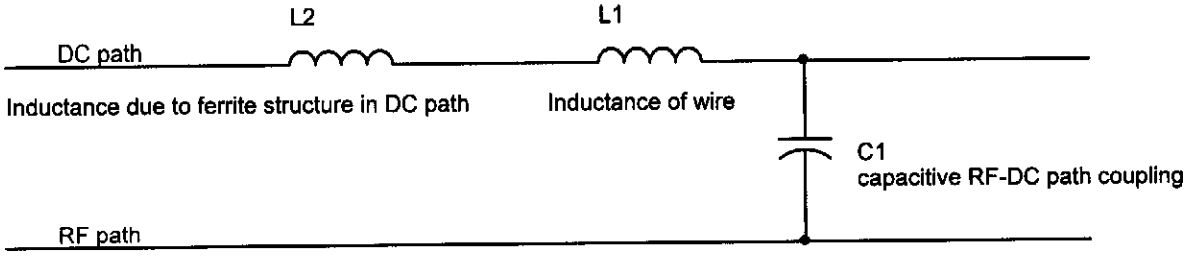

Figure 180 A simple lumped element model of the RF-DC coupling

The RF/DC isolation at 20MHz is measured as 35.455dB and at 80MHz as 21.05dB. If we assume that the wire has an inductance of 1nH/mm, and is 30mm in length then at 20MHz and 80MHz it will have an impedance of 3.77Ω and 15.08Ω respectively. This impedance is relatively small and can be ignored. By taking the isolations measured at 20MHz and 80MHz, the impedance of the DC coupling

path can be found as shown in (5.1) for the two cases, assuming that the impedance into port 2 is 50Ω as was assumed during measurement.

$$\begin{aligned} isolation_{dB} &= 10\times\log\left(\frac{P_{port3}}{P_{port1}}\right) = 20\times\log\left(\frac{I_{port3}}{I_{port1}}\right) \\ &\rightarrow \left(\frac{I_{port3}}{I_{port1}}\right) = 10^{\frac{isolation_{dB}}{20}} \\ &= [0.016875\ 0.088614] \\ &\text{but:} \\ \left(\frac{I_{port3}}{I_{port1}}\right) &= \frac{50}{50+impedance_{DC}} \\ \rightarrow impedance_{DC} &= [2913.92\Omega\ 514.25\Omega] \end{aligned} \tag{5.1}$$

From this we can approximate the lumped element value of the coupling capacitance to the DC path at 20MHz and 80MHz respectively as shown in (5.2).

$$\begin{aligned} C_{coupling} &= \frac{1}{2\times\pi\times f\times impedance_{DC}} \\ &= \frac{1}{2\times\pi\times[20e6\ 80e6]\times[2913.92\Omega\ 514.25\Omega]} \\ &= [2.73pF\ 3.86pF] \end{aligned} \tag{5.2}$$

We will take the coupling capacitance as approximately 3pF. If we model the wire coupling using this computed coupling capacitance and wire inductance, the measured and ADS simulated coupling compare as shown in Figure 181.

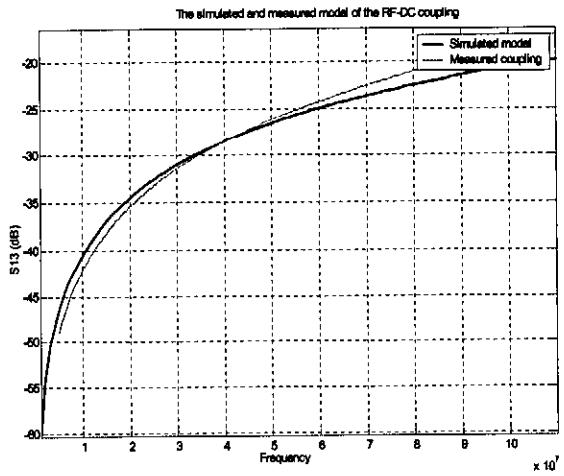

Figure 181 The modelled and measured coupling between the DC wire and the RF path in the feed test jig

The addition of ferrite elements in the DC path will not affect the coupling capacitance, but will introduce inductive impedance into the DC path. The measurement of S13 in Figure 179 suggest that the LC circuit realized between the coupling capacitor and the added inductance in the DC path becomes resonant in the frequency range of interest, decreasing the amount of RF/DC isolation achieved. In order to prevent the resonance of the LC circuit, an additional lumped capacitor was added in parallel with the inductive ferrites. The measured coupling between port 1 and port 3 with and without a 1nF capacitor in parallel with the ferrite element is shown in Figure 182.

The measurement results do not show such a great improvement in the isolation as simulations suggest it might, but about a 5dB improvement in the isolation on the LF side, and 10dB near 100MHz is realized.

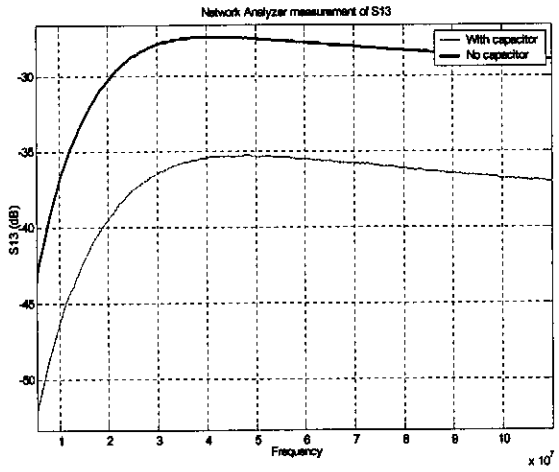

Figure 182 The measured isolation between port 1 and port 3 of the feed test jig with and without a 1.1nF capacitor in parallel with the ferrite choke element

5.2. The mono-static prototype probe

In this section, we will describe the realization and construction of a prototype probe structure. During the period of this report, three prototype structures were developed. All three of these structures are very similar, and only the final structure will be presented here.

The antenna and electronics housing is shown in Figure 183. A split copper pipe was used to house the electronics, providing easy access. The split pipe must be closed, and covered with aluminium tape once the electronics has been inserted into the housing, so that no interference with the antenna operation will result from the split in the copper pipe. The detail of the connection of this pipe section to the loaded-strip antenna sections is shown in Figure 184. A threaded hole is provide in the brass connection section, to allow for a good RF screw connection to the strip. The loaded strip antenna sections were realized by etching a 6mm track along the centre of a 12mm wide PC board section, leaving 3mm gaps for the loading resistors at the correct positions.

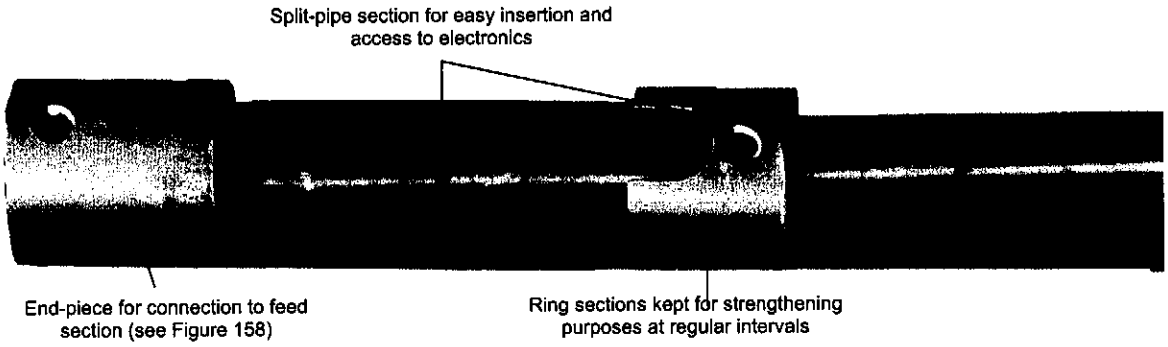

Figure 183 The split-pipe structure used to house the probe electronics, while facilitating easy access.

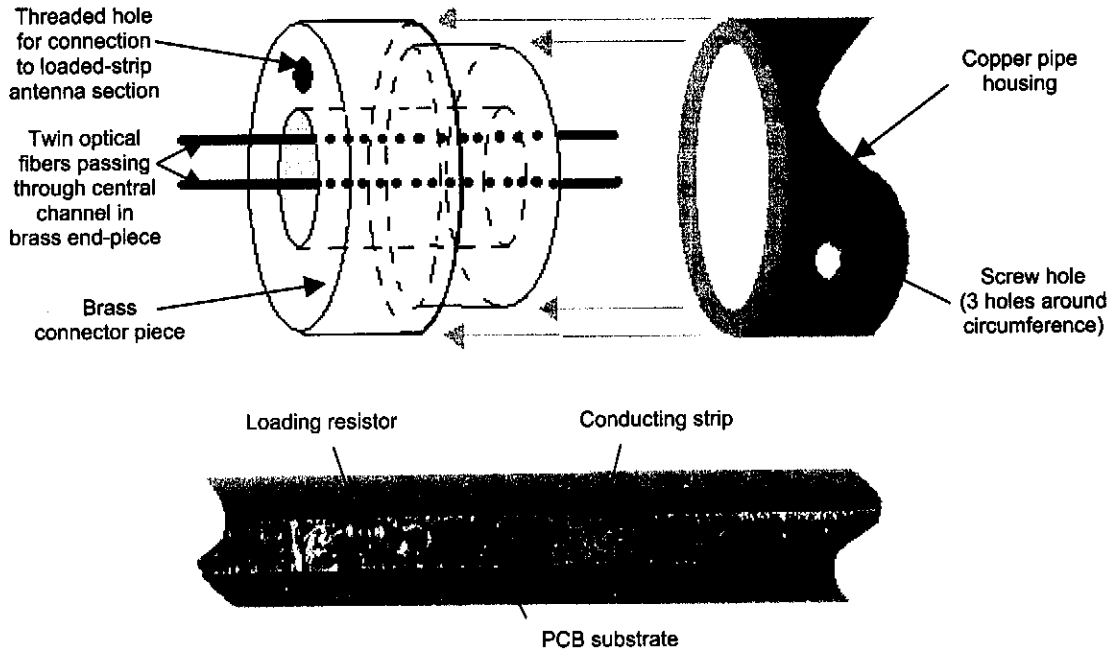

Figure 184 The brass connection piece between the copper pipe housing the electronics and battery pack, and the loaded-strip antenna sections; form of the loaded strip section

The feed section of the probe was realized as shown in Figure 173. The detail of the physical structure is shown in Figure 185.

Figure 185 Detail of the Feed section structure, and the connection to the electronics

Two battery packs were employed for testing purposes. The first pack consists of 15 D-type batteries, identical to those used in the current system. The second battery pack consists of 12 AAA-type NiMh batteries. This battery pack is considerably smaller and lighter than the D-type option. Both battery packs are able to support the operation of the receive- and transmit electronics, but the operational lifetime of the AAA-type pack is considerably shorter.

The completed probe structure is housed inside a PVC pipe section. The pipe performs two main functions. The most critical of these is to provide isolation form any conductive fluids in the borehole. In addition to this, the PVC pipe affords mechanical strength and protects the probe from breakage, during both transportation and deployment.

Two methods of assembling the probe structure, in order to gain access to the battery pack and the probe electronics were considered. The first option is depicted in Figure 186. In this case, a threaded connection point is added in the PVC pipe, at the feed point of the antenna. The antenna feed mechanism of Figure 173 is modified by adding a machined male MCX-type connector to the end of the copper pipe through which the DC power lines are fed, and recessing a female MCX-type connector into the brass disk terminating the copper pipe housing the battery pack of the probe. The probe is then accessed for maintenance, or to charge the batteries, simply by separating the two sections of the probe structure. The second option is rather more simplified. In this case, the probe housing is made of a single section of PV pipe, which must be opened at one end to remove the electronics for maintenance or to recharge the battery pack. In order to allow for easy initialisation of the probe in an operational environment, a small hole is drilled in the PVC housing, to provide access to an on-off switch. This hole must be well plugged during deployment, so that no fluid in the borehole can enter the probe.

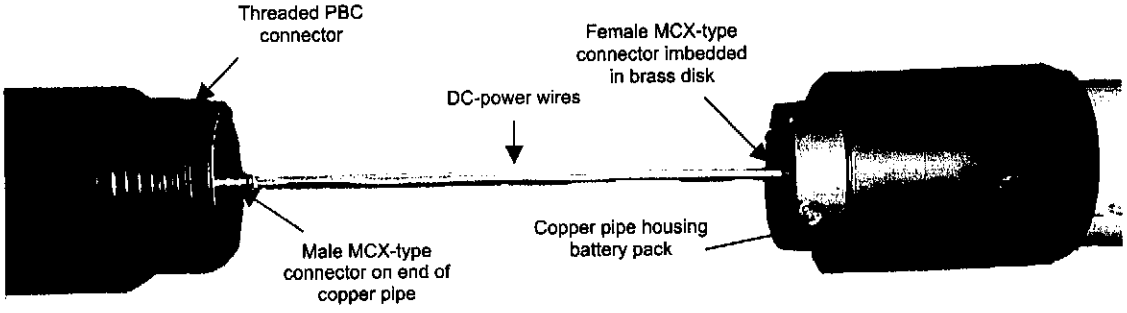

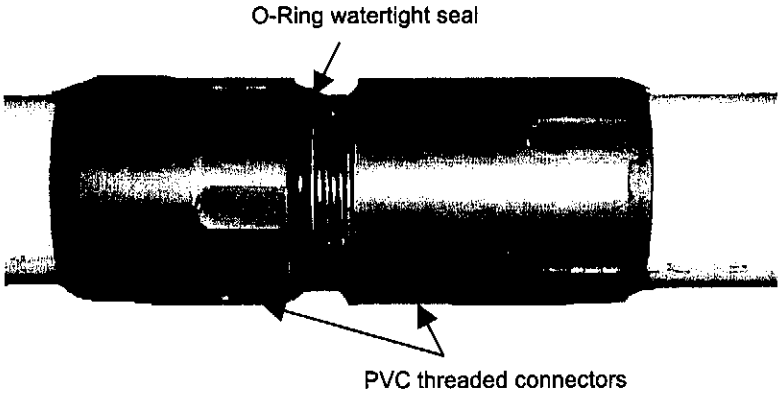

Figure 186 The antenna feed-point decoupling mechanism for the 2-section prototype probe structure

5.3. Conclusions

The following goals were achieved during the study outlined in this chapter.

- A basic BHR probe structure incorporating a balanced antenna and balanced feed was designed, realized and improved based on field observations.
- The isolation of the battery pack from RF coupling at the antenna feed point was considered. A method to limit this coupling using RF chokes was introduced and verified.
- The probe structure was successfully used to house mono-static and on-board DAQ test electronics for deployment in field tests.

During prototype development and testing, a number of factors relating to the structure and layout of the mono-static probe were identified.

- The split-pipe housing structure proved to be a good housing for the electronics, providing easy access during maintenance and manufacturing. Measurements suggest that by closing and sealing the pipe structure once the electronics has been inserted, extremely good shielding from both ambient environmental signals, and from potential coupling fields between currents induced on the antenna structure and the operational electronics is achieved.
- The antenna feed structure operates very well, and is relatively easy to manufacture and assemble. The connection between the electronics and the feed structure must be made very carefully, using screws to reduce stress on the solder joint.
- The ferrite chokes employed on the power-supply lines seem to operate well.

- Provision of access to the probe only by removal of the end plug of the PVC housing proved to be very impractical. The on/off switch access-hole employed in the side of the structure housing is not acceptable, particularly in the case were the probe is deployed in a wet borehole

- The central PVC screw-type connection shown in Figure 186 operates well, but the method of accessing the battery pack and switching on the probe must be carefully considered. The probe operation can be simplified by the inclusion of an accessible on/off switch and coupling points to the battery.

- Manufacture of the feed structure and connection mechanism must be performed extremely accurately, to improve the structural and operational reliability.

- The connection method between the un-damped copper pipe sections and the loaded strip sections of the antenna operates well, and can be easily converted to allow for more than one loaded strip section.

- The internal layout of the probe must allow for the use of the shortest possible un-damped section length. By using AAA-type batteries, the battery pack of the probe can be shortened considerably, and although the operation time of the probe is considerably shortened, it is still acceptable for a general BHR measurement. Careful consideration of the total power consumption of the probe electronics is necessary to determine the minimal battery requirements.

- The possibility of laying out the transmit and receive electronics in such a way that they can be placed on above the other, rather than head-to-tail in the copper pipe housing in order to shorten the space required for the probe electronics.

- The probe layout makes provision for the inclusion of additional electronics. This expansion space was put to use during field tests with a prototype on-board autonomous DAQ system. Careful consideration of the coupling, power and spatial requirements of additional electronics is necessary when additional electronics are added to the probe.

Chapter 6 Integration and comparative test results

In this chapter, we will discuss the practical testing of the mono-static probe components, and the integrated system. We will begin by considering the integration of the separate components of the mono-static system. Prototype operation will be analysed based on bench and field test results. The prototype field test results will also be compared to survey results using an existing BHR system (employing LEMO optical technology rather than the 'ST'-type technology outlined in chapter 1) to give a relative indication of the quality of the data gathered using the prototype system.

6.1. The mono-static receiver

Two mono-static receivers were considered during prototype field-testing. The first receiver included a low-noise front-end (TN7101), and the second receiver was tested without a front-end component. We will refer to these receivers as the high-gain and low-gain receivers respectively.

The low-gain receiver will have a theoretical maximum gain of approximately 50dB, while the high-gain receiver will have a maximum gain of approximately 70dB. Both of these receivers were implemented with no STC for the field tests that we will consider in this section, unless otherwise stated.

Figure 187 shows the raw data results of a field test survey performed with the existing BHR system at Bleskop mine during 2002, in a 150m long borehole. Figure 188 shows two surveys performed with a high gain (74dB; no STC) amplifier and a medium gain amplifier (fixed gain; 54dB) respectively. (Note that an onboard DAQ system developed by J. Hargreaves was used for the measurements with the high-gain and low-gain receivers, while the existing system employed the existing optical DAQ system.) A grey arrow indicates a typical feature observed in all three datasets. Figure 191 shows data gathered using a low gain STC receiver (45dB swept gain) at Bleskop. This data was gathered in a different borehole to that of Figure 188. Data gathered in the same borehole using the existing BHR system is however shown for comparison.

The data of Figure 187 and Figure 188 (gathered in the same borehole at Bleskop) processed in Seiswin[23] by removing the first break delay, applying AGC (automatic gain control with default Seiswin settings) and a band-pass filter (10MHz-100MHz) to the data is shown in Figure 189 to Figure 192. A short discussion of the observations that can be made form each set of results is given after each figure. The major characteristics that we expect to observe by comparing the different sets of data are:

- Better bandwidth and resolution is expected in the data captured with the onboard DAQ as compared to the data captured using the existing system DAQ (this is largely related to improved bandwidth of the onboard DAQ used for field tests, rather than to the receiver itself)

- Improved sensitivity (but also greater danger of saturation) for the fixed high-gain receiver
- Poorer noise figure for the STC swept low-gain receiver, as no LNA front end was used (higher output noise floor; shorter time to noise capture point)
- The effect of the STC sweep transients introduced by the AD8367, and the degree to which these transients cause a loss of data during post processing.
- The effect of STC on the noise capture point of the receiver chain as the noise figure will decrease with the gain sweep
- There is a possibility that ringing, and other undesired effects will be observed in the antenna operation. This is because the physical prototype antenna structure used was not identical to the structure designed in Chapter 2 and also due to the presence of conductive water in the borehole during measurements.

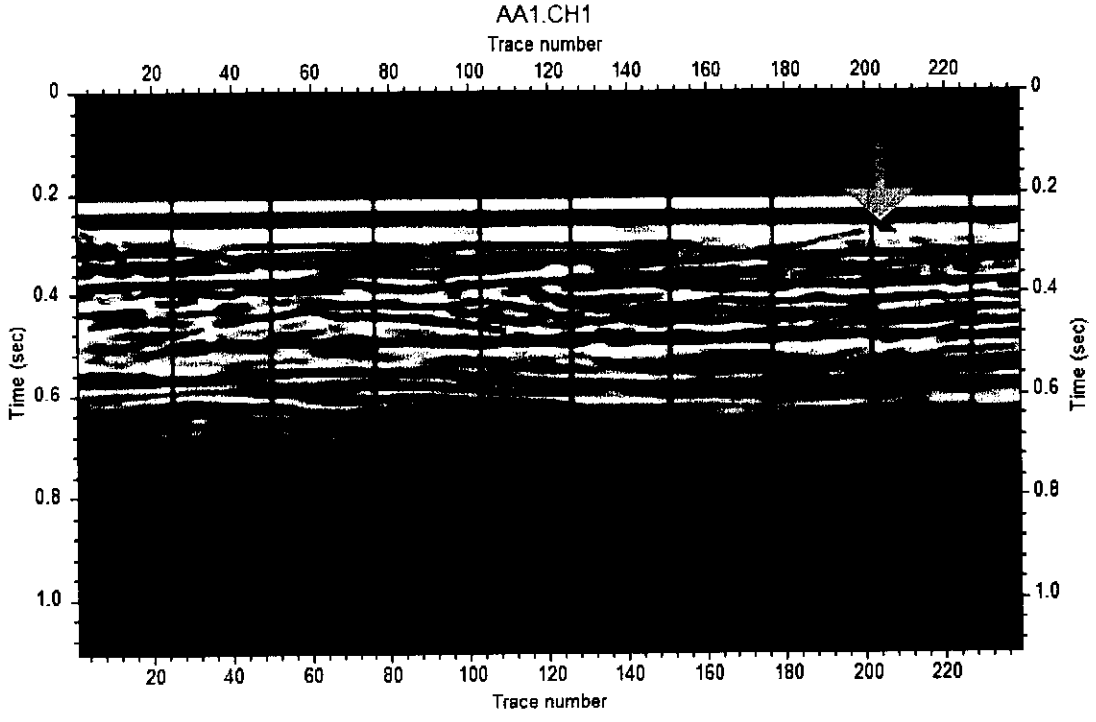

Figure 187 Raw operational BHR data measured using the existing BHR system and the existing optical DAQ deployed in a borehole at Bleskop

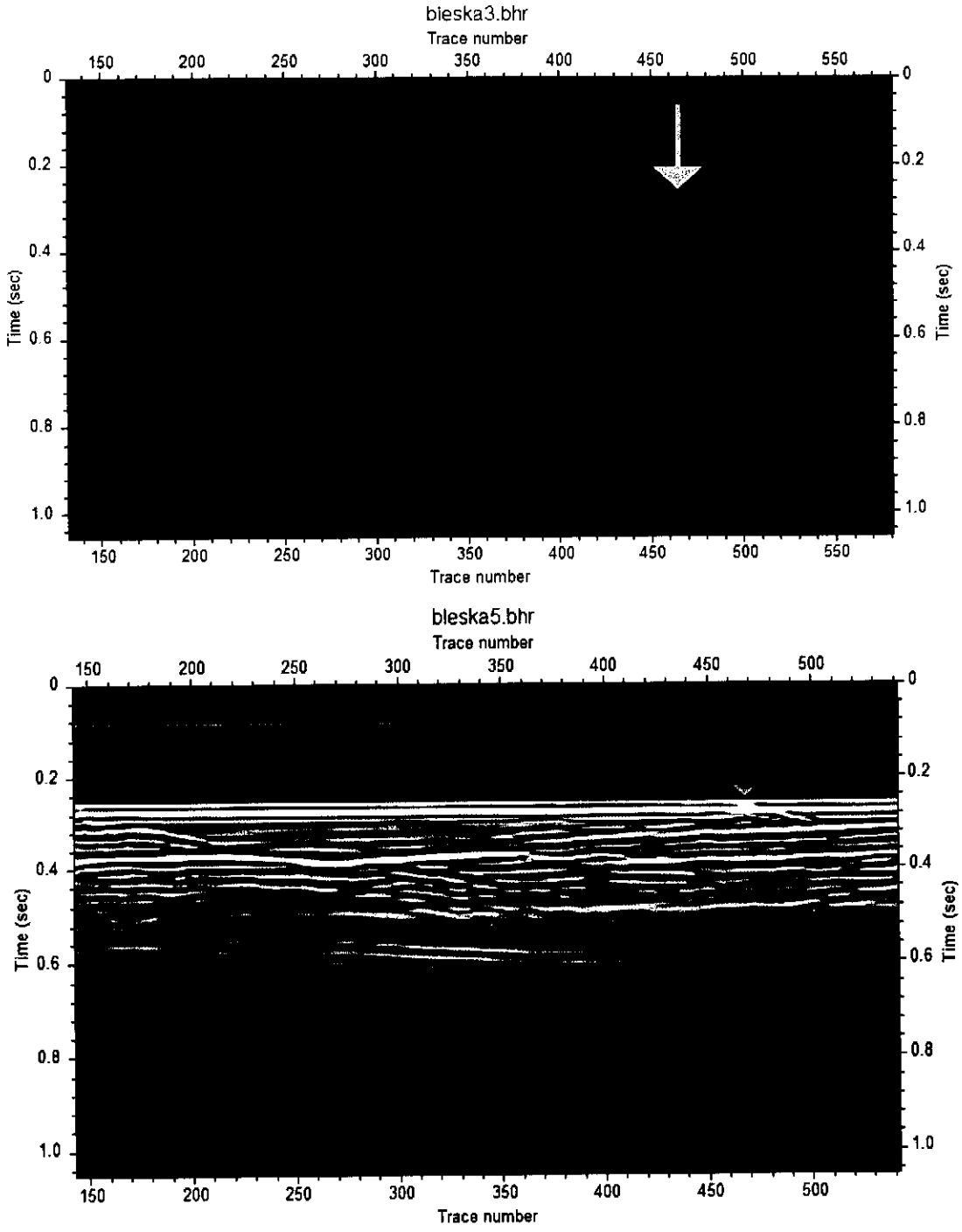

Figure 188 Raw operational BHR data measured using the fixed medium gain (top figure) and fixed high gain (bottom figure) receivers in a prototype probe structure with a transmitter-spacer combination of the existing system and an onboard DAQ system deployed in the same borehole at Bleskop

The raw data of Figure 188 and that of Figure 187 show very similar features, and (particularly for the high gain measurement) antenna-ringing effects are apparent. It its immediately apparent that the data measured with the on-board DAQ (Figure 188) has higher bandwidth content than the data of Figure

187, as expected. Saturation effects and an improved relative range and sensitivity are observed in the fixed high-gain data. After processing the data as discussed, we get the results shown in Figure 189 and Figure 190.

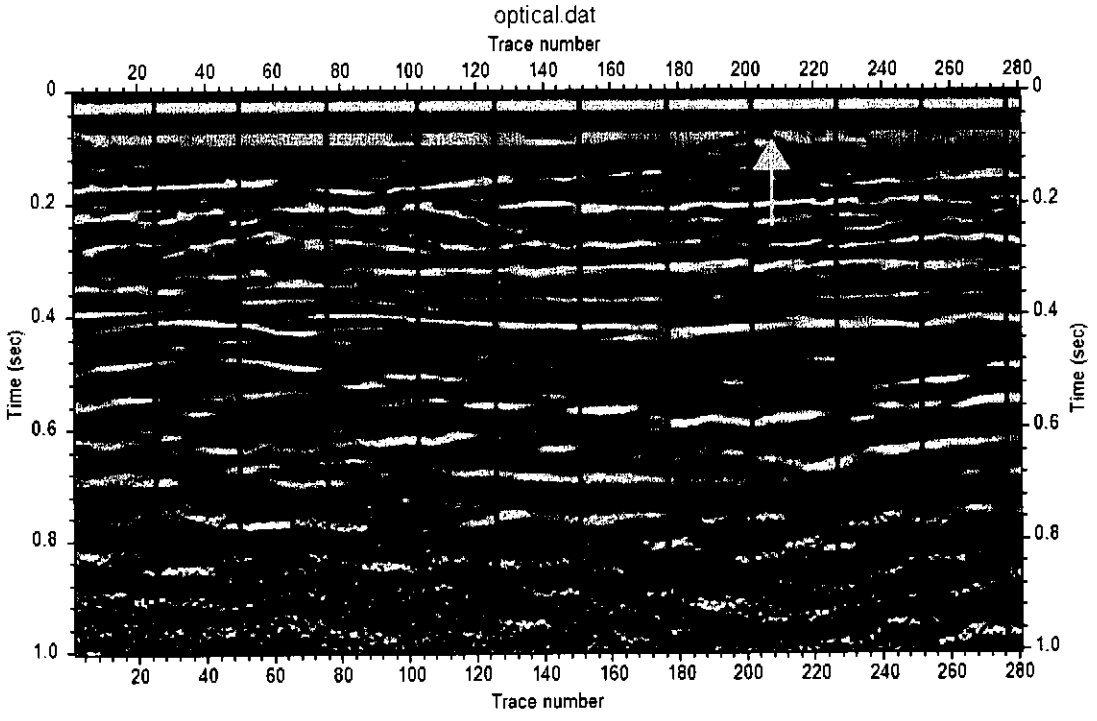

Figure 189 The processed data (filtered with a 10MHz-100MHz band pass filter and with AGC applied) of Figure 187, gathered at Bleskop

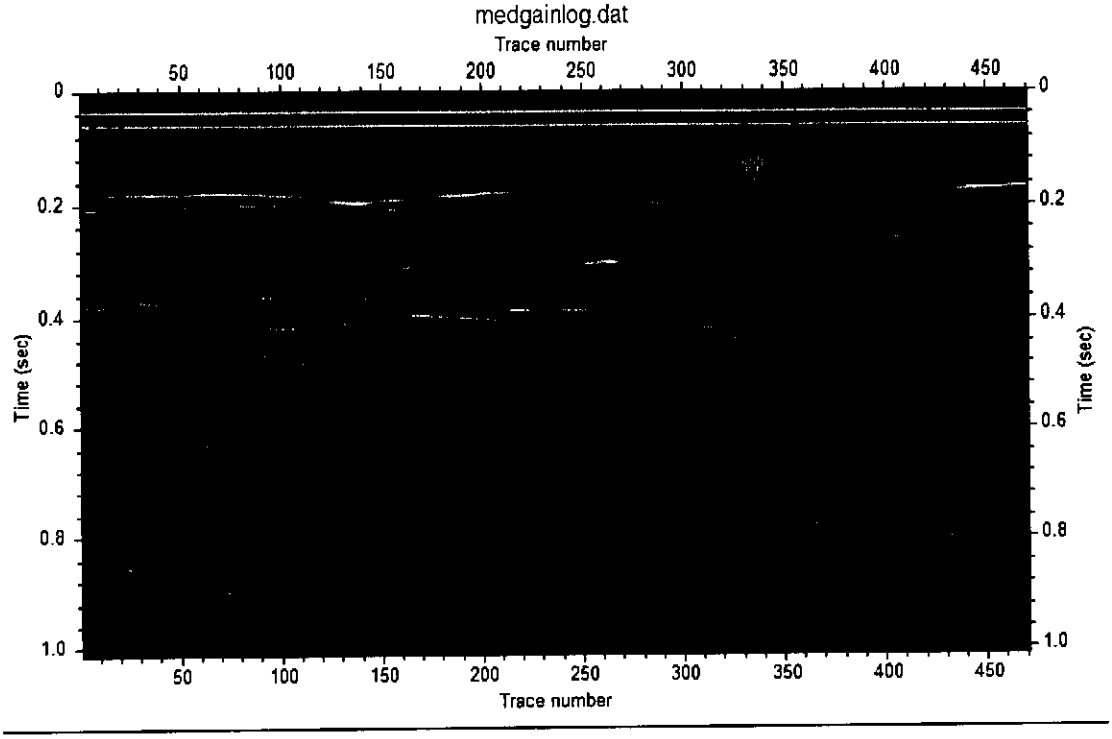

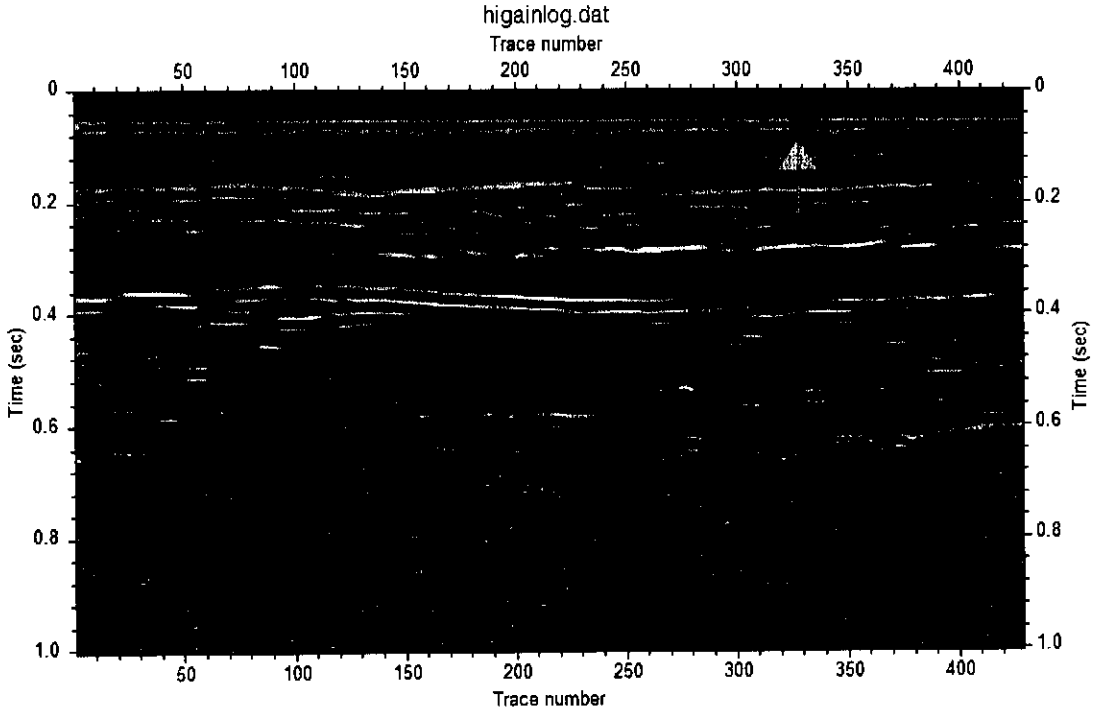

Figure 190 The processed data (filtered with a 10MHz-100MHz band pass filter and with AGC applied) of Figure 188, gathered at Bleskop

The processed data confirms the observations made on the raw data. The noise capture point of the high-gain receiver is slightly longer, but saturation effects remain evident for about 40ns after the first break. The effect of the DAQ bandwidth improvement remains clear for the onboard logger.

Raw BHR data gathered in a second borehole at Bleskop using the existing system, and an STC receiver as designed in Chapter 3 are shown in Figure 191.

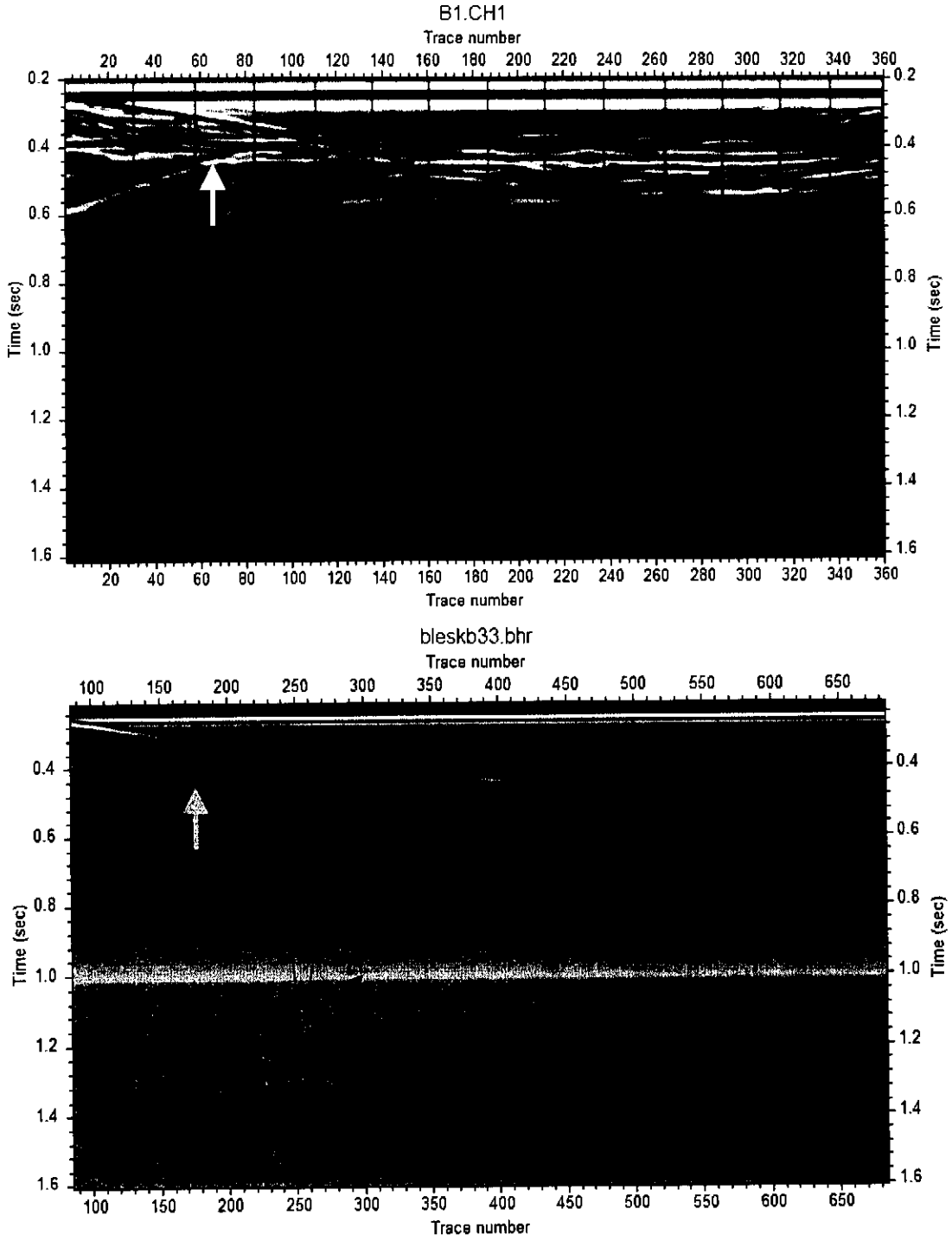

Figure 191 Raw operational BHR data measured using the full existing system (top) and a low gain STC receiver in a prototype probe structure in conjunction with a transmitter-spacer combination of the existing system and an onboard DAQ system (bottom) deployed in the same borehole at Bleskop

The sweep transients of the STC component are clear in the data of Figure 191. The effect of processing to remove these artefacts will be discussed in connection with Figure 192, which shows the

data after it has been filtered (10MHz to 100MHz band pass filter) and after automatic gain control has been applied (default Seiswin settings).

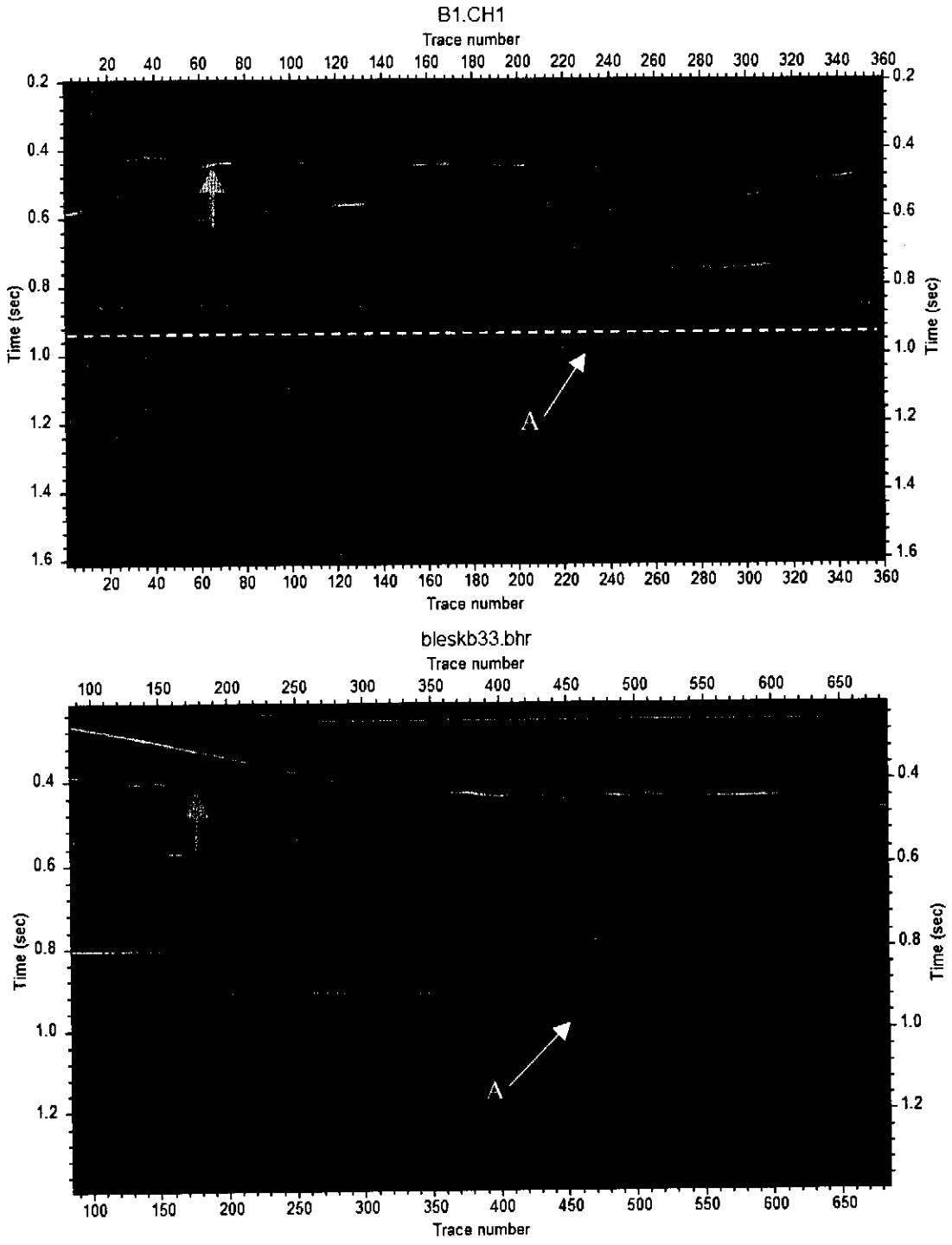

Figure 192 The processed data (filtered with a 10MHz-100MHz band pass filter and with AGC applied) of Figure 191, gathered at Bleskop

The processed data of the STC receiver, including removal of the sweep transient effects, compares extremely well with the data measured with the existing system up to 850ns. In the band between 850ns and 1μs, data loss is however apparent, due to one of the STC sweep transients. After the sweep transient effect has passed, a feature (labelled A) is observed. This suggests that the system is still sensitive enough at this point to detect geological features. The data would in fact seem to show that this feature is clearer in the STC data than in the data acquired using the existing system, despite the higher noise figure and lower peak gain of the STC system. Removal of the sweep transient effects is necessary to verify this observation, and determine the exact noise capture point of the receiver.

6.2. The transmitter and antenna structure

The antenna structure used in prototype testing was described in section 2.6.2. The results presented indicate that the antenna will radiate more efficiently (around 8-10 times more) than the antenna used in the current system. Impedance simulations however indicate the possibility that the antenna may become resonant in certain environments, and show ringing effects, which are unacceptable despite the improved efficiency. Field tests were performed to show the operation of the mono-static transmitter designed by Van der Merwe (see [9]) and the prototype antenna structure in comparison to the existing BHR system. Comparative measurements were made using the set-up shown in Figure 193.

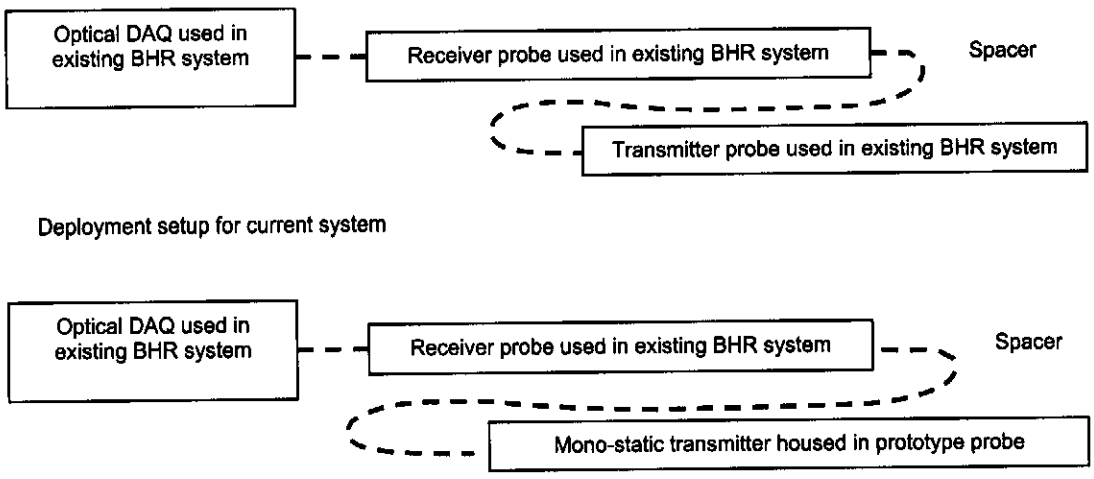

Figure 193 The deployment set-up used to perform comparative field measurements to show the operation of the mono-static transmitter and prototype antenna with respect to the current BHR system

Comparative processed measurement results for the two deployment strategies shown in Figure 193 are given in Figure 194. From these shown results, we can make a number of observations. Firstly, the extra feature in the data profile measured with the existing BHR system (indicated with a white dashed line labelled A) is due to a string of drill rods present in an adjacent borehole during the profile with the

existing system, and not during the profile using the mono-static transmitter and prototype antenna. It is apparent that there is recognizable data approximately 100ns longer in time with the mono-static transmitter/antenna configuration, and that the high frequency content of the mono-static transmitter/antenna configuration is better.

The form of the pulses radiated by the two transmitter topologies is clearly different. This difference can be ascribed to two factors. The first factor is that of the excitation pulse form. The existing transmitter radiated only on a single falling edge, while the mono-static transmitter excites the antenna with a 20ns pulse (i.e. two radiating edges separated by less than 20ns). This excitation difference implies that the pulse form radiated by the existing structure will have a monocycle form, while the mono-static transmitter will excite the radiation of a Ricker-type pulse form. The receiver antenna will differentiate the received E-field pulse, resulting in the expected received pulse forms shown for the existing and mono-static transmitter/antenna respectively. From a data interpretation point of view, the monocycle-type pulse form is more desirable, as the data appears less cluttered. De-convolution and reconstruction of the data, to remove the received pulse form effects may be considered to improve the clarity of the data. The second factor that contributes to the different pulse form observed in the mono-static transmitter/antenna results is the near resonant operation of the prototype radiating structure. It seems from consideration of the separate traces of the acquired data that the antenna does indeed show resonant or ringing characteristics, and causes extensive deformation of the radiated pulse form. Despite this certain reflective features can still be observed in the data, and it seems as if the mono-static transmitter performs well.

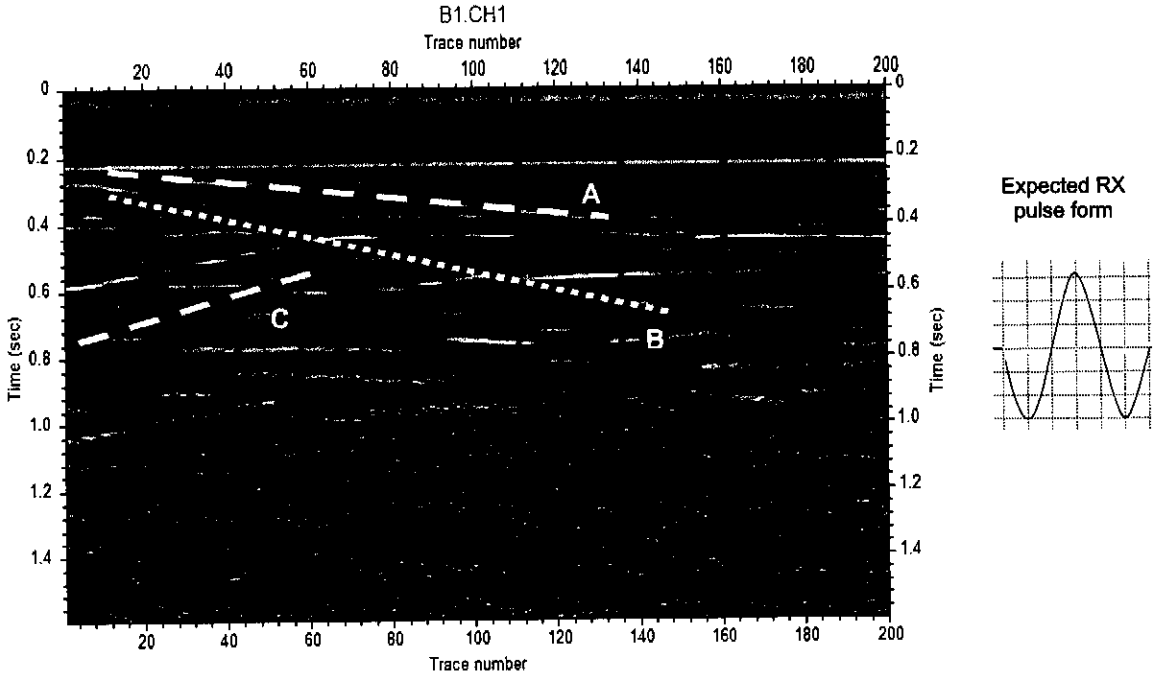

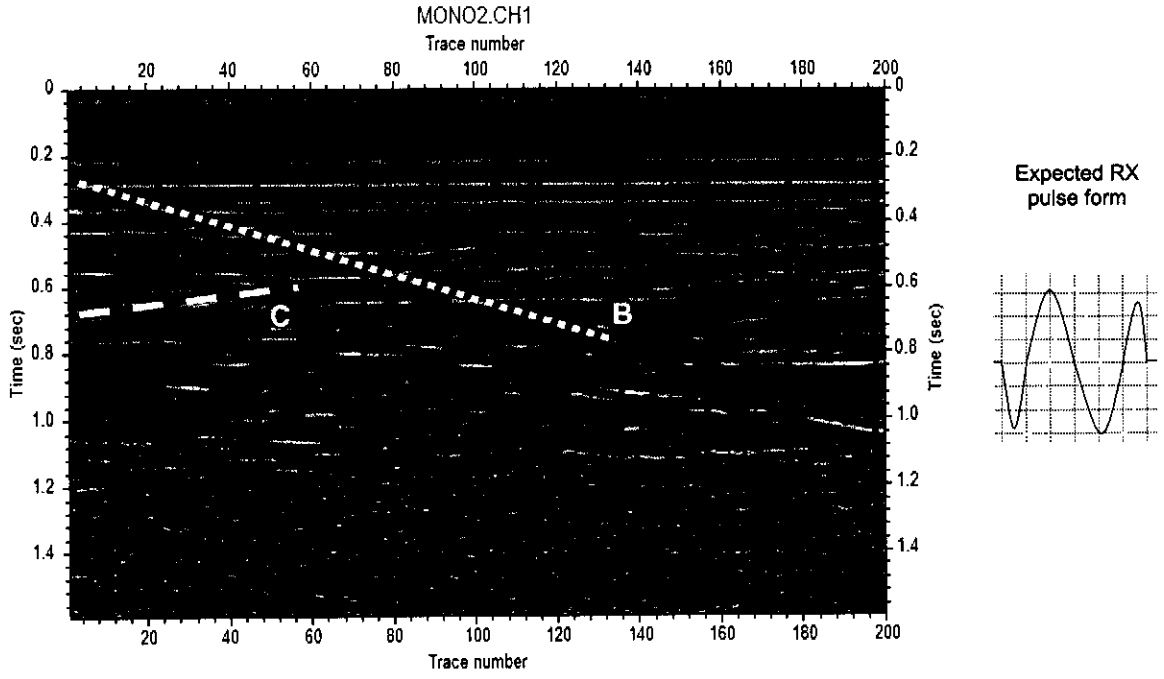

Figure 194 The comparative processed data acquired using the two deployment set-ups of Figure 193. ***Top panel****: Standard set up of existing radar;* ***Bottom panel****: deployment including mono-static transmitter prototype*

Figure 195 shows two comparative traces acquired at the same point in the borehole, for the existing and the mono-static transmitters. The data is shown both in its raw form, and after processing with a filter (10MHz-100MHz) and AGC. The extraction of a single pulse form from such a trace, to enable direct comparison of the pulse forms is extremely difficult, but the 'ringing' effect of the near resonant prototype antenna is very apparent. The ADS computed expected radiated pulse forms for the prototype antenna and the existing antenna (assuming the relevant excitation form) in an environment close to the one in which the field tests were performed are shown in Figure 196. These radiated fields will induce a signal with a derivative form of the pulses shown in Figure 196 at the receiver antenna feed point. Field test results seem to indicate that the resonant effects are even more pronounced than the simulated case.

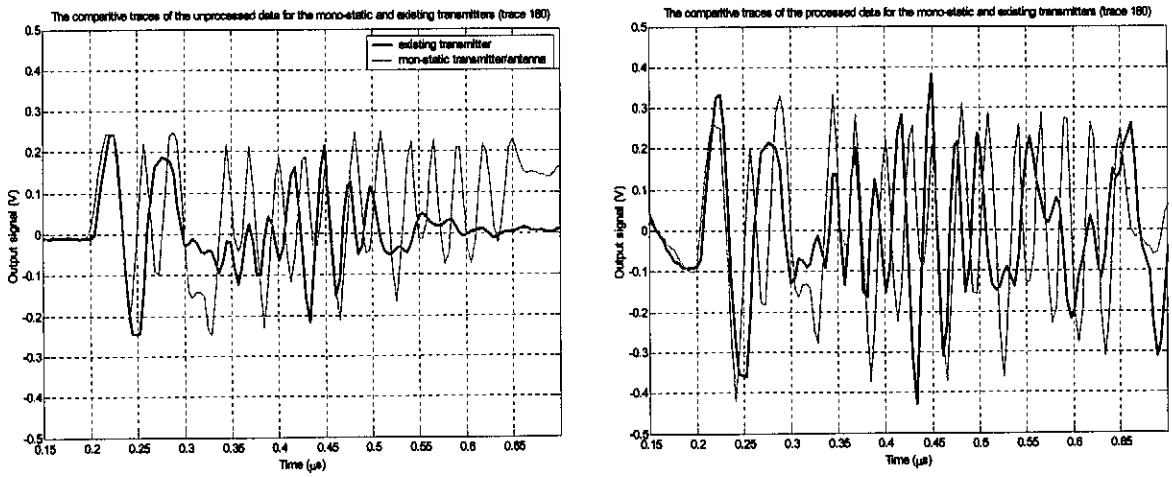

Figure 195 A selected trace from the data of Figure 194, before and after basic processing (filtering and AGC application)

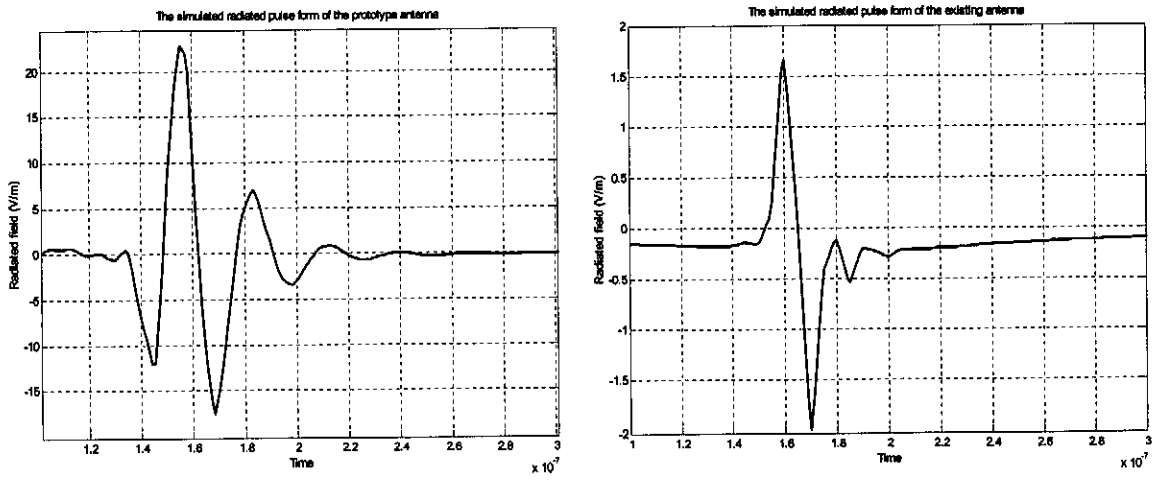

Figure 196 The ADS predicted radiated pulse forms for the existing BHR transmitter, and the mono-static transmitter prototype-antenna probe

Chapter 7 Conclusions

In this chapter, we will summarize the conclusions reached during the study period of this report, and consider future work to be done with regard to the topics considered.

7.1.1. The BHR antenna structure

Radiating structures employed in existing BHR systems have a number of limitations.

- The structures are asymmetrical, and show squinting effects, up to a maximum of around 10° at higher frequencies within the band of interest.
- The real input impedance is relatively high (above 150Ω over the frequency band of interest), and the structure presents a very large capacitive imaginary impedance (around 600Ω at low frequencies).
- The pulse form radiation properties of the antennas are good, but radiation is inefficient (pulse efficiency below 5%).

During the development of a balanced antenna structure for mono-static application, the following conclusions were reached:

- Symmetrical resistive loading is an effective method of improving the pulse radiation properties of a balanced dipole antenna, at the cost of pulse radiation efficiency. The transient response of the antenna can be improved with a lighter loading than is ideal for the steady state response.
- Modification of the standard resistive profile application policy is necessary to provide for the housing of the probe electronics inside the antenna structure. Careful consideration of the travelling wave current reflection caused by this modification shows that a relatively light loading is optimal.
- 20% of a full Wu-King loading on the modified symmetrical radiating structure delivers an antenna that has good pulse form radiation characteristics (the same as for the existing antenna, but with no HF squinting) and good relative efficiency (approximately 10 times better pulse efficiency than the existing antenna).
- The operational environment of the antenna has a large effect on the operation of the structure. The major effects are:

- The permitivity of the rock propagation material causes frequency and impedance scaling of the antenna properties. These direct effects are damped by the borehole and probe housing structure, but remain considerable.

- The PVC housing of the probe has very little effect on the antenna operation.

- The air gap or potting material layer between the antenna structure and the PVC housing layer has a large (mostly detrimental) effect on the antenna operation. This effect is particularly large in the case of the air gap. These effects can be reduced by the choice of antenna loading topology.

- The borehole in which the probe is deployed is potentially the most critical environmental factor on the antenna operation, due to the large variation of the material properties. The permitivity properties of the borehole-filling material are not as critical as the conductivity of the material, as the permitivity effects are damped in an operational BHR environmental model due to the limited thickness of the layer. Conductive water in the borehole is extremely detrimental to the operation of the antenna structure.

- Employing an antenna topology that effectively approximates a thick dipole that fills the entire cross-sectional volume of the PVC housing can dramatically reduce the effect of an air gap or potting. The use of multiple loaded strips around the circumference of the volume, or a loaded cylindrical structure are two methods of doing this. Full model simulations indicate that the improvement is considerable.

- The realization of an environmentally tolerant, broadband antenna with good radiation efficiency is only possible for limited environmental variation. An antenna structure, using a multiple strip loading, modified dipole topology was designed that is relatively tolerant to the borehole environment. Extreme changes in the permitivity of the propagation material, however have a large effect on the input impedance of the structure. For mono-static application, is suggested that such a structure be employed. By careful calibration of the monostatic estimator dummy load, using a lumped element model of the antenna impedance for the expected nominal rock permitivity, good, stable mono-static isolation can be achieved.

- Analysis of the radiating structure used for prototype field-testing show that although it operates well in a simple environment, its impedance characteristics are relatively poorly in a BHR environment (particularly for mono-static application), and resonant effects are very probable. This can be identified as one of the major reasons for failure of the mono-static prototype during field-tests.

7.1.2. The mono-static BHR receiver electronics

The fixed gain receivers used in existing BHR systems are impractical for mono-static application due to their saturation and clipping characteristics. By implementing variable gain in the receiver chain, these effects can be reduced. The following conclusions were reached during the receiver development.

- Automatic gain control is not a practical solution for damping of initial transients in a pulsed system.
- Sensitivity time control with a specific sweep profile is a more promising solution.
- Variable gain implementation using the chosen component was tested, showing that STC presents a good solution to mono-static receiver saturation limitations. The operational limitations of the specific component with regard to noise figure and the achievable maximum sweep gradient suggest that another component should be considered.
- Despite the non-ideal operation of the variable gain component, the concept of the application of variable gain is sound, and is a good solution to the mono-static receiver problem.
- Care must be taken during the layout of the receiver to prevent oscillation and unwanted coupling on the board, which will compromise the dynamic range and linear operation of the amplifier chain.

7.1.3. The mono-static probe housing and layout

During the development of a probe structure and layout, the following conclusions were reached:

- The probe layout was designed with the battery on one side of the central feed point and the probe electronics on the other.
- A balanced feed structure for the symmetrical antenna was developed, and shown to operate well. This feed structure includes a choked DC feed through path.
- The possibility of a breakable connection in the centre of the probe structure to allow for easy probe access and transportation proved to be a possibility. The mechanical robustness of such a break point must be considered.

7.1.4. Operational consideration of the mono-static BHR system

- Bench measurement of the mono-static receiver, connected to an operational mono-static transmitter and circulator show that the system does work under both ideal and non-ideal load conditions.

- Bench measurement of the reflection capturing capabilities of the mono-static system show that reflections returning to the receiver port at most 100ns after triggering of the transmitter are detectable for practical load conditions.

- Leakage of the 2MHz transmitter clock signal onto the receiver port was observed.

- Field measurement of the mono-static receiver sub system, deployed in the mono-static probe structure, with and without STC was compared to results acquired using an existing BHR system, indicating that the receiver performs well. Successful interfacing of the receiver to an experimental on board DAQ was achieved and verified.

- The sweep transients introduced by excessively fast sweeping of the VGA gain can be removed by calibration of acquired data, but as shown with field test measurements, the transients may result in an irreversible loss of data.

- Field measurements of the mono-static transmitter subsystem suggest that it functions well. Qualitative comment in this regard is difficult, due to both the differences between the excitation pulse form used in the existing BHR system, and the mono-static transmit pulse form and the poor characteristics of the prototype antenna used during the field tests (as mentioned in 7.1.1).

7.1.5. Future work

7.1.5.1. The antenna

Wideband antenna realization within the constraints of the BHR operational environment is very difficult, especially when the great variation within the environment is concerned. The design and characterization of different loading profiles and structures to be used under different environmental conditions, particularly for different ambient permitivities, is one method of partially overcoming this difficulty. Optimisation of structures for specific typical environments, by alteration of the loading profile and loading positions needs to be further considered.

The practical realization and implementation of a multiple loaded strip antenna or a loaded cylindrical antenna structure must be performed and its operation verified during field-testing.

The extraction of lumped element approximations of antenna impedances must receive further attention. By improving the dummy load assumed in the estimator of the mono-static circulator, the isolation can be improved. The possibility of altering the dummy load to match different antennas under different conditions must be considered in order to improve the isolation stability and general operation of the mono-static system.

7.1.5.2. The receiver

Sensitivity time control is an effective method of realising an acceptable receiver for mono-static application. The noise figure and sweep transients of the component used in this study suggest that a better component must be found and implemented. The low noise front end of the receiver chain needs further consideration, as the components employed for this purpose proved to still be sensitive to saturation, with slow recovery.

The effects of losses in the antenna-receiver feed path of the mono-static circulator are critical to the dynamic range and general operation of the system. These effects need careful consideration, and must be reduced before a practical operational system can be realized.

The clock coupling to the receiver port of the mono-static circulator must be removed.

The possibility of employing a complex gain control signal, digitally generated by onboard control electronics can be considered. This type of control may be intelligent and adaptive, improving the operational robustness of the mono-static system.

7.1.5.3. The probe structure

The feed structure and DC feed methods used in the prototype probes designed during this study period are effective, and easy to realize. Further consideration of a mechanism whereby the probe can be accessed for maintenance and for recharging of batteries without compromising the structural reliability is needed.

The mechanical realization of multiple strip and loaded cylindrical antenna structures as part of the probe structure must be considered.

Bibliography

[1] **P.J. van der Merwe and B.K. Woods**, 'The GEOMOLE Borehole Radar System Incorporating ST-type Optics and the Optics-free Transmitter', Report presented June 2002

[2] **P. Annan**, 'Eighth International Conference on Ground Penetrating Radar-Tutorial 1: Introduction to GPR', May 2000

[3] **J. Hargreaves**, *'A Multichannel Borehole Radar for Three Dimensional Imaging'*, PhD thesis, University of Oxford, Trinity term 1995

[4] **S. Keller**, *'Design of Impedance Loaded Antennas for Broadband Radar Applications'*, Diploma thesis, University of Stellenbosch, Stellenbosch, South Africa, July 2000

[5] **M.W. Van Rooyen**, *'Simple Broadband Measurement of Balanced Loads Using a Network Analyser '*, MSc Thesis, University of Stellenbosch, Stellenbosch, November 2000

[6] **M.D. Van Wyk**, *'An active Antenna for Borehole Pulsed Radar applications'*, MscEng thesis, University of Stellenbosch, Stellenbosch, South Africa, December 2001

[7] **P. Le Roux Herselman**, *'Detecting Geological Defects in the Bushveld Igneous Complex'*, PhD Thesis, University of Stellenbosch, Stellenbosch, South Africa, March 2003 (in preparation)

[8] **B.K. Woods**, *'Development of a Pulsed Borehole Radar Receiver Front-end'*, Dissertation report, University of Stellenbosch, November 2000

[9] **P.J. Van der Merwe**, 'The design of a monostatic ultra wide band VHF pulsed radar for detection of close-in targets', MSc.Eng thesis, University of Stellenbosch, March 2003

[10] **D.M. Pozar**, *'Microwave Engineering'*, Second edition, John Wiley & sons, 1988

[11] **W.L. Stutzman and G.A. Thiele**, *'Antenna Theory and Design'*, John Wiley & sons, 1998

[12] **A. Ishimaru**, 'Electromagnetic Wave Propagation, Radiation and Scattering', Prentice Hall, 1991

[13] **C.A. Balanis**, *'Advanced Engineering Electromagnetics'*, John Wiley & sons, 1989

[14] **S. Ramo, J.R. Whinnery and T Van Duzer**, *'Fields and Waves in Communication Electronics'*, Third Edition, John Wiley & sons, 1993

[15] **H.A. Haus and J.R. Melcher**, *'Electromagnetic Fields and Energy'*, Prentice Hall, 1988

[16] **T.T. Wu and R.W.P. King**, *'The Cylindrical Antenna with Non-reflecting Resistive Loading'*, IEEE Transactions Antennas and Propagation, vol. AP-13, pp. 369-373, May 1965. See corrections [17]

[17] **T.T. Wu and R.W.P. King**, *'The Cylindrical Antenna with Non-reflecting Resistive Loading-corrections'*, IEEE Transactions Antennas and Propagation, vol. AP-13, pp. 998, Nov 1965. See original [16]

[18] **R.L. Finney and G.B Thomas**, *'Calculus'*, Second Edition, Addison-Wesley Publishing Company, 1994

[19] **A.R. von Hippel**, *'Dielectric Materials and Applications'*, M.I.T. Press, 1961

[20] **J.G. Proakis and D.G. Manolakis**, *'Digital Signal Processing principles, algorithms and applications'*, Third edition, Prentice Hall, 1996

[21] **R.W.P. King, G.S. Smith, T. T. Wu and M. Owens**, *'Antennas in matter'*, MIT Press, Cambridge, Mass, 1981

[22] **D.M. Claasen**, *'Electromagnetic characterization of a wideband borehole radar imaging system'*, Doctoral thesis, University of Oxford, 1995

[23] **M. Li**, *'Seismic applications of interactive computational methods'*, MSc thesis, University of Sydney, 2000

[24] **Hewlett Packard**, *'Fundamentals of RF and Microwave Noise Figure Measurement '*, Application note 57-1

[25] **Agilent**, *'Spectrum Analyser Basics'*, Application note 150, Agilent Technologies

[26] **ADS user manual**, Agilent technologies, 2002

[27] **FEKO user manual**, EMSS, 2000

[28] **I. Mason**, Personal correspondence between Prof. I Mason (Sydney University) and Yuping Toh (Analog devices), 6 November 2002

[29] **J.H. Cloete**, Personal communication, July 2002

Appendix A.

A.1. Propagation mechanics and the GPR problem

Maxwell's equations describing the observed electromagnetic behaviour of matter are given in (A.1).

$$\begin{aligned} \nabla \times \bar{E}(\bar{r}) &= -j\omega \bar{B}(\bar{r}) \\ \nabla \times \bar{H}(\bar{r}) &= j\omega \bar{D}(\bar{r}) + \bar{J}(\bar{r}) \\ \nabla \bullet \bar{D}(\bar{r}) &= \rho(\bar{r}) \\ \nabla \bullet \bar{B}(\bar{r}) &= 0 \end{aligned} \qquad \text{(A.1)}$$

Basic wave propagation in terms of the relevant material properties of the propagating medium can be summarized as shown in (A.2). This description is based on the time evolution of an EM wave, adhering to Maxwell's laws.

$$\begin{aligned} W(x,t) &= e^{-j(kx-\omega t)} \\ k &= k_0\sqrt{\varepsilon_r} \\ \mathrm{k}_0 &= \omega\sqrt{\varepsilon_0\mu_0} \\ \varepsilon_r &= \frac{\varepsilon}{\varepsilon_0} - j\frac{\sigma}{\omega\varepsilon_0} \\ &\text{where} \\ &\text{x=distance traveled} \\ &\text{t=time} \\ &\text{k=propagation constant} \\ \omega &\text{=angular frequency (rad/s)} \\ \sigma &\text{=material conductivity} \\ \varepsilon_0, \mu_0 &= \text{free space constants} \end{aligned} \qquad \text{(A.2)}$$

To simplify the description of EM wave propagation, we can describe the propagation in terms of the propagation velocity and attenuation. For complex media, both of these properties are vector properties, with directional dependence.

In homogeneous media, the attenuation constant is given by $\alpha = k_0 n''$ where $n = \sqrt{\varepsilon_r} = n' - jn''$ is the complex refraction index of the propagation medium material. The propagation velocity in a material is defined by considering the phase constant, β, where $\beta = k_0 n' = \frac{2\pi}{\lambda} = \frac{\omega}{v}$, and v is the phase velocity for a signal of wavelength λ.

It is clear from these definitions that both the propagation and attenuation of propagating waves in a dielectric medium are frequency dependant. Generally, for a pure dielectric material, the attenuation and propagation velocity are related to the frequency as shown in Figure 197. There are two clearly defined regions, where the relationship between the attenuation and frequency are different, due to the different propagation mechanisms that dominate in the two regions. Below the transition frequency of the propagation medium (F_t), diffusion and conduction mechanisms dominate, while above F_t, electromagnetic energy propagates as a self-maintaining wave. In both regions, the gradient of log(α) vs. log frequency is constant, and generally positive (i.e. lower frequency signals propagate slower and with less attenuation). The transition frequency of a given material can be determined approximately by computing the frequency at which the loss tangent of the material is equal to one. The relational gradients in the regions above and below F_t can be computed as shown in (A.3).

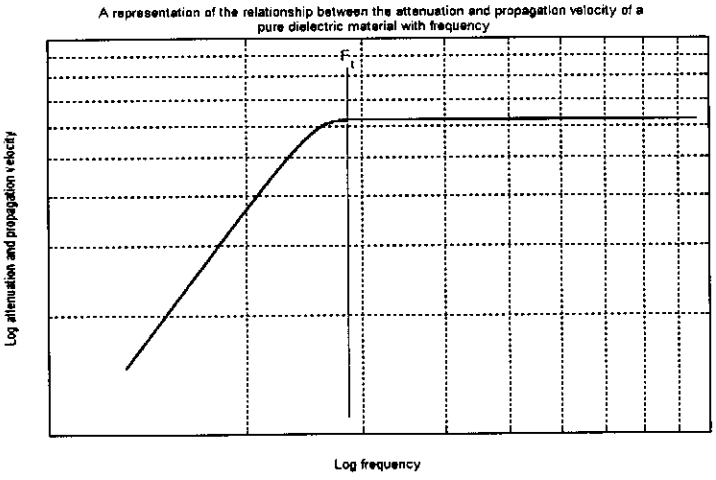

Figure 197 The form of the attenuation vs. frequency and propagation vs. frequency properties of a pure dielectric material, showing the transition frequency

$$\begin{aligned} \text{Below } F_t &\Rightarrow Gradient(\alpha) = \sqrt{\frac{\omega\mu\sigma}{2}}; Gradient(v) = \sqrt{\frac{2\omega}{\mu\sigma}} \\ \text{Above } F_t &\Rightarrow Gradient(\alpha) = \frac{\sigma\sqrt{\mu_0}}{2\sqrt{\varepsilon_0\varepsilon_r}}; Gradient(v) = \frac{c_0}{\sqrt{\varepsilon}} \end{aligned} \qquad \text{(A.3)}$$

For wideband pulse applications like the BHR application considered in this report, the frequency dependence of attenuation and propagation velocity is of extreme importance, as it will directly affect the propagating pulse form, and thus also the resolution of received data. The exact effects of complex propagation media on the form of a propagating EM pulse is an advanced topic, and we will not explicitly derive the effects here. More information concerning EM propagation in complex media may be found in the literature [12],[7].

At an interface between two media with different electromagnetic properties, any incident propagating EM wave will be partially reflected as the fields on either side of the boundary adjust to adhere to the electromagnetic boundary value requirements at the interface under consideration. For dielectric media, the reflection at a planar boundary can be simply described using a reflection coefficient description, similar to that used in basic transmition line theory. Assuming that the two media either side the boundary have different permitivities and permiabilities, and that both media may be lossy (complex ε_r and/or μ_r), we can define two sets of reflection (Γ) and transmition (T) coefficients for the parallel and perpendicularly polarized component of the incident wave respectively as shown in (A.4). (Perpendicular and parallel polarization are defined in Figure 198. Note that any travelling wave can be decomposed into two components that are parallel and perpendicularly polarized to any planar boundary.)

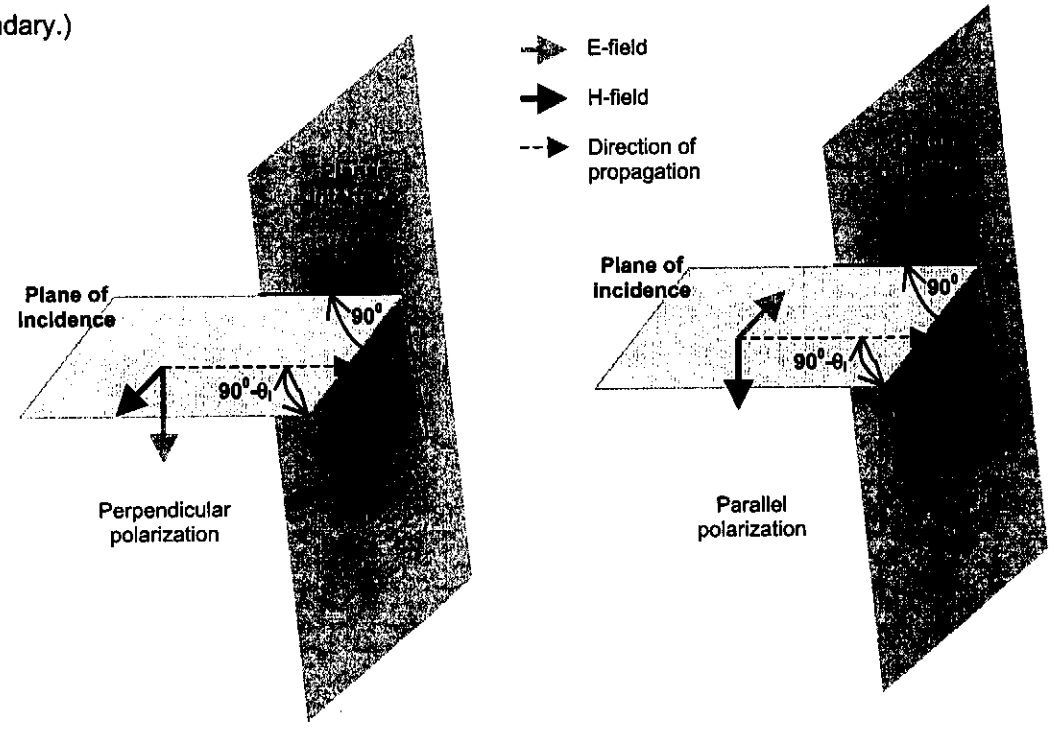

Figure 198 The definition of the perpendicular and parallel-polarized components of a propagating EM wave incident on a planar interface

Parallel polarization

$$\Gamma_p = \frac{Z_2 - Z_1}{Z_2 + Z_1}; T_p = \frac{2Z_2}{Z_1 + Z_2}\frac{\cos\theta_i}{\cos\theta_t}$$

where

$$Z_2 = \frac{k_2\cos(\theta_t)}{\omega\varepsilon_2}; Z_1 = \frac{k_1\cos(\theta_i)}{\omega\varepsilon_1}$$

and

θ_i = angle of incidence; θ_t = angle of transmition

Perpendicular polarization

$$\Gamma_s = \frac{Z_2 - Z_1}{Z_2 + Z_1}; T_s = \frac{2Z_2}{Z_1 + Z_2} \qquad \text{(A.4)}$$

where

$$Z_2 = \frac{\omega\mu_2}{k_2\cos(\theta_t)}; Z_1 = \frac{\omega\mu_1}{k_1\cos(\theta_i)}$$

and

θ_i = angle of incidence; θ_t = angle of transmition

Again, a more detailed consideration of the physical implications of these formulae for complex media is a difficult task, and will not be performed here, but we will rather refer to the general concepts of radio wave propagation, attenuation and reflection as presented thus far. More detail about the behaviour of waves in complex media, and reflection of propagating waves at complex media interfaces may be found in the literature [12],[7].

Based on this brief introduction to the propagation mechanics of an electromagnetic wave in a complex dielectric medium, a number of conclusions can be reached that to a large degree define the essence of the GPR/BHR problem. Let us consider the time evolution of the case described in Figure 199, with the help of a 'bounce diagram'.

The trigger pulse will be transmitted from the transmitter to the DAQ along the optical cable (ε_r=5; v=134.07x10^{6}m/s), at the same time as a travelling EM pulse is radiated into the rock in which the borehole is drilled (ε_r=6; v=122.39x10^{6}m/s). The radiated pulse will propagate to the first planar interface, where percentage of the incident energy will be reflected back towards the BHR probe (Γ=0.25). The transmitted energy will propagate on (ε_r=10; v=94.803x10^{6}m/s), toward the second planar interface, where reflection will again occur (Γ=-0.429). Transmitted energy will propagate to the BHR target body (ε_r=4; v=149.90x10^{6}m/s), and a percentage of the incident energy will be scattered in the direction of the BHR probe, depending on the relative electromagnetic properties, the size and the shape of the body.

The pulse reflection energy of each of these reflections will be received at the DAQ at the time points at the y=-100m point on the bounce diagram.

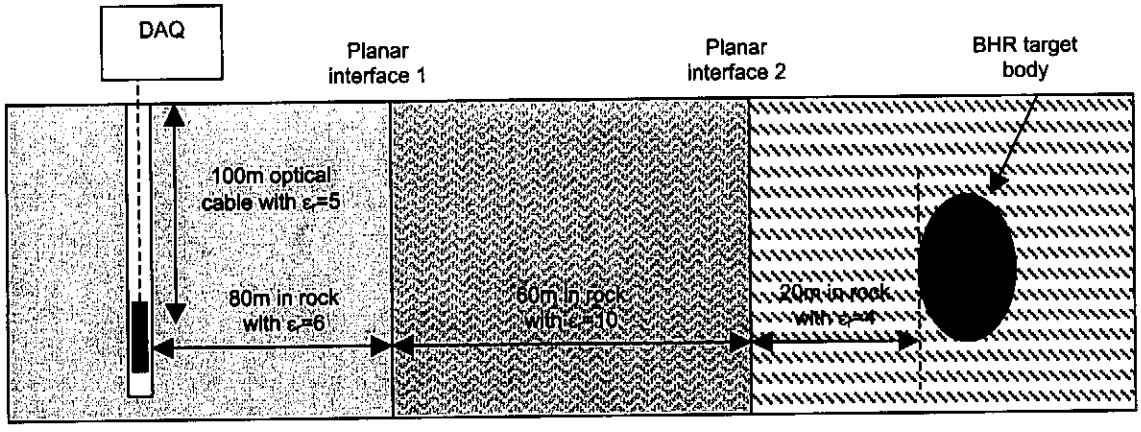

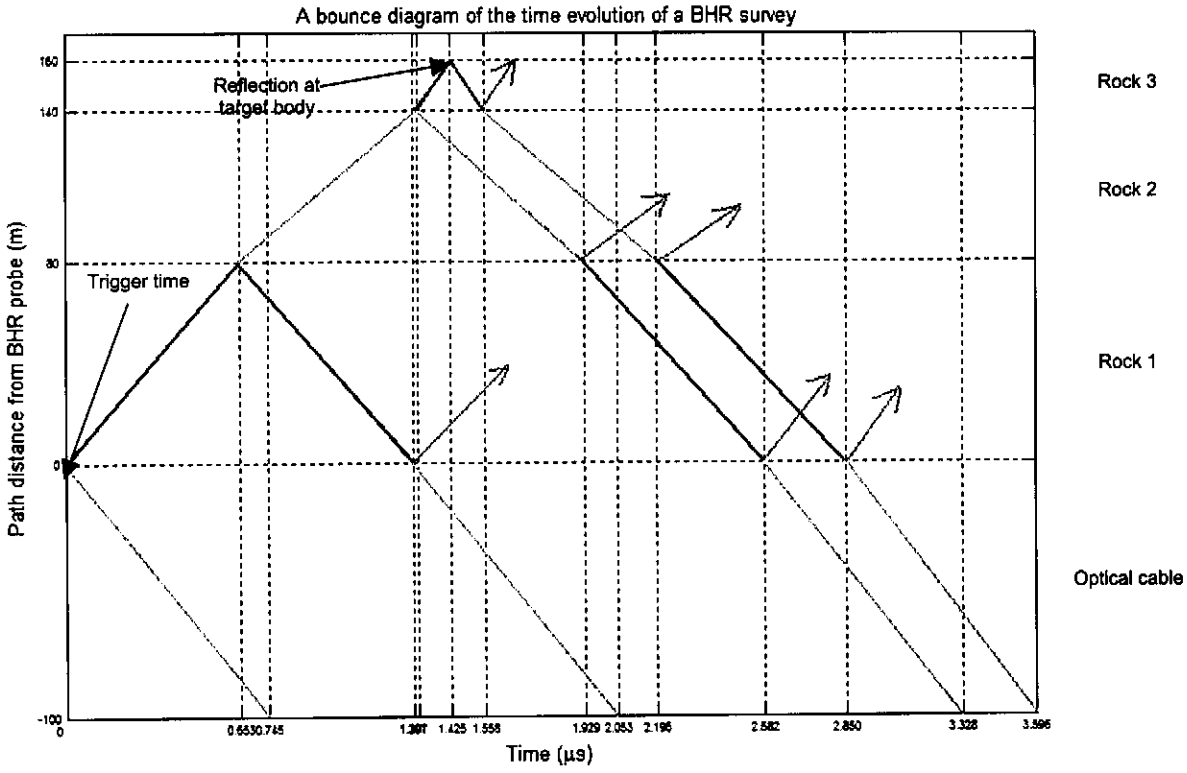

Figure 199 A bounce diagram showing the time evolution of a typical BHR acquired data trace

This type of analysis is used to extract the observed geological topography, by combining known information about the approximate structures and propagation characteristics in the survey region with the observed time evolution of the received signal at a specific point. It is clear that bounce-type analysis can only deliver the distance to the target position. Directional information has to be inferred based on the known geology.

A.2. A short introduction to the interpretation of BHR data

The post-processing and interpretation of BHR data, in order to extract the observed geological features is a relatively complex problem, and requires that a basic idea of certain expected features be combined with the data, in order to provide a spatial reference point for observations.

Typical raw and processed (using Seiswin[23]) BHR data is shown in Figure 200. Two typically observed events are shown in the processed data, a linear event, and a parabolic curve event.

The BHR data is generated by plotting consecutive acquired traces next to each other, and applying a smooth relief contour shading to the data (colour dependant on signal level). The data is generally viewed from above. The axes of the BHR data are trace number and time. The trace number axis is used as a spatial reference, with a 'blank' zero trace inserted into the data to the data every 5m during radar deployment. These 'blank' traces can be seen in the data shown in Figure 200.

In order to give a basic feel for how BHR data can be interpreted, we will describe the structures that could produce the two typical forms indicated in the processed data of Figure 200. These type of intuitive derivations of the form, positions and structure of reflecting objects must be combined with known geological information about the survey area in order to specifically identify reflecting targets.

The linear event is typical of a large, relatively flat planar object, such as an interface between two different rock layers. It is clear that the interface under consideration is not parallel to the borehole trajectory, and as the BHR probe is moved along the borehole, the propagation time to and from the BHR probe decreases, indicating that the borehole is approaching the interface. A simplistic representation of this case is given in Figure 201.

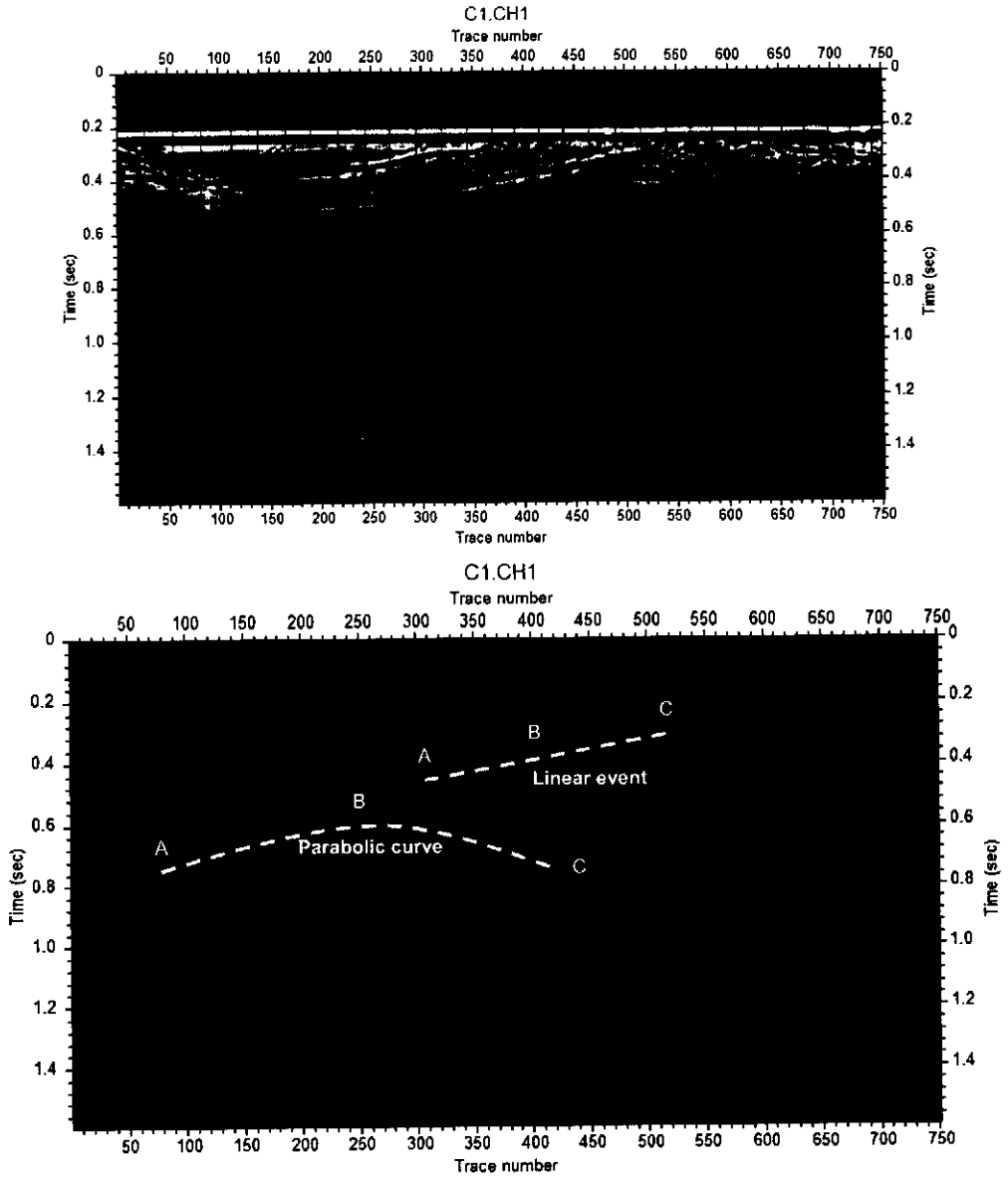

Figure 200 Typical raw and processed BHR acquired data

The parabolic or curved event it typical of a body near which the BHR shot-line passes. As the deployed probe approaches the body, the reflection times to and from the body shorten, following a typical curved trajectory. When the probe is at the position in the borehole that is closest to the reflecting body, the curve will reach its apex, and the propagation time to and from the reflecting body will begin to increase, again following the typical curved trajectory. A simplistic representation of the physical structure implied by this event is given in Figure 201.

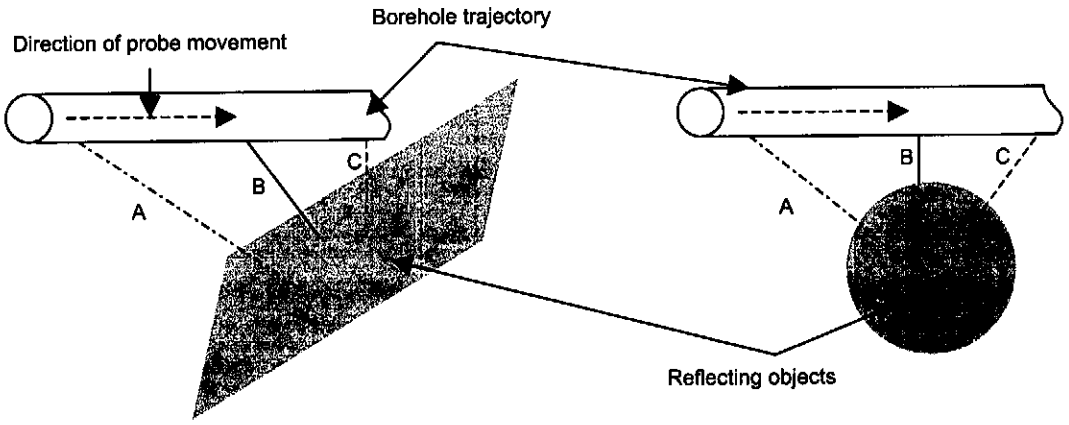

Figure 201 A schematic representation of the two cases that will typically generate the linear- and curved-events indicated in Figure 200.

As mentioned in Appendix A.1, BHR survey data is able to provide relative distance, but not relative directional information. The plots of Figure 200 are thus effectively a 1-dimensional representation of the 3-dimentional space around the BHR probe, as a function of time and position. Useful interpretation is thus heavily reliant of prior knowledge of reference structures, and approximate geology of the area.

Appendix B.

B.1. A balanced antenna measurement method

The measurement of the characteristics of a symmetrical antenna structure is often complicated by the need for a true balanced feed method for accurate measurement results. There are a number of feed structures and methods that can be used to balance the antenna feed during measurement. These methods however are generally not effective over very large bandwidths.

One general solution to the balanced feed problem (the ¼-wavelength balun) is outlined in Figure 202.

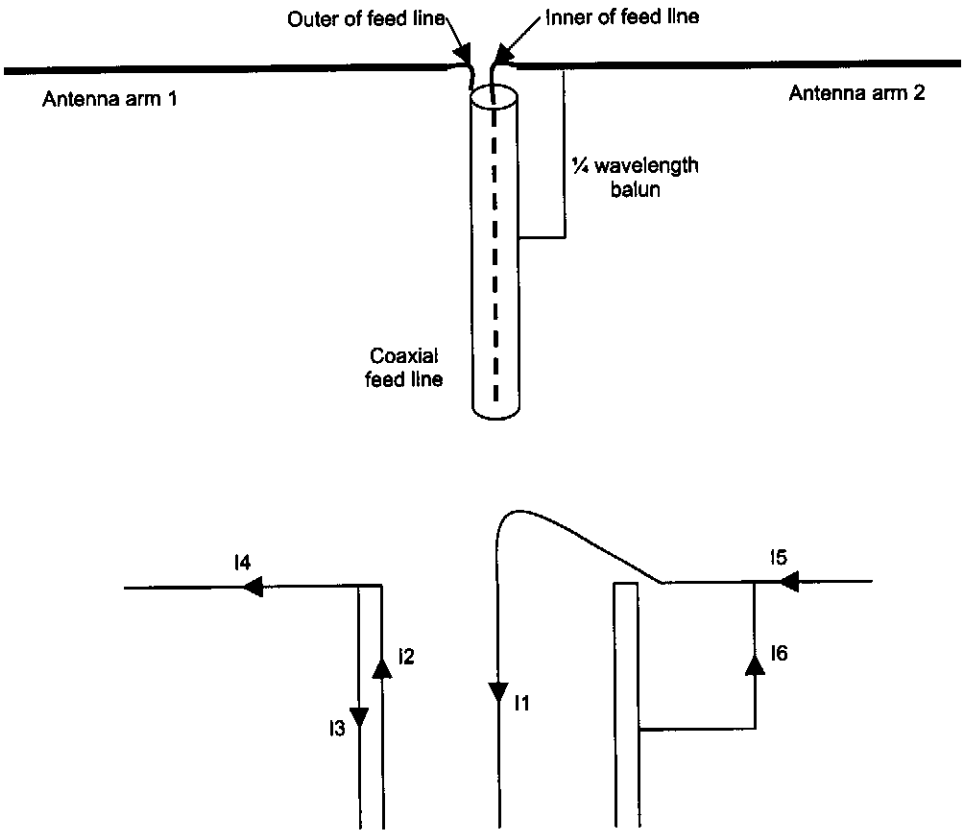

Figure 202 The structure and detail of the feed currents on a general 1/4-wavelength balun feed structure

At high enough frequencies, there are 3 current paths, rather than two on the coaxial feed line structure. The first path (labelled I1) is on the central conductor of the coaxial feed line. The second path (labelled I2) is on the inside of the coaxial conducting sheath, and the third path (labelled I3) is on the outside of the coaxial conductive sheath. For a balanced feed, we require that the magnitude

of the currents induced by the source on the two antenna arms be equal (i.e. I5=I4). We know, however, that by Kirschoff's current summation law that (B.5) is true.

$$\begin{aligned} I1 &= I5 \\ I1 &= I2 \\ I4 &= I2 - I3 \end{aligned} \qquad \text{(B.5)}$$

By implication, I4 is thus not equal to I5, but rather I5=I4-I3. By addition of the balun current path (labelled I6), this unbalanced state can be alleviated, forcing I4=I5. The length of the balun conductor is chosen as ¼ of the excitation wavelength, so that at the excitation frequency of interest, the connection between the driven arm and the outer coaxial conductor appears as an open circuit (short transformed through a ¼ wavelength section of transmition line). This ¼ wavelength requirement for balanced feed operation intrinsically introduces a narrow operational bandwidth of the feed, and as with most balun methods, this is not suitable for accurate broadband BHR measurements. For more detail on the ¼ wavelength balun, as well as other balanced feed methods, see [11], section 5.3.

All the applications referred to in this report employ a bandwidth of the order 1:10. For antenna measurements, this requirement suggests that a non-standard balancing method is necessary. A method developed by Mel van Rooyen and K.D Palmer [5] that employs a calibrated feed jig structure, giving very good bandwidth measurement capabilities was used. The theory of this method is outlined as follows.

The physical measurement set-up is shown in Figure 203. The measurement procedure consists of 3 steps. First, the balanced load is removed, and a good short circuit at the feed point is made. The full 2-port S-parameters of the shorted feed jig structure are then measured for later calibration and processing of the measured data. Next, the balanced load is connected as shown, and again the full 2-port S-parameters are measured at the same frequency points used during the jig calibration measurement. The final step in the measurement procedure is the processing of the measured data to calibrate the effect of the feed jig section out, and to extract antenna characteristics of the load from the 2-port S-parameter measurement data.

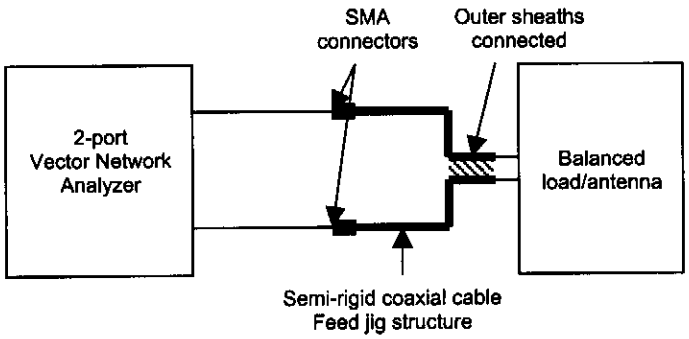

Figure 203 The measurement set-up for wideband measurement of a balanced antenna structure

The calibration and antenna characteristic extraction procedure is based on the model of Figure 204, which can be used to model any balanced load structure.

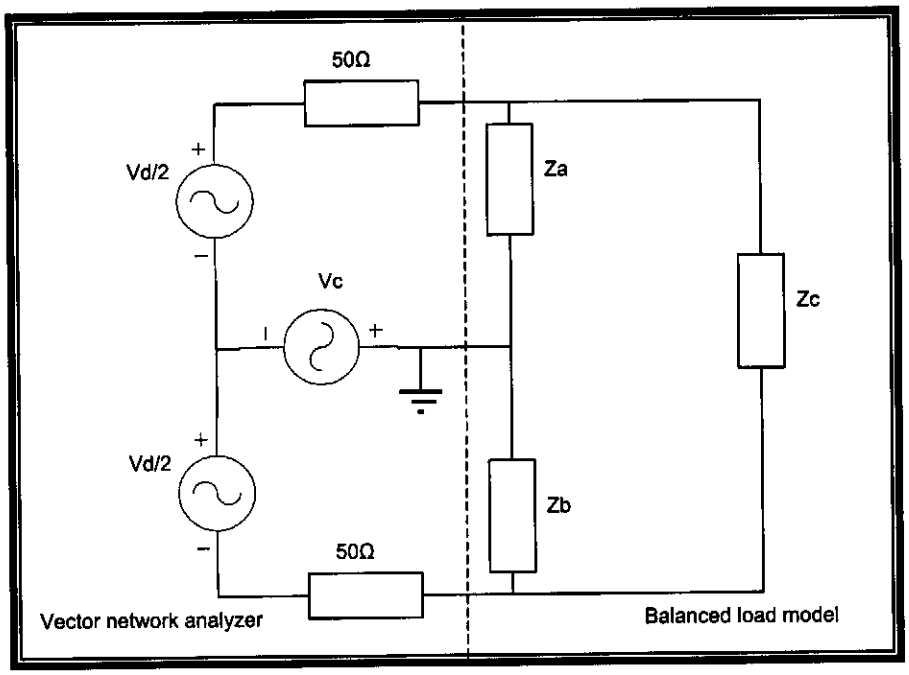

Figure 204 The model used for data processing and extraction of the wideband antenna characteristics of a balanced antenna load

V_c and V_d are the common and differential components of the excitation voltage respectively. The differential and common mode impedances of the load structure are given by (B.6).

$$Z_{common} = Z_a // Z_b$$
$$Z_{differential} = Z_c // (Z_a + Z_b) \quad \text{(B.6)}$$

The raw measured 2-port data of the shorted feed jig and the measured load 2-port data are processed using a MATLAB procedure written by Van Rooyen. Detail of this procedure is available in his MSc thesis report [5].

B.2. Operational detail of the ADS/FEKO time-domain modelling procedures

In section 2.1.3, a computational method for time domain modelling of the operation of a radiating structure for a given time-domain excitation was introduced. By importing FEKO simulation results of the reflection coefficient at the feed point of the structure and the radiated E-field at a point in space for the given excitation (unity excitation, zero phase) in the form of a 2-port model where $S11=S11_{simulated}$ and $S21=E\text{-}field_{radiated}$, we can define the antenna as a 2-port component in ADS.

The form of the ADS 1-port and 2-port models is as follows [26].

1-port model:

#	Hz	S	RI	R	impedance
5000000	9.81E-01	-1.76E-01			
11052600	8.92E-01	-4.02E-01			
17105300	6.53E-01	-6.20E-01			
23157900	2.00E-01	-5.88E-01			
29210500	6.32E-02	-1.28E-01			

Frequency unit

Frequency points

Real $(S11)_{Simulated}$

Imaginary $(S11)_{simulated}$

2-port model:

Frequency unit

E-field (Imag)

S12(real)=0

S22 (real)=0

#	Hz	S	RI	R	50			
1.00E+07	9.26E-01	-2.05E-01	0.002093	-2.05E-01	0	0	0	0
1.47E+07	8.80E-01	-2.79E-01	0.004206	-2.79E-01	0	0	0	0
1.95E+07	8.23E-01	-3.48E-01	0.007032	-3.48E-01	0	0	0	0
2.42E+07	7.51E-01	-4.09E-01	0.010748	-4.09E-01	0	0	0	0
2.89E+07	6.64E-01	-4.57E-01	0.015582	-4.57E-01	0	0	0	0
3.37E+07	5.61E-01	-4.84E-01	0.021794	-4.84E-01	0	0	0	0

Frequency points

S11 (real)

S11 (Imag)

E-field (real)

S12(imag)=0

S22 (imag)=0

We want to determine the feed current and the field radiated for an applied excitation voltage. The interaction between the source and the antenna is critical to the derivation of accurate results. In order to show the operation of this modelling method, we will consider three cases.

- Continuous wave sinusoidal excitation
- Pulsed excitation assuming an ideal source
- Pulsed excitation assuming a practical excitation electronics topology, to quantify the effects of interaction between the antenna and the driving electronics in the time domain

An ideal feed source can be represented in two ways, by using a Thevenin-Norton source transformation as shown in Figure 205.

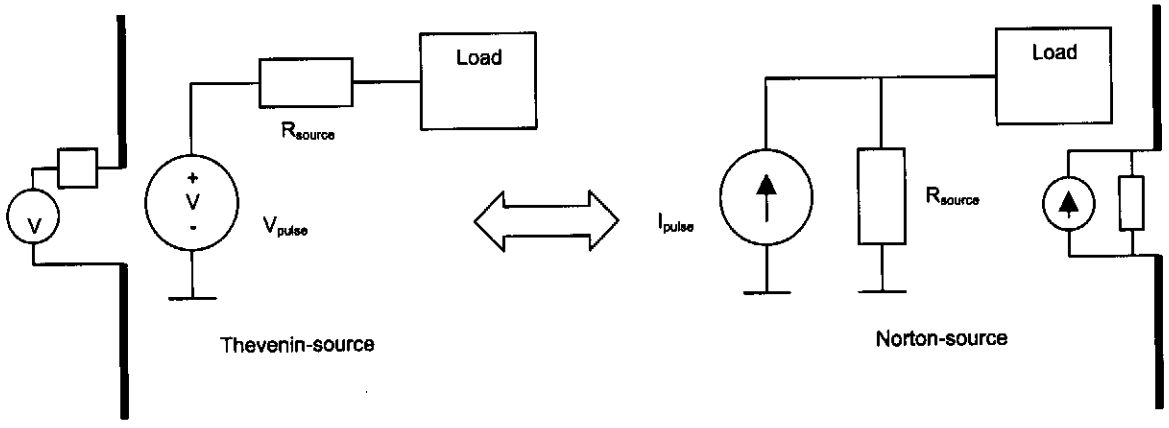

Figure 205 The two source forms used for ADS approximation of a matched antenna feed

CW sinusoidal excitation

If we apply an ideal CW source to the antenna, we expect to be able to identify two regions in the antenna response to the excitation. The first part of the response will be the transient response just after the source has turned on. The second part is the steady state response of the antenna after the transient has passed. The ADS model with an ideal 50Ω CW source is shown in Figure 206. The simulation results, showing the computed broadside radiated field and the feed current of the antenna with a simple wire dipole antenna load simulated in FEKO in air, for a 30MHz sinusoidal excitation is shown in Figure 207. The transient response and steady state can be seen clearly in the results. Also shown in Figure 207 is the comparative steady state radiated field and the derivative of the feed

current. It is clear that in the steady state the field and the feed current derivative have the same form. During the transient period, however this is not so, due to the phase effects of the finite propagation time of the turn- on transient, as discussed in 2.1.3.

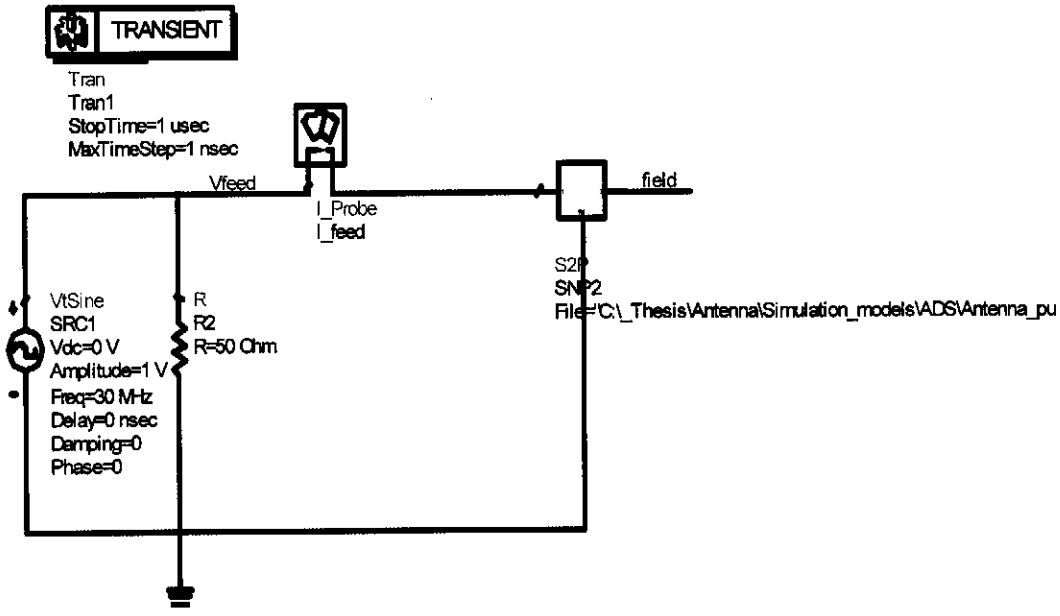

Figure 206 The ADS model used to determine the time-domain operation of an antenna structure with continuous wave excitation

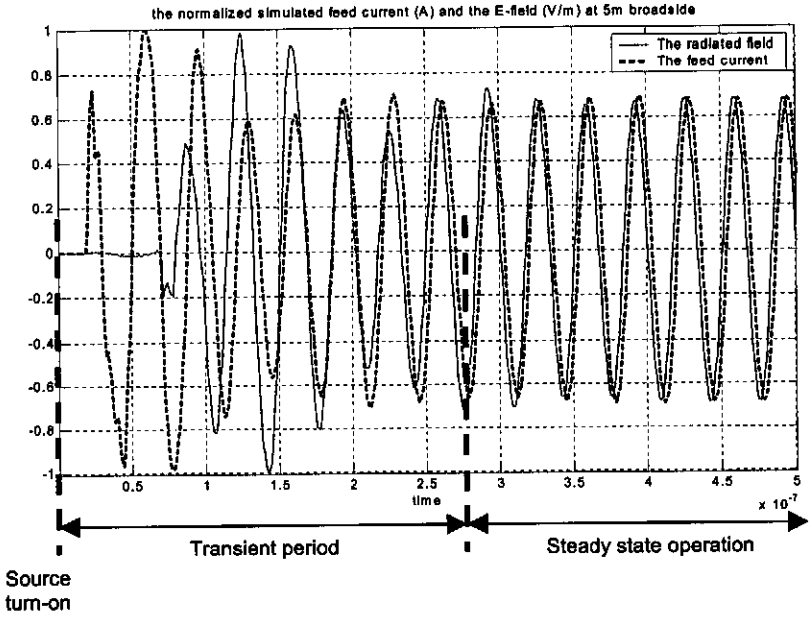

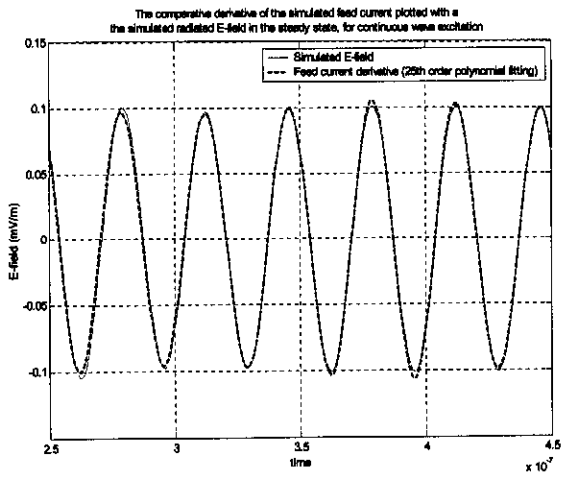

Figure 207 ***Top****: the transient and steady state radiation of a simple wire dipole antenna for 30MHz sinusoidal excitation;* ***Bottom****: the steady state feed current derivative and the steady state radiated field*

For pulsed applications, it is the transient response of the antenna that is of interest, rather than the CW response.

Pulsed excitation (ideal source)

Because the antenna is not matched to the source at all frequencies, reflection of any broadband feed pulse will occur at the antenna feed-point. The incident pulse current minus this reflected pulse will then be the current pulse form that excites the antenna structure. We thus want to compute this differential pulse. In order to show the feed reflection phenomenon, let us consider the ADS model shown in Figure 208, which employs a 50Ω matched transmition line between the antenna feed and the source point. The inclusion of transmition line introduces a time delay between the source pulse and the time when the pulse reaches the antenna feed point. As this TX-line section is shortened, the time between the source pulse, and the return of the reflected pulse will be less and less, until they begin to overlap and add. When the TX-line length is zero, only the difference between the source and reflected pulse will be observed at the feed point. This difference is then the form that we require to show the pulsed current that excites the antenna structure. The 50Ω source impedance of the pulse source ensures that no reflection of the reflected pulse that returns through the TX-line can occur. The pulse at the antenna feed is thus not influenced by the antenna-source mismatch. The FEKO-computed reflection coefficient of the simulated antenna is computed for a 50Ω system, so that the input reflection of the 2-port model will be correct when the antenna is driven with a 50Ω source feed.

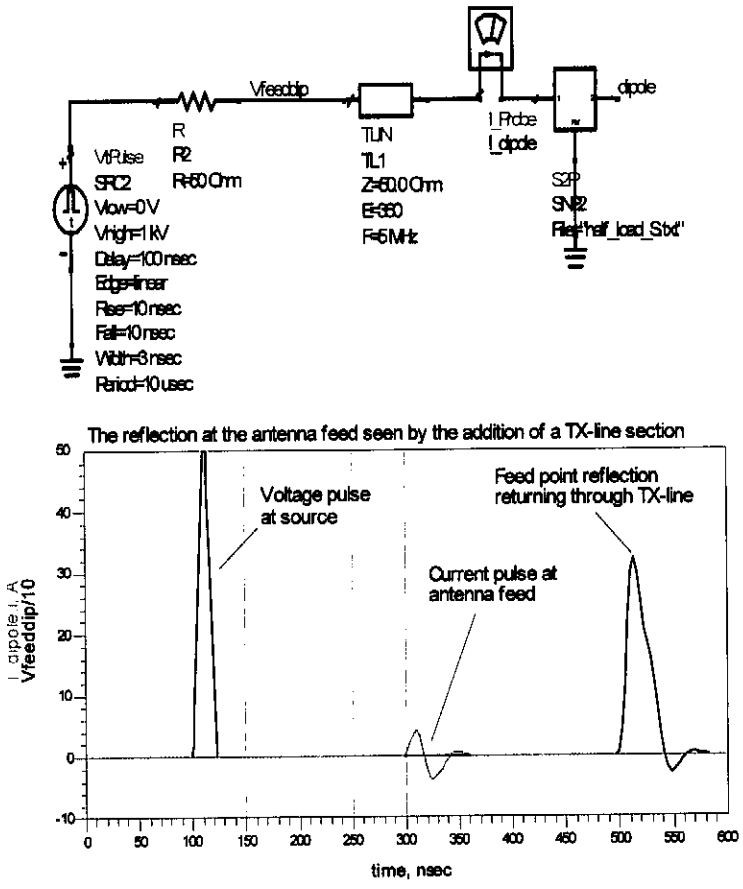

Figure 208 An ADS model incorporating a TX-line section to show the source pulse reflection at the antenna feed point

Interaction between a practical antenna structure and practical drive electronics

By driving a 2-port model of a given antenna structure directly with an ADS model of a practical transmitter topology, the loading and interaction between the electronics and the antenna can be characterized. Figure 209 shows an ADS model of a mono-static transmitter topology (similar to the one discussed in Chapter 4), with a 2-port antenna model load. This model can be used to model the operation of the transmitter isolation, the radiated fields and the loading effects of the antenna structure under consideration. If only the interaction of the antenna and the electronics with respect to the antenna impedance is of interest, then the use of a simple lumped element approximation of the antenna structure, similar to those introduced in section 2.5.2.3 may be used. This type of lumped element approximation is also particularly useful in the optimisation of the 'dummy' load employed for a specific antenna structure.

A few typical simulation results, showing the predicted leakage signal on the receiver port and the radiated E-field for a few antenna structures considered in this report are shown in Figure 210.

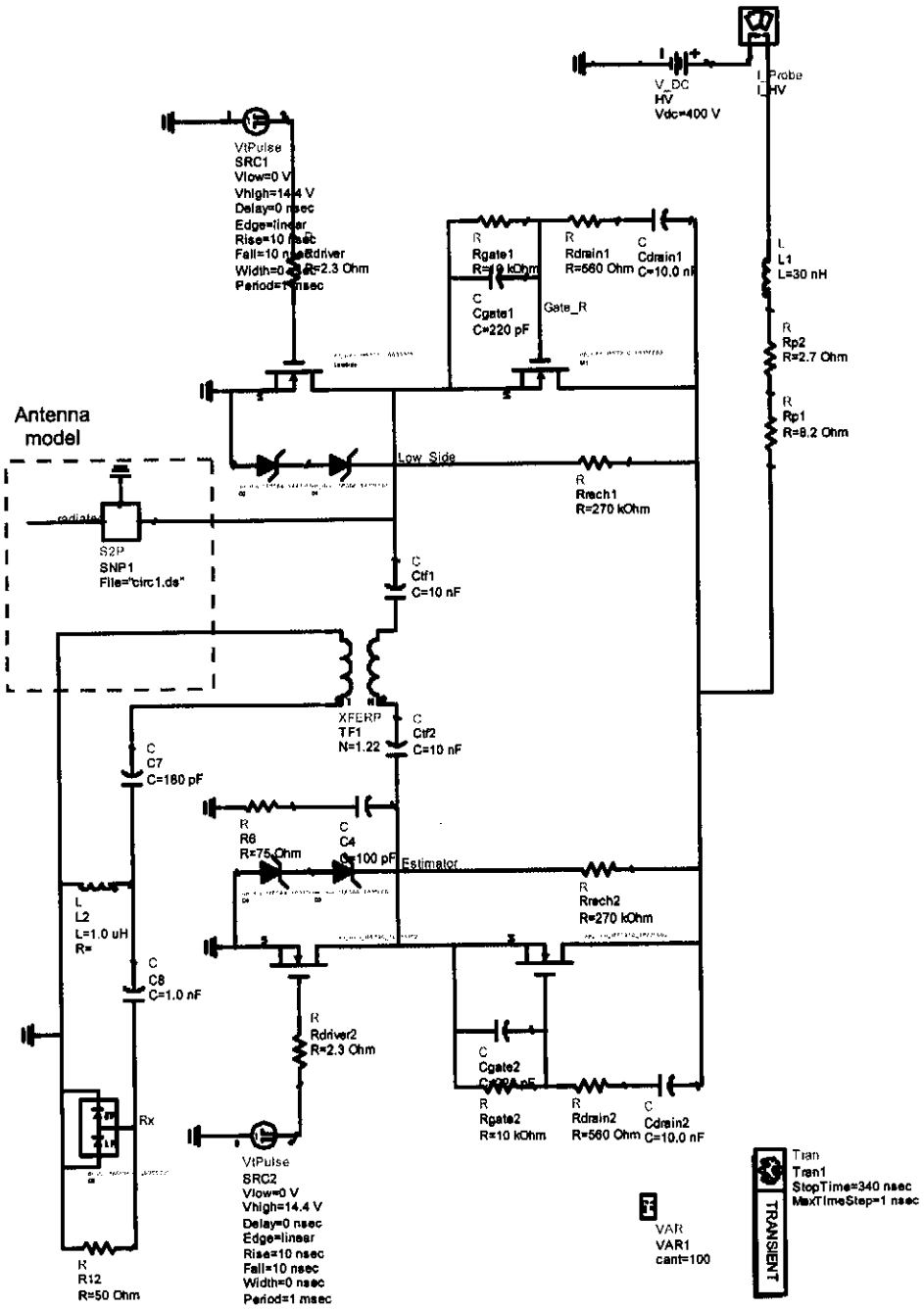

Figure 209 An ADS model of a practical transmitter topology used to determine the interaction between the antenna structure and the transmitter electronics

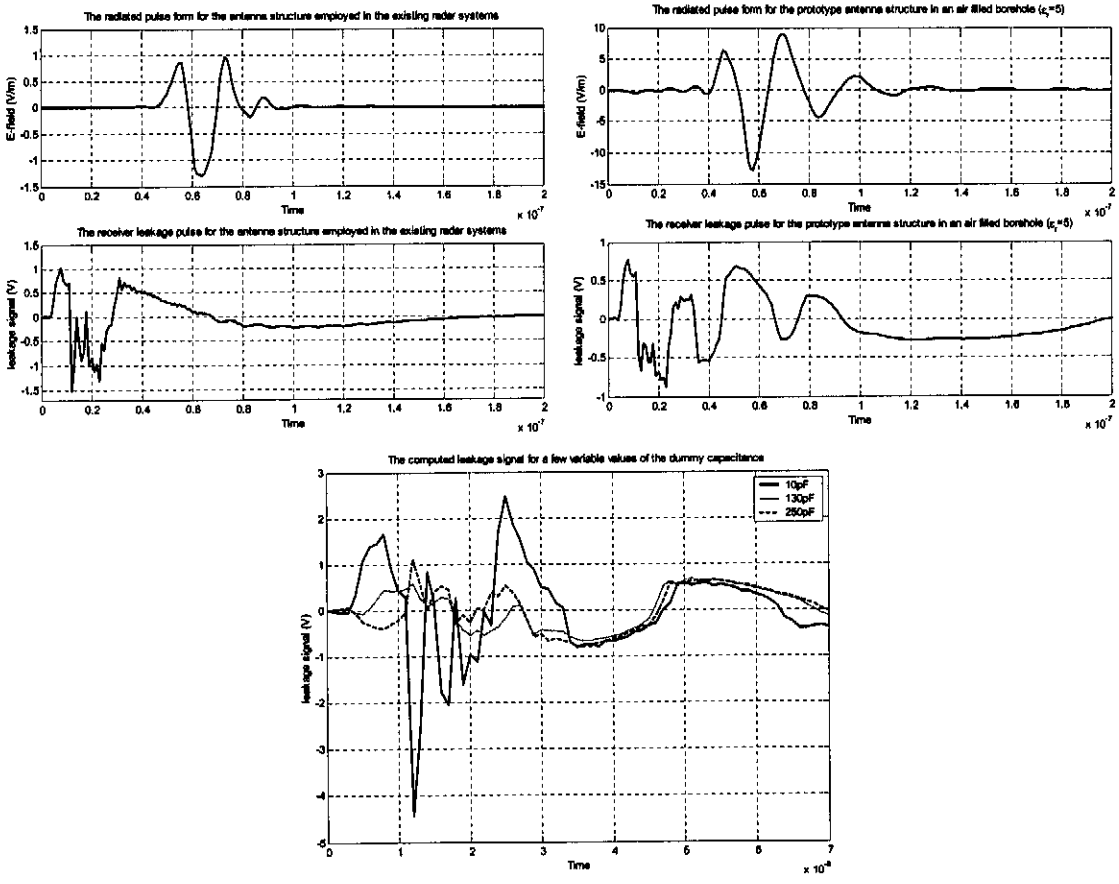

Figure 210 Typical simulation outputs of the interaction between an ADS 2-port antenna model, and a model of the operational transmitter circuitry

The operation of the mono-static transmitter/isolator topology (described in Chapter 4) with the antenna used in the existing structure, and with the antenna used for prototype testing n this report as a load, are shown. Also shown is a typical optimisation result for the value of a lumped component in the dummy load. The 130pF case seems to approximate the antenna impedance well, and give good isolation, while the other two values provide relatively poor isolation.

In order to incorporate the simulation of received reflections at the antenna port, we can apply a simple modification of a 2-port antenna model, by defining S12 as 1+j0 at all frequencies. If the output port of the antenna component is then driven with a source, as shown in Figure 211, the received signal at the receiver port due to the applied excitation can be computed. A simulation result showing the radiated field and applied received fields and the given antenna structure and receiver port signal are shown in Figure 211.

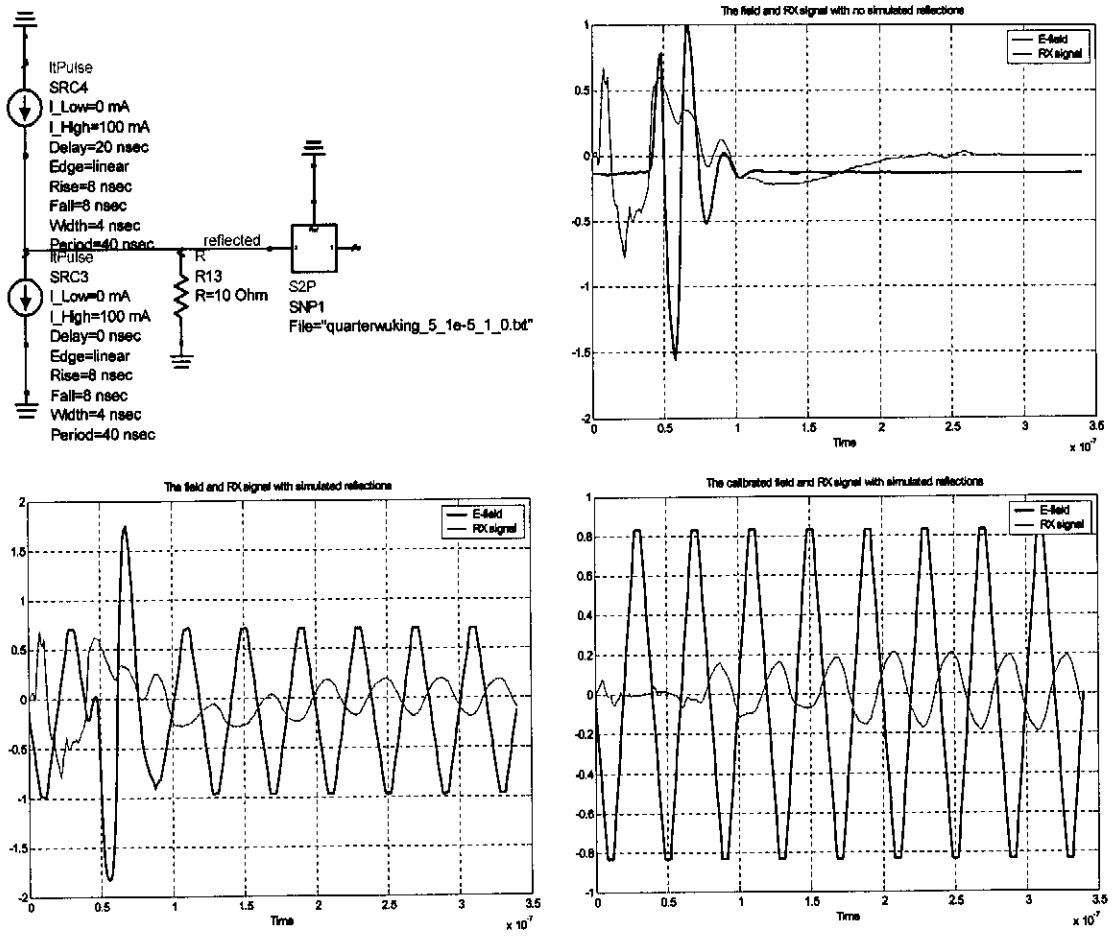

Figure 211 The modification of the antenna model to include a simulated reflection signal, and typical simulation results

The simulation results of Figure 211 were calibrated by subtracting the no-reflection signals from the reflection signal results. The receiver port signal for the shown received reflection excitation suggests that reflection data can be observed 75ns after the trigger signal. The losses in the antenna-to-receiver path, and the effect of the filter on the pulse form are clear.

This type of simulation is presents a very powerful method of predicting the operation of a system in different environments, and under different conditions. Practical factors that are not considered in this type of model, like coupling, component non-idealities and tolerances, inaccuracies in the antenna model etc. will cause variation in the practical realization, but a very good idea of the general operation of a given topology under realistic conditions can be quickly achieved.

B.3. FEKO modelling of antennas and the BHR operational environment

The antenna environment of the BHR structure was shortly described from an electromagnetic point of view in section 2.2. Both the geometry of the environment, and the properties of the individual materials are of importance.

In order to model the operational environment in FEKO, we must define each of the dielectric layers in Figure 37 around the antenna structure. In the ideal case, these layers would be axially infinite in length, but this would make the meshing matrices, and thus also the computation time extremely long. If we assume, however that all of the antenna structures under consideration in this study have nulls in their axial direction at all frequencies, by symmetry, the effect of a non-infinite borehole length on the operation of the antennas will be extremely small. The effect of a shortened borehole on the operation of the non-symmetrical antenna structures used in the existing BHR system, as considered in section 2.4.2 will be larger, due to the asymmetry of the structures, and thus the frequency dependence of the radiation pattern. Investigation, however, by M Van Wyk [6], and also during this report period, shows that the effect is negligibly small.

The 1st extreme case, shown in Figure 37 is modelled as shown in the FEKO models of Figure 212. The antenna structure is defined inside a dielectric region, representing the PVC pipe housing, with given properties. The ambient properties of the infinite area around the model of the structure are then assigned values that model rock.

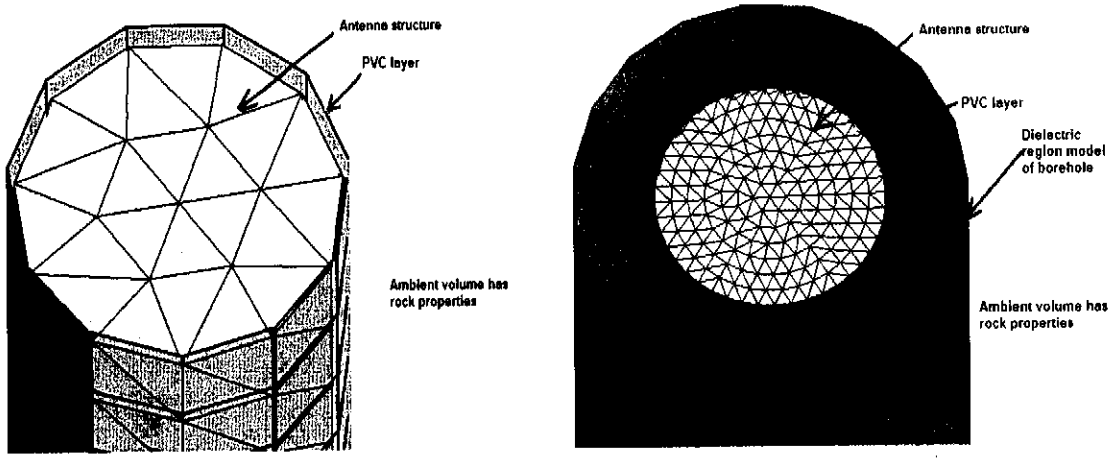

Figure 212 Sections of the FEKO models of the two extreme environmental cases of Figure 37

The 2nd extreme case includes the effect of a borehole around the probe structure. A cross-section of a typical FEKO model of this type is also shown in Figure 212. The dielectric volumes defining the borehole and the PVC pipe structure are realized by defining a dielectric regions, containing metallic

structures using the ME and DI cards. (In the case of a simplified wire dipole structure, the PVC layer can be represented by a thick dielectric coating, defined by the CO card.)

The ambient rock volume properties are defined by selecting the desired values in the EG card, after the full geometry has been defined.

One important factor that must be considered is that when the PVC pipe structure is defined as a closed dielectric region, all of the metallic elements inside that region are modelled as being fully imbedded in the relevant dielectric. This implies that any gap between the PVC pipe structure and the antenna structure will also be filled with a dielectric material with the same properties as PVC. For the realization of extremely accurate models of practical structures, this must be considered. In order to model the case where there are air gaps or potting material between the antenna and the PVC pipe, a 3rd dielectric layer must be added.

Axial sections of three FEKO models, defining the three possible structures described here were presented during the course of this report, but are repeated in detail in Figure 213 to Figure 214.

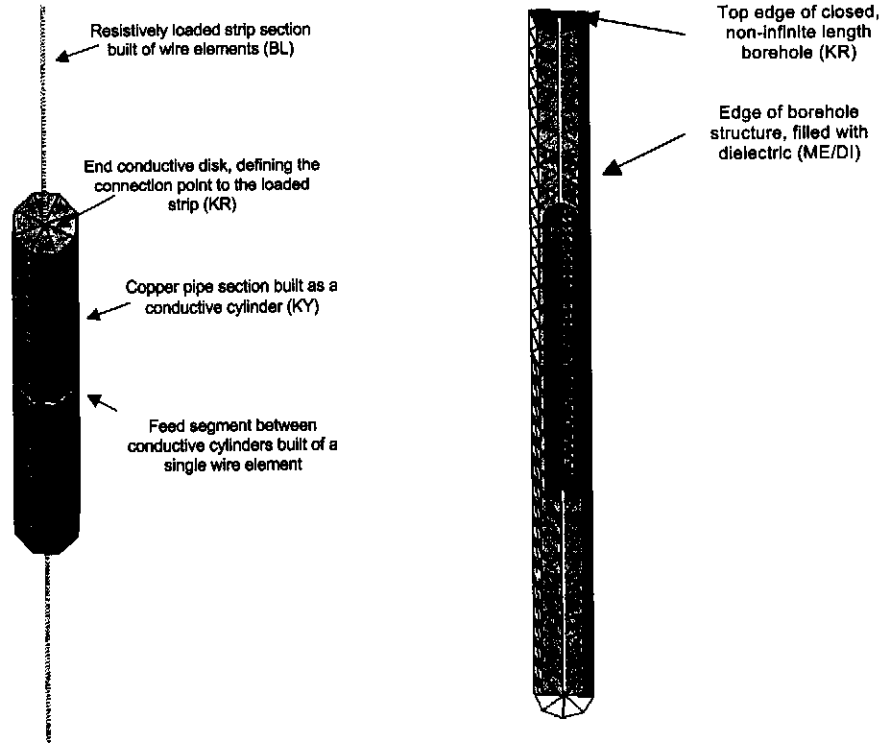

Figure 213 The FEKO model of the simplistic case of an antenna embedded directly in rock, and the same structure in a closed borehole

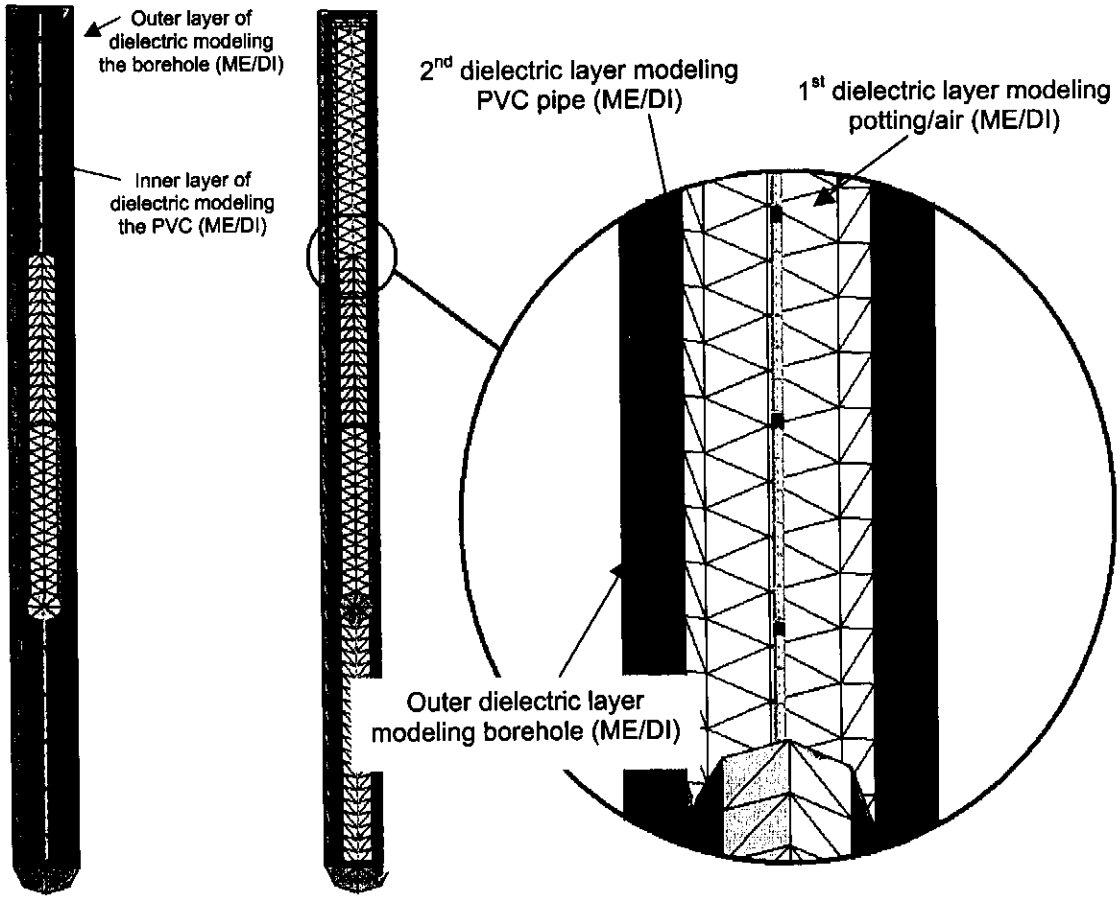

Figure 214 Detail of FEKO models, including the effect of the PVC pipe probe housing, and potting material/air-gaps

The computational cost of the complex models of Figure 214 is very severe, particularly in the case where 3 separate cylindrical dielectric layers are included. In order to decrease the computation time and effort, electrical symmetry on the perpendicular plane, and magnetic symmetry on the two parallel planes was used in all cases. Further reduction in computation time requires that the model be simplified so that the number of mesh elements that comprise the structure is reduced. Certain simulations using full antenna models with three dielectric layers proved to have a computation cost that was inhibitive for the available resources. In these cases, results generated using slightly simplified models were used. It was also found that for certain complex environmental cases, no sensible results could be realized by simulation.

B.4. The derivation of the Wu-King profile

This appendix is based on an appendix in the thesis report of S Keller. It will be shown that by addition of a continuous resistive loading profile to an excited dipole antenna structure, a current distribution can be obtained that consists only of an travelling wave component that moves outward from the feed point.

The vector potential $A_z(z)$ on the surface of the antenna with an internal impedance of $z^i(z)$, carries a total current $I_z(z)$ and is driven by at z=0 by a delta function generator with emf V_o satisfies the one dimensional equation of (B.7), if a time dependence of $e^{j\omega t}$ is assumed.

$$\left(\frac{\partial^2}{\partial z^2}+k_o^2\right)A_z(z)=\frac{jk_o^2}{\omega}\left[z^i(z)I_z(z)-V_o\delta(z)\right] \qquad \text{(B.7)}$$

The internal impedance per unit length is expressed as a function of the axial coordinate z by (B.8).

$$z^i(z)=\frac{1}{2\pi a d(z)\sigma(z)} \qquad \text{(B.8)}$$

For a circular tube, the impedance can thus be varied by varying the wall thickness d(z) or the conductivity σ(z). The vector potential on the surface of the antenna is given by (B.9).

$$A_z(z)=\frac{\mu_0}{4\pi}\int_{-h}^{h} I_z(z')K(z,z')dz' \qquad \text{(B.9)}$$

$$\text{where } K(z,z')=\frac{e^{-jk_0r}}{r} \text{ and } r=\sqrt{(r-r')^2+a^2}$$

The ratio of the vector potential to the current along an antenna is approximately constant making it possible to set $I_z\psi = \int I_z(z)K(z,z')dz'$, where ψ is the magnitude of the current at its maximum point.

Using this approximation and the notation $f(z)=\frac{4\pi}{\zeta_0\psi}z^i(z)$, and setting the intrinsic impedance to $\zeta_0=\sqrt{\frac{\mu_0}{\varepsilon_0}}=120\pi\Omega$, we can approximate (B.7) by (B.10).

$$\left[\frac{\partial^2}{\partial z^2}+k_0^2-jk_0f(z)\right]I_z(z)=-\frac{j4\pi k_0}{\zeta_0\psi}V_0\delta(z) \qquad \text{(B.10)}$$

At all points, except the driving point, the currents must satisfy (B.11).

$$\left[\frac{\partial^2}{\partial z^2}+k_0^2-jk_0f(z)\right]I_z(z)=0 \qquad \text{(B.11)}$$

It can be shown by direct substitution that if $f(z)=\frac{2}{h-|z|}$ then $I_z(z)=C(h-|z|)e^{-jk_0|z|}$ is a solution to the differential equation of (B.11).

This solution represents a current wave travelling in the direction of increasing $|z|$ (i.e. from the feed point towards the open ends of the antenna). This implies that there is no reflected wave at the antenna end points. In order to determine the value of the unknown constant C, we apply the Lorenz condition $\left(\Phi(z)=\frac{j\omega}{k_0^2}\frac{\partial A_z(z)}{\partial z}\right)$ together with $A_z(z)=\frac{\mu_0}{4\pi}\psi C(1+jk_0h)e^{-jk_0|z|}$.

By assuming symmetry around the feed point (i.e. $\Phi(z)=\Phi(-z)$ for $z\geq 0$) and defining the driving voltage by $V_0=2\Phi(0)$, we derive the constant C as in (B.12).

$$C=\frac{j2\pi\omega\varepsilon_0V_0}{\psi(1+jk_0h)} \qquad \text{(B.12)}$$

Combining this constant with the assumed solution form, the final current distribution is given by (B.13).

$$I(z)=\frac{2\pi V_0}{\zeta_0\psi(1-\frac{j}{k_0h})}\left(1-\frac{|z|}{h}\right)e^{-jk_0|z|} \qquad \text{(B.13)}$$

The continuous resistive loading profile that is needed to obtain this unidirectional travelling current wave is obtained as in (B.14).

$$Z^i(z)=\frac{\zeta_0\psi}{2\pi}\frac{1}{h-|z|}=\frac{60\psi}{h-|z|} \qquad \text{(B.14)}$$

where the coefficient 60 is in ohms

The expansion parameter for this profile (ψ) is the ratio of the vector potential to the current at the driving point. The definition of this ratio depends on the total length of the dipole structure (2h), the radius of the dipole (a) and the design frequency at which the unidirectional current wave will be achieved. For the case where $k_0 a \ll 1$ and $a \ll h$, which can be assumed to be true for all structures under consideration in this report, the following approximation for the expansion parameter can be made.

$$\psi = 2\left[\sinh^{-1}\left(\frac{h}{a}\right) - C_{\text{int}}\left(2k_0 a, 2k_0 h\right) - jS_{\text{int}}\left(2k_b a, 2k_b h\right)\right] + \frac{j}{k_0 h}\left[1 - e^{-2k_0 h}\right]$$

where C_{int} and S_{int} are the generalized sine and cosine integrals given by:

$$C_{\text{int}}(b,x) = \int_0^x \frac{1-\cos W}{W}\,du \qquad \text{(B.15)}$$

$$S_{\text{int}}(b,x) = \int_0^x \frac{\sin W}{W}\,du$$

where

$$W = \sqrt{u^2 + b^2}$$

The profile for a given dipole structure can be computed by numerical solution of the integrals of [1] and selection of a few loading values at discrete points on the antenna structure by integration of the continuous loading profile form of [5]

B.5. Minimum squared-error fitting algorithm

In order to determine the lumped component values that result in a lumped element model of the input impedance of n antenna structure, determined by simulation, we wish to fit a given function describing the input impedance of the lumped model to the impedance curve delivered by the simulation results by manipulation of the lumped model parameters. The basic method used to do this is:

- Fit a polynomial to the data points representing the simulation results. This is done in MATLAB using the polyfit command.
- Compute the value of the fitted polynomial at regular frequency points along the curve. This is done using the MATLAB polyval command.

Determine the symbolic impedance function of the lumped element circuit to which the characteristic impedance is to be fitted in terms of the radial frequency (w) and the lumped element values. This is done using basic circuit theory.

Select a range for each of the lumped element parameters determined in the previous step.

Using a nested for loop structure, cycle through all the possible combinations of the function parameters, computing the impedance as a function of frequency at each point.

For each combination of lumped parameters, determine the sum of the square of the difference between the impedance function computed impedance and the fitted polynomial impedance at each frequency point (i.e.

$$Error_{sum\_squared}(parameter_1, parameter_2, parameter_3, ...) = \sum_{\omega=\omega_{min}}^{\omega_{max}} \left[\left(Z_{polyfit}(\omega) - Z_{impdance\_function}(\omega, parameter_1, parameter_2, parameter_3, ...) \right)^2 \right]$$

). This is then the sum-squared- error value for each possible combination of lumped parameters.

The combination of parameter values at which the sum-squared-error is a minimum value is then chosen as the parameter set at which the model will fit the impedance characteristic best.

Using the determined lumped element parameter values, the derived form of the lumped impedance model can now be plotted.

The MATLAB code used to perform this algorithm for the simple model of Figure 56, represented by the impedance characteristic function of equation (2.12) is as follows. This code was used to generate the standard loaded dipole lumped element models referred to in this report.

```
% This is an m-file to fit a circuit impedance function to a given measured/simulated
%  Input impedance of an antenna using a simple lumped element model

clc
clear all

% The simulated/measured impedance (frequency real imaginary)
d=[**data format: Frequency ; Real ; Imaginary**];

f=d(:,1);w=f*2*pi*1e6;
red=d(:,2);
imd=d(:,3);

data=red+j.*imd;

% fit a polynomial to the simulated data
datafit=polyfit(w,data,4);

% Determine the fitted polynomial values at chosen frequency points
w=linspace(10e6*pi*2,100e6*2*pi,100);
dataval=polyval(datafit,w);

% At the same frequency points, determine the minimum squared error by sweeping the parameters
ca=linspace(10e-12,100e-12,11);
ra=linspace(10,3000,11);
r=linspace(10,300,11);
c=linspace(10e-12,200e-12,11);

for o=1:11
```

```
o
for p=1:11
   for n=1:11
      for m=1:11
         r1=ra(o);
         r2=r(n);
         c2=c(m);
         c1=ca(p);
         wc1=j*w.*c1;
         wc2=j*w.*c2;
         wc1c2=-w.^2*c1*c2;
         Znum=r1+1./wc1+r2+1./wc2;
         Zden=r1*r2+r1./wc2+r2./wc1+1./wc1c2;
         Z=Zden./Znum;

         error=abs(dataval-Z);
         sqerror=sum(error.^2);
         if n==1
            if m==1
               if o==1
                  if p==1
                     minerror=sqerror;
                     c1fin=c1;
                     r1fin=r1;
                     c2fin=c2;
                     r2fin=r2;
                  end
               end
            end
         end
         if sqerror<minerror
            minerror=sqerror;
            c1fin=c1;
            r1fin=r1;
            c2fin=c2;
            r2fin=r2;
         end
      end
   end
end
end

% Using the determined parameters, plot the resultant impedance characteristic for comparison
r1=r1fin;
c1=c1fin;
r2=r2fin;
c2=c2fin;

wc1=j*w.*c1;
wc2=j*w.*c2;
wc1c2=-w.^2*c1*c2;
Znum=r1+1./wc1+r2+1./wc2;
Zden=r1*r2+r1./wc2+r2./wc1+1./wc1c2;
Z=Zden./Znum;

figure;plot(w/(2*pi*1e6),real(Z),'r',w/(2*pi*1e6),imag(Z),'r--',d(:,1),d(:,2),'k',d(:,1),d(:,3),'k--','linewidth',2);
legend('model impedance (real)','model impedance (imaginary)','simulated impedance (real)','simulated impedance
(imaginary)');grid on;box on;xlabel('Frequency (MHz)');ylabel('Impedance (\Omega)');
gtext(['r2=',num2str(r2),';  c2=',num2str(c2),'  r1=',num2str(r1),'  ;c1=',num2str(c1)]);
```